UNIVERSITY OF SOUTHAMPTON

FACULTY OF ENGINEERING AND THE ENVIRONMENT

Sustainable Energy Research Group

School of Civil Engineering and the Environment

Energy extraction by large tidal turbine arrays at sites around the Channel Islands

by

Daniel Stephen Coles

Thesis for the degree of Doctor of Philosophy

March 2017

UNIVERSITY OF SOUTHAMPTON

ABSTRACT

FACULTY OF ENGINNERING AND THE ENVIRONMENT

Thesis for the degree of Doctor of Philosophy

ENERGY EXTRACTION BY LARGE TIDAL TURBINE ARRAYS AT SITES AROUND THE CHANNEL ISLANDS

Daniel Stephen Coles

Tidal flows contain a predictable source of renewable energy that can be extracted using large tidal turbine arrays to generate clean, secure electrical power to meet rising demand. Studies of specific coastal sites around the UK generally conclude that electricity generation using large tidal turbine arrays can supply up to 20% of UK electricity demand. However these estimates vary depending on the method used, with many reliant on low temporal and spatial resolution flow data and crude methods for modelling energy extraction. To investigate these potential sources of error, a new 2D hydrodynamic model was built with significantly improved spatial and temporal resolution to simulate tidal flows around the Channel Islands, located off the West of the Cotenin Peninsula in Normandy, France. The most energetic flows at Alderney Race, Casquets and Big Russel were selected for detailed study.

Energy extraction by large arrays was simulated using the distributed drag method, where an area averaged array drag is applied uniformly over the array plot area. Laboratory experiments were conducted using porous fences to simulate flow through large, regular, multi-row arrays to quantify the accuracy of a commonly used array drag parameterisation. Results show agreement between experimental load cell measurements of fence drag and the numerical formulation of array drag within 10%. This was in part due to close agreement between the depth averaged velocity and the level of wake recovery between each row, which was robust over a wide range of fence spacings. Results from a simple force balance indicate that for rough beds, the presence of the porous fence arrays increased the contribution of drag from the bed by up to 95% due to an increase in pressure drag on roughness strips secured to the flume bed. These findings have implications for regional scale tidal turbine array modelling, where array layout along with site specific characteristics such as turbulence intensity and bed profile determine the validity of the distributed drag approach.

The distributed drag method was implemented in the hydrodynamic model to quantify an upper bound for energy extraction at each site. Based on the distribution of mean ambient kinetic power and suitable depths, ambient flow simulations estimate the total area suitable for tidal energy development is likely to be up to 70% smaller than previously predicted. Energy extraction results confirm that Alderney Race contains the majority of the Channel Islands resource, where an upper bound of 5.1 GW exceeds that of the Pentland Firth, the best known site for tidal energy development in the UK by 35%. This was followed by Casquets (0.47 GW) and then Big Russel (0.25 GW). Increased drag in Alderney Race caused flow to be diverted through Casquets, resulting in an increase in volume flux of up to 25% and an increase in extracted power of up to 75%. This interdependency highlights the need for array layouts at Alderney Race and Casquets to be designed in tandem, otherwise the total energy extraction is likely to be under estimated.

Within Alderney Race simulations were run with arrays overlaid on regions of high mean kinetic power distribution. To assess array feasibility, results were compared with the output of the London Array, the world's largest offshore windfarm, using mean generated power per swept area as a suitable metric for comparison. The analysis indicates that an array in the most energetic region of Alderney Race with the same array density but covering an area a tenth of the size can achieve a mean power output per total swept area of 2.2 kW/m^2, ten times that of the London Array.

Table of Contents

List of Tables

List of Figures

DECLARATION OF AUTHORSHIP

I, Daniel Stephen Coles declare that this thesis entitled:

Energy extraction by large tidal turbine arrays at sites around the Channel Islands

And the work presented in it is my own and has been generated by me as the result of my own original research.

I confirm that:

1. This work was done wholly or mainly while in candidature for a research degree at this University;
2. Where any part of this thesis has previously been submitted for a degree or any other qualification at this University or any other institution, this has been clearly stated;
3. Where I have consulted the published work of others, this is always clearly attributed;
4. Where I have quoted from the work of others, the source is always given. With the exception of such quotations, this thesis is entirely my own work;
5. I have acknowledged all main sources of help;
6. Where the thesis is based on work done by myself jointly with others, I have made clear exactly what was done by others and what I have contributed myself;
7. Parts of this work have been published as:

Coles DS, Blunden LS, Bahaj AS, 2016, Experimental validation of the distributed drag method for simulating large marine current turbine arrays using porous fences, International Journal of Marine Energy, Elsevier, Vol 16, pp. 298-316.

Coles DS, Blunden LS, Bahaj AS, 2017, Assessment of the energy extraction potential at sites around the Channel Islands, Energy Journal, Elsevier, Vol 124, pp. 171-186.

Signed: .....

Date: 16/03/2017……

Acknowledgements

I would like to extend thanks to the following:

-EPSRC and the Supergen Marine programme that funded this research.

-my supervisors Prof. AbuBakr Bahaj and Dr. Luke Blunden for their support and guidance.

-Alderney Commission for Renewable Energy (ACRE) and Alderney Renewable Energy Ltd (ARE) for the supply of bathymetry and AWAC velocity data in Alderney Race, which were used to validate the English Channel Model.

-Jean-Michel Hervouet and fellow Telemac developers and forum users for their help with computational modelling problems, of which there were many.

-Dr Toru Tsuzaki, Karl Scammel, Dr Brad Keogh and Khilan Shah for their support in operating the Chilworth indoor flume.

Notation

A Amplitude of tidal constituent

A_a Total frontal area of all porous fences within an array

A_f Frontal area of a single porous fence

A_s Swept area of tidal turbine

A_p Plot area of an array – the area within the perimeter of the array

B Body force acting on control volume

C_a Array drag coefficient

C_b Bed drag coefficient

C_d Turbine drag coefficient

C_e Area averaged array drag coefficient

C_f Porous fence drag coefficient

C_p Turbine power coefficient

d Zero plane displacement

d_{90} Roughness diameter with 90% finer by weight

F_a Array drag force acting normal to the flow

F_b Bed drag force acting normal to the flow

F_d Turbine drag force acting normal to the flow

F_f Fence drag force acting normal to the flow

F_W Weight force of fluid

Fr Froude number

f Nodal amplitude correction factor

G Universal gravitational constant

G Phase of tidal constituent

g Acceleration due to gravity

h Depth

I Turbulence intensity

k_s Effective Nikuradse grain roughness height

I Turbulence intensity

L Characteristic length scale

l_a Longitudinal array length

l_f Longitudinal spacing between fences

l_z Fence height

M Mass of planet

N Total number of tidal constituents

n Row number

P Turbine power

P_A Average available power

P_K Average kinetic power

P_E Average extracted power

P_M Maximum average power potential

p Pressure

t Time

Q Volume flux

R Distance between the centre of mass of the Earth and Moon

Re Reynolds number

Ro Rossby number

r Turbine radius

s Scale ratio

t Time

U Streamwise velocity

U_0 Ambient streamwise velocity

U' Velocity fluctuation in the streamwise direction

$\overline{U}$ Depth averaged streamwise velocity

u Nodal correction factor

u_* Friction velocity

V Transverse velocity

V Equilibrium phase

V' Velocity fluctuation in the transverse direction

W Vertical velocity

W' Velocity fluctuation in the vertical direction

w Flume width

x Distance downstream of turbine

z Vertical height above boundary surface

z_0 Roughness length

Greek alphabet

α Wake entrainment constant

δ Boundary layer thickness

γ Forcing constant

η Free surface elevation

θ Flume bed slope angle

κ Von Karman constant

λ Array density; the ratio of total frontal device swept area to array plot area

ρ Density of fluid

τ Shear stress acting over a surface or bed

φ Latitude

ω Angular speed of tidal constituent

Ω Angular speed of rotation

Subscripts

e Earth

H Hub height

I Inertial

i Inlet

j Index representing tidal constituent

M Model

m Moon

max Maximum

n Turbine/fence row number within array

o Outlet

P Prototype

r Roughness

s Sub-array

t Turbine

$trans$ Transition

v Viscous

w Wake

x Streamwise

y Transverse

z Vertical

0 Ambient

1 Lower

2 Upper

∞ Equilibrium

Superscripts

+ New value due to presence of array

Acronyms

ACRE	Alderney Commission for Renewable Energy
ADCP	Acoustic Doppler Current Profiler
ARE	Alderney Renewable Energy Ltd
AWAC	Acoustic Wave and Current Profiler
CM	Centre of mass
COP	Conference of Parties
FAB	France-Alderney-Britain
RANS	Reynolds Averaged Navier Stokes
SIF	Significant Impact Factor

Chapter 1: Introduction

1.1 Background

The development of new methods for generating electrical power have been born from fears predominantly relating to increasing energy demand, energy security and global warming. A recent study regarding the former by the U.S Department of Energy estimates the global demand for energy will increase by 56% in the next three decades, largely in the developing world due to rising prosperity from economic growth, causing shortfalls in supply (U.S. Energy Information Administration 2014). Developed countries such as Japan have also experienced times of insufficient supply, where after the 2011 Fukushima nuclear disaster all 42 nuclear reactors were shut down, creating a 33 GW gap in electrical power generation equating to 23% of total supply. As a result government asked businesses and households to reduce electricity consumption by up to 15% to avoid blackouts.

Measures to avoid supply shortages normally rely on importing energy from countries with a surplus, with little control over cost. This was true in Germany where wholesale electricity costs were estimated to have risen 11% in 2015 as a result of increased natural gas imports from Russia after nuclear reactors were shut down (Knopf et al. 2012), also as a consequence of the Fukushima nuclear disaster.

Compounding the problem further are findings that to avoid dangerous atmospheric warming greater than 2°C above pre industrial levels, anthropogenic carbon emissions must be reduced significantly (International Panel on Climate Change 2014). In 2015 during the 21st Conference of Parties (COP21), 187 countries set out a new legally binding agreement effective in 2020 to limit warming to around 1.5°C. This relies heavily on rapidly phasing out the use of fossil fuels for electrical power generation, paving the way for renewable technologies.

Marine currents are one such source of renewable energy with the potential to generate clean predictable electrical power at suitable sites, determined predominantly by high velocities and appropriate depths. The relative planetary motion of the Earth and Moon around the Sun force the cyclic motion of the oceans tides which when constricted by channels and headlands on the continental shelf provide regions of high kinetic energy density. This energy can be extracted using large arrays of subsea turbines driven by these fast moving currents, which in turn drive generators to produce electrical power. Currently no such arrays exist and single device operation is limited mainly to prototype testing of single devices (Myers & Bahaj 2010; A. S. Bahaj et al. 2007) or the interaction between only a few devices (Bahaj & Myers 2013). The future

deployment of large tidal turbine arrays is reliant on the development and validation of methods for modelling large scale energy extraction to reduce uncertainty in energy yield forecasts. Conclusions from a recent review by the Offshore Renewable Energy Catapult states that investor concerns about high/unquantified risk from energy yield uncertainty are a major barrier to mainstream deployment (Offshore Renewable Energy Catapult 2015). Quantifying and reducing uncertainty in energy yield estimates can increase investor confidence in the industry and reduces the risk of unsuccessful projects.

1.2 Large arrays

First generation tidal turbines are rated at approximately 1 MW, so for significant power generation large arrays with hundreds of devices are needed, similar to windfarms (Bahaj 2011; Vennell et al. 2015). The power generated by a tidal turbine is highly sensitive to the tidal stream velocity. Within an array of turbines, the velocity is influenced by the ambient inflow velocity and turbulence, the co-existence of multiple superimposed wakes from upstream turbines, wake added turbulence and local bathymetry, limiting the ability to predict power generation and optimise array layouts. Since generated power is a function of the velocity cubed, to maximise array power the longitudinal row spacing between turbines must be sufficiently great that downstream velocity deficit within the wake of upstream turbines is minimised. On the other hand there will be a limit on the acceptable longitudinal spacing between a given number of turbine rows to reduce cabling costs (Culley et al. 2016). This will also minimise the array footprint from a spatial planning point of view, so as not to encroach on areas where other industries such as fishing and shipping operate. It will also be necessary to quantify the potential environmental impact of large arrays such as enhanced levels of sediment transport depending on the proximity of turbines to sandbanks (Haynes 2015). These considerations make it unlikely that single row arrays spanning the width of a channel can realistically be implemented, as has been considered in the past (Garrett & Cummins 2005; Blanchfield et al. 2008; Draper et al. 2014; Walters et al. 2013). There is now a need to understand the flow dynamics through multi-row array layouts to maximise energy extraction and spatial efficiency whilst also whilst minimising environmental impact and array footprint at specific sites.

1.3 The Channel Islands

Figure 1.1 shows the location of Alderney Race, Casquets, Big Russel, North West Guernsey and North East Jersey, five sites located around the Channel Islands. The sites have been identified as

suitable for tidal energy development based on suitable velocities and depths for first and second generation tidal turbines (Environmental Change Institute 2005).

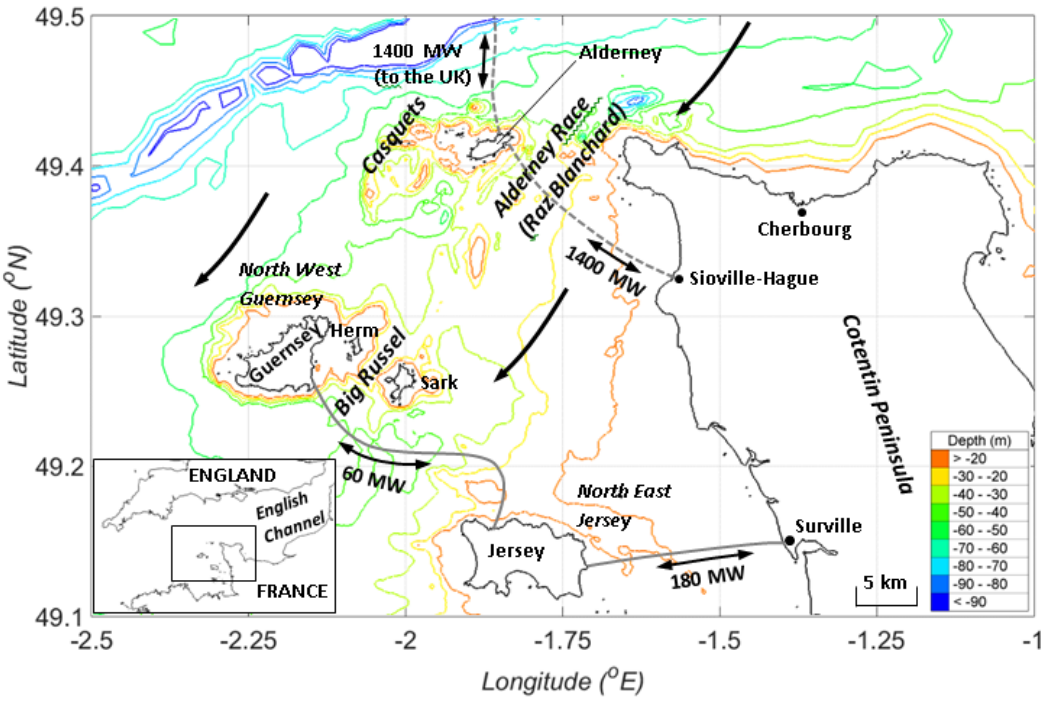

Figure 1.1 The Channel Islands, with the location of Alderney Race (Raz Blanchard), Casquets, Big Russel, North West Guernsey and North East Jersey. Arrows show the direction of the dominant ebb tide. The routes and capacity of interconnector cables are also shown.

Within Alderney Territorial Waters, the regulator Alderney Commission for Renewable Energy (ACRE) have divided the waters in Alderney Race and the Casquets into 94 rectangular blocks for developers to lease as shown in Figure 1.2. Each lease plot has an area of 1 square mile but significantly different bathymetry and velocity characteristics. In 2008 Alderney Renewable Energy Ltd (ARE) secured a 65 year license from ACRE along with the States of Alderney to develop tidal energy projects within 48 of these plots.

The first proposed large array within Alderney territorial waters is a 300 MW array, consisting of 150 x 2 MW devices with subsea gravity bases (Race Tidal 2014). Installation is expected to begin in 2020 but currently no formalised array location or turbine layout has been agreed upon. The proposed turbines have a diameter of 16 m, however the whole device including the support structure is 26 m wide and 18 m high, so significantly more than the turbine in isolation. The turbine structure uses its own weight to penetrate the sea bed with rock spikes, removing the need for drilling, pilling or pinning operations that cause significant noise to disrupt local ecology. It has initially been proposed to position each turbine within a 40 x 200 m grid using a staggered formation, which is assumed to be satisfactory to avoid turbine wake interaction with

neighbouring turbines (ABPmer 2013). This assumption is based upon limited wake data so there is high degree of uncertainty associated with this assumption, bringing into doubt claims that if fully developed, Alderney waters could provide up to 6 TW h of electrical power per year (Race Tidal 2014).

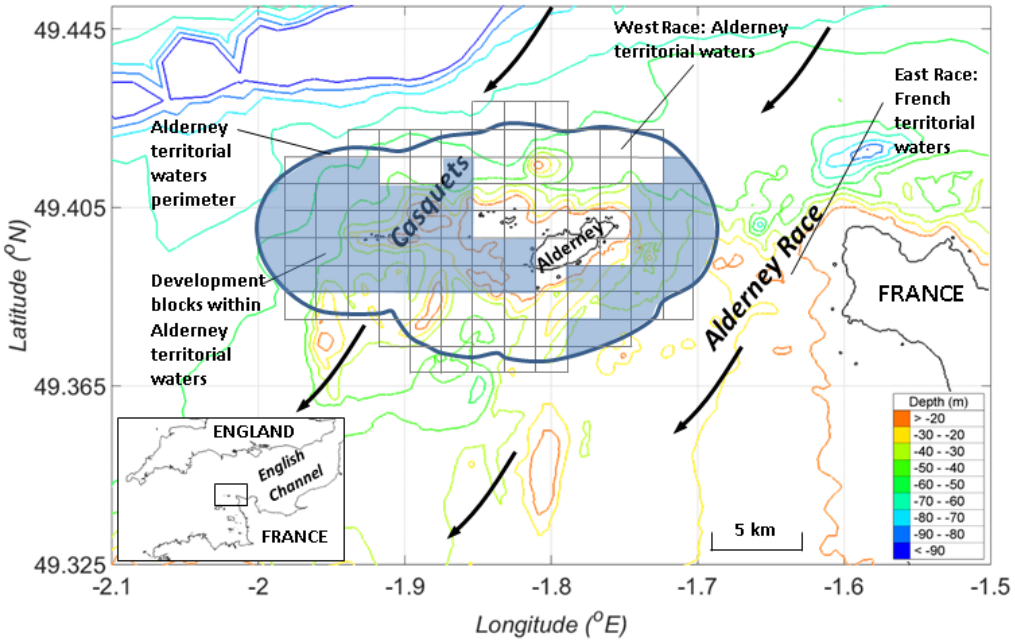

Figure 1.2 Location of development blocks (shaded) set out by Alderney Commission for Renewable Energy (ACRE) over Alderney Race and Casquets within Alderney territorial waters. Arrows show the direction of the dominant ebb tide.

Given that Alderney's peak demand for electricity is only 1.5 MW, it has been proposed that the array will supply electricity to Alderney, Britain and France using a new 1.4 GW capacity subsea electrical interconnector termed FABlink linking France with the UK, with construction due to start in 2018 (FAB Link Limited 2016). The cable routes and capacity of subsea cables connecting Alderney, Jersey and Guernsey to mainland France and the UK are shown in Figure 1.1.

Regarding the French territorial waters in the West Race, French government issued a call for expression of interest in 2013 to support and deploy pilot tidal farms. This initiated plans to install 4 x 1.4 MW Alstrom devices in 2017. Strategically Alderney Race offers France a significant resource which if harnessed will aid in meeting its targets to achieve 32% electricity generation from renewables by 2030.

Table 1.1 summarises previous estimates for the generated power from tidal stream turbine arrays in Alderney Race (also known as Raz Blanchard), the largest site with the greatest tidal energy resource in the Channel Islands.

Table 1.1 Summary of previous estimates for the annual power generation at Alderney Race using large tidal turbine arrays.

Study	Array capacity	Estimated power	Capacity factor
(Energy Technology Support Unit 1993)	2.4 GW	5.2 TW h/year	0.26
(European Commission 1996)	1.9 GW	6.5 TW h/year	0.4
(Bahaj & Myers 2004)	0.84 GW	7.4 TW h /year	0.4
(Myers & Bahaj 2005)	1.5 GW	1.35 TW h/year	0.1

Whilst the resource at Alderney Race is significant, estimates vary between 1.35-7.4 TW h/year depending on the method used and size of array considered. This wide range in estimated power generation suggests that current methods cannot predict the resource to a sufficiently high level of certainty. In general studies rely on low spatial and temporal resolution flow data and simplistic methods for modelling energy extraction that neglect the effects tidal turbine(s) have on the surrounding flow and available resource.

Further energy yield uncertainty arises from unclear regulation. For example, it is conceivable that the power generated by the first array to be installed in Alderney Race could be detrimentally affected by the change in flow field caused by the later installation of a second large array in a neighbouring lease plot. Currently there is no understanding of how this interaction between arrays should be addressed. This extends to site-site interaction. For example Alderney Commission for Renewable Energy (ACRE) is responsible for licensing and regulating the operation, deployment and management of all forms of renewable energy on the island and in its territorial waters. The East Race lies in French territorial waters so is regulated by the French government. Currently there is no clear understanding of how best to optimise Alderney Race for electricity generation, where interaction between arrays within the East and West Race as well as Casquets will inevitably become important, requiring cooperation between ACRE and French regulators.

Given the range and uncertainty in previous results as demonstrated in Table 1 for Alderney Race, the Channel Islands sites were chosen as suitable case study locations where valuable added knowledge could be contributed to improve confidence in energy yield predictions. Improving the current state of the science can lead to increased future investment in tidal energy on the path to reducing carbon emissions from electricity generation.

1.4 Aims and objectives

The aim of this work is to quantify the electrical power that can be generated using large tidal turbine arrays at sites around the Channel Islands using regional scale hydrodynamic modelling techniques. This will be fulfilled by completing the following objectives:

1. Experimentally validate a method for parameterising array drag in regional scale 2D hydrodynamic models.
2. Build and validate a 2D hydrodynamic model to simulate flow around the Channel Islands at improved temporal and spatial resolution.
3. Quantify energy extraction by large tidal turbine arrays at suitable sites around the Channel Islands.
4. Establish feasibility metrics for assessing energy extraction by large scale tidal turbine arrays at sites around the Channel Islands.

1.5 Report structure

Chapter 1: Introduces tidal energy technology, the challenges in developing tidal sites for electrical power generation using large arrays and the suitability of sites located within the Channel Islands.

Chapter 2: Literature review of previous research relevant to development of models for simulating flow through large tidal turbine arrays and resource assessments quantifying energy extraction at sites around the Channel Islands.

Chapter 3: Outline of experimental method used to characterise flow through large arrays of porous fences in a recirculating flume. Results are presented later in Chapter 5 to validate a method for modelling large arrays numerically in 2D hydrodynamic models.

Chapter 4: Methodology for the modelling approach taken to simulate tidal flows and energy extraction using large arrays at sites around the Channel Islands.

Chapter 5: Results from experimental flume testing of flow through large arrays of porous fences, with a study validating the parameterisation of array drag in a 2D numerical formulation of array drag.

Chapter 6: Validation of the English Channel model, followed by characterisation of ambient flow at Alderney Race, Casquets, Big Russel, North West Guernsey and North East Jersey.

Chapter 7: Results estimating energy extraction at Alderney Race, Casquets and Big Russel. Results compared with recorded output data from the London Array, the world's largest offshore windfarm.

Chapter 8: Conclusions and suggestions for further work

.

Chapter 2: Review of methods for estimating energy extraction from large arrays

2.1 Overview

To date, tidal turbine research has focused predominantly on single turbines and small cluster arrays of up to ten turbines (A. S. Bahaj et al. 2007; A. Bahaj et al. 2007; Brutto et al. 2015). Inside large, multi-row arrays, the power generated by individual turbines is affected by additional factors (in comparison to isolated turbines) such as array scale blockage, the co-existence of multiple superimposed wakes and wake added turbulence. This chapter reviews methods developed for characterising these in-array flow features and their effects on the performance of individual turbines within large arrays. Focus is given to regular turbine layouts (i.e. equal longitudinal spacing between straight rows and equal lateral spacing between turbines in each row), which have received significant attention in the relevant field of wind energy research to establish the overall performance of large windfarms. This review was conducted to establish the most suitable method to develop and implement in proceeding chapters to quantify energy extraction at sites within the Channel Islands.

2.2 'Large array' definition

In literature 'large tidal turbine array' has not been clearly defined and instead the classification of array size varies widely depending on the research approach. One perspective is to define a large array as blocking more than 2% - 5% of a channel's cross section, so that the array influences the channel scale dynamics enough that the power output per turbine differs by more than 5% from that of an isolated turbine (Vennell et al. 2015). These changes include an increase in head loss across the array and a decrease in volume flux through the array (Sutherland et al. 2007), however this definition implies that for a small channel a large array can consist of only two turbines. Observations from windfarms (Barthelmie et al. 2005) and scaled down experiments (Chamorro & Porté-Agel 2011; Harrison 2008) show 'large arrays' with more than 4 rows reach equilibrium conditions, where after the fourth row the flow dynamics between each row repeat and the wake recovers to the same magnitude by the point it reaches the next row. For tidal arrays this is caused by a balance between the longitudinal pressure gradient driving the flow and the drag from turbines and the seabed. The repeating flow pattern between turbine rows gives an even distribution in drag

amongst turbine rows. This finding supports an area averaged approach such as the distributed drag method, where drag is applied uniformly over the array plot area. The array plot area is defined as the total plan area taken up by the array (discussed in 2.3.2). Other definitions give a clearer indication of the energy extraction potential of the array, where a large array exceeds a specific array capacity or predicted annual generation for example.

For this work, an array is defined as 'large' if it has more than four equally spaced rows to investigate equilibrium conditions as flow develops through arrays. Assuming the lateral and longitudinal spacing between devices does not exceed realistic values for spatially efficient array development of approximately 5 and 20 diameters respectively, this also satisfies the Vennell (2015) definition where turbines no longer perform as isolated turbines due to influences of the array on the flow dynamics.

2.3 Area averaged methods

2.3.1 Boundary layer approach

In early windfarm research a boundary layer approach was adopted to quantify the velocity reduction through large windfarms (Templin 1974; Newman 1977; Crafoord 1979; Moore 1979; Bosanyi et al. 1980). In this approach the forces on individual turbines are evenly distributed horizontally over the windfarms plot area to produce a uniform increase in surface shear stress. For an atmospheric boundary layer in the absence of turbines the ambient velocity varies logarithmically with height above the ground as described by 2.1,

$$U_0(z) = \frac{u_*}{\kappa} ln\left(\frac{z}{z_0}\right) \qquad 2.1$$

where $U_0(z)$=ambient streamwise velocity at height z, z=height above the boundary surface, u_*=friction velocity, κ=Von Karman constant and z_0=roughness length. It is assumed that whilst the addition of a windfarm alters the velocity within the windfarm, the vertical velocity distribution remains logarithmic in nature with a new friction velocity and roughness length. The new logarithmic velocity profile is described by Equation 2.2:

$$U(z) = \frac{u_*^+}{\kappa} ln\left(\frac{z}{z_0^+}\right)$$

2.2

Where $U(z)$=streamwise velocity at height z within the windfarm, u_*^+= new friction velocity with the addition of the windfarm) and z_0^+=new roughness length with the addition of the windfarm. (I.e. superscript + denotes the new value of friction velocity and roughness length due to the addition of the windfarm). Within the windfarm, the shear stress acting over the farms plot area is the sum of the surface shear (commonly known as the 'terrain shear') and the additional shear caused by the turbine drag which is given by Equation 2.3 :

$$\tau = \rho\left((u_*^+)^2 + \frac{1}{2}\lambda C_d U^2\right)$$

2.3

Where τ=shear stress, ρ=fluid density, u_*^+=friction velocity (with the addition of the windfarm), λ=turbine density, C_d=turbine drag coefficient and U=streamwise velocity within the windfarm. Turbine density is defined as the ratio of the total swept area of all turbines within the farm to the plot area of the farm, where the plot area is defined as the area within the perimeter of the farm.

Commonly it is assumed that the windfarm reduces the terrain shear contribution in comparison to the ambient case without the windfarm in place. Alternatively one study assumes the reduction in surface shear stress is negligible (Newman 1977). Crafoord (1979) assumes that shear stress is proportional to the square of velocity 0.15 m above the ground. In (Templin 1974) the same approach is adopted but relates surface stress to an equivalent sand grain roughness height. Moore (1979) assumes the relevant velocity to be below the turbine blades, suggesting that terrain shear may increase with the addition of the windfarm.

Based upon three measurements taken below hub height two rows into the Norrekaer Enge II windfarm, Frandsen (1992) assumed a dual-logarithmic velocity distribution in the vertical plane within windfarms, where the profiles meet at the hub height of the turbines. This dual-log velocity distribution is illustrated in Figure 2.1, which also shows the shear stress between the two logarithmic velocity profiles and the external turbine force.

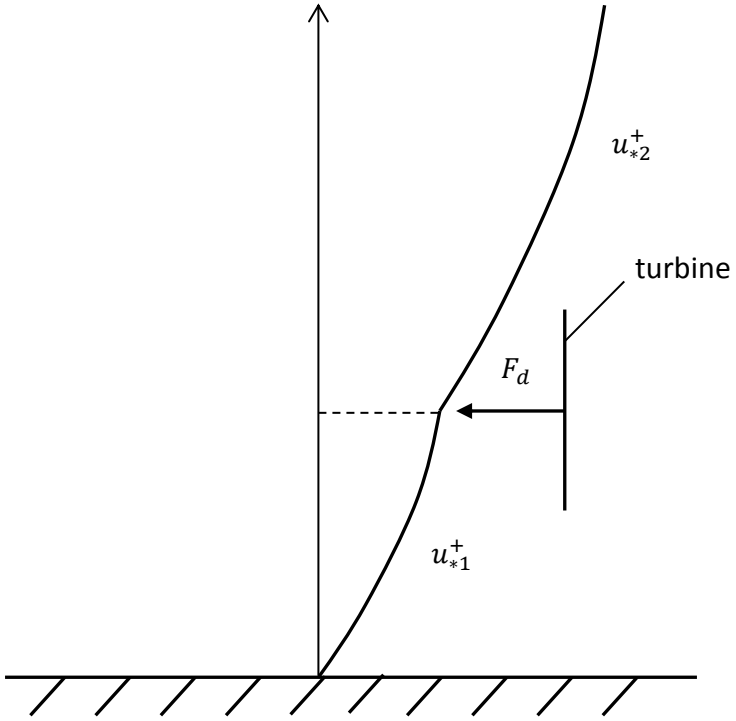

Figure 2.1 Illustration of the dual-logarithmic velocity profile, corresponding friction velocities and turbine drag force acting inside a control volume inside a windfarm.

A force balance between the two logarithmic layers illustrated in Figure 2.1 gives:

$$F_d = \rho((u_{*2}^{+})^2 - u_{*1}^{2}) \qquad 2.4$$

Where F_d=turbine drag force, ρ=fluid density, u_{*1}^{+}= friction velocity of the lower logarithmic velocity profile within the windfarm and u_{*2}^{+}= friction velocity of the upper logarithmic velocity profile within the windfarm. Frandsen (1992) assumed the roughness height below hub height remains unchanged with the inclusion of a windfarm, whilst above hub height the geostrophic drag law relates the geostrophic wind, coriolis variable and roughness length to the shearing stress at the Earth's surface for planetary boundary layers (Swinbank 1974). This allows the equations to be solved for velocity at hub height to give the spatially averaged hub height velocity inside large windfarms.

The sparse nature of data collected at Norrakaer Enge II wind farm brings into question the validity of the dual log assumption. Calaf (2010) applied a similar force balance with three separate layers, the first below the turbine, the second in the turbine region and the third above the turbine, yielding

a higher upper layer roughness height than those predicted by a dual log profile, which was significant when comparing results for power using high density windfarms.

For windfarms, at some point above the array conditions reach a free stream fixed by external conditions, where the loss of momentum from the drag on turbines is replenished by the flow above. For tidal turbine arrays, the boundary layer extends all the way up to the free surface, where the fraction of the boundary layer (or in this case depth) occupied by devices is significantly higher. The flow in this case is driven by the longitudinal pressure gradient due to the sea surface slope (Campbell et al. 1998).

Blunden (2009) used boundary layer theory based on flow through windfarms and submerged vegetation to develop a method for modelling flow through large tidal turbine arrays. To quantify the area averaged array drag coefficient, Blunden introduced a zero plane displacement, which is the vertical distance above the bed at which obstacles cause the velocity to reduce to zero. This is physically equivalent to the mean height above the bed of momentum absorption by the bed (Raupach et al. 1991) and can be found by calculating the centroid height of the drag profile in the roughness (Thom 1971). Using the approach taken by Frandsen (1992) a dual logarithmic velocity profile that meets at hub height was assumed within the array. The depth averaged velocity deep inside the array was defined as:

$$\overline{U} = \frac{1}{h}\left(u_{*1}^{+}\int_{0}^{z_H}\frac{1}{\kappa}\, ln\frac{z}{z_{0,1}^{+}}dz + u_{*2}^{+}\int_{z_H}^{h}\frac{1}{\kappa}ln\left(\frac{z-d}{z_{0,2}^{+}}\right)dz\right)$$

2.5

Where $\overline{U}$=depth averaged velocity, h =water depth, u_{*1}^{+}=friction velocity of lower velocity profile within the array, u_{*2}^{+}=friction velocity of upper velocity profile within the array z_H=vertical height above the bed to the turbine hub height, κ is the Von Karman constant, z=vertical distance above the boundary surface, $z_{0,1}^{+}$=roughness length of the bottom logarithmic profile, d=zero plane displacement and $z_{0,2}^{+}$= roughness length of the upper logarithmic profile. The new friction velocity of the lower logarithmic velocity profile is given as the sum of the resistive forces:

$$(u_{*1}^{+})^2 = \frac{1}{2}(C_b + \lambda C_e)\overline{U}^2$$

2.6

Where C_b=bed drag coefficient, λ=array density and C_e=area averaged array drag coefficient. The depth averaged velocity within the array is now known as a function of the new hub height velocity

so that the area averaged array drag coefficient can be found as a function of the other parameters. Questions left unanswered by this work include:

1. Is it correct to assume there is an even, area averaged distribution in drag amongst turbines within regular arrays?

2. What is the velocity distribution within and above the array? If it is logarithmic, at what height above the bed does it start and at what height do the two profiles meet?

3. What is the distribution of total drag resisting the flow between the turbines and the bed, and how is this affected by bed roughness properties?

2.3.2 Distributed drag method

An area averaged array drag coefficient is typically implemented in regional scale 2D hydrodynamic models in the early stages of resource assessment to quantify far field flow effects of large arrays (Bourban et al. 2013), optimise array shape (Ahmadian & Falconer 2012), quantify array-array interaction (Draper et al. 2014), quantify sediment dynamics (Thiebot et al. 2015) and quantify energy extraction (Draper et al. 2014; Walters et al. 2013; Plew & Stevens 2013; Karsten et al. 2012; Karsten et al. 2008; Blanchfield et al. 2008; Sutherland et al. 2007).

In this approach the array drag is applied uniformly over the array plot area (Jean-Michel Hervouet 2007; Plew & Stevens 2013; Walters et al. 2013) and parameterised using,

$$F_a = \frac{1}{2}\rho \overline{U}^2 C_d A_a \qquad 2.7$$

where F_a=array drag force acting normal to the flow, ρ=fluid density, $\overline{U}$=depth averaged velocity within the array, C_d=turbine drag coefficient and A_a=swept area of all turbine rotors within the array. Typically for tidal turbines a drag coefficient of 0.8 is used based on experiments of a scaled down tidal turbine, which assumes turbine drag is a function of the upstream volumetric velocity averaged over the turbine swept area (A. S. Bahaj et al. 2007). The shear stress acting on the bed is made up of a bed shear stress and added array shear stress. The added shear stress induced by the array over the array plot area is:

$$\tau^+ = \frac{F_a}{A_p}$$

2.8

Where τ^+=shear stress added by the array, F_a=array drag force acting normal to the flow and A_p=array plot area. This stress is added to the momentum equations to give an extra depth averaged source term in the form:

$$\frac{\tau^+}{\rho h} = \frac{\lambda C_d}{2h}|\overline{U}|\overline{U} = \frac{C_e}{h}|\overline{U}|\overline{U}$$

2.9

Where ρ=fluid density, h=depth and λ =array density, defined as the ratio of the total swept area of turbines within the array to the plot area. C_e is the area averaged array drag coefficient,

$$C_e = \frac{1}{2}\lambda C_d$$

2.10

The area averaged array drag coefficient is added to the bed drag coefficient to give the 2D formulation of combined drag as a shear stress acting over the array plot area (Plew & Stevens 2013):

$$\frac{\tau}{\rho h} = \left(\frac{C_b + C_e}{h}\right)|\overline{U}|\overline{U}$$

2.11

Where τ=shear stress (made up of a bed and array stress contribution) and C_b=bed drag coefficient.

2.3.3 Potential sources of error

Within 2D regional scale models, the velocity distribution is averaged over the depth so it is not possible to obtain volume averaged velocities over the turbine swept area directly from the model. Instead it is common practise to estimate array drag using Equation 2.7, which uses a depth averaged velocity obtained directly from the hydrodynamic model (Pérez-Ortiz et al. 2013; Draper et al. 2014; Adcock et al. 2013). Figure 2.2 illustrates the issue with using a depth averaged velocity to estimate the drag on turbines within arrays. For the case of a prominent wake incident on a downstream turbine as shown by the green velocity profile, the depth averaged velocity significantly over-predicts the velocity over the turbine swept area. In this case Equation 2.7 would significantly

over-estimate the turbine drag. This is likely to contribute a significant error to the overall array drag estimated using Equation 2.7.

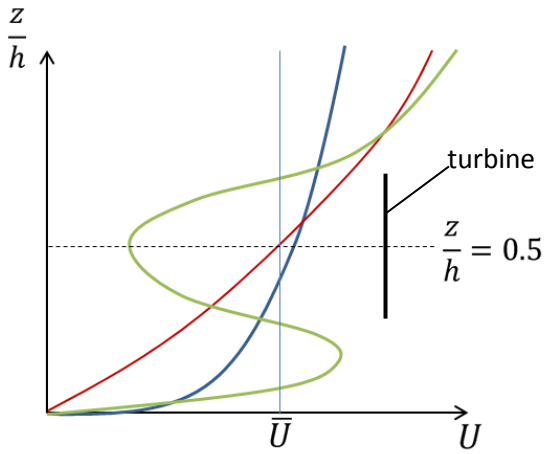

Figure 2.2 Illustration of typical flow distributions in the vertical plane within arrays of porous fences, all with the same depth averaged velocity. Dotted horizontal line intercepts each flow profile at the centroid height of the fences, *z/h*=0.5.

Conversely for the velocity profile illustrated by the blue line in Figure 2.2 , the depth averaged velocity under-predicts the velocity over the turbine swept area. Turbines within the first row exert a high drag force on the flow since they are incident on fast moving ambient flow. This creates a high velocity deficit within the wake downstream of the first row of turbines. Assuming the second row of turbines are positioned within the wake of the upstream row, this significantly reduces the drag force exerted by turbines within the second row. This uneven distribution in drag amongst the first two turbine rows cannot be modelled by an evenly distributed drag.

Field and experimental measurements show that after the second or third row of turbines the flow develops to an equilibrium state where there is an even distribution in drag amongst turbines within subsequent downstream rows (Barthelmie et al. 2005; Chamorro & Porté-Agel 2011). The distributed drag approach is more suited to modelling array drag within this equilibrium region but is likely to be erroneous over the first few rows of the array where there is an uneven distribution in drag amongst turbine rows.

Finally it is plausible that the presence of an array could affect the bed drag coefficient relative to the natural state in the absence of turbines as a result of flow acceleration (Moore 1979) and increased Reynolds stress in the region directly below the turbine (Myers et al. 2008).

An experimental methodology to quantify these potential sources of error is outlined in Chapter 3 using flume experiments to characterise the flow through porous fence arrays, with results presented in Chapter 5.

2.4 Kinematic models

Kinematic models developed for windfarms use linear expansion of the far wake to quantify the velocity deficit downstream of turbines. Recent studies use this approach to optimise the placement and therefor energy capture of individual turbines within a large arrays by minimising detrimental wake interference effects (Marmidis et al. 2008; Emami & Noghreh 2010; Kusiak & Song 2010; Saavedra-Moreno et al. 2011). This analytical approach remains the industry standard for windfarm design in industry.

The simple analytical wake model developed by Jensen (1983) for a single turbine assumes momentum is conserved in the uniform wake that spreads linearly as a function of downstream distance away from a turbine. Equation 2.12 describes the velocity downstream of a turbine,

$$U(x) = U_0\left(1 - \frac{2}{3}\left(\frac{r}{r + \alpha x}\right)^2\right) \qquad 2.12$$

where U= streamwise velocity, U_0=ambient streamwise velocity, r=turbine radius, x=distance downstream of the turbine and α=wake entrainment constant that describes the level of mixing between fast moving bypass flow and the wake. Figure 2.3 illustrates the uniform distribution in velocity across the wake, which assumes the wake is fully mixed by the time it reaches the next downstream turbine. It is also assumed that the velocity just downstream of the turbine is one-third that of the upstream velocity. More recent work assumes a Gaussian distribution in wake velocity deficit validated against high resolution wind-tunnel measurements (Bastankhah & Porté-Agel 2014). Results show the 'top hat' approach adopted by Jensen (1983) tends to underestimate the wake deficit at the wake centre and overestimate it around the wake edge.

Based on empirical data Jensen (1983) assumes that for normal wakes the entrainment constant is 0.1. More recent work that quantifies the wake downstream of a porous disk in a fluid flow shows the wake entrainment is dependent on the ambient turbulence intensity, so will vary depending on site specific conditions (Blackmore et al. 2013; Blackmore et al. 2014).

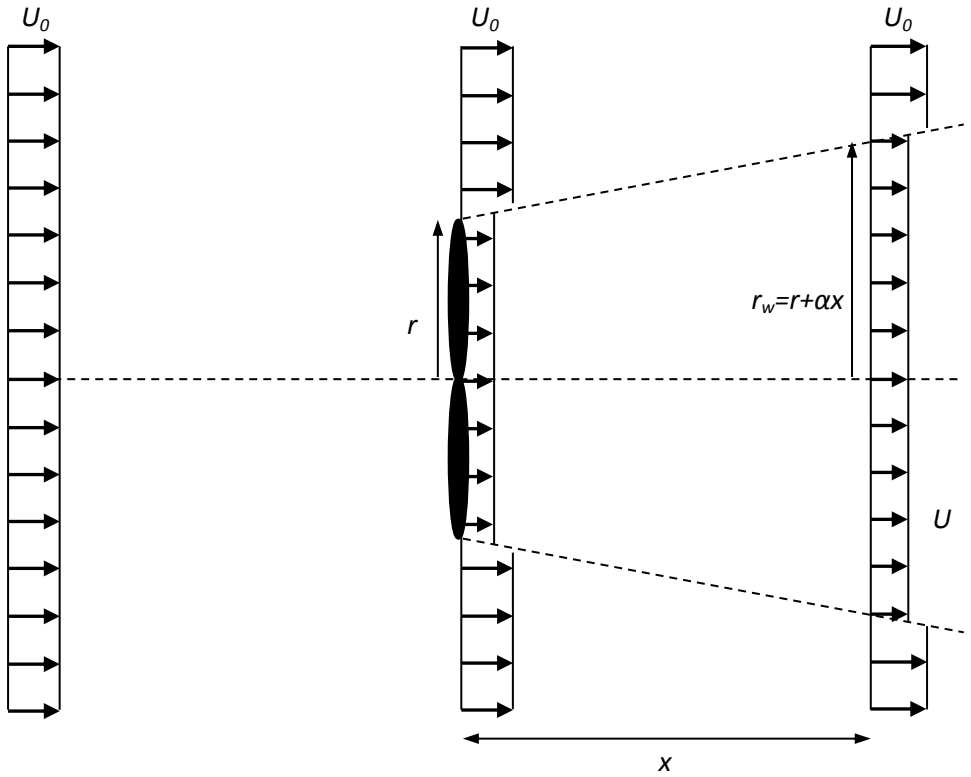

Figure 2.3 'Top hat' flow distribution downstream of wind turbine used to develop simple kinematic model.

Brutto (2015) adapted the method originally developed by Jensen (1983) for windfarms for an array of five tidal turbines positioned one behind the other at 10 diameter spacing, as well as an array of ten staggered devices. Results were validated against results from a three dimensional numerical model using actuator disks to simulate each device, showing velocity agreement mostly within 5%. The influence of ambient turbulence intensity on wake expansion was investigated by running a three dimensional numerical model using actuator disks simulations with ambient turbulence intensities of 8%, 15% and 20%. Results show significantly improved wake recovery at higher ambient turbulence intensity as would be expected, caused by enhanced mixing between the wake and bypass flow. Curve fitting was used to relate the wake entrainment constant to the expansion of the wake radius giving agreement within 5% of computational results in the far wake 10 diameters downstream of the turbine.

$$\alpha = 0.5I_0 + 0.02$$

2.13

Where α= wake entrainment constant and I_0=ambient turbulence intensity. The validity of this model is still unclear and experimental validation is needed. This is especially prevalent given that it has been shown experimentally by Blackmore (2014) that the entrainment constant is also a function of the integral length scale of the flow, which quantifies the length scale of the energy containing turbulent eddies within the flow.

Jensen (1983) also assumes the wake can expand freely so that there is no interference with the ground, which supresses downward wake expansion due to the presence of a physical boundary, hence reducing wake recovery which is likely to overestimate wake recovery. The model agrees within 12% of velocity measurements in the wake downstream of a vertical axis wind turbine (Vermeulen et al. 1979). Good agreement was indicated with hub height wake measurements downstream of a 20 m diameter wind turbine using a wake entrainment constant of 0.1, however the exact level of agreement was not quantified.

The model developed by Jensen (1983) was applied to an array with ten rows, with each row containing a single turbine. Equation 2.14 describes the velocity downstream of the wind turbine in row *n*, where the row furthest upstream is row one and row numbers ascend downstream of row 1.

$$\frac{U_n}{U_0} = 1 - \left(1 - \frac{1}{3}\left(\frac{U_{n-1}}{U_0}\right)\right)\left(\frac{r}{r + \alpha x}\right)^2$$

2.14

Where U_n=streamwise velocity downstream of row n, U_0=ambient streamwise velocity, r=turbine radius, x=distance downstream of the turbine and α= wake entrainment constant. This leads to an asymptotic expression for the equilibrium velocity in front of downstream turbines inside a large array, where for equilibrium conditions:

$$\frac{U_n}{U_0} - \frac{U_{n+1}}{U_0} = 0$$

2.15

$$\frac{U_\infty}{U_0} = 1 - \frac{2x}{1 - x};\ x = \frac{1}{3}\left(\frac{r}{r + \alpha x}\right)^2$$

2.16

Where U_∞=equilibrium streamwise velocity, which is the velocity within the equilibrium region of the array. Using momentum conservation it was shown that for an infinitely large number of wind

turbines where wake cross sectional area expands linearly with downstream distance, wake expansion must be proportional to $x^{1/2}$ to ensure asymptotically a non-vanishing and non-increasing velocity, assuming no lateral wake interaction (Frandsen et al. 2006).

2.4.1 Potential sources of error

For tidal turbine applications, as arrays are built up by adding more turbines, the total array drag increases. This causes an array scale blockage effect, creating an increase in head across the array (through an increase in depth upstream of the array), a reduction in the upstream velocity and flow redirection around the array. This change to the surrounding flow field impacts upon the power generated by the array and so as the number of turbines within an increases, the applicability of kinematic models diminishes.

The validity of kinematic models over a wide range of ambient conditions has not been investigated. For example, defining the wake entrainment constant is problematic as it is influenced by many factors such as turbulence intensities and length scales, which can be induced by many factors such as the turbine itself, surrounding turbines and the bed. Jensen (1983) suggests 0.1, Barthelmie (2006) suggests 0.075 for onshore wind turbines and 0.05 for offshore, while Barthelmie & Jensen (2010) and Cleve (2009) suggest 0.04.

Ainslie (1985) developed a wake model using the Navier-Stokes equations with an eddy viscosity to model turbulent stresses (Reynolds stresses), solved using an implicit finite difference scheme. Ambient turbulence was modelled using an eddy viscosity defined in terms of the mean square ambient turbulence, which depends on the length scales and isotropy of the turbulence. Reynolds stresses due to shearing in a non-turbulent ambient flow were also accounted for based on centreline velocity deficit and a function for the build-up in turbulence in the near wake as a function of downstream distance based on empirical wake data. Results from the model are generally in good agreement with experimental data, however the same issue arises that the scaling factors for the ambient turbulence contribution to the eddy viscosity are tuned based on experimental data of a specific flow condition.

2.5 Coupled boundary layer- kinematic models (Array flow regimes)

Frandsen (2006) identified three regimes within large arrays. Regime 1, (also referred to as the transition zone) (Chamorro & Porté-Agel 2011) typically comprises the first three rows. In this region wakes expand axi-symmetrically and it is assumed that there is no lateral merging between adjacent

wakes, which relies on a large enough lateral spacing between turbines within the same row so that wakes do not encroach laterally on each other. This supports the approach of kinematic models to describe the velocity field, assuming the wake expansion coefficient can be accurately defined and blockage effects are not significant. Field measurements from the Horns Rev windfarm show that within regime 1, there is a high initial velocity deficit downstream of the first row, resulting in an initial drop in power from turbines in row 1 to 2 of 65%. This creates an uneven distribution in drag amongst the first three rows (Barthelmie et al. 2005; Frandsen et al. 2006), suggesting that an area averaged approach to flow modelling such as the distributed drag method is not suitable in regime 1.

In regime 2, which occurs directly downstream of regime 1, wakes merge laterally, impacting the rate of wake expansion. Various superposition schemes have been implemented to superimpose the velocity deficit of overlapping wakes. This includes the linear superposition of wakes used by Katic (1986) where the kinetic energy deficit of a mixed wake is assumed to be equal to the sum of the energy deficits for each wake, which agrees well with full scale measurements of wake interaction between two turbines. However, this approach can lead to error, such as negative velocities due to the superposition of multiple wakes (A. Crespo, J. Hernandez 1999).

In regime 3 (also referred to as the equilibrium region) the energy extracted by turbines is replenished from the boundary layer above, causing an even distribution in velocity and therefor even drag between turbine rows. This is supported by field measurements from the Horns Rev windfarm that show that the power generated by turbines in rows 4-10 levelled out to approximately 60% of turbines in row 1. Experiments by Chamorro et al. (2011) showed this regime starts downstream of row 6, where the flow above the top tip height was logarithmic and independent of position relative to turbine rows. This supports the application of area averaged methods, which for large-scale atmospheric models assumes a logarithmic boundary layer and the array drag is parameterised by an additional surface roughness or an added drag term in the distributed drag method. It is unclear at this stage if the same is true for large tidal stream turbine arrays given that there is no infinite boundary layer for momentum exchange above the array.

2.6 Experimental models

Neither area-averaged nor kinematic models are capable of yielding definitive estimates of power output from large arrays for a wide range of ambient conditions and array designs. Instead there is a reliance on a synthesis of theoretical, small scale experiments and full scale observational data to validate models as was the case in early windfarm research (Milborrow 1980). Scaled down

experiments can aid in providing a theoretical basis for parameterising adjustable coefficients that determine wake expansion, velocity deficit and array drag over a wide range of ambient conditions and array layouts in constrained flow to validate large tidal turbine array models.

2.6.1 Windfarms

Experimental testing of windfarms has shown the existence of an equilibrium velocity deficit inside large arrays, where the velocity recovers to the same magnitude downstream of each consecutive row to give an even distribution in drag amongst turbine rows. For example results from wind tunnel testing where groups of 37, 49 and 97 rotors in arrays were positioned in a scaled atmospheric boundary layer show equilibrium conditions observed after 5 rows, where turbines in the equilibrium region generated 52% less power than the power of turbines in row 1 in an array with seven rotor diameter spacing between rows (Builtjes 1979). Turbulence generated by upstream turbines enhanced momentum diffusion leading to faster wake recovery downstream devices, which reached equilibrium after approximately 4 rows. This same behaviour has been observed more recently in wind tunnel testing with an array of thirty model wind turbines in ten rows (Chamorro & Porté-Agel 2011). Each row contained three turbines with four diameter lateral spacing and seven diameter longitudinal spacing between rows. Results show the mean velocity and turbulent statistics reached equilibrium as close as the third or fourth row in the region below the top tip height of the turbines. The mean power output stabilized to approximately 51% of the first row with an ambient turbulence intensity of just 1% in the centre of the wind tunnel and upstream velocity of 2.5 m/s. This has also been observed at the Horns Rev wind farm, a full scale array consisting of eighty turbines in ten rows with seven diameter longitudinal and lateral spacing between devices (Barthelmie et al. 2005). Ambient wind velocities between 8-10 m/s and relatively low ambient turbulence intensity of 8% show the power levelling off after the 3rd row to approximately 60% of the first row.

2.6.2 Tidal arrays

The flow through large tidal turbine arrays was investigated experimentally using four porous fences, which simulate a densely packed row of turbines with no lateral spacing between turbines (Harrison 2008). This reduced the problem to two dimensions (vertical and longitudinal) as flow variations in the lateral direction were ignored. The fences had a height of 0.1 m and width of 0.95 m, and were placed in a flume with 1.37 m width. The flume was run with 0.3 m depth and an inlet velocity at mid depth of 0.23 m/s, which when scaled up with the channel Froude number corresponds to a full scale tidal velocity of approximately 2.5 m/s and 30 m channel depth. Fences

were positioned in the flume at mid depth, with longitudinal spacing between fences kept at seven fence heights and even spacing either side to the flume walls. Acoustic Doppler Velocimeter (ADV) measurements of velocity were taken downstream of one fence only, then behind two fences only and so on, along with load cell measurements of the force on each fence. Results show the velocity and turbulence intensity incident on each subsequent fence tending towards an equilibrium value, causing similar values of drag coefficient. The experiment was extended to a configuration of six fences and results show the velocity deficit at each fence location tending to a steady value of approximately 40% of the upstream ambient velocity. Turbulence intensity increased with each subsequent fence and consequently the wake recovered more slowly downstream of the most upstream fence (referred to as Fence 1 from now on), where turbulence intensity was lowest. These findings support the distributed drag method for modelling large arrays because a constant velocity through each row results in an even distribution in drag amongst each row, however parameterisation of the area averaged array drag still requires validation.

2.6.3 Reproducing turbulent boundary layers

In comparison with typical laboratory scale flows, site measurements show that tidal flows are highly turbulent with intensities typically around 10% (Thomson et al. 2012; Milne et al. 2013). Turbulence intensity affects both the mean drag coefficient of tidal turbines by up to 20% (Blackmore et al. 2014) and the rate of wake recovery, however little attention has been given to methods for recreating these tidal conditions in scaled down physical models (Bahaj & Myers 2003).

Perry (1969) categorised the scales characterising the roughness geometry of roughness strips spanning the width of a channel running perpendicular to the direction of flow. The roughness strips considered had rectangular cross section. The pitch ratio, defined as the ratio of the roughness height to horizontal roughness strip was used to define the roughness strip geometry. For a pitch ratio less than four (i.e. wall roughened by sparsely spaced roughness strips), the spacing between roughness strips is sufficient for separation, reattachment and further detachment to occur in the cavities between ribs. The ribs shed large eddies up into the outer flow, increasing turbulence intensity and intensifying mixing with the roughness sub layer to augment momentum exchange between the roughness sub layer and the outer layer. This was referred to k-type roughness. Roughness with pitch ratio less than four is referred to as d-type roughness. For d-type roughness the space between adjacent ribs contains a stable eddy with limited interaction with the bulk flow. Results from Large Eddy Simulations show greatest interaction with the outer flow for a pitch ratio of ten (Cui et al. 2003) which agree well with experiments carried out by Krogstad (1992) and

Okamoto (1993). Results from these works were used to design roughness strips implemented in flume experiments to enhance the vertical distribution of ambient flow and turbulence intensity in flume experiments as outlined in Chapter 3, with results from this work are presented in Chapter 5.

Green (1998) used electromagnetic current meter measurements of tidal flows at four sites with different distributions of horse mussels acting as roughness elements to show that k-type roughness also increases the bed drag coefficient, defined as the proportion of mean kinetic energy dissipated by turbulence. Estimates for the bed drag coefficient agreed with the effective Nikuradse equivalent sand roughness approach (Marriott & Jayaratne 2010). Nikuradse measured the flow over boundaries covered in sand particles with height k_s. For rough turbulent logarithmic boundary layer flows it was found that the roughness length $z_0 = k_s/30$. Based on measurements of hydraulically rough river flow over gravel beds, Bray (1982) gives an expression for the effective Nikuradse grain roughness height in terms of the diameter of the roughness with 90% finer by weight:

$$k_s \approx 3d_{90} \tag{2.17}$$

Where k_s= effective Nikuradse grain roughness height and d_{90}= diameter of the roughness with 90% finer by weight. Using these relationships the bed drag coefficient is approximated as (Tassi 2014):

$$C_b = 2\left(\frac{\kappa}{\log\left(\frac{12h}{k_s}\right)}\right)^2 \tag{2.18}$$

Where C_b=bed drag coefficient, κ=Von Karman constant and h=depth. Whilst this is a useful guide for estimating the bed drag coefficient, it is acknowledged that roughness spacing, pattern and variation in roughness element size will inevitably lead to spatial and directional variations.

2.7 Review of regional scale resource assessment around the Channel Islands

Previous studies identify Alderney Race, Casquets, Big Russel, North West Guernsey and North East Jersey (Figure 2.4) as sites with suitable conditions for energy extraction by large tidal turbine arrays in the Channel Islands, based on high velocities and suitable depths (Energy Technology Support Unit 1993), (Black and Veatch 2005), (Environmental Change Institute 2005) and (Owen 2005).

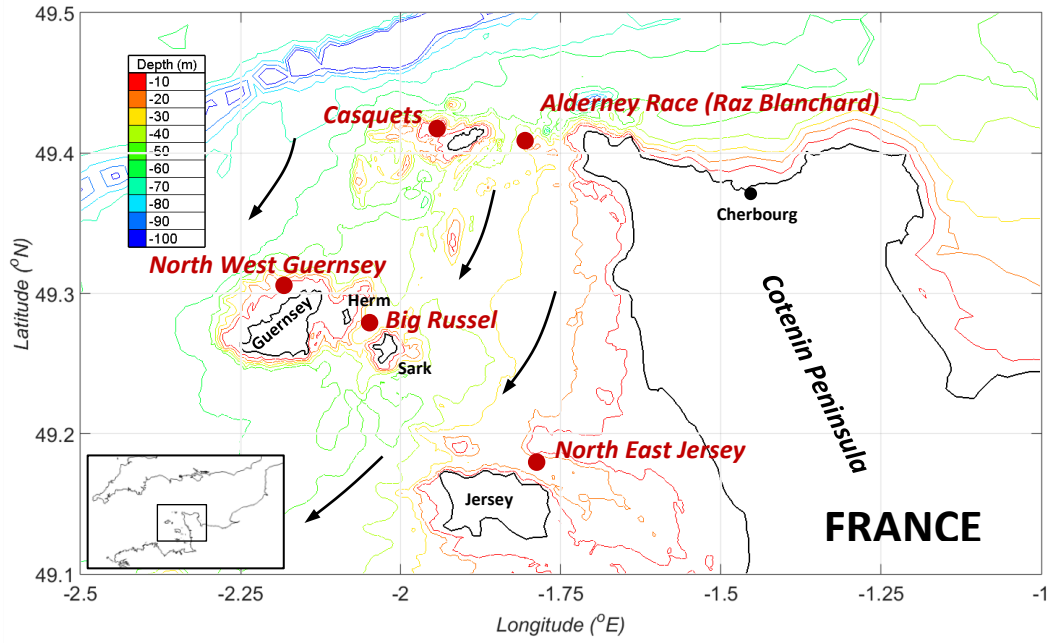

Figure 2.4 Location of Alderney Race, Casquets, Big Russel, North West Guernsey and North East Jersey. Arrows show the direction of the dominant ebb tide.

Results from the latter are summarised in Table 2.1 (Owen 2005), showing a comparison between site characteristics such as the width of the cross section considered, the average depth, peak velocity and energy flux at each site. Whilst the method used for obtaining these results relies on low resolution flow data (as discussed in more detail below), the work provides a useful initial qualitative comparison of flow characteristics that determine each site's suitability for energy extraction. This is best summarised by the right hand column, which shows the mean energy flux per unit cross sectional area, indicating that Alderney Race contains the highest mean energy density and total mean flux. In the proceeding text the methodologies used in previous studies to estimate the power that could be generated at each site are assessed, with a main focus on Alderney Race as it has received considerably more attention. Results are summarised in Table 2.2. Assessments of

Casquets, Big Russel, North East Jersey and North West Guernsey employ the same methodologies presented for Alderney Race so are quantified separately afterwards.

Table 2.1 Comparison of flow features at Alderney Race, Casquets, North West Guernsey, Big Russel and North East Jersey in order of mean flux per unit cross sectional area, taken from results by Owen (2005).

Site	Width (m)	Average depth (m)	Peak velocity (m/s)	Energy flux (GW h /year)	Energy flux (MW h/m^2/year)
Alderney Race	4936	40	4.5	3628	18
Big Russel	4056	24.5	2.6	822	8.27
Casquets	7810	79	2.4	2933	4.75
NE Jersey	2599	23	2.6	282	4.72
NW Guernsey	10199	69.7	2.1	2530	3.56

2.7.1 Alderney Race

Table 2.2 summarises estimates for the energy yield from tidal stream turbine arrays located in Alderney Race using the Farm, Kinetic Flux and Power potential methods. These methods are reviewed here to highlight uncertainties in these estimates.

2.7.1.1 Farm method

In the farm or 'per-generator' approach, the output of a single device is estimated using actuator disk theory, which states that the power generated by a turbine in unconstrained flow is a proportion of the kinetic power through its swept area. The coefficient of power defines the rotor efficiency, which based on experimental results is a function of velocity but typically takes a value of 0.3 over the operating velocities of a turbine in many studies. The output of an array of turbines is then estimated by simply scaling up the result for a single device, thereby neglecting the effect of wake interference with downstream devices.

This method was implemented at Alderney Race in (Energy Technology Support Unit 1993). Velocities were obtained from tidal stream atlases and tidal diamonds on navigational charts and scaled based on the variation in tidal range at Dover, where flow at the turbine was assumed to be 90% of surface flow and rated velocity was equal to 85% of maximum velocity. Array plot areas (defined as the plan area taken up by the array of turbines) were designated in depths greater than 20m where mean spring peak velocities exceeded 2 m/s, covering an area of 68 km^2, giving an estimated mean power output of 623 MW and annual output of 5200 GW h/year. A similar approach was taken in (European Commission 1996), where arrays were considered in regions where peak tidal stream velocities exceed 1.5 m/s. This covered an area of 102 km^2, giving an estimated yield of

Table 2.2 Summary of results from literature that quantify available and extractable power at Alderney Race.

Study	Data source	Method	Estimated power (TW h/year)
(Energy Technology Support Unit 1993)	Navigational charts	Farm, array covers 68 km^2 in waters deeper than 20 m. Array capacity=2.4 GW.	5.2 (Extractable power, capacity factor=0.26)
(European Commission 1996)	Navigational charts	Farm, array covers 102 km^2. Array capacity=1.9 GW.	6.5 (Extractable power, capacity factor=0.4)
(Bahaj & Myers 2004)	Admiralty tidal stream atlas NP 264	Farm, assuming a 5% wake deficit within sub arrays. Array capacity of 0.84 GW.	7.4 (Extractable power, capacity factor=0.4)
(Myers & Bahaj 2005)	Admiralty tidal stream atlas NP 264	Farm combined with BEM simulation to optimise turbine performance, asymptotic wake deficit assumed within subarrays based on momentum theory. Array capacity=1.5 GW.	1.35 (Extractable power, capacity factor=0.1)
(Black and Veatch 2005), Phase I	Tidal stream atlases, admiralty charts	Kinetic energy flux through 3.3 km cross section of Alderney Race with SIF=20%.	1.37 (Available power)
(Black and Veatch 2005), Phase II	Tidal stream atlases, admiralty charts and the Marine Energy Atlas (DTI 2007)	Kinetic energy flux through 5 km cross section of Alderney Race with SIF=20%.	0.61 (Available power)
(Black and Veatch 2005), Phase II	Tidal stream atlases, admiralty charts and the Marine Energy Atlas (DTI 2007)	Kinetic energy flux through 5 km cross section of Alderney Race with SIF=12%.	0.37 (Available power)
(Owen 2005)	Admiralty tidal stream atlas NP 264	Kinetic energy flux through 5 km cross section of Alderney Race with SIF=20%.	0.73 (Available power)
(Black and Veatch 2011a), Phase III	Marine Energy Atlas (DTI 2007)	Maximum average power potential with SIF=12%.	2.25 (Available power)
(Coles et al. 2015)	European Shelf 2008 OTIS regional tidal solution (Egbert et al. 2010)	2D hydrodynamic model of English Channel, distributed drag method used to simulate energy extraction from single row array spanning 5.8 km with blockage, ε=0.4 and array capacity=0.21 GW.	0.92 (Extractable power, capacity factor=0.5)

6.5 TW hr/year using an efficiency curve to define the coefficient of power as a function of velocity. In both studies the spatial variation in velocity was not considered, as velocity data at a single location was used to characterise the whole of Alderney Race. In reality there is high spatial variability in velocity across Alderney Race, caused by uneven coastlines and bathymetric features. Any small error in velocity results in high error in power, given that power is dependent on the cube of velocity, bringing into question the accuracy of these works.

In (Bahaj & Myers 2004) admiralty tidal stream atlas NP 264 was used to obtain spring and neap velocity data in the East and West Race. Linear interpolation between spring and neap tides was used to obtain velocities for days in between. Data was then extrapolated to give 12.5 hour tidal cycles. This simplified the variation in tidal cycle which is approximately between 12 hours 20 minutes and 12 hours 50 minutes. It was also assumed that the period between spring and neap tides remained constant at 7 days throughout the year. In reality this varies between 6 -8 days, however an average value of 7 is representative. At times when velocities were less than 1.1 m/s, it was assumed the flow contained too little energy for turbines to be operational. Three different turbine diameters of 14m, 20m, and 25m were considered. Turbines were deployed in suitable depths to ensure they were not incident on low velocity flow close to the seabed in the bottom 25% of the total depth and the upper 7m of the water column where waves cause cyclic loading. This also helped to maximise the total deployed swept area. Turbines were positioned in sub arrays with 18 diameter longitudinal spacing between rows and five diameter lateral spacing between devices. Longitudinal spacing between sub arrays was at least 500m. In total sixteen devices were used in each subarray, giving a total installed capacity of 3243 MW. Annual energy output for each turbine was then calculated at hourly intervals over 1 year with a power coefficient of 0.3, which was assumed conservative to incorporate gear box, generator, transformer and transmission losses. A rated velocity of 2.5 m/s and 4 m/s were assumed in the West and East parts of the Race respectively to make use of the higher velocities in the shallower East Race. The velocity downstream of each row inside a sub array was assumed to be 95% of the upstream row to account for wake losses. Zero losses were assumed between sub arrays. Results show that an estimated energy yield of approximately 7.4 TW h could be generated from the arrays considered, with 65% of this contributed from the subarrays on the East Race. Based on this result the energy density per swept area of subarrays in the East and West Race was 73 MW h/m^2 and 21 MW h/m^2 respectively, where in general flow in the West Race is deeper and therefore slower.

In follow up work to this (Myers & Bahaj 2005), a blade element momentum software package was used to simulate pitch controlled turbine blade designs over various flow regimes to optimise the turbine power coefficient. Array layout differed from previous work (Bahaj & Myers 2004),

with the global array consisting of subarrays containing 20 devices, in two rows of ten. Minimum lateral and longitudinal spacing between sub arrays was set at 200m and 500m respectively. Longitudinal spacing between rows in each subarray was fifteen diameters. A kinematic model approach was used to quantify the velocity within the wake downstream of rows of turbines within each subarray. BEM simulations were used to estimate the power coefficient of each turbine. The BEM simulation does not simulate the effects of close lateral spacing between devices that causes blockage effects that results in flow diversion. The sub-arrays had a total rated capacity of 1496 MW and a total annual energy yield of 1.34 TW h. Results showed the East side of the Race has the greatest resource.As discussed in Chapter 2.4.1, this kinematic approach does not consider the array scale blockage effect, where the added hydraulic resistance of a sub-array causes flow re-direction around the sub-array, which is likely to impinge on neighbouring sub-arrays. For this reason it is questionable to assume that the ambient flow field is representative of the inflow conditions into the sub-arrays.

2.7.1.2 Kinetic flux method

As the name implies, the kinetic energy flux method quantifies the total energy flux through a cross section of a site. This is then multiplied by a 'significant impact factor' (SIF) to estimate the proportion of the total kinetic energy flux that could be extracted without exceeding an arbitrarily defined decrease in upstream flow rate.

In (Owen 2005) the same method used in (Bahaj & Myers 2004) was used to obtain data describing the temporal variation in flow through Alderney Race. Bathymetry data was obtained from British Geological Survey maps. Where necessary linear interpolation was used to generate bathymetry and velocity data within the Race at 210 m spatial resolution. A $1/7^{th}$ power law was used to describe the vertical velocity distribution. Based on this assumption volume and kinetic fluxes were estimated through the Race giving a kinetic flux of 3.6 TW h/year through a 5km section with an average depth of 40m. An SIF was arbitrarily set at 20%, giving 0.73 TW h/year of power available for power generation.

In (Black and Veatch 2005) the same methodology was implemented. Phase I of this work obtained site dimensions from hydrographic surveys presented by the Energy Technology Support Unit (1993) and the European Commission and (1996) and used an SIF of 20% to give an estimated technically extractable resource of 1.3 TW h/year across a 3.3 km wide, 33 m average depth section of the Race.

Phase II reviewed the input parameters used in Phase I by cross checking flow data with the Marine Energy Atlas (MEA) (DTI 2008). The MEA uses data from the Proudman Oceanographic

Laboratory to quantify the distribution in kinetic energy density over the Western European Continental Shelf at 1.8 km resolution. Whilst this improves flow data resolution in comparison to previous studies, it is still unable to resolve high energy flow through Alderney Race at adequate accuracy for power calculations. Based on findings a significant reduction was made in mean neap/spring peak velocities of 67 % and 54% respectively. In addition the width of Alderney Race was increased from 3.3 km to 5 km and the depth was increased from 33 m to 39 m. Only a single value of depth was used in calculations so the variation in depth across the Race was not considered directly. Simple 1D theoretical channel models were used to estimate suitable SIF values of generic flow regimes based on the assumption that a 10% reduction in mid-range flow velocities or 0.2m reduction in tidal range will ensure ecological systems remain 'relatively unaffected'. This resulted in a reduction in SIF to 12% and a reduction in technically extractable resource of 70% to 365 GW h/year. Significant uncertainty in results exists due to differences between velocity data from the Marine Energy Atlas (MEA) used as a primary source of data and Tidal Stream Atlases. Uncertainty in results was estimated at ±30%, however no explanation for how this was derived was given.

2.7.1.3 Power potential method

In (Garrett & Cummins 2004) the relationship between kinetic energy flux and maximum extractable power was shown to be specific to a particular site, giving no basis to the assumption that a global fraction (or SIF) of kinetic energy flux is applicable to all sites.

As turbines are added, there is an increase in the difference between free surface elevation upstream and downstream of the array. The added turbine drag reduces the volume flux through the energy extraction zone. Assuming alternative flow paths exist, the increase in hydraulic resistance of the turbines causes flow to divert around the area of added drag, taking the path of least resistance. The energy dissipated by the array is the product of the head loss across the array and the volume flux through the energy extraction zone. Initially when drag is added the increase in head drop has a dominating effect over the decrease in volume flux, causing the dissipated energy to increase. As further drag is added, the reduction in volume flux has an increasingly significant effect, where at the upper bound it suppresses the increase in head drop, causing the dissipated power to decrease, hence giving an upper bound for power potential, termed the maximum average power potential. Equation 2.19 quantifies the analytical solution for the maximum average power potential of a channel as (Garrett & Cummins 2005):

$$P_m = \gamma \rho g (\eta_i - \eta_o) Q_{max} \qquad 2.19$$

Where P_m=Maximum average power potential, ρ=density of fluid, g=acceleration due to gravity, η_i=free surface elevation at the inlet of the channel, η_o=free surface elevation at the outlet of the channel, Q_{max}=maximum volume flux through the channel in the undisturbed case and γ=forcing constant that gives the theoretical limit of energy extraction, which is dependent on whether the channel is drag-dominated (where flow and head difference are in-phase) or an inertia-dominated channel (where they are 90° out-of-phase) (Draper et al. 2014). Therefor this dynamic balance is indicated by the phase lag of the flow rate behind the driving head (Garrett & Cummins 2005). Typically the coefficient lies between 0.16 and 0.22.

2D hydrodynamic models of generic tidal regimes such as tidal streams based on Alderney Race were developed to simulate the large scale impact of hypothetical levels of energy extraction (Black and Veatch 2011b). Here a tidal streaming regime is defined as the physical response of the tidal system to maintain continuity when a current is forced through a constriction. Data from the latest 2008 Marine Energy Atlas was used as input data.

A distributed drag was applied uniformly over the region of interest to simulate energy extraction from large tidal turbine arrays. Results from the generic models were used to inform a suitable SIF value, based on the change to the ambient flow caused by energy extraction. Based on results from the generic tidal streaming hydrodynamic model, a value of SIF=12.5% was used for Alderney Race, however the Race is unlikely to be fully representative of the idealized case, especially as alternative flow channels are available around the North West coast of Alderney and bathymetry varies significantly across its width. Results from Equation 2.19 were multiplied by the SIF, giving a technically extractable resource of 2.25 TW h/year. Uncertainty in results was estimated to have increased in comparison with the Phase II study to +30%/-45% based on significant discrepancies between flow data from the Marine Energy Atlas and the tidal diamond. It was concluded that further work is required to quantify what proportion of the extracted energy can be ascribed to useful electrical power generation.

2.7.2 Casquets

Table 2.3 summarises results from previous studies discussed in 2.7.1 used to estimate the extractable and available power at Casquets, located on the opposite side of Alderney to Alderney Race. In general studies vary significantly because of the vast range of areas considered, which also affects the mean depth within the array plot area.

Table 2.3 Summary of results from literature that quantify available and extractable power at Casquets

Study	Method	Estimated power (TW h/year)
ETSU (Energy Technology Support Unit 1993)	Farm, array covers 215 km^2. Installed capacity=2.5 GW.	2.9 (Extractable power, capacity factor=0.14)
(European Commission 1996)	Farm, array covers 190 km^2 with a mean depth of 115 m. Array capacity=0.37 GW.	1.3 (Extractable power with capacity factor of 0.4)
(Black and Veatch 2005), Phase I	Kinetic energy flux through 8 km wide, 115 m deep cross section with SIF=20%.	1.6 (Available power)
(Black and Veatch 2005), Phase II	Kinetic energy flux through 8 km wide, 80 m deep cross section with SIF=8%.	0.4(Available power)
(Owen 2005)	Kinetic energy flux through 8 km wide, 70 m deep cross section with SIF=20%.	0.6 (Available power)
(Black and Veatch 2011b)	Power potential, site covers 61 km^2 in flows with a mean depth of 22 m using SIF=8%.	1.9 (Available power)

2.7.3 Big Russel

Big Russel is a channel located between the islands of Herm and Sark in the Bailiwick of Guernsey. The channel is 4 km wide and 25 m deep, making it relatively shallow compared with the other sites. Peak flows reach approximately 2.6 m/s. High variation in estimated available power arises from large discrepancies in the cross sectional geometries (Black and Veatch 2005; Owen 2005) to estimate the kinetic flux through Big Russel. Based on data from TCarta bathymetry (TCarta 2014), the average depth across the narrowest section of big Russel is approximately 33 m, so lies somewhere between the two.

Table 2.4 Summary of results from literature that quantify available and extractable power at Big Russel.

Study	Method	Estimated power output (TW h/year)
ETSU (Energy Technology Support Unit 1993)	Farm, array covers 90 km^2 in flows deeper than 20 m. Installed capacity=1 GW.	2.0 (Extractable power with capacity factor of 0.24)
(Black and Veatch 2005), Phase I	Kinetic Energy Flux through 2.7 km wide, 48 m deep cross section with SIF=20%.	0.3 (Available power)
(Owen 2005)	Kinetic energy flux through 4 km wide, 24 m deep cross section with SIF=20%.	0.16 (Available power)

2.7.4 North West Guernsey

Guernsey is grid connected to mainland France via an 85 MW sub-sea cable running from Surville France to Jersey, which extends to Guernsey via a 50 MW cable. In 2000, 500 GW h of electricity was imported from France, with 14% used on Guernsey. There is high variability in estimated power output at the North West Guernsey site, predominantly due to considerable variation in site plot area.

Table 2.5 Summary of results from literature that quantify available and extractable power off the North West coast of Guernsey.

Study	Method	Estimated power output (TW h/year)
(Energy Technology Support Unit 1993)	Farm, array covers 366 km^2 in flows deeper than 20 m. Installed capacity=2.2 GW	4.4 (Extractable power with capacity factor of 0.24)
(European Commission 1996)	Farm, array covers 221 km^2 in flows with mean depth of 57 m. Array capacity=0.4 GW.	1.7 (Extractable power with capacity factor of 0.5)
(Black and Veatch 2005), Phase I	Kinetic Energy Flux through 10 km wide, 57 m deep cross section with SIF=20%.	0.5 (Available power)
(Owen 2005)	Kinetic energy flux through 10 km wide, 70 m deep cross section with SIF=20%.	0.5 (Available power)

2.7.5 North East Jersey

On top of the methods discussed, a separate study (IT Power 2011) took field measurements from ADCP deployments to quantify the temporal and spatial variation in tidal flows during January 2010. The study concludes that the available energy off the North West coast of Jersey is 0.36 TW h/year. The study also took field measurements off the South coast of Jersey, however flows were significantly lower so were not considered feasible for tidal energy development at this stage. Whilst varied, results in Table 2.6 suggest tidal energy could contribute a significant amount of Jerseys 0.72 TW h annual demand for electricity. Typically the flow off the North East coast of Jersey is shallower than the other sites, potentially making installation and maintenance easier to undertake.

Table 2.6 Summary of results from literature that quantify available and extractable power off the North East coast of Jersey.

Study	Method	Estimated power output (TW h/year)
(Energy Technology Support Unit 1993)	Farm, array covers 20 km^2 in flows deeper than 20 m. Array capacity=1.17 GW.	1.4 (Extractable power with capacity factor of 0.14)
(European Commission 1996)	Farm, array covers 58 km^2 in flows with mean depth of 58 m and average flows of 1 m/s. Array capacity=0.2 GW.	0.65 (Extractable power with capacity factor of 0.37)
(Black and Veatch 2005), Phase I	Kinetic Energy Flux through 2.5 km wide, 22 m deep cross section with SIF=20%.	0.16 (Available power)
(Owen 2005)	Kinetic energy flux through 2.5 km wide, 20 m deep cross section with SIF=20%.	0.05 (Available power)
(Black and Veatch 2011b)	Power potential, site covers 35 km^2 in flows with a mean depth of 21 m with SIF=20%.	1.1 (Available power)
(IT Power 2011)	Field measurements.	0.36 (Available power)

2.8 Summary

This review has identified uncertainty in methods used to quantify the tidal energy resource. Regional scale studies to date have mainly implemented simple kinematic models that are unable to quantify the extent to which array-scale blockage modifies the surrounding flow field and as a result the power performance of the arrays. They also rely on low spatial and temporal resolution flow data which in some cases is expected to give error in power predictions of up to 45% (Black and Veatch 2005).

Empirical data showing equilibrium flow conditions within large arrays supports the distributed drag method for modelling large arrays, where the added array drag is distributed evenly over the array plot area. Critically this method is capable of modelling array scale blockage effects. Experimental validation is now needed to quantify the effects of uneven drag distribution within the transition region at the upstream end of arrays and the effects of row spacing and bed roughness on the onset of equilibrium conditions and total added drag. Ultimately this can lead to a better understanding of the validity of the distributed drag method from modelling large arrays within regional scale hydrodynamic models.

Chapter 3: Methodology for experimental flume testing of porous fence arrays

3.1 Overview

This chapter presents an experimental methodology designed to obtain measurements necessary to validate a method for parameterising the area averaged array drag coefficient, which is implemented in the distributed drag method. The experiment characterises flow through arrays of porous fences. Each porous fence simulates the wake effects downstream of densely packed rows of turbines inside large arrays. Relevant theory related to scaling is presented in Appendix A.

3.2 Experimental setup

Figure 3.1 shows a plan and elevation view of a recirculating flume with 19 m working section, width of 1.37 m and inlet depth of 0.3 m, which was used with porous fences positioned perpendicular to the flow.

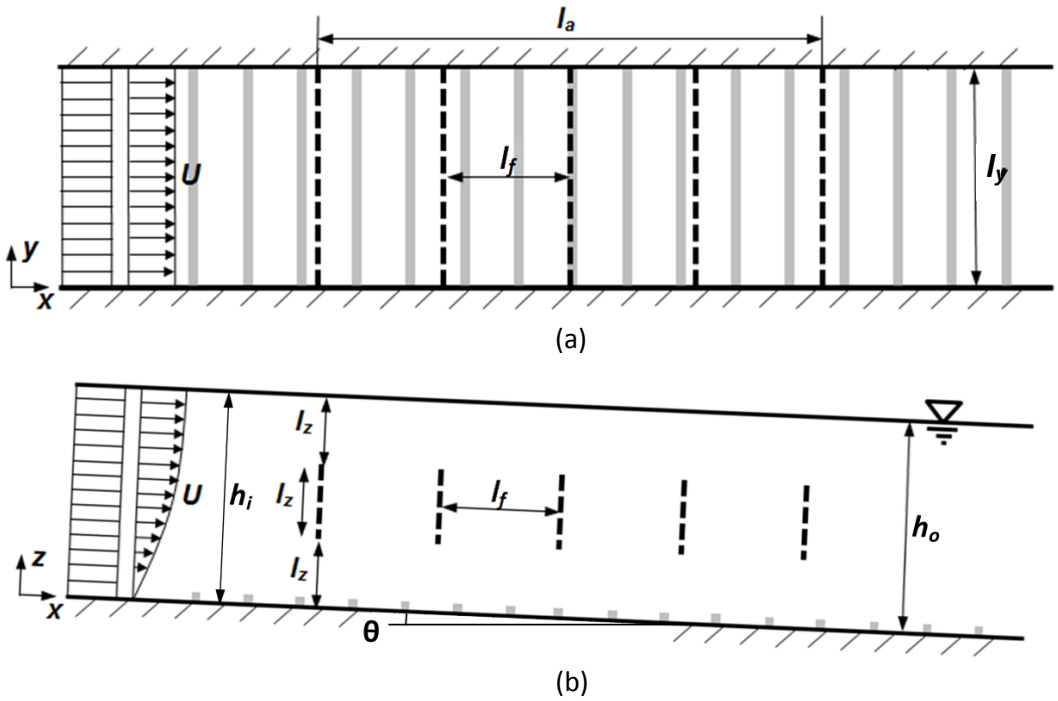

Figure 3.1 Experimental setup showing (a) Plan view and (b) Elevation view of porous fences positioned in the recirculating flume with flow straighteners at the inlet and bed roughness attached to the flume bed shown by grey strips. In the case of this experiment, bed slope angle, θ=0.09°, so is exaggerated for demonstrative purposes.

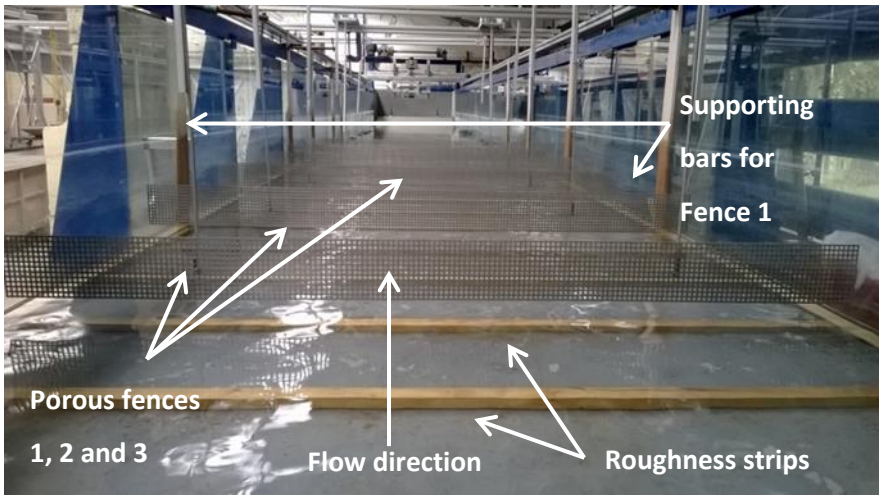

Figure 3.2 Porous fences positioned in the flume. Bed roughness positioned on the flume bed. Raised weir at flume outlet shown at the far end.

The fences had a height of 0.1 m and width of 1.34 m and were placed at a centroid height of 0.15 m. The fences had 5 x 5 mm square perforations positioned at 8 mm centres, giving a porosity of 0.39. A low porosity was chosen to ensure a significant change in elevation, velocity and thrust was observed. Additionally, previous experiments conducted by Harrison (2008) using fences with higher porosity (greater open area) exhibited deformation when incident on high flow.

K-type roughness with a pitch ratio of ten was used to alter the flow statistics such as turbulence intensity to levels representative of high energy sites such as the Pentland Firth and Alderney Race, a feature that wake recovery is dependent on. The roughness strips had square cross sections with a height of 0.03m. The longitudinal spacing between roughness strips was 0.3m.

Table 3.1 outlines the experiments undertaken. Initially the flume was run without porous fences to characterise the ambient flow. For this initial flow characterisation, the flume was first run without bed roughness. This is referred to as Case A from now on. Centreline measurements of vertical velocity distribution were obtained along the centreline of the flume. Lateral velocity profiles were also obtained across the flume width (along the y-axis) to quantify the boundary layer from the flume side walls. Additionally the head drop between the flume inlet and outlet was measured using ultrasonic distance measurers. The flume was then run with the addition of the roughness strips secured to the flume bed and measurements were repeated. This is referred to as Case B from now on.

Experiments were then run with seven different array layouts (Table 3.1). Each fence was positioned in the flow using two narrow vertical bars (2mm) connected 0.42 m from the centre of the fence. It was assumed these had no effect on the flow along the centreline of the flume where

measurements were taken. The first fence in each array was positioned 6m downstream of the flow straightener at the flume inlet. The array length and number of fences within each array was dictated by the uniform row spacing, where the last fence was positioned no further than 6 m downstream of the first so as not to encroach on the flume outlet. In total six spacings between fences were used. This was seen as a sensible range to ensure varying degrees of interaction between fences and the wake of upstream fences so that this behaviour on the overall array drag could be investigated. The number of fences was reduced with increasing row spacing so that each array took up approximately the same plot area and length. First arrays were positioned in the flume using Case A, these arrays are referred to as Cases A1 to A7 from now on. For Cases A1-A7 measurements of velocity, head drop across the array and fence drag were obtained. Afterwards, added bed roughness was secured to the bed and the experiments were repeated. These arrays are referred to as B1 to B7 from now on.

Table 3.1 Characteristics of seven different arrays used in the experiment. Spacing and array length are given in multiples of fence height.

Case	Array density	No. fences	Fence Spacing	Array length	Bed roughness
Ambient flow (without and with bed roughness)					
A	0	0	-	-	No
B	0	0	-	-	Yes
Without bed roughness					
A1	0.016	1	-	-	No
A2	0.033	2	60	60	No
A3	0.070	4	19	57	No
A4	0.078	5	16	64	No
A5	0.092	6	13	65	No
A6	0.117	7	10	60	No
A7	0.159	10	7	63	No
With bed roughness					
B1	0.016	1	-	-	Yes
B2	0.033	2	60	60	Yes
B3	0.070	4	19	57	Yes
B4	0.078	5	16	64	Yes
B5	0.092	6	13	65	Yes
B6	0.117	7	10	60	Yes
B7	0.159	10	7	63	Yes

3.3 Rationale for using porous fences

At laboratory scale static porous disks/fences have been shown to reproduce the axial velocity flow field in the far wake (distances greater than approximately 5 diameters) downstream of a rotor (A. Crespo, J. Hernandez 1999) when the thrust coefficient of the disk is matched to the turbine it is simulating. Porous disks/fences dissipate energy in the wake through turbulence generation. No mechanical energy is extracted from the flow as with real turbines, so the energy contained in the near wake will be different. Additionally there is no turbine rotation which causes vortex sheets to shed from the trailing edge of the rotor blades and blade tips, generating blade vortices, however this phenomenon is also confined to the near wake region. Therefore porous fences have been chosen as a suitable method to simulate the far wake effects of turbines in large arrays, with a minimum spacing between rows of 7 diameters.

Porous fences simulate the wake downstream of densely packed turbine rows with no lateral spacing between adjacent turbines. This neglects lateral velocity variations but allows vertical shear velocity (Harrison 2008). By neglecting lateral spacing between turbines, the specification of array layout is reduced to only the longitudinal spacing between fences and array density, which is the ratio of the frontal area of all fences within the array to the plan area of the array. The geometric simplicity of porous fence arrays allows the experimental setup of arrays to be varied quickly to maximise data capture over a wide range of array densities.

Crucially porous fences provide a suitable way of quantifying the three potential sources of error identified in previous chapters, which are the discrepancy between the depth averaged velocity and the velocity through each fence, the uneven distribution in drag amongst fences and the change in the bed drag contribution to the total added drag caused by flow modification by the array.

One limitation of porous fences is that they do not allow staggered arrays to be modelled, where downstream turbines are offset from the turbine directly upstream to avoid wake interaction. EMEC guidelines recommend staggered arrays for optimal power generation but acknowledge that there is no clear definition for the optimal lateral and longitudinal spacing between turbines (Legrand 2009). Based on wind farm modelling staggering is thought to be important within the transition region of the array where wakes have not merged laterally but becomes less important further into the array after the transition zone (Fence 3) where wakes mix laterally and a more homogeneous flow field develops (Frandsen 1992). Given this uncertainty in array design, as well as the limited amount of experimental velocity data through large arrays, the adoption of porous fences were considered a suitable first step to providing a comprehensive experimental dataset for validating computational models.

3.4 Scaling

In open channel sub critical flows, gravity forces dominate over inertial forces (Cruise et al. 2007). For this reason Froude scaling was used to give dynamic similarity between a typical full scale array and the experimental model. The flume experiment was scaled based on field measurements recorded at the Sound of Islay, where velocities reach 2.5 m/s in depths of 37 m, giving a Froude number of 0.13 (Milne & Sharma 2011). To achieve dynamic similarity the experimental model used a flow depth of 0.3 m and an inlet velocity at mid depth of 0.23 m/s. Full scale tidal stream turbines will be positioned at approximately mid depth with a diameter equal to around one third of the flow depth. For this reason a centroid height of the porous fences of 0.15 m was used to ensure geometric scaling with a scale factor of 0.008. For a description of scaling theory, please refer to Appendix A.

3.5 Measurements

A downward looking Acoustic Doppler Velocimeter (ADV) with 150 mm^3 sampling volume was used to measure the velocity upstream of the array, at a distance of 4m downstream of the flow straightener (i.e. 2m upstream of the first row in the arrays). A sampling frequency of 200 Hz was used to capture turbulence properties of the flow. Velocity profiles and turbulence intensity profiles between fences were obtained using a sideways looking ADV along the centreline of the flume at 0.01, 0.03, 0.06, 0.09, 0.12, 0.15, 0.18, 0.22 and 0.27 cm above the flume bed. Three profiles between each fence were obtained, with the longitudinal spacing between profiles depending on the fence spacing. Profiles were obtained at one fence height upstream of each fence (the closest the ADV could be positioned upstream of a fence), three fence heights downstream of each fence and one profile halfway in-between these positions to obtain the widest range in between fences.

Two load cells positioned 0.355 m either side of the centreline of each fence were used to measure the reaction on the supporting structure of each fence. An ultrasonic distance sensor (Senix Toughsonic TSPC-30 series) was used to measure flow depth along the centreline of the flume. With prior knowledge of the flume bed level, which drops almost linearly from inlet to outlet by 25mm, the free surface elevation drop across each array was obtained. A discharge meter (Sonteq IQ Plus) positioned at the flume outlet measured discharge for each case. Measurements were used alongside depths to obtain depth averaged velocities.

3.6 Data reduction

All velocities were normalised by the velocity measured upstream of the arrays at mid depth, which remained constant at 0.23 m/s. Turbulence intensity was calculated as the root-mean square of the turbulent velocity fluctuations with respect to the mean velocity:

$$I = \frac{\sqrt{\frac{1}{3}\left(\langle U'^2\rangle + \langle V'^2\rangle + \langle W'^2\rangle\right)}}{\sqrt{U^2 + V^2 + W^2}} \quad 3.1$$

Where I =turbulence intensity, U', V', W'=fluctuating velocity components in the streamwise, transverse and vertical directions respectively and U, V, W=velocity components in the streamwise, transverse and vertical directions respectively. The fence drag coefficient of each porous fence was calculated using:

$$C_f = \frac{F_f}{\frac{1}{2}\rho A_f U_0^2} \quad 3.2$$

Where C_f=fence drag coefficient, F_f=drag force acting on a single porous fence normal to the flow (obtained from load cell measurements), ρ=fluid density, A_f=frontal area of the fence and U_0=streamwise ambient velocity upstream of the array.

3.7 Area averaged array drag validation

3.7.1 Parameterisation of array drag

To test the approach taken in 2D hydrodynamic resource assessments, array drag was estimated using the following steps:

A. Obtain the relationship between the streamwise ambient velocity upstream of a single porous fence and its drag coefficient by measuring the force exerted on the fence by the flow over a range of upstream velocities. Note that typically it is assumed that the drag coefficient of a single turbine (or in this case a single fence) is applied to the whole array, so that the array force is:

$$F_a = \frac{1}{2}\rho \overline{U}^2 C_f A_a$$

3.3

Where F_a=total array drag force, ρ =fluid density, $\overline{U}$=depth averaged streamwise velocity within the array, C_f=fence drag coefficient and A_a=total area of all porous fences within the array.

B. Obtain the true array drag coefficient from experimental measurements using:

$$C_a = \frac{F_a}{\frac{1}{2}\rho \overline{U}^2 A_a}$$

3.4

Where C_a=array drag coefficient, F_a=total array drag force (obtained from experimental load cell measurements of the drag force on each porous fence within the array), ρ =fluid density, $\overline{U}$=depth averaged streamwise velocity within the array and A_a=total frontal area of all porous fences within the array.

C. Compare experimental load cell measurements of array drag and array drag coefficient using Equation 3.3 and 3.4.

3.7.2 Bed drag

Chapter 2 identified uncertainty relating to the effect arrays have on bed drag compared with ambient bed drag in the absence of arrays. Most studies assume the array has a negligible effect on bed drag. In some studies it is assumed that the presence of the array accelerates flow under it, thereby augmenting the contribution of bed form drag in the case of rough beds (Moore 1979; Cui et al. 2003).

To quantify the potential change in bed drag opposing the flow as a result of the presence of porous fence arrays, the force balance given by Equation 3.5 was resolved along the *x* axis parallel to the flume bed.

$$\int_{z=0}^{h_i} \rho g z \, dA_i - \int_{z=0}^{h_o} \rho g z \, dA_o + F_W sin\theta - F_b - F_a$$

3.5

Where z=vertical height above boundary surface, h_i=inlet depth, h_o=outlet depth, ρ=fluid density, g=acceleration due to gravity, A_i=inlet cross sectional area, A_o=outlet cross sectional area, F_W=weight component force of fluid, θ=bed slope angle, F_b=bed drag force acting normal to the flow, F_a=total drag force on all fences within the array acting normal to the flow.

Figure 3.3 shows the force balance, where the square grey blocks on the flume bed are roughness strips used to augment ambient turbulence intensity. Results from the force balance were used to quantify the new bed drag coefficient for each array listed in to compare with the ambient bed drag in the absence of porous fence arrays.

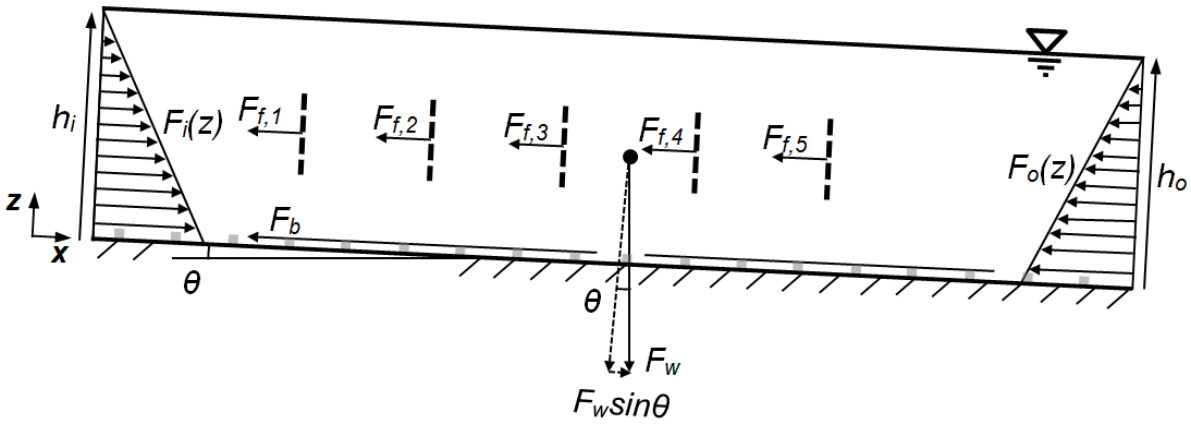

Figure 3.3 Elevation view of recirculating flume experiment, showing the force balance. Bed slope angle, θ=0.09°, so is exaggerated for demonstrative purposes.

Chapter 4: Methodology for modelling energy extraction at sites around the Channel Islands

4.1 Overview

Chapter 2 highlighted that previous assessments characterising flow at sites around the Channel Islands have relied upon low temporal and spatial resolution flow data and simplistic methods for modelling energy extraction, bringing into question the validity of results quantifying available and extractable power. To generate a more reliable velocity data set, a 2D hydrodynamic model of the English Channel was built using Telemac 2D to simulate the flow dynamics around the Channel Islands. This chapter details the methodology used to setup and validate the hydrodynamic model, as well as the methods used to quantify available and extractable power at Alderney Race, Casquets, Big Russel, North West Guernsey and North East Jersey. Relevant theory related to simulating the tides is presented in Appendix A.

4.2 Numerical modelling approach

The Channel Islands cover an area of approximately 5,000 km^2. To model flows over this regional scale, computational capability becomes an important consideration. Whilst it is acknowledged that 3D numerical modelling is within the capabilities of high performance computing, no such model has currently been implemented for resource assessment purposes to quantify energy extraction at the regional scale. This is predominantly because expected run time exceeds what is sensible to generate results, where often models must be run for 1 month of simulation time to capture the cyclic variation of the tides. Given the simplistic nature of resource assessments conducted around the Channel Islands to date (covered in Chapter 2), adopting a 2D hydrodynamic modelling approach provides the next logical step in better defining the cyclic variation in flow around the Channel Islands.

A 2D hydrodynamic software package was chosen that satisfied the following three criteria:

1. Parallel processing – Allows multi-core processing to decrease run time by segmenting the domain and executing program commands simultaneously for each segment.

2. Unstructured meshing – To discretize the domain with localised grid resolution in areas of interest around Alderney, Casquets, Big Russel, North West Guernsey, North East Jersey

and regions of high flow gradients such as at the continental shelf and around coastlines where there are significant step changes in depth.

3. Open source – To allow access to subroutines to modify features such as array drag parameterisation and boundary condition implementation.

Available coastal hydrodynamic software include Mike 21, FVCOM, Anuga Hydro, Telemac 2D, Polcoms and Ecomsed 2D. Telemac 2D was chosen as most suitable as it filled all three criteria, as well as there being significant in house expertise.

4.3 Pre-processing

4.3.1 Bathymetry

Bathymetry was obtained from three sources; the first was from the global General Bathymetric Chart of the Oceans (GEBCO) (Kapoor 1981) at 30 arc-second (approximately 900m) resolution, generated by combining ship depth soundings and interpolation between sounding points. The second was from TCarta Marine (TCarta 2014) at 90 m resolution, covering bathymetry in the English Channel. The third was 1m horizontal resolution, multi-swath data set obtained during surveys carried out by Osiris Projects and Seastar Survey in the West of Alderney Race over the South Banks off the south coast of Alderney. The bathymetry was projected to Mercator coordinates, which Telemac 2D requires for large domains where the curvature of the Earth is significant.

4.3.2 Mesh generation

Figure 4.1 shows the unstructured, triangulated, finite element mesh generated using the pre-processing software Blue Kenue, showing the location of the three open boundaries. Figure 4.2 shows a zoomed in view of the mesh around the Channel Islands. To determine suitable mesh resolution, regions were allocated within the domain based on their likely mesh resolution requirement to capture the necessary scales of flow. The first region covers the majority of the domain where depths exceed 80m (Region 1) stretching throughout the domain where depth is high relative to local changes in bathymetry.

Region 2 incorporated the perimeter of the Channel Islands following the 50m depth contour, the maximum approximate depth for turbines to be installed. The third region covers the five areas of interest for energy extraction within the Channel Islands where energy extraction was simulated. Initially the mesh in Region 1 was refined until no significant improvement in amplitude and phase

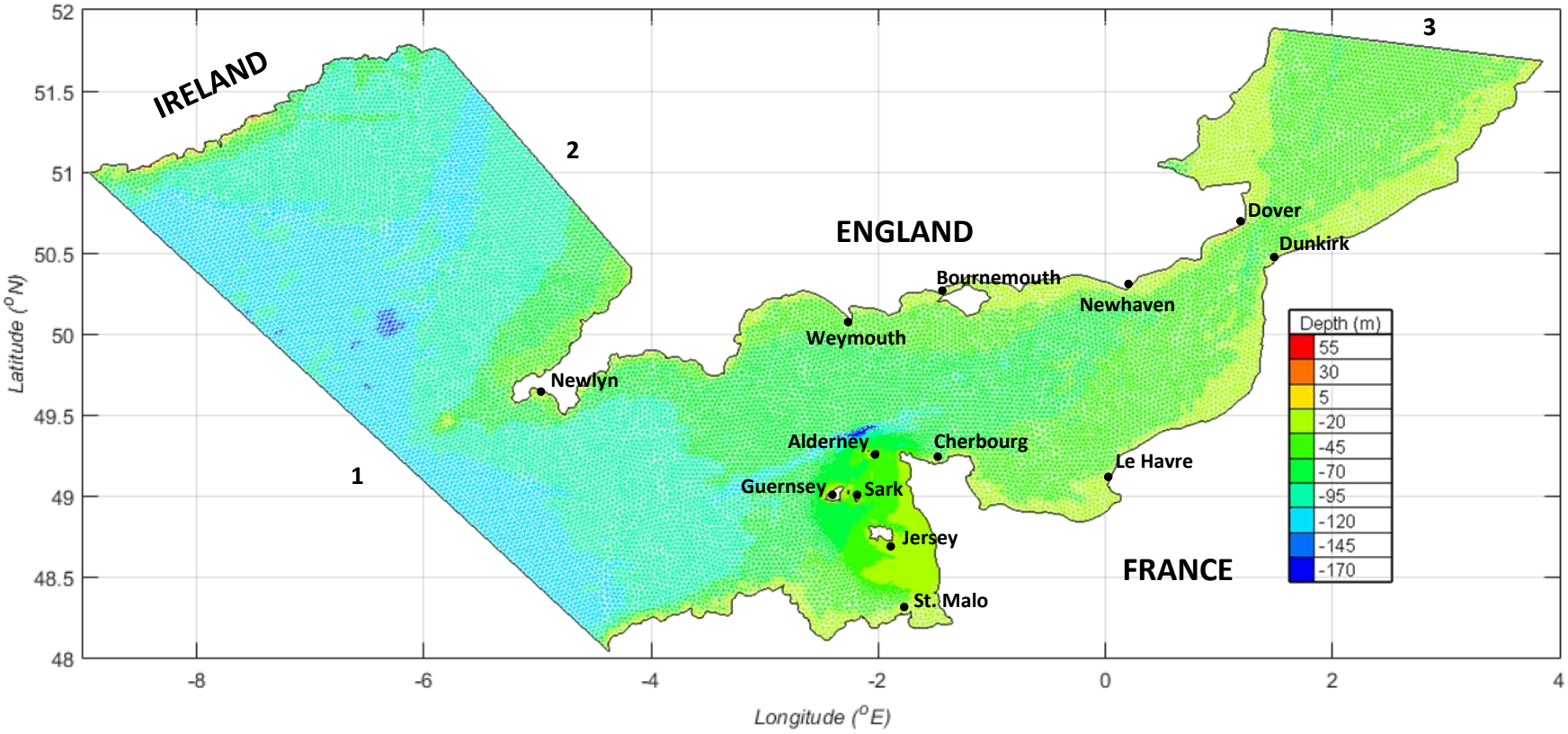

Figure 4.1 English Channel domain with finite element mesh, the location of three open boundaries in the Atlantic Ocean (1), Irish Sea (2) and English Channel (3) and the location of thirteen ports around the domain used for tidal gauge validation.

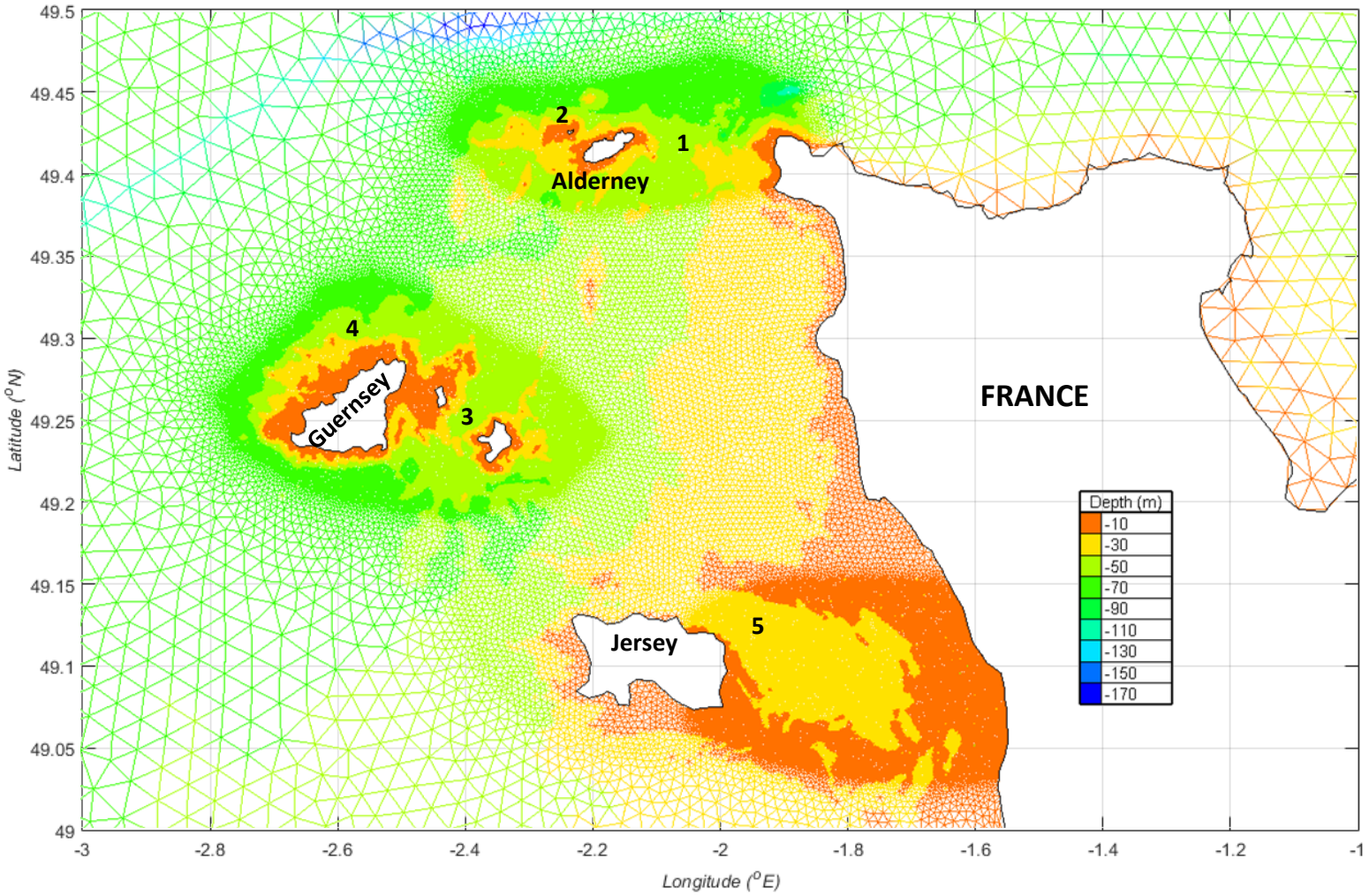

Figure 4.2 Finite element mesh in the Channel Islands, showing variable resolution in regions of interest for tidal energy development; Alderney Race (1), Casquets (2), Big Russel (3), North West Guernsey (4) and North East Jersey (5).

validation results was achieved, resulting in a mesh resolution of 5 km. This was then repeated within Region 2, giving a 1 km mesh resolution. Finally Regions 3 were resolved using 250 m mesh resolution, with flow data in Alderney Race from AWAC deployments also used to check mesh independence had been achieved . Any further improvement to mesh resolution showed no significant improvement in simulating the flow dynamics around the domain in terms of M_2 amplitudes, phases and flow data and no difference in estimated energy extraction.

4.3.3 Boundary conditions

The model was forced by imposing elevation time series' along liquid boundaries calculated from tidal harmonic analysis (theory covered in Appendix A). For each node on an open boundary, the amplitudes and phases of nine tidal constituents (M_2, S_2, N_2, K_2, K_1, O_1, P_1, Q_1 and M_4) where obtained from the Tide Model Driver (TMD) Matlab package (Egbert et al. 2010; Pawlowicz et al. 2002).

Matlab code was written to generate elevation boundary conditions applicable to any defined location. This allowed the position of the open boundaries to be adjusted to reduce domain size (thereby reducing run time) whilst maintaining accuracy. Initially, open boundaries were strategically positioned over regions where the European shelf high resolution atlas used by TMD to extract amplitudes and phase data (European shelf high resolution solution) had been verified by open ocean and coastal gauges (Egbert et al. 2010). The domain size was then incrementally decreased by moving the open boundaries closer to the Channel Islands, however this caused a detrimental effect on the level of agreement between simulated free surface elevations and current velocities in comparison with field measurements.

The horizontal velocity components are not defined at the liquid boundary, making the model 'under-constrained' in nature at these points. Thompson boundary condition were applied which uses the method of characteristics to calculate the horizontal velocities (Lang 2010).

4.3.4 Model parameters

The Coriolis acceleration term was included in the hydrodynamic equations as the scale of the domain is large (exceeding 100 km). To take into account the effect of astral forces, the tide generating force was also imposed. The model used the default wetting and drying scheme in Telemac 2D for simulating flow in shallow region. A constant viscosity coefficient of 10^{-4} Ns/m^2 was used to account for molecular and turbulent viscosity, the default value recommended in Telemac 2D. Bed friction was defined using the effective Nikuradse friction coefficient, applied

uniformly over the whole mesh. Sensitivity studies of both eddy viscosity and bed friction were conducted to determine their effect on flow dynamics and energy extraction, with bed friction also used as a tuning parameter to calibrate the model. The solver accuracy was 0.001 (default value) which defines the accuracy required during solution of the propagation step, using a time step of 1 minute. An example steering file with description of each setting is included in Appendix D.

4.3.5 Model tuning

Bed drag coefficient was used as a tuning parameter to calibrate the model. Equation 2.18 was used to determine a realistic range of values of bed drag coefficient based on the assumption that the physical roughness height is less than 10% of the depth. Table 4.1 summarises the values of bed drag coefficient used in the calibration study, showing the range of roughness diameter with 90% finer by weight and effective Nikuradse sand roughness heights as a proportion of depth. Equation 2.18 shows that bed drag coefficient is likely to fall between 0.013 and 0.13. Tidal gauge and tidal stream results were recorded for each bed drag coefficient implementation to compare with published measurements and establish the most suitable bed drag coefficient based on the hierarchy in 4.3.6.

Table 4.1 Variation in roughness diameter and effective Nikuradse sand roughness for the range of bed roughness coefficients, where d_{90}=roughness diameter with 90% finer by weight, h=depth and k_s=effective Nikuradse equivalent sand roughness

Bed drag coefficient	d_{90}/h	k_s/h
0.130	$1.1\text{x}10^{-1}$	$3.3\text{x}10^{-1}$
0.091	$5.5\text{x}10^{-2}$	$1.6\text{x}10^{-1}$
0.052	$1.4\text{x}10^{-2}$	$4.2\text{x}10^{-2}$
0.035	$3.5\text{x}10^{-3}$	$1.1\text{x}10^{-2}$
0.025	$1.1\text{x}10^{-3}$	$3.2\text{x}10^{-3}$
0.013	$5\text{x}10^{-5}$	$1.5\text{x}10^{-4}$

4.3.6 Validation

The following data hierarchy was used to validate the model with the aim to recreate the most accurate flow conditions around the Channel Islands:

1. ADCP data in Alderney Race - Data from three out of three AWAC deployments conducted as part of the Osiris project were used to validate tidal stream velocities.

Comparison was made between major and minor axis amplitudes, phase and inclination between the modelled and real world velocity datasets for both M_2 and S_2 constituents.

2. Tidal elevations in/around the Channel Islands at Alderney, Guernsey, Sark, Jersey, Cherbourg and St. Malo - Comparison was made between M_2 and S_2 constituent amplitudes and phases at each port to compare with real values obtained from Admiralty charts (UK Hydrographic Office 2014). Location of each port is shown in Figure 4.1.
3. Tidal elevations at remaining ports - Using the same approach as described above for the remaining seven ports located on the French and South England coastlines.

After tuning the model using the methodology described in 4.3.6, the model was re-run with a new start date of 9/11/2014 for a period of 1 month. The accuracy of tidal constituent amplitudes and phases were then re-analysed to quantify the accuracy of the model for this new run period.

Tidal elevation and velocity validation was conducted using the Matlab package T-tide (Pawlowicz et al. 2002), which performs harmonic analysis on tidal signals extracted from the model to give constituent amplitudes and phases to compare with real values obtained from Admiralty charts (UK Hydrographic Office 2014). At the start of the simulation, at all point within the domain the velocity is zero and the free surface elevation is flat. Before obtaining any meaningful results, time must be allowed for the flow field within the domain to respond to the prescribed elevation conditions at the open boundaries. This time is described as “spin-up”. For each computation 1 day of spin up was used. Longer spin up times of 2 and 3 days had no significant impact on results.

4.4 Post-processing

4.4.1 Site characterisation

Once validated, the model was run to characterise the ambient flow regime over a 1 month period. The average distribution of kinetic power was calculated using Equation 4.1 to assess each site’s suitability for tidal energy extraction.

$$P_K = \frac{1}{t}\int_0^t \frac{1}{2}\rho U^3 C_P A_S \; dt \qquad 4.1$$

Where P_K=average kinetic power (averaged over time t), t=time, ρ=fluid density, C_P=turbine power coefficient, A_S=swept area of the tidal turbine.

Since in this early stage energy extraction was not modelled, the farm approach was adopted, where it was assumed that individual turbines in large arrays perform as isolated turbines with no impact on the natural flow regime. A turbine diameter of one third of depth was implemented and the turbine power coefficient was kept constant at 0.3.

4.4.2 Energy extraction using tidal turbine fences

A tidal turbine fence is a wide array of turbines laid out perpendicular to the flow. This array layout has been adopted in literature for previous assessments of the Pentland Firth (Draper et al. 2014), Vancouver Island (Sutherland et al. 2007) and Minas Passage (Walters et al. 2013). It has been adopted in this work to directly compare the results obtained at Alderney Race, Casquets and Big Russel with these other high potential tidal sites.

Figure 4.3 shows the plot area of the tidal fences spanning the width of Alderney Race, Casquets and Big Russel. Energy extraction was simulated by applying an area averaged array drag coefficient to the existing parameterisation of bed drag, applied uniformly over an array plan area. The fetch of each energy extraction strip (i.e. the longitudinal distance between the site inlet and outlet parallel to the direction of flow where drag was applied) was determined based on the distribution of mean ambient kinetic flux power to cover the most energetic regions where tidal energy development is most likely to be carried out.

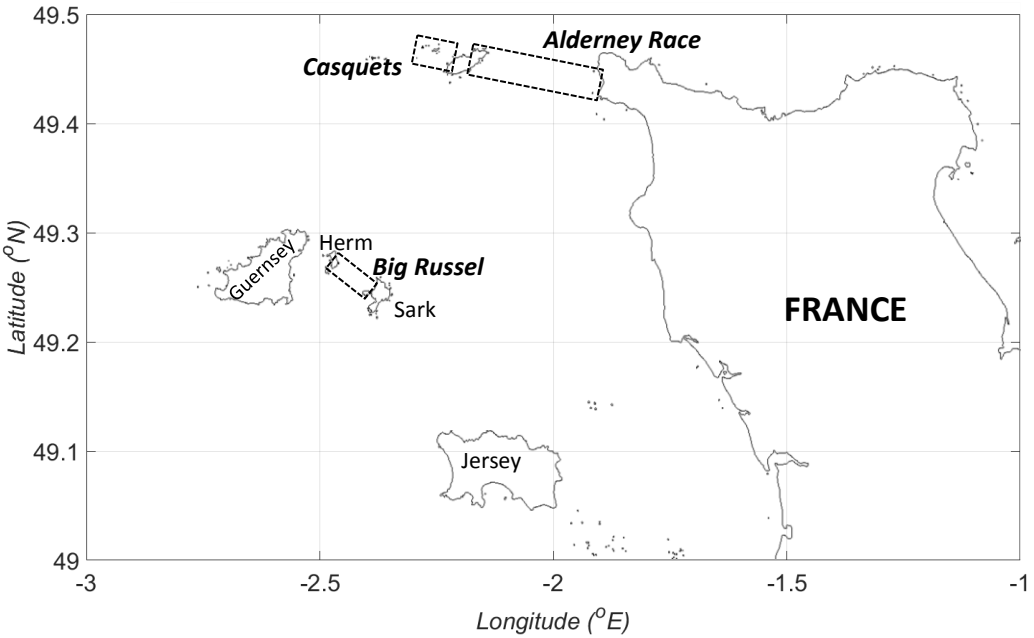

Figure 4.3 Location of tidal fences used to simulate energy extraction using an added distributed drag in Alderney Race, Casquets and Big Russel.

A summary of the simulations undertaken to quantify energy extraction are summarised in Table 4.2. Cases F1-F7 are referred to when discussing results in Chapter 7.2.

Table 4.2 Summary of the 7 tidal fence energy extraction cases (F1-F7) simulated using the English Channel model.

Case	Energy extraction location	Objective
F1	Alderney Race	Quantify the maximum average power potential, as well as a realistic level of energy extraction.
F2	Casquets	As above (Case F1).
F3	Big Russel	As above (Case F1).
F4	Alderney Race + Casquets	Quantify level of interaction between sites based on upper bound levels of energy extraction and realistic levels of energy extraction for the two sites.
F5	Alderney Race + Big Russel	As above (Case F4) for the two sites.
F6	Casquets + Big Russel	As above (Case F4) for the two sites.
F7	Alderney Race + Casquets + Big Russel	As above (Case F4) for the three sites.

For each case listed in Table 4.2, the area averaged array drag coefficient was increased incrementally to simulate more turbines until the total energy dissipated by the added drag reached a maximum (known as the maximum average power potential as discussed in Chapter 2.7.1.3 and any further increase in drag caused a reduction in total energy dissipation. The average extracted power was calculated using Equation 4.2 by integrating over the plot area and with respect to time (Draper et al. 2014):

$$P_E = \frac{1}{t}\int_0^t \left(\iint_{A_p} \rho C_e |\overline{U}|^3 dA \right) dt \qquad 4.2$$

Where P_E=average extracted power, t=time, A_p=array plot area, ρ=fluid density, C_e=area averaged array drag coefficient and $\overline{U}$=depth averaged streamwise velocity. Results for maximum power potential were compared with the analytical solution described by Equation 2.19 where values of amplitude of head difference across the length of each site and maximum volume flux were obtained from ambient flow results from the Telemac English Channel model. For cases F4-F7 where energy extraction was simulated at multiple sites, the effects of energy extraction on the energy extraction at the others was quantified.

The simulations were then re-run using an area averaged array drag coefficient of 0.015, which represents a more realistic level based on turbine layout limitations (Legrand 2009). In these cases the available power was also estimated using,

$$P_A = \frac{\lambda}{2}\frac{1}{t}\int_0^t \left(\iint_{A_p} \rho C_p |\bar{U}|^3 dA \right)$$

4.3

Where P_A=average available power, λ=array density, t=time, A_p=array plot area, ρ=fluid density, C_p=power coefficient and $\bar{U}$=depth averaged streamwise velocity.

4.4.3 Model sensitivity

The English Channel model uses a uniform bed roughness coefficient throughout the domain. In reality bed drag coefficient is influenced by local topography, bed roughness and depth so varies temporally, spatially and directionally, which can affect estimates for energy. To test the sensitivity of energy extraction results, bed drag coefficient was varied over the realistic range presented in Table 4.1. For each sea bed drag case, tidal fences were used to model energy extraction at Alderney Race, Casquets and Big Russel. For each case generated array power was estimated to quantify sensitivity to bed drag coefficient.

4.4.4 Sub-array modelling

Sub-array modelling was implemented within the English Channel model using the distributed drag method. The sub-array layouts were reproduced from the sub-array work originally implemented by Bahaj et al. (2004). Figure 4.4 shows the layout of the sub arrays in Alderney Race (Bahaj & Myers 2004). For consistency, a rated velocity of sub-arrays in the West Race and East Race was 2.5 m/s and 4 m/s respectively was implemented, as was done in the original study.

Results were compared with those obtained using low spatial and temporal resolution flow data and the kinetic flux method in (Bahaj & Myers 2004) to assess the effects of array scale blockage on the surrounding flow field and estimated power generation.

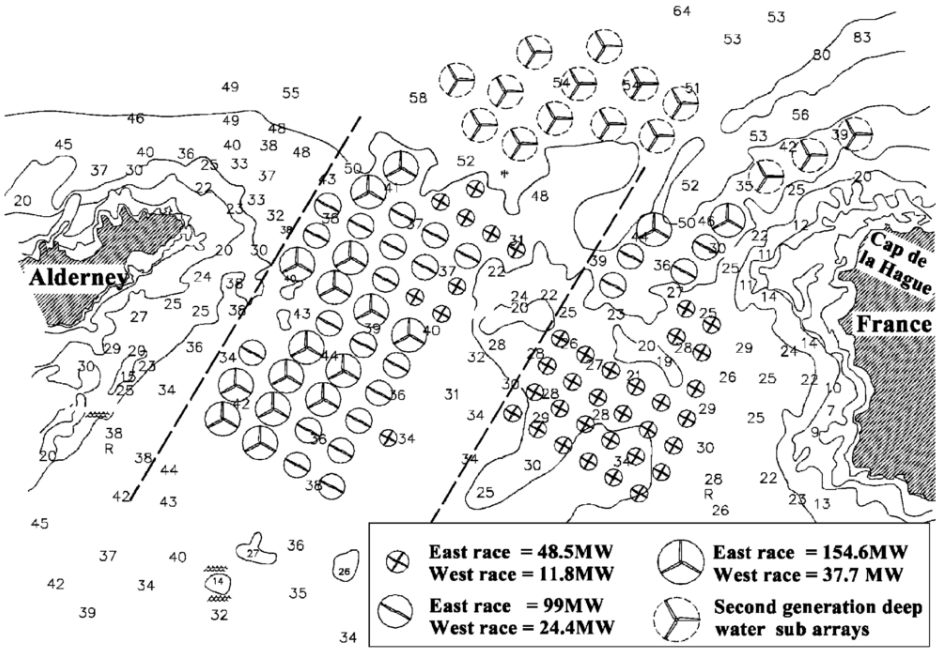

Figure 4.4 Sub-array layout and array capacity in Alderney Race (Bahaj & Myers 2004).

4.4.5 Array modelling

Arrays were sized and positioned based on the distribution of mean ambient kinetic energy flux (Equation 4.1) within depths limited to between 15-50m. Ambient flow results were used to estimate the mean annual generated power per swept area for isolated turbines using the kinetic flux method.

Based on results, three array plots were set out in Alderney Race as shown in Figure 4.5 and detailed in Table 4.3. A fourth potential Array plot in Casquets was also identified. For all arrays suitable depths were limited to between 50m and 15m. Simulations were run for a range of array densities (0.01, 0.02, 0.04, 0.06, 0.08) for each of the four arrays. Results from these simulations are presented in Chapter 7.4.

For each array, simulations were run for a range of realistic array densities using the distributed drag method and the available power was calculated using Equation 4.3. Mean annual available power per swept area was used as a metric for comparing the output of each array with that of the largest operational offshore windfarm, the London Array.

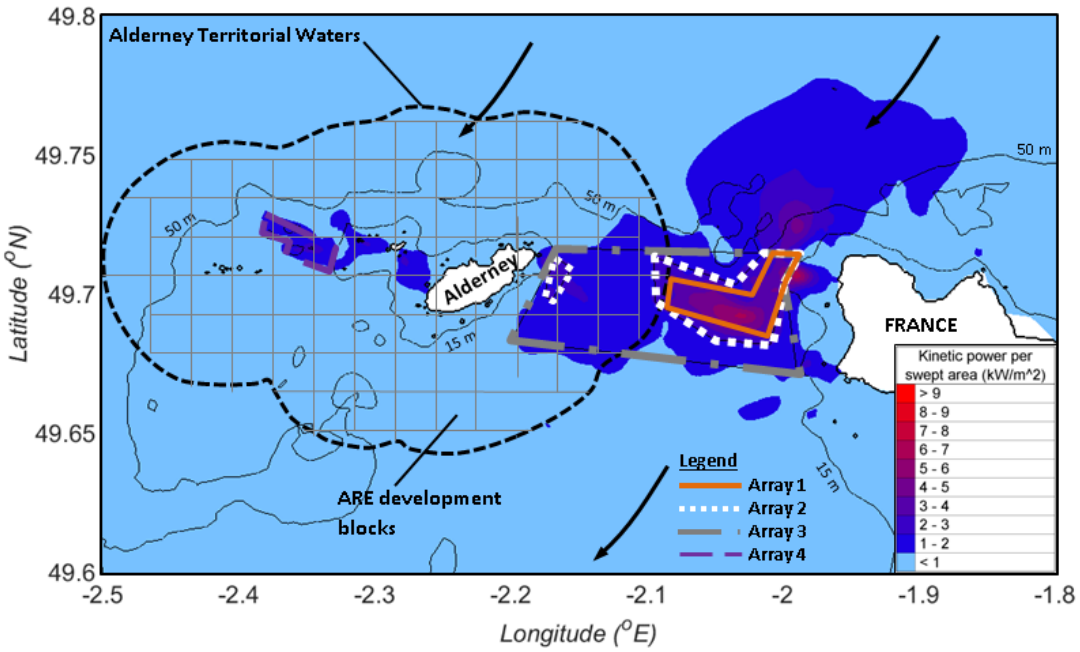

Figure 4.5 Arrays 1,2,3 and 4 located in Alderney Race and Casquets over regions of highest time averaged kinetic power per swept area within depths ranging between 15 m and 50 m. Arrows show the direction of the dominant ebb tide.

Table 4.3 Characteristics of Array layouts 1, 2, 3 and 4 used to simulate energy extraction in Alderney Race and Casquets based on mean annual power per swept area using the kinetic flux method. Total array lot area and range of array densities are outlined.

Case	Time averaged kinetic power per swept area (kW/m^2)	Total array plot area (km^2)	Array densities simulated
Array 1: Alderney (small)	>3	9	0.01, 0.02, 0.04, 0.06, 0.08
Array 2: Alderney (medium)	>2	17	0.01, 0.02, 0.04, 0.06, 0.08
Array 3: Alderney (large)	>1	52	0.01, 0.02, 0.04, 0.06, 0.08
Array 4: Casquets	>1	3	0.01, 0.02, 0.04, 0.06, 0.08

Chapter 5: Experimental results from flume testing

This Chapter presents results that expand upon a journal paper published in the International Journal of Marine Energy by Coles et al. (2016).

5.1 Overview

Chapter 2 identified three potential sources of error in the distributed drag method for modelling large tidal turbine arrays. In summary these are:

1. Discrepancy between the velocity through the turbine rotors within large arrays and the depth averaged velocity used to parameterise turbine and array drag.
2. An uneven distribution of drag amongst rows in the transition zone, which typically covers the first three rows at the upstream end of the array.
3. The potential change in the bed drag contribution to the total added drag as a result of the installation of arrays.

To quantify these potential errors, the methodology presented in Chapter 3 was carried out to obtain the necessary experimental measurements of velocity, fence drag and elevation drop across arrays of porous fences. This chapter uses experimental results to critically assess the validity of the distributed drag method for modelling energy extraction by large tidal turbine arrays.

5.2 Ambient flow characterisation

5.2.1 Mean flow

Figure 5.1 shows the ambient streamwise velocity distribution in the vertical plane along the centreline of the flume using Case A (without added bed roughness) and Case B (with added bed roughness) plotted alongside the depth averaged velocity in each case. The elevation is normalised by depth and velocities are normalised by upstream velocity at mid depth, as is the case in all graphs in this chapter. For Case B the velocity profile is plotted from profiles obtained directly above a roughness strip as well as in between two roughness strips. In the lower half of the water column the velocity increases directly above the roughness strip due to the increased blockage caused by the roughness strip. In the upper half of the water column the velocity is reduced in comparison with the velocity between two roughness strips. Figure 5.1 shows that for

both Case A and B, the velocity at height $z/h \approx 0.4 \approx e^{-1}$ is equal to the depth averaged velocity, which is an expected result for any logarithmic velocity profile (Raupach et al. 1991).

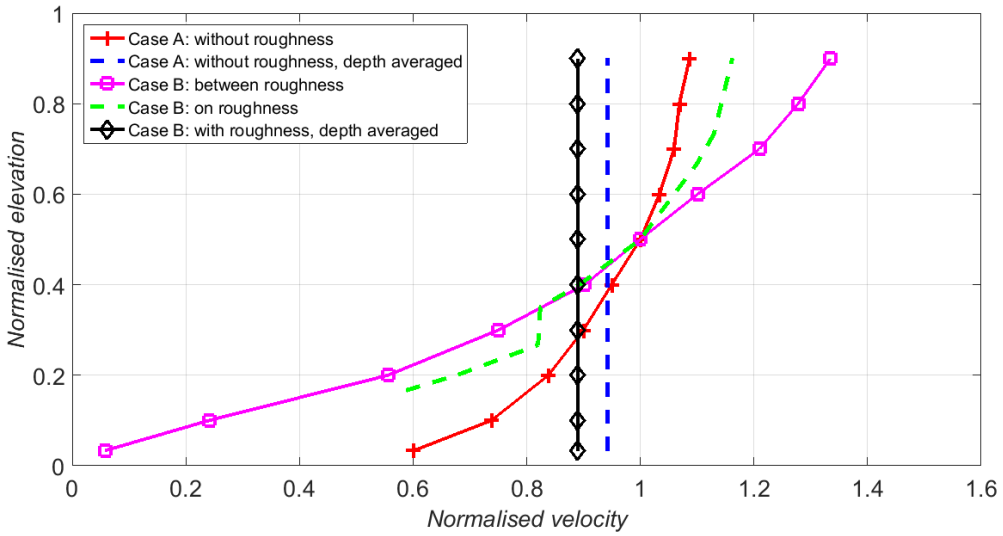

Figure 5.1 Ambient streamwise velocity distribution in the vertical plane for flow using Cases A and B. Results are plotted alongside the depth averaged velocity in both cases.

In Case A the depth averaged velocity was 0.215 m/s, 6% lower than the mid depth streamwise velocity. Similarly in Case B, the depth averaged velocity was recorded as approximately 10% lower than the mid depth velocity. A consequence of this related to depth averaged computational models is that the drag from the first fence will be underestimated when adopting the approach taken by (Plew & Stevens 2013), where the depth averaged velocity is used to calculate the force on a turbine (or fence in this case) using Equation 2.7, and that the force on a fence is related to flow at hub height (mid depth) only. This error is quantified in 5.4.3 by comparing the estimated array drag from the experiment with results from Equation 2.7.

Figure 5.2 shows the same centreline velocity profiles plotted in Figure 5.1 but plotted on a logarithmic y-axis. In Case A a logarithmic boundary layer exists in the bottom half of the water, where all velocity measurements fit within 10% of a logarithmic distribution with a roughness length of $2\text{x}10^{-4}$ m and a friction velocity of 0.014 m/s. Figure 5.2 shows the vertical distribution in velocity is logarithmic above z/h=0.1, where the flow is displaced vertically by the roughness sub layer (Raupach et al. 1991). In Case B a logarithmic boundary layer exists, however this time the roughness length has increased by an order of magnitude to $2\text{x}10^{-4}$ m and the friction velocity has approximately doubled to 0.034 m/s in comparison with Case A.

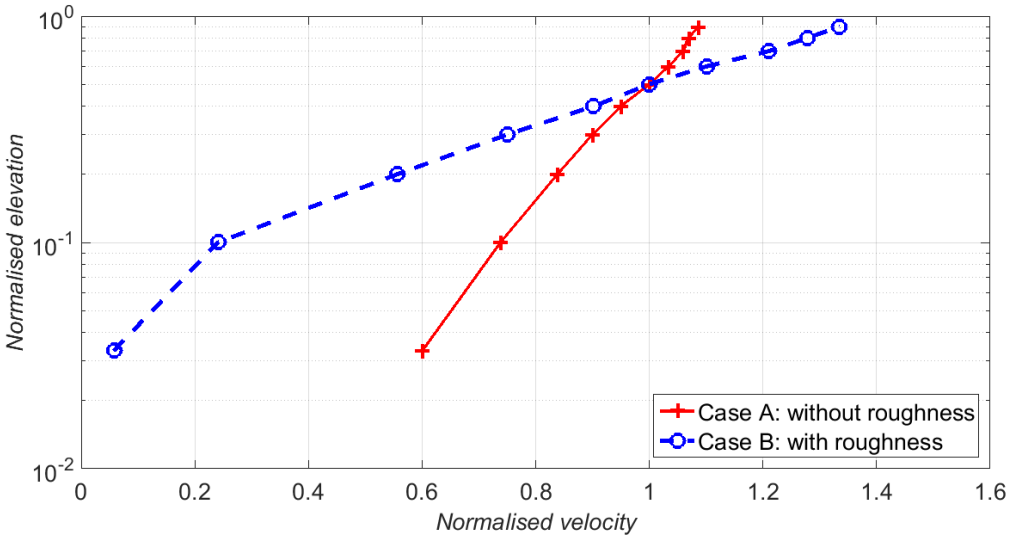

Figure 5.2 Logarithmic distribution in ambient streamwise velocity using Cases A and B.

Table 5.1 gives a comparison of the roughness length and friction velocity obtained in the flume experiments with field measurements in literature, where roughness length is normalised by depth and friction velocity is normalised by mid-depth velocity. The velocity profile in Case A is comparable with data obtained in the Irish Sea (Elliott 2002), where ship mounted ADCP measurements in depths of approximately 50 m show a logarithmic velocity profile in the lower 50-60% of the water column except at times of slack tide. Friction velocity was obtained from the gradient of the logarithmic flow distribution in the vertical plane, agreeing within 10% of the friction velocity measured in the Easter Irish Sea (Elliott 2002).

In general for Case B the normalised roughness length is at least two orders of magnitude greater than field measurements. This was a result of the roughness strip height, which was 10% of the depth, which prohibits the logarithmic layer from forming close to the bed. For Case B the normalised friction velocity was also significantly higher than field measurements in the Irish Sea, Port Angeles and Colvos Passage. This was also caused by the roughness strips, which shed large eddies off their leading edge to augment turbulence intensity, increasing shear stress. The Froude number measured in the Irish Sea and Port Angeles were both approximately 0.1, similar to that of the flume experiment, which was 0.13.

Table 5.1 Estimated roughness length (normalised by depth) and friction velocities using Case A: without roughness and B in comparison with flume testing and tidal sites quoted in literature.

Case	Flow description	z_0/h	u_*/U
Case A: without roughness	Flume with untampered bed, paint finish, h=0.3m, U_0=0.23 m/s, Fr= 0.13.	6.6×10^{-4}	0.061
Case B: with roughness (in cavity)	Flume with k-type roughness, constructed using wooden strips spanning the flume width and roughness strip pitch ratio of 10, h=0.3m, U_0=0.23 m/s, Fr= 0.13.	6.6×10^{-3}	0.157
Case B: with roughness (on strip)	Flume with k-type roughness, constructed using wooden strips spanning the flume width and pitch ratio of 10, h=0.3m, U_0=0.23 m/s, Fr= 0.13.	6.6×10^{-2}	0.135
Eastern Irish Sea (Elliott 2002)	Ship borne ADCP measurements taken off the North West coast of Anglesey in Liverpool Bay, with peak velocities of 1.2 m/s, h=50m, Fr= 0.13.	6.4×10^{-6}	0.056
Port Angeles, Washington State, USA (Sternberg 1968)	Complex bed composition of sand, gravel and rocks as large as 0.15 m protruding up to 0.1m above sand, varying in distribution and density within relatively small areas. Surface velocities of 2 m/s, h=42m, Fr= 0.1.	5.2×10^{-5}	0.047
Colvos Passage, Washington State, USA (Sternberg 1968)	Logarithmic mean flow profiles occurred throughout. Bed composed of sand deformed into irregular roughness elements with elevation of the order 5-7cm.Surface velocities of up to 0.5 m/s, h=30m, Fr= 0.03.	2.1×10^{-6}	0.030

5.2.2 Ambient turbulence intensity

Figure 5.3 shows the streamwise, transverse and vertical turbulence intensity distribution in the vertical plane for Cases A and B. Results from Case A agree within 5% of measurements taken at Nodule Point, Admiralty Head (Thomson et al. 2012) and the Sound of Islay (Milne et al. 2013) in the lower 20% of the water column. Maximum recorded velocities of 1.8 m/s at z/h=0.2 and 3.2 m/s at z/h=0.14 were obtained at Nodule Point and Admiralty Head respectively whilst in the Sound of Islay the mean velocity reached 2.5 m/s at z/h=0.1. Transverse and vertical turbulence intensities compare less well, with (Milne et al. 2013) observing approximately 9-10 % and 7-8% turbulence intensities in the transverse and vertical directions respectively, giving a ratio of streamwise turbulence intensity to transverse and vertical intensities of 1:0.75:0.56 for the Sound

of Islay. Flume measurements give the same ratio as 1:0.57:1.57, showing significantly higher turbulence intensity in the vertical direction relative to the streamwise and transverse directions.

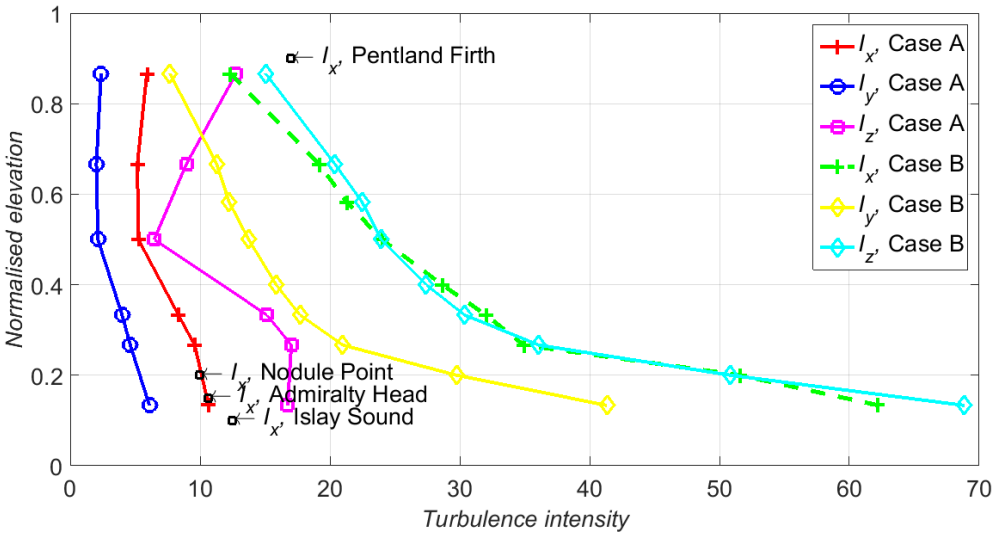

Figure 5.3 Distribution of ambient streamwise (*x*), transverse (*y*) and vertical (*z*) turbulence intensity in the vertical plane for Cases A and B.

In Case B turbulence intensity was enhanced in the streamwise, transverse and longitudinal directions with the addition of the roughness strips. Eddies shed off the leading edge of each roughness strip significantly increased turbulence intensity to enhance mixing between the flow in the roughness layer and the outer flow, augmenting momentum exchange (Cui et al. 2003; Trembanis et al. 2004). This shows reasonable agreement with ADCP measurements taken in the Pentland Firth where turbulence intensities of 17% were recorded close to the free surface (Hardwick et al. 2015).

5.2.3 Hydraulically rough flow

Analysis of the flume bed surface showed that for Case A, 2 mm variations in bed surface elevation occur over multiple randomly selected regions of the flume, where typically this variation occurred over a 10 mm length. The theory and criteria for hydraulically rough flow is presented in Appendix A. This result indicates it is unlikely that the flow is hydraulically rough for Case A.

The criteria for hydraulically rough flow is met easily for Case B given that the physical roughness height is 0.03 m. In Case B Reynolds number similarity is reached, which implies that U_0/u_* is independent of Reynolds number, making it dependent on the features of the roughness only

(Raupach et al. 1991). This means results obtained using Case B are also applicable to higher ambient upstream streamwise velocities. However this is not the case for Case A.

5.2.4 Force balance

Table 5.2 shows experimental results of the hydrostatic, weight component and bed drag forces and the depth averaged velocities calculated at the inlet and outlet. The bed drag force was obtained using the force balance described by Equation 3.5. For Case A bed drag was very low; less than 5% of the weight component force and the resultant hydrostatic force. For case B the frontal area of the roughness strips increased the form drag due to the pressure difference either side of each roughness strip, increasing bed drag significantly as a result (Cui et al. 2003). In Case B the bed drag force was 25% of the weight component force and 30% of the resultant hydrostatic force.

Table 5.2 Experimental measurements of depth, depth averaged streamwise velocity and hydrostatic force at the inlet and outlet, as well as the weight component force and bed drag force. Inlet and outlet measurements taken 5 m and 13 m downstream of the flow straighteners at the flume inlet respectively.

Case	Inlet depth	Outlet depth	Inlet depth averaged velocity	Outlet depth averaged velocity	Inlet hydrostatic force	Outlet hydrostatic force	Weight component force	Bed drag force
A	0.295m	0.310 m	0.249 m/s	0.237 m/s	585 N	646 N	63 N	2 N
B	0.289	0.301 m	0.223 m/s	0.209 m/s	559 N	607 N	61 N	14 N

5.3 Velocity characterisation within porous fence arrays

5.3.1 Single fence – Cases A1 and B1

Figure 5.4 shows the wake velocity downstream of a single fence using Case A1, which demonstrates that momentum transfer between the wake and bypass flow above and below the fence was insufficient to recover the flow completely after a distance of 18 fence heights downstream of the fence, at which point the mid depth velocity had recovered to 82% of the ambient upstream streamwise velocity. A consequence of this is that additional fence(s) positioned downstream of the first will be in the wake of fence 1. Based on previous experimental

results of the wake downstream of a porous fence (Myers & Bahaj 2010) and the spatial constraints that are likely to impact on array design, it is highly likely that this will be a feature of full-scale array layouts. Wakes profiles in Figure 5.4 show that for Case A, the assumption of a dual log profile made by Blunden (2009) is not valid in the wake region captured in these experiments, which extends to 24 fence heights downstream of the fence.

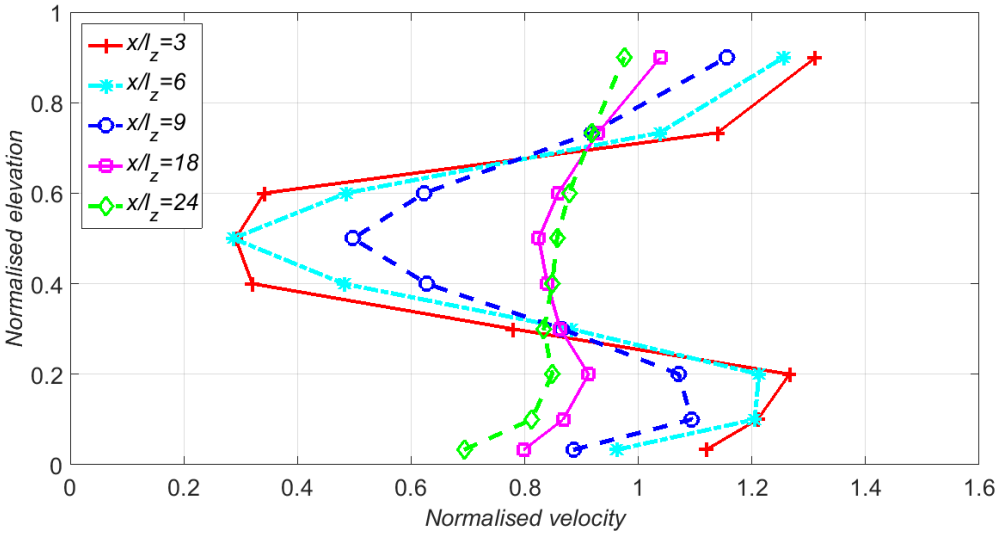

Figure 5.4 streamwise velocity distribution in the vertical plane at locations downstream of a single fence positioned perpendicular to the flow (Case A1).

Figure 5.5 shows the wake velocity downstream of a single fence using Case B1. For Case B1, higher ambient turbulence intensity enhanced momentum transfer between the wake and bypass flow to improve near wake recovery in comparison with Case A1. This is illustrated in Figure 5.6, which shows streamwise velocity at locations downstream of a single fence using Cases A1 and B1. For Case A1 the near wake velocity recovers much slower than in Case B1. The consequence of this is that for arrays with a low fence spacing the force incident on downstream fences is likely to be lower in comparison with Case B arrays. This will result in a lower total array drag assuming the same upstream conditions.

Figure 5.6 shows that in the far wake (i.e. at positions greater than 20 fence heights downstream of the fence) the wake velocities both recover to approximately 87% of the upstream velocity. Further downstream the wakes in Case A1 and B1 follow the same trend, which implies the wakes are independent of ambient turbulence intensity in the far wake region.

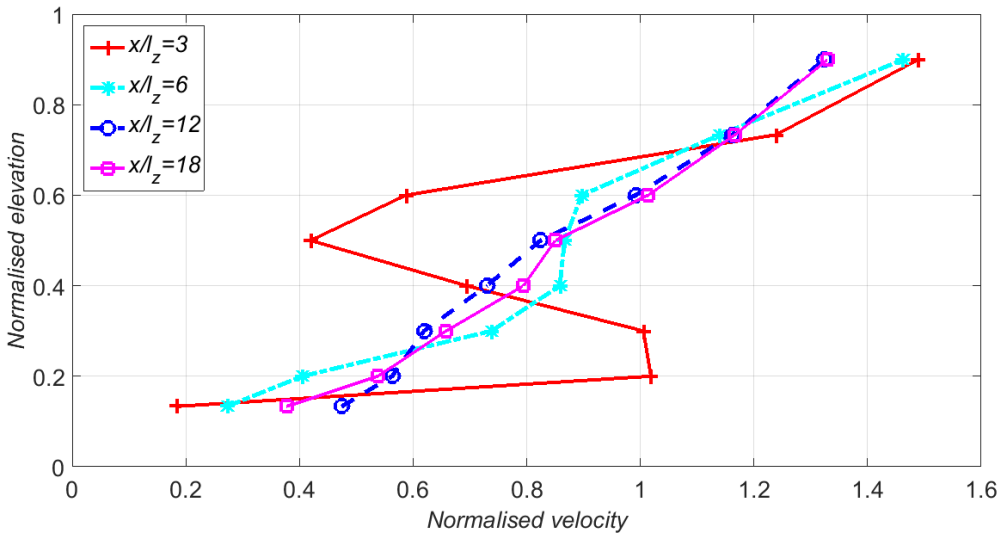

Figure 5.5 Streamwise velocity distribution in the vertical plane at locations downstream of a single fence positioned perpendicular to the flow (Case B1).

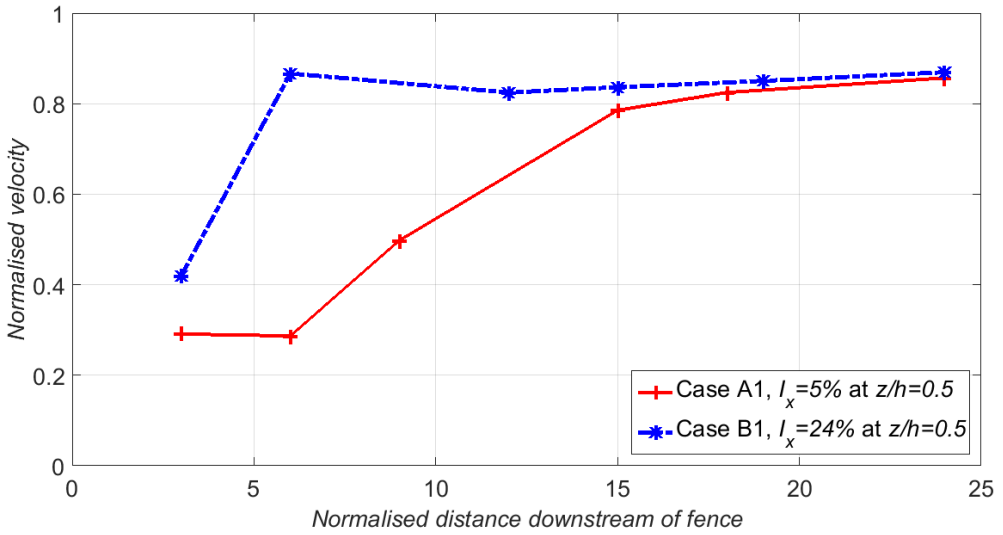

Figure 5.6 Mid depth centreline streamwise velocity downstream of a single fence of Cases A1 and B1. Distance downstream of fence is normalised by the fence height.

5.3.2 Multi- fence arrays – Cases A1 and B1

Figure 5.7 shows the streamwise velocity distribution in the vertical plane at six fence heights downstream of fences 1-5 in array Case A7. Out of all fences in the array, the velocity through Fence 1 was greatest since it is free from the wake of any upstream fences. As a result the reduction in momentum through fence 1 was also greatest, creating a high wake velocity deficit downstream (and increased bypass velocity above and below the fence to satisfy continuity) so that the velocity at mid depth hitting Fence 2 was significantly reduced. In the region between fence 1 and 3, the flow transitioned to an equilibrium state, where the drag from fences and the bed is in balance with the longitudinal pressure gradient and weight component that drives flow through the array. In this transition region at Fence 2 the depth averaged velocity was approximately 250% greater than the mid depth velocity because of the presence of the wake from Fence 1. This would incur a significant error in the depth averaged force attributed to Fence 2 in a depth averaged drag formulation such as Equation 2.7.

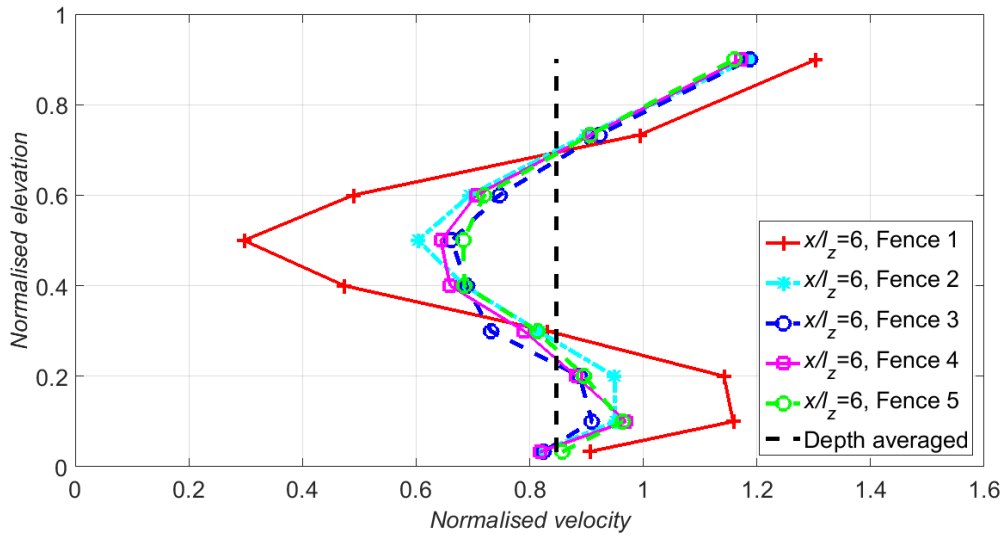

Figure 5.7 Streamwise velocity distribution in the vertical plane 6 fence heights downstream of fences 1-5 for Case A7.

By Fence 3 the flow reached an equilibrium condition where the opposing forces on the flow (i.e. the fence drag and bed drag) were closely balanced against the longitudinal pressure gradient and weight component driving the flow so that the wake downstream of successive fences recovered to approximately the same magnitude. This is true for all of the arrays considered in this study. To demonstrate this Figure 5.8 and Figure 5.9 shows the streamwise velocity distribution in the vertical plane at twelve and eighteen fence heights downstream of fences 1-5 in array Case A5 and A3 respectively. For these cases the spacing is greater between fences, giving the wake more opportunity to recover between fences. As a result the mid depth velocity shows improved

agreement with the depth averaged value in comparison with Case A7. The bypass velocity below and above the fences reduces, caused by momentum exchange with the wake directly above and below it. This recovers the mid depth velocity in the wake, where for Case A3 only fence 1 is in the transition zone as all other velocity profiles fall on one another and mid depth and the mid depth velocity was within 5% of the depth averaged velocity.

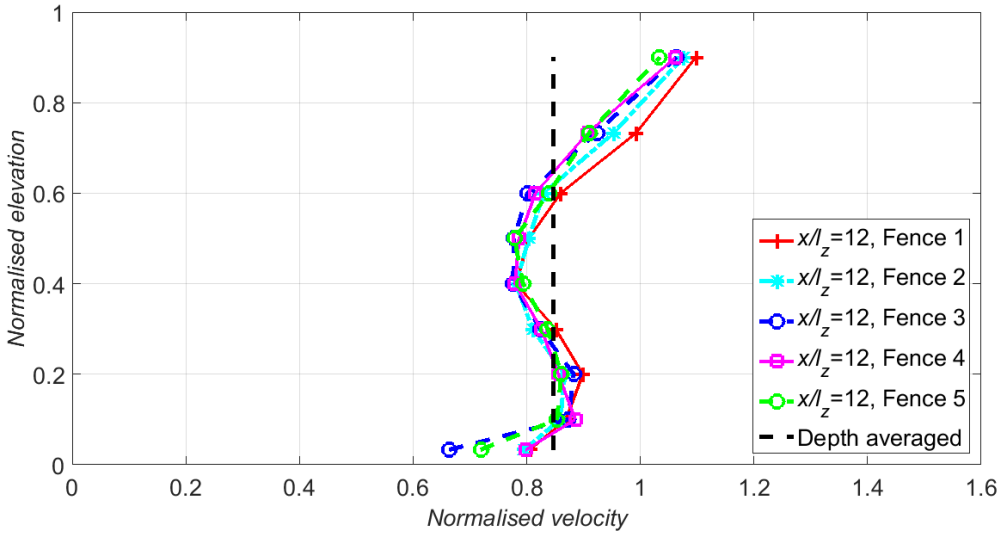

Figure 5.8 Streamwise velocity distribution in the vertical plane 12 fence heights downstream of fences 1-5 for Case A5.

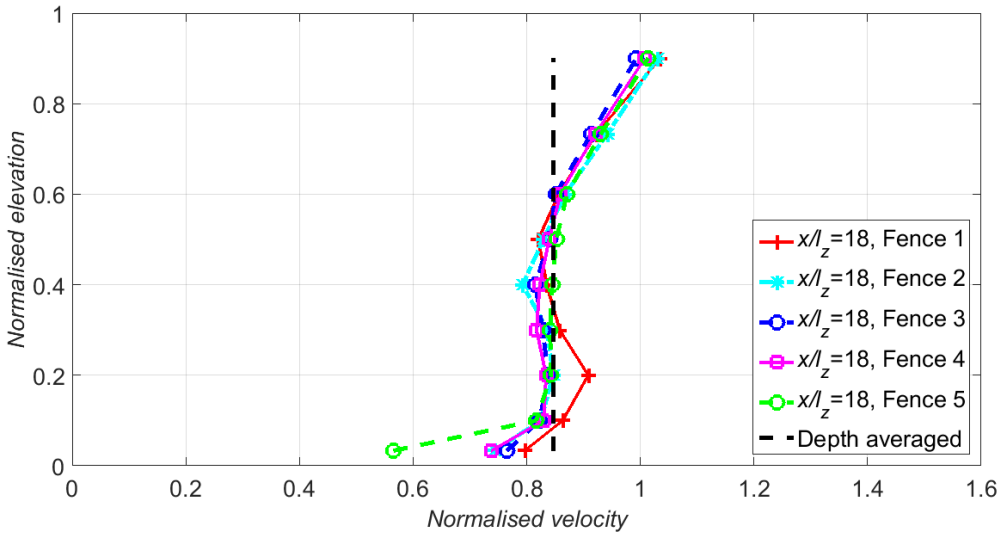

Figure 5.9 Streamwise velocity distribution in the vertical plane 18 fence heights downstream of fences 1-5 for Case A3.

Figure 5.10 shows that equilibrium conditions were reached after a minimum of three rows for array Cases 3-7, where the velocity through each remaining downstream equilibrium fence

(downstream of the three transition fences) was within ±2.5% of the velocity through the final fence.

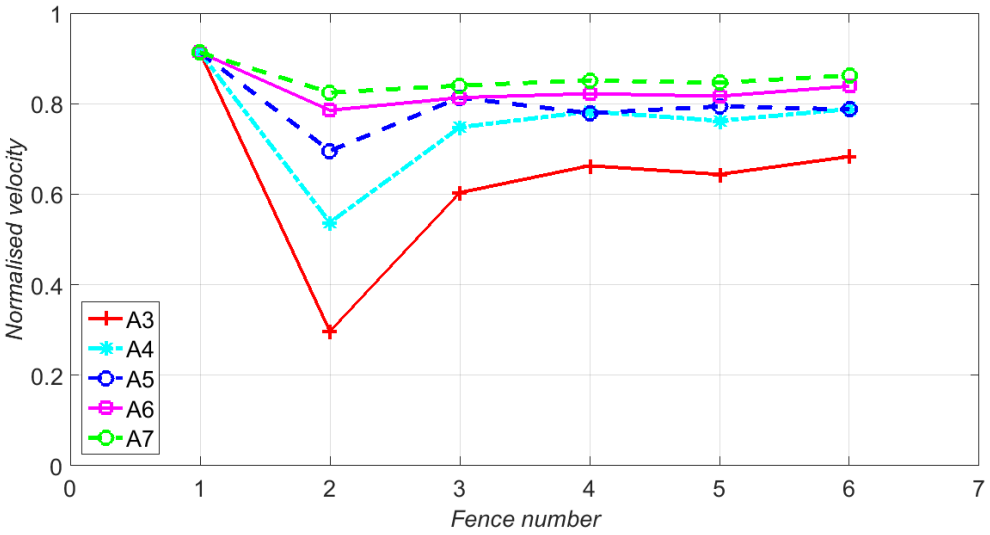

Figure 5.10 Streamwise mid depth velocity through successive fences for array Case A3, A5 and A7.

Figure 5.11 shows the streamwise velocity distribution in the vertical plane at six fence heights downstream of fences 1-5 in array Case B7. The augmented ambient turbulence intensity enhanced mixing between the bypass and wake flow so that the wakes were far less prominent in comparison with Case A7. As a result the mid-depth wake velocity within the arrays showed a closer agreement with the depth averaged velocity in comparison with A7. The same can be said of the velocity profiles obtained within array Cases B5 and B3, which are plotted in Figure 5.12 and Figure 5.13 respectively.

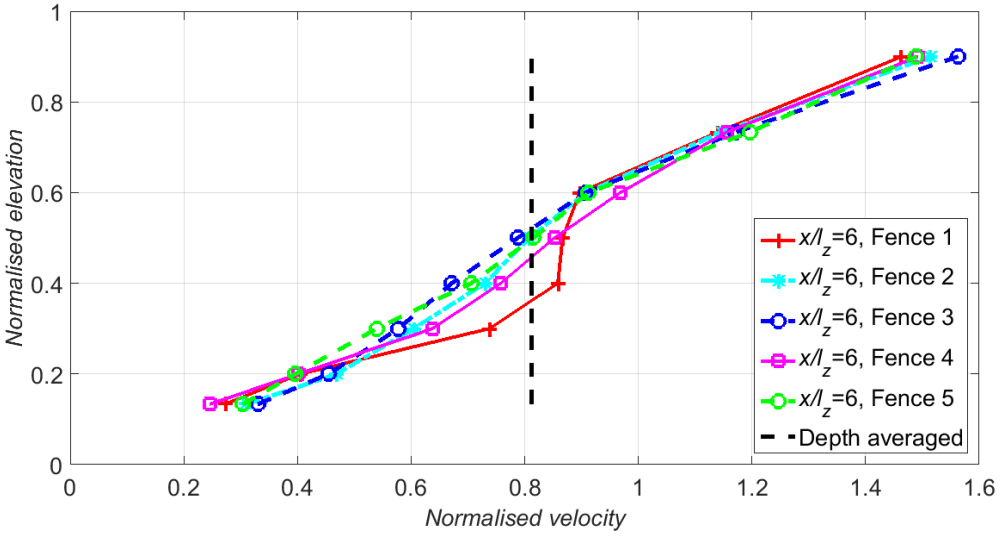

Figure 5.11 Streamwise velocity distribution in the vertical plane 6 fence heights downstream of fences 1-5 for Case B7.

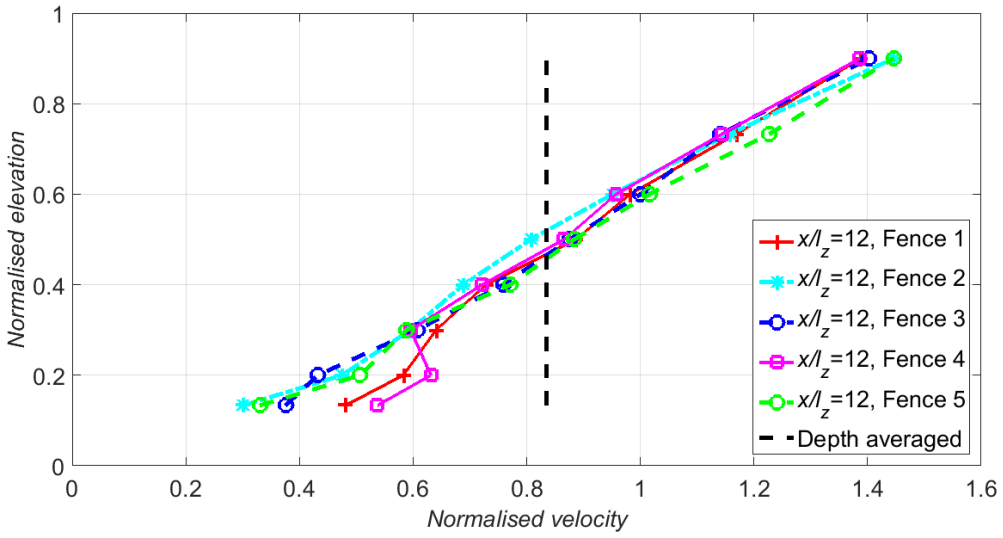

Figure 5.12 Streamwise velocity distribution in the vertical plane 12 fence heights downstream of fences 1-5 for Case B5.

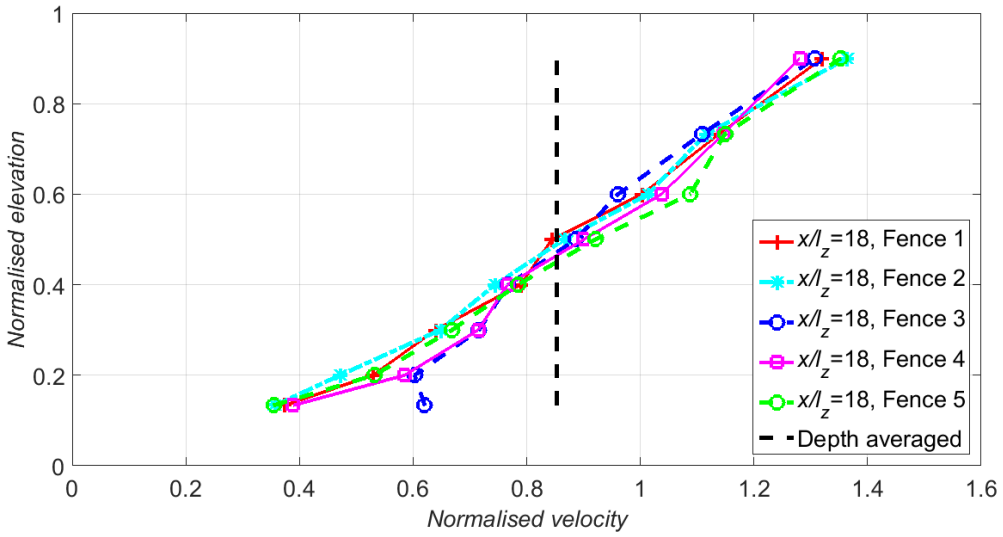

Figure 5.13 Streamwise velocity distribution in the vertical plane 18 fence heights downstream of fences 1-5 for Case B3.

Figure 5.14 shows the mid depth stream wise velocity within arrays B3, B5 and B7. The velocity appears relatively unchanged as the flow develops through successive fences, implying that the transition region has been removed completely by the augmented ambient turbulence intensity, which enhances mixing between the wake and the bypass flow. This will be discussed further in 5.4.2 in relation to the distribution in drag amongst the fences within each array.

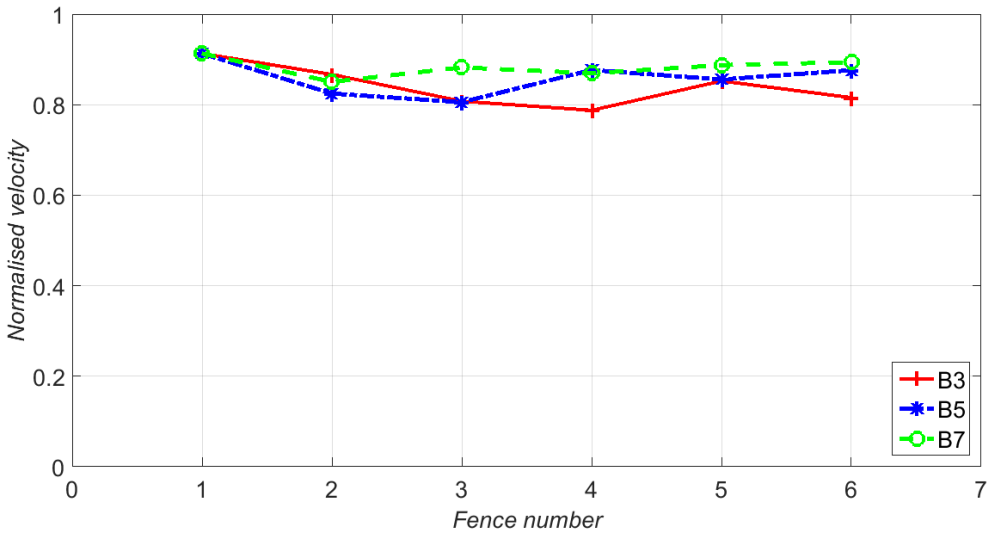

Figure 5.14 Streamwise mid-depth velocity through successive fences for array Case B3, B5 and B7.

Figure 5.15 shows the relationship between the equilibrium velocity at mid-depth within each array and the array density, which is defined as the ratio of the total frontal area of all fences within the array to the array plot area.

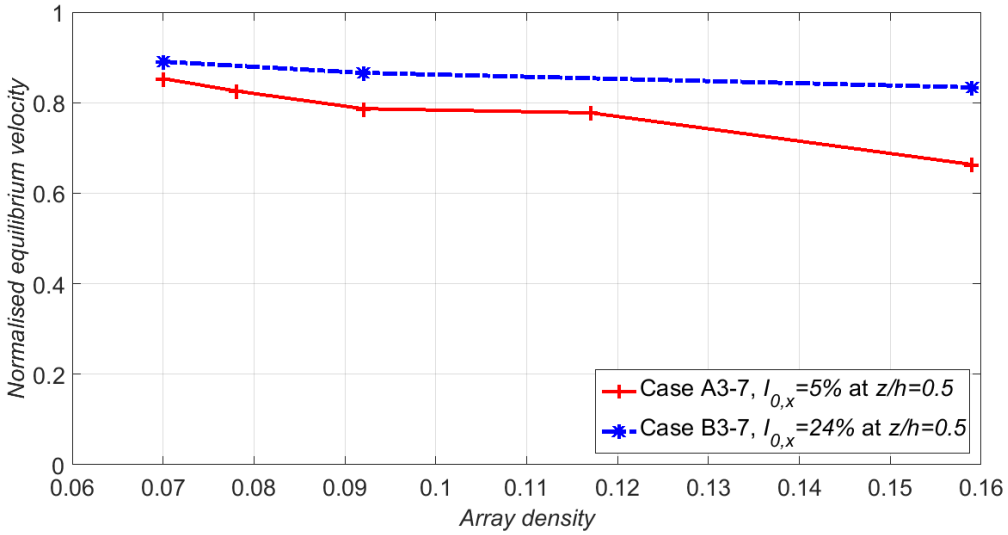

Figure 5.15 Variation in equilibrium velocity with array density using Array cases A3-7 and B3-7. Results normalised by upstream velocity at mid depth.

For array Cases B3-7 there was a 6% reduction in equilibrium velocity as array density increased from 0.070 (Case B3) to 0.159 (Case B7). Over the same array density range, array Cases A3-7 gave a 23% reduction in equilibrium velocity. To determine whether it is beneficial to add an additional row to a tidal turbine array in a pre-defined plot area, the power generated by the added row must be greater than the reduction in power generated by the existing rows due to the reduction

in equilibrium velocity with increased array density. This can only be understood with site specific array optimisation given that wake recovery is dependent on ambient turbulence intensity.

5.4 Array drag characterisation

5.4.1 Single fence – Cases A1 and B1

The drag coefficient of a single fence was parameterized using the upstream mid depth velocity. This adopts the approach taken in literature to parameterize the drag on a model tidal turbine (A. S. Bahaj et al. 2007). An alternative approach to parameterizing array drag is to use the upstream volume averaged velocity over the fence area to consider the variation in velocity within the cross sectional area of the fence or disk. It was found from analysis of the velocity distribution in Figure 5.1 that for the inflows considered here, the upstream velocity at the centroid height of the fence fell within 2% of the upstream volume averaged velocity over the fence area for Case A and B. These results are summarised in Table 5.3 , which also gives a comparison with the depth averaged velocity.

Table 5.3 Comparison between the centroid height velocity, volume averaged velocity and depth averaged velocity.

Case	Mid depth velocity	Volume averaged velocity	Depth averaged velocity
A	0.231 m/s	0.234 m/s	0.217 m/s
B	0.236 m/s	0.240 m/s	0.210 m/s

Figure 5.16 shows the relationship between the drag coefficient of a single fence and the upstream velocity at mid depth. Upstream Reynolds number is also plotted, where the hydraulic radius is the characteristic length scale and the upstream velocity at mid depth is the characteristic velocity scale. For Case A1, the fence drag coefficient remained approximately constant with upstream velocity at 1.54.

In contrast the drag coefficient of the fence reduced significantly for flow in Case B1 with increasing upstream velocity, both when the fence was positioned half way between roughness strips and directly above a roughness strip in more constrained flow. This is likely to be related to the eddies shed off the roughness, which are a function of the upstream velocity.

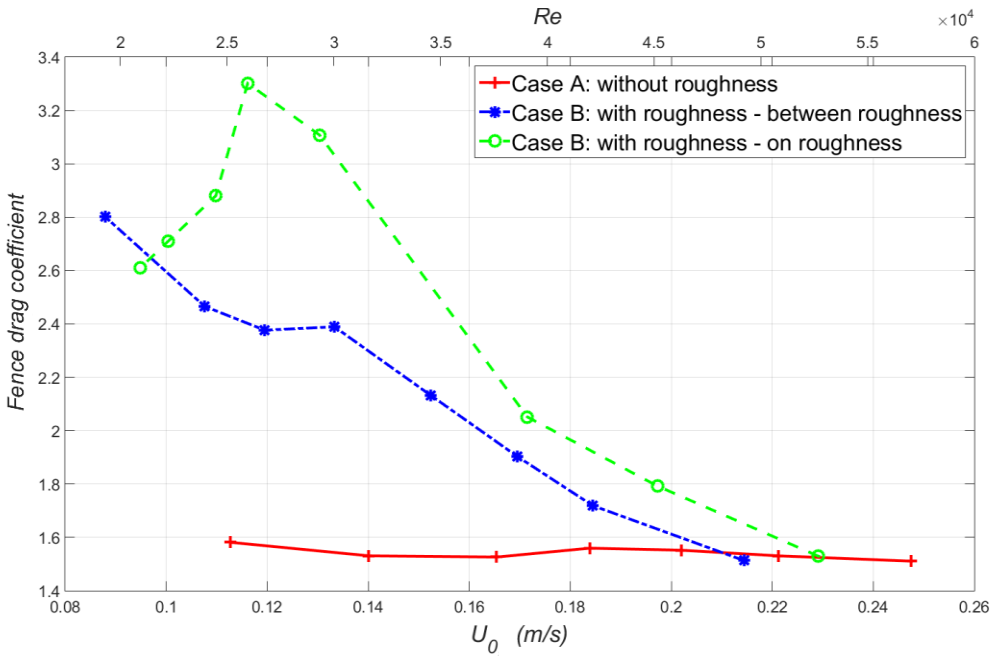

Figure 5.16 Variation in the drag coefficient of a single fence with upstream Reynolds number using Cases A1 and B1.

For Case B1, with upstream velocity greater than 0.15 m/s, the drag coefficient reduced linearly with upstream velocity. The average of the two velocity profiles was used to obtain this linear relationship between the drag coefficient on the fence and the upstream velocity, which is expressed by Equation 5.1:

$$C_f = 3.5 - \frac{Re}{2.5 \times 10^4} \qquad 5.1$$

Where C_f=drag coefficient of the porous fence and Re=upstream Reynolds number.

In literature, a common approach to estimating the drag of an array of turbines is to use the drag coefficient obtained for a single isolated turbine, then scale up the drag based on the total number of turbines within the array. To demonstrate this for the case of an array of porous fences, this approach would give an array force defined by Equation 5.2:

$$F_a = \frac{1}{2}\rho \bar{U}^2 C_f A_a \qquad 5.2$$

Where F_a=array drag force, ρ=fluid density, $\overline{U}$=depth averaged velocity within the array at the fence locations, C_f= drag coefficient of the porous fence and A_a=the total frontal area of each fence in the array. For Case A the fence drag coefficient is 1.54 (Equation **Error! Reference source not found.**), for Case B the fence coefficient is defined by Equation 5.1.

5.4.2 Multi-fence array drag – Cases A2-A7 & B2-B7

Figure 5.17 shows the drag coefficient of each fence within array Cases A3-A7. Results show that for the arrays considered here the drag force is always greatest on fence 1, since it is located out of any wake flow since it is the furthest fence upstream. In all cases there is a noticeable reduction in drag on fence 2, which is located in the wake of fence 1. This creates an uneven distribution in drag amongst fences 1 and 2 and is most noticeable for Case A7, with the lowest spacing between fences. This gives less opportunity for wake recovery between fences, as was illustrated by the velocity profiles within the arrays in Chapter 5.3.2. By fence 3 the drag reaches a steady value, so that there is an even distribution in drag amongst fences 3, 4 and 5. The magnitude of this drag is dependent on the spacing between fences, where a greater fence spacing allows greater wake recovery between fences and as a result a greater evenly distributed fence drag amongst fences 3, 4 and 5.

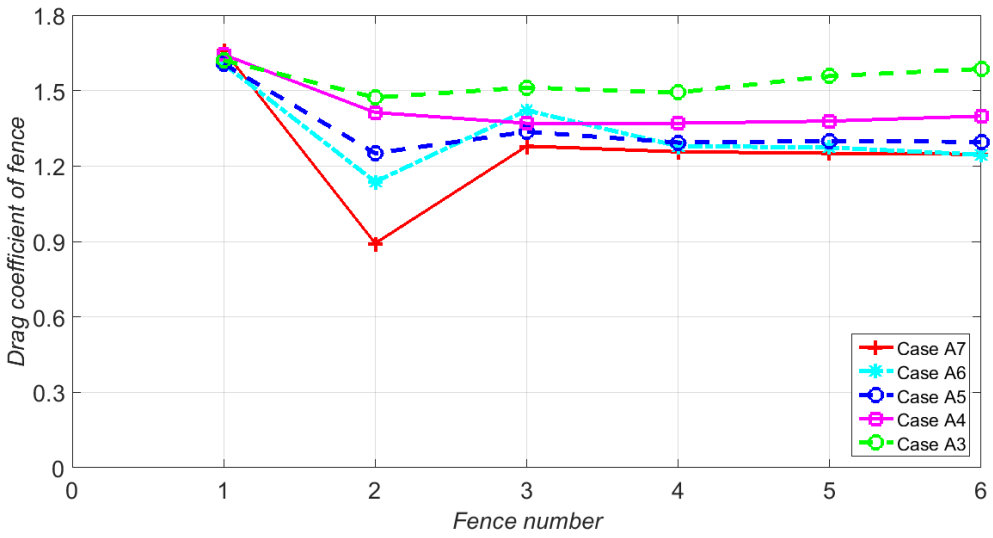

Figure 5.17 Drag coefficient of fences within array Cases A3-A7.

Figure 5.18 shows the drag coefficient of each fence within array Cases B3, B5 and B7. Results show the same trend as for array Cases A3-A7, where in general the drag on fences 3-5 levels out to give an even distribution in drag in the equilibrium region. The uneven distribution in drag amongst fences 1 and 2 is far less noticeable in comparison with Case A3-7, since the drag coefficient of fence 2 remains relatively high from augmented wake recovery downstream of

fence 1 as a result of higher levels of ambient turbulence intensity. This reduces the uneven distribution in drag in the transition region in comparison with Cases A3, A5 and A7.

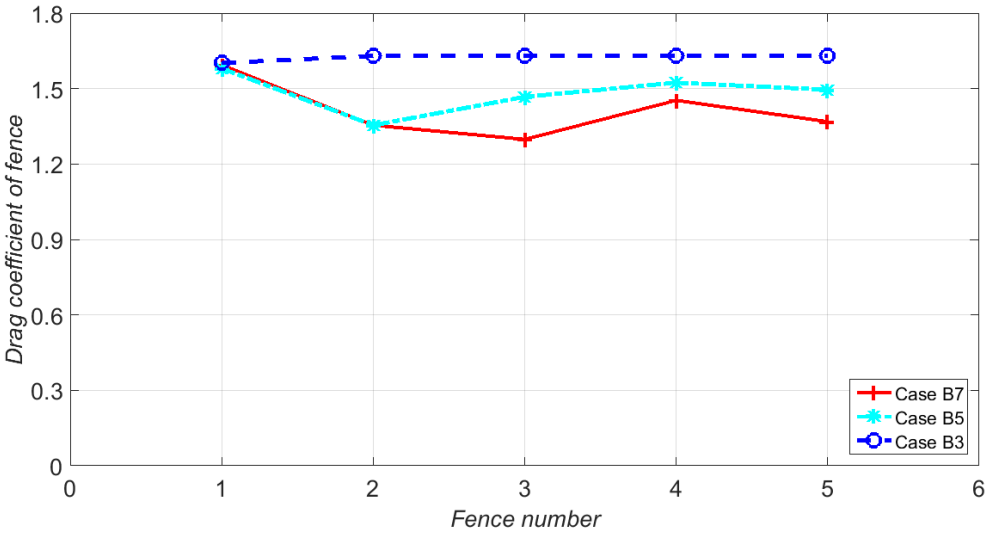

Figure 5.18 Drag coefficient of fences within array Cases B3, B5 and B7.

Results in Table 5.4 quantify the average force on transition fences (fences 1-3), equilibrium fences (fence 4 onwards) as well as all fences within array Cases A3-7 respectively using load cell measurements of the force on each individual fence.

Table 5.4 Average fence force amongst fences in the transition region (fences 1-3), equilibrium region (fences 4 onwards) and the whole array for array Cases A3-7.

Array case	Array density	Average drag on transition fences (N)	Average drag on equilibrium fences (N)	Average drag on all fences (N)
A3	0.070	5.69	5.44	5.57
A4	0.078	5.22	5.00	5.10
A5	0.092	4.93	4.59	4.73
A6	0.117	4.89	4.47	4.63
A7	0.159	4.24	4.17	4.19

In general, the average force on fences within the transition region is within 10% of the average force on fence in the equilibrium region (fence 4 onwards) and within 5% of the average force on each fence in the whole array over all array densities. Therefore even within the transition zone where there can be a highly uneven distribution of drag amongst the first three fences, the average force within this region was still representative of the total array average.

5.4.3 Array drag parameterisation

Results from the force balance (Equation 3.5) are shown in Table 5.5 and Table 5.6 for array Cases A1-7 and Cases B1-7 respectively. As fences were added, the total array drag opposing the flow increased. This resulted in an increase in upstream depth with array density, whilst downstream depth was independent of array density so remained the same for all cases. This led to an increase in the hydrostatic force driving flow downstream with increasing array density to counter the increase in array drag. Ultrasonic distance measurements along the centreline of the flume show that flow depth upstream of any given array was less than the flow depth downstream so that depth increased across the array. Since the flume bed elevation drops approximately linearly with distance downstream of the inlet, free surface elevation also dropped across the arrays.

Table 5.5 Experimental measurements of inlet depth taken at 5 m downstream of the flume inlet, outlet depth taken at 13m downstream of the flume inlet, depth averaged inlet and outlet velocities, hydrostatic forces at the flume inlet and outlet, the weight component force, array force and bed drag force using a force balance for array Cases A1-7.

Case	Array density	Inlet depth	Outlet depth	Inlet depth averaged velocity	Outlet depth averaged velocity	Hydrostatic force at inlet	Hydrostatic force at outlet	Weight component force	Array force	Bed drag force
A1	→0	0.295	0.310	0.242	0.231	585	646	63	6	~0
A2	0.033	0.297	0.310	0.242	0.231	593	646	63	12	~0
A3	0.070	0.299	0.310	0.228	0.220	601	646	63	22	~0
A4	0.078	0.301	0.310	0.235	0.229	609	644	64	25	~0
A5	0.092	0.303	0.311	0.238	0.232	615	648	64	29	~0
A6	0.117	0.303	0.310	0.248	0.242	617	646	64	33	~0
A7	0.159	0.305	0.310	0.235	0.232	625	646	64	46	~0

For array Cases A1-7 the estimated bed drag was very low, as was the case for the ambient flow regime. The force balance implies that the bed drag is insignificant in comparison to hydrostatic and weight component individual force terms. In some cases the force balance gave a bed drag less than 0, which was caused by error in inlet and outlet depth measurements. For array Cases

B1-7 there was a significant increase in the bed drag force, which is discussed further in Chapter 5.5.

Table 5.6 Experimental measurements of inlet depth taken at 5 m downstream of the flume inlet, outlet depth taken at 13m downstream of the flume inlet, depth averaged inlet and outlet velocities, hydrostatic forces at the flume inlet and outlet, the weight component force, array force and bed drag force using a force balance for array Cases B1-7.

Case	Array density	Inlet depth	Outlet depth	Inlet depth averaged velocity	Outlet depth averaged velocity	Hydrostatic force at inlet	Hydrostatic force at outlet	Weight component force	Array force	Bed drag force
B1	→0	0.290	0.300	0.234	0.226	565	605	61	6	16
B2	0.033	0.292	0.300	0.228	0.222	573	605	62	11	19
B3	0.070	0.295	0.300	0.226	0.222	583	605	62	19	21
B4	0.078	0.296	0.300	0.219	0.216	587	605	62	24	20
B5	0.092	0.297	0.301	0.239	0.236	593	609	62	32	14
B6	0.117	0.298	0.300	0.212	0.210	595	605	62	32	21
B7	0.159	0.296	0.295	0.212	0.213	589	585	62	49	16

Figure 5.19 shows a comparison between the array drag coefficient obtained using Equation **Error! Reference source not found.** for a single fence (which is typically used to parameterise array drag in regional scale hydrodynamic models), and the true array drag coefficient obtained from load cell measurements of all fences within array Cases A1-7. This analysis uses the methodology in Chapter 3.7.1.

For array density less than 0.07, the array drag coefficient derived from the drag on a single fence (Equation **Error! Reference source not found.**) underestimates the true array drag coefficient derived from the drag on all fences within the array, but remains within 10% of the true value.

As array density exceeds 0.07, the single fence drag coefficient starts to overestimate the true array drag coefficient. This is caused by the slow moving wake from upstream fences which impedes on downstream fences, reducing the drag on fences within the arrays. Depth averaged velocity does not account for this as was shown in Figure 5.7 for array Case A7.

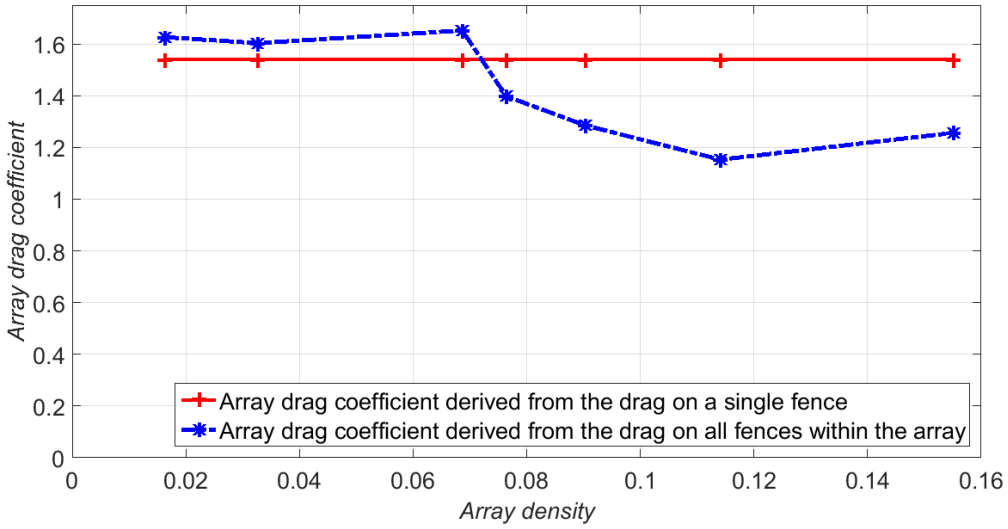

Figure 5.19 Comparison between the array drag derived from a single fence and the true array drag coefficient obtained from the drag on all fences within the array for Cases A1-7.

The change in depth between the array inlet and array outlet results in a change in depth averaged velocity through the array, as shown in Table 5.5 and Table 5.6. In the most extreme case of array Case A7, there is a 3.5% change in depth averaged velocity, which is significant for approximations of array drag coefficient. This was accounted for by averaging the depth averaged velocity squared over array length by assuming a linear free surface elevation drop across each array. This assumption has been verified using the backwater curves method (Chow 1959) and a simple 2D numerical model that simulates the linear rate of change of free surface elevation over a distributed drag for flow in an open channel with the same input parameters as the experiment.

Figure 5.20 shows a comparison between the array drag coefficient obtained using Equation 5.1 for a single fence (which is typically used to parameterise array drag in regional scale hydrodynamic models), and the true array drag coefficient obtained from load cell measurements of the drag force on all fences within array Cases B1-7.

The comparison shows agreement within 10% over the whole array density range. This was due to enhanced wake recovery as a result of augmented ambient turbulence intensity as was shown in Figure 5.6 so that the depth averaged velocity was approximately equal to the velocity through each porous fence. Under these conditions there is an even distribution in drag over all fences, limiting the uneven distribution in drag to the first fence only.

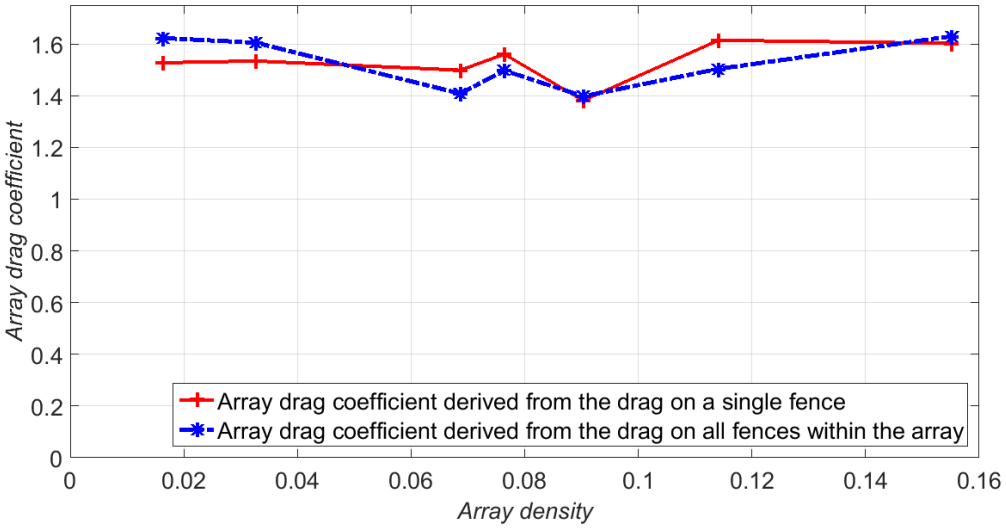

Figure 5.20 Comparison between the array drag derived from a single fence and the true array drag coefficient obtained from the drag on all fences within the array for Cases B1-7.

In depth averaged numerical models the area averaged array drag is applied uniformly over the array plot area. This drag is defined in the momentum equations (Equation 3.16) in terms of an equivalent array drag coefficient. Figure 5.21 shows a comparison between the area averaged array drag coefficient obtained from the drag on a single fence (which is typically used to parameterise array drag in regional scale hydrodynamic models), given by:

$$C_e = \frac{1}{2}\lambda C_f \tag{5.3}$$

where C_e=area averaged array drag, λ=array density and C_f=fence drag coefficient, and the true area averaged array drag coefficient, given by:

$$C_e = \frac{1}{2}\lambda C_a \tag{5.4}$$

Where C_a=array drag coefficient obtained from Equation 3.3. Results show the same trend as Figure 5.19 where for array density less than 0.07, agreement between the two methods is within 7%. Any further increase in array density resulted in an error exceeding 10%, where array drag was overestimated because the depth averaged velocity within the array does not account for the variation in velocity in the vertical plane caused by the upstream fence wake. In general results are encouraging given that realistically array density is not likely to exceed 0.07, which

corresponds to a lateral (tip-to-tip) and longitudinal spacing between turbines of just 1 and 5.5 diameters respectively.

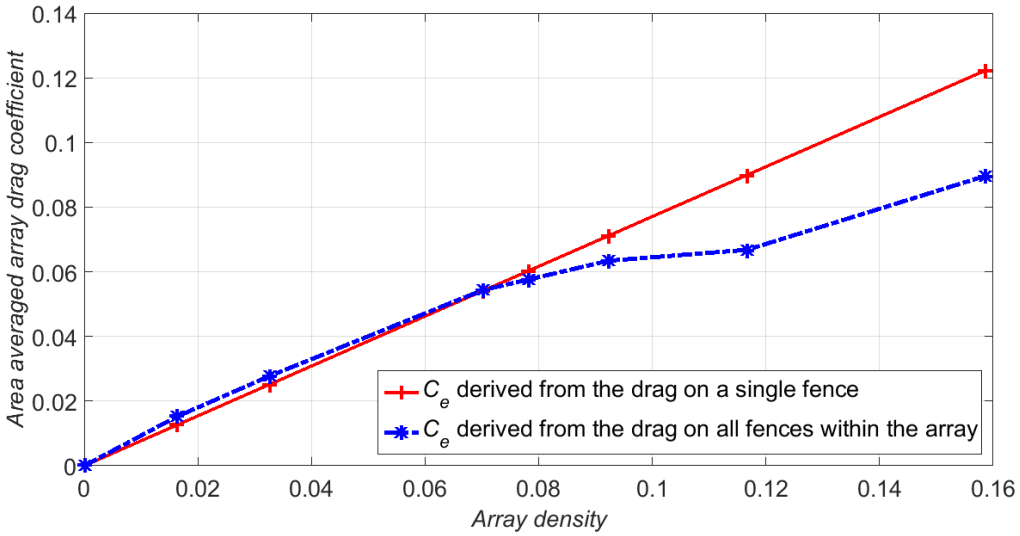

Figure 5.21 Comparison between the area averaged array drag coefficient derived from a single fence and the true array drag coefficient obtained from the drag on all fences within the array for Cases A1-7.

For array Cases B1-7 (Figure 5.22), agreement between results was within 5% over the entire array density range with the exception of array B4.

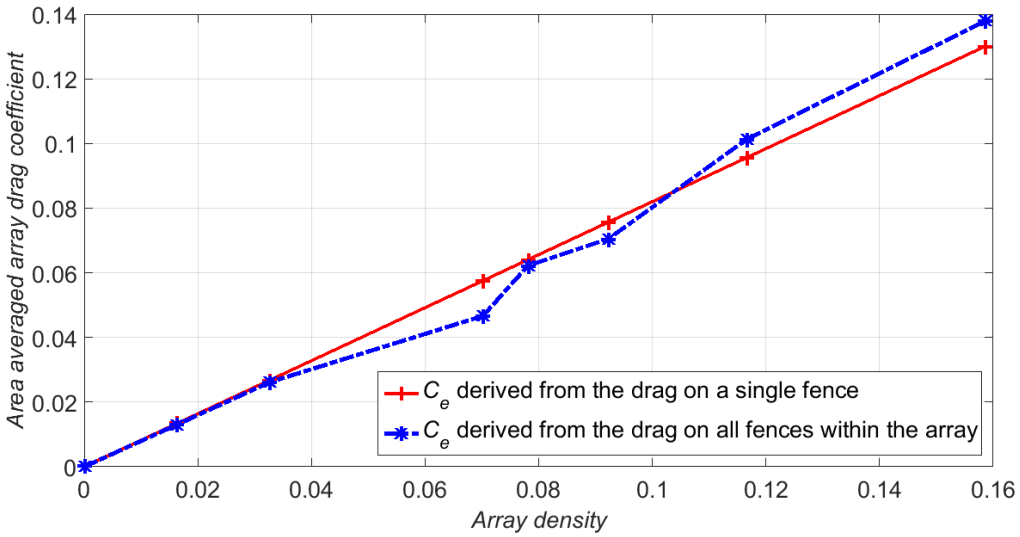

Figure 5.22 Comparison between the area averaged array drag coefficient derived from a single fence and the true array drag coefficient obtained from the drag on all fences within the array for Cases B1-7.

These results demonstrate the robustness of the simple array drag parameterisation described by Equation 3.3 to simulate array drag in the distributed drag method within the realistic limits of array density and inflow turbulence intensity.

5.5 Bed drag coefficient

Results from the force balance presented in Table 5.2 and Table 5.6 were used to estimate the change in bed drag opposing the flow as a result of the presence of arrays. Array Cases A1-7 were not used in this analysis as bed drag was very low, resulting in some cases where a force balance gave a negative solution for bed drag, as discussed in Chapter 5.2.4.

Figure 5.23 shows the relationship between array density and the ratio of the bed drag coefficient with the arrays in position to the ambient bed drag coefficient in the absence of arrays. Results show that the addition of porous fence arrays increases the bed drag coefficient significantly, where for array case B6 the new bed drag coefficient was 185% of the ambient bed drag coefficient.

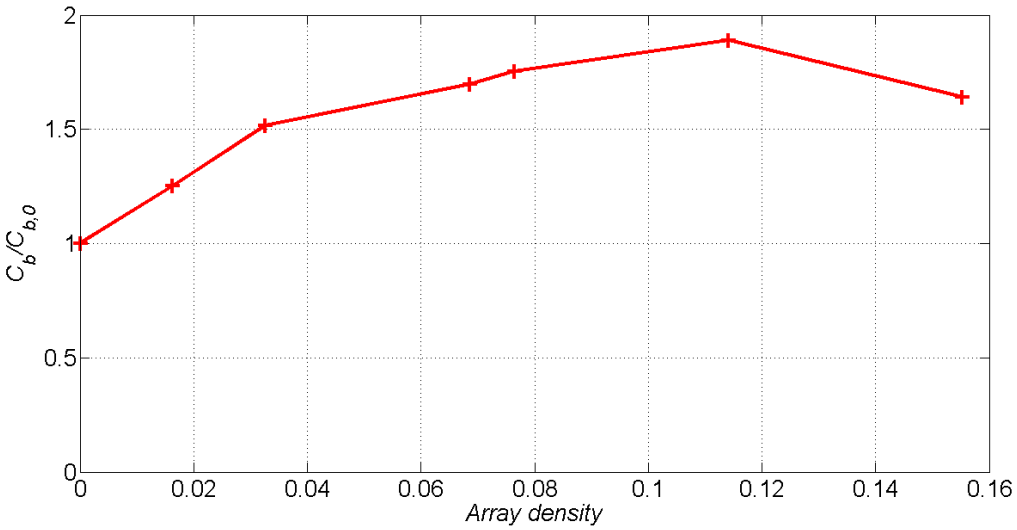

Figure 5.23 Relationship between array density and the ratio of the bed drag coefficient with the arrays in position to the ambient bed drag coefficient in the absence of arrays for Cases B1-7.

Figure 5.24 shows the increase in bed drag and area averaged array drag with increasing array density. As array density increases, there is an increase in the bed drag and area averaged array drag coefficients. The contribution of the added bed drag coefficient accounts for between 10-20% of the total added drag from the bed and the arrays over the array density range considered. As a consequence, neglecting the added bed drag contribution to the total added drag coefficient will lead to array drag being underestimated. This will lead to the array power also being

underestimated and will also lead to a misrepresentation of the change in surrounding flow dynamics and array wake that could have a knock on effect when quantifying the environmental impact of arrays at a specific site using regional scale depth-averaged hydrodynamic modelling.

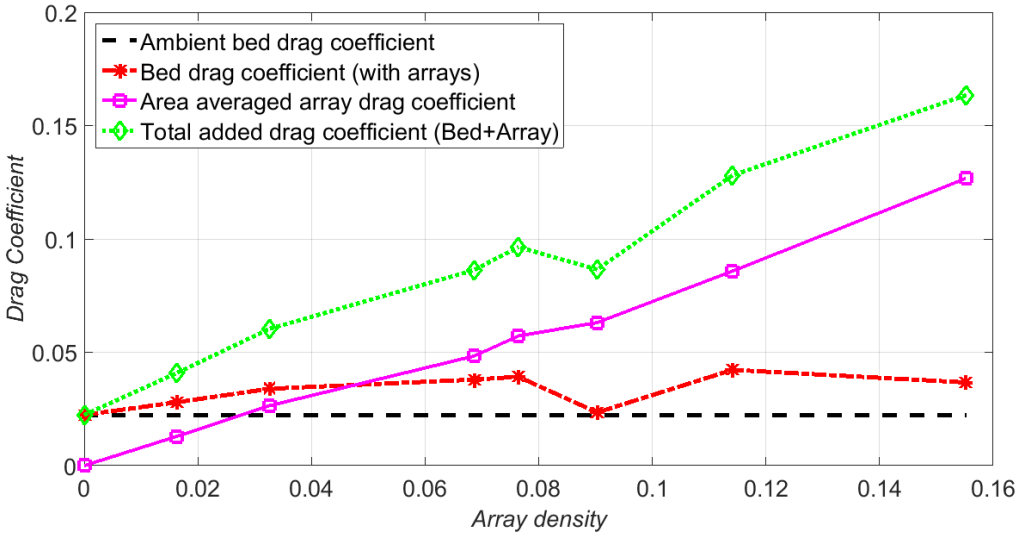

Figure 5.24 Relationship between array density and the bed drag coefficient, area averaged array drag coefficient and the total added bed drag coefficient from the bed and the arrays using Cases B1-7. The ambient bed drag coefficient from Case B is also shown for comparison.

The increase in bed drag coefficient with array density is attributed in part to an increase in bed shear in the bottom third of the water column directly below the bottom edge of each fence close to the bed. Figure 5.25 and Figure 5.26 shows the shear profile within Cases A7, A5 and A3 and Cases B7, B5 and B3 respectively. The profiles are an average of measurements between fences within the equilibrium region of the arrays. For both roughness cases as array density increased, the spatially averaged shear stress directly below the fence and close to the bed also increased. The shear in this region is commonly used to estimate bed drag (Biron et al. 2004).

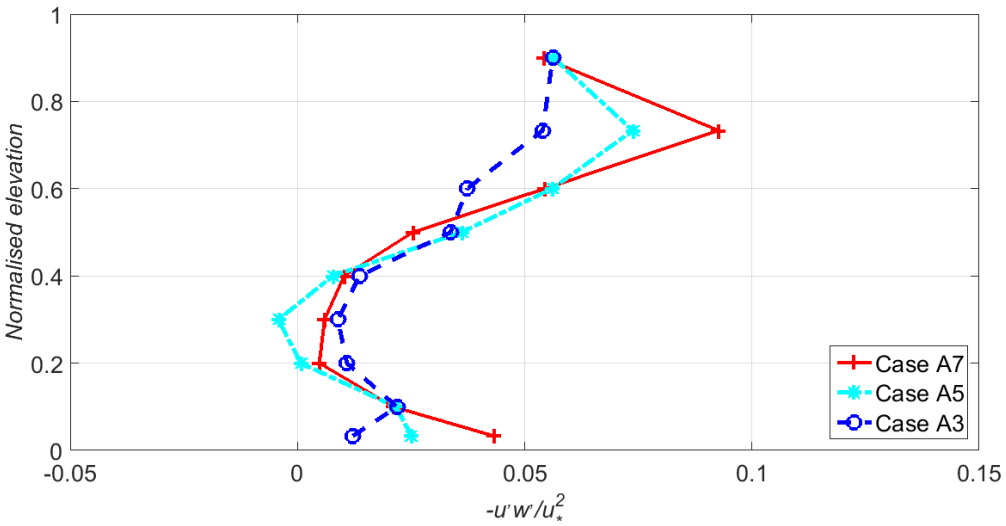

Figure 5.25 Shear stress distribution in the vertical plane downstream of equilibrium fences in Cases A7, A5 and A3. Results are normalised by ambient friction velocity squared.

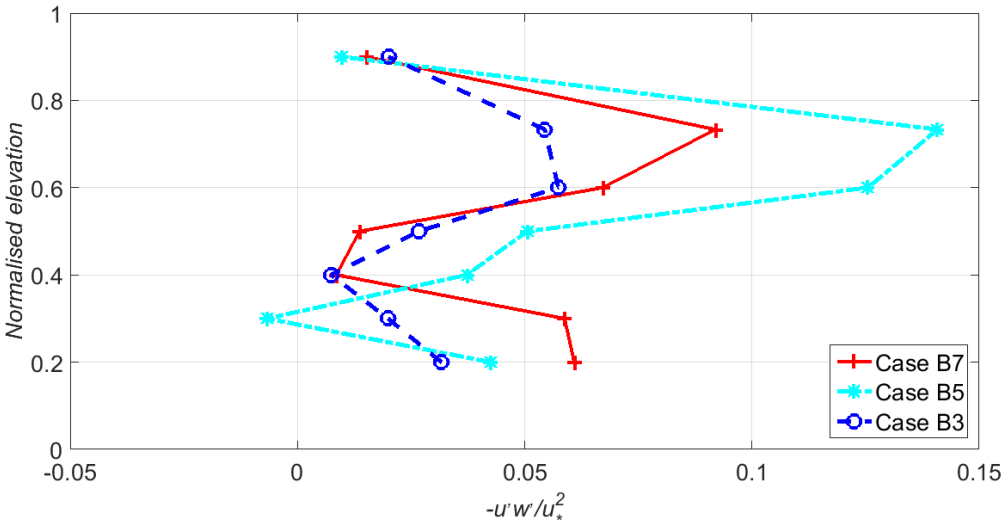

Figure 5.26 Shear stress distribution in the vertical plane downstream of equilibrium fences in Cases B7, B5 and B3. Results are normalised by ambient friction velocity squared.

The presence of the roughness strips reduced the open area under each fence, causing greater flow acceleration in this region compared to flows over array Cases A1-7. The interaction between this accelerated flow and the frontal area of each roughness strip increased the contribution of bed form drag opposing the flow (also called pressure drag) given by the difference in pressure between the front and back of each roughness element. Large Eddy Simulations (LES) of flow over k-type roughness show that pressure drag is significantly greater than the frictional drag component acting on roughness surface, where recirculation downstream of each roughness element causes the frictional drag to act in the flow direction (Cui et al. 2003). Form drag would

be less significant using Cases A1-7 as the frontal face of the roughness is significantly smaller, so protrudes less into the oncoming flow.

Figure 5.26 shows a region of high shear above the fence top edge height where the slow moving wake meets the fast moving bypass flow. At high array density the spatially averaged shear at this height is relatively high because there are many fences causing this interaction. As array density reduces fences are taken away, causing this interaction to occur less frequently resulting in a reduction in spatially averaged shear stress between the upper wake and bypass flow. Array Case B5 and B7 needs repeating as unexpectedly it does not follow this trend. This may be as a result of a higher upstream Reynolds number in Case B5 or error in the positioning of the Acoustic Doppler Velocimeter.

5.6 Conclusions

The validity of the distributed drag approach was dependent on the rate of wake recovery downstream of each fence relative to fence spacing and the ambient turbulence intensity. For the two inflow conditions used here, if wake recovery was sufficient relative to row spacing the depth averaged velocity was representative of the velocity through the fences. In general for array densities in the realistic range suitable for full scale deployment (i.e. less than 0.07), the distributed drag approach was shown to be robust in estimating array drag within 10% of experimental measurements. Accuracy improved for lower array densities and higher ambient turbulence intensity, two features that improve wake recovery.

For high density arrays (i.e. greater than 0.07) in low ambient turbulence intensity flows, wakes from upstream fences impeded strongly on downstream fences so that the depth averaged velocity over-estimated the velocity through the fences significantly. This led to array drag being overestimated by more than 10% when using the depth averaged array drag parameterisation.

High density arrays gave an uneven distribution in drag amongst the first three rows within the transition zone. However, the average force on transition fences was still within 10% of the average force on all fences within each array. This suggests that the error in total array drag incurred from the uneven distribution in drag in the transition region should not be significant.

For Cases B1-7, the addition of porous fence arrays to the flow increased the bed drag by up to 185%, which accounted for up to 20% of the total added drag. When implementing the distributed drag method, this added bed drag caused by the presence of arrays must be accounted for, otherwise the total added drag from the array and the bed will be underestimated. This will reduce the impact the array has on the flow dynamics in terms of flow reduction inside

the array and flow redirection around it, making it likely that extracted array power will be overestimated. For smoother beds such as in Cases A1-7 this error was far less significant because the bed drag is a smaller proportion of the total drag, which is dominated by the array drag.

Chapter 6: Hydrodynamic model validation and ambient flow characterisation around the Channel Islands

6.1 Introduction

In Chapter 2 it was concluded that regional scale studies quantifying the available and extractable tidal energy at sites around the Channel Islands have in general relied upon low temporal and spatial resolution data, bringing into doubt the validity of results (Energy Technology Support Unit 1993; Bahaj & Myers 2004; Myers & Bahaj 2005; Black and Veatch 2005; Turner & Owen 2007). To improve the state of the art, the methodology outlined in Chapter 4 was used to build a new 2D hydrodynamic model of the English Channel. This Chapter first presents results that validate the English Channel model to give confidence in its ability to accurately simulate tidal flows around the Channel Islands. Validated ambient results are then used to assess the suitability of Alderney Race, Casquets, Big Russel, North West Guernsey and North East Jersey for tidal energy development.

6.2 Model calibration

6.2.1 Tidal stream calibration

Table 6.1 and Table 6.2 summarise the tidal stream velocity results, giving a comparison between AWAC measurements and simulated results of M_2 and S_2 major and minor axis magnitudes, phases and inclinations respectively for a uniform bed roughness coefficient of 0.025. In selecting the most suitable bed roughness coefficient, emphasis was placed on M_2 amplitudes and phases since it is the dominant constituent. Full results for a range of bed drag coefficients are given in Appendix B, which show that phase, inclination and minor axis amplitudes were relatively insensitive to bed roughness coefficient. A bed drag coefficient of 0.025 was selected as most suitable, where all M_2 major axis amplitudes were within 10% of measured values and phases and inclination are within 10° with the exception of inclination at T61. M_2 and S_2 tidal stream ellipses are plotted in Figure 6.1 and Figure 6.2 to help visualise the results in Table 6.1 and Table 6.2.

Table 6.1 Comparison of major axis amplitudes, phases, inclinations and minor axis magnitudes of M_2 currents from Telemac model with AWAC measurements at T61, T74 and T75 deployments. Numbers in brackets show the level of agreement with AWAC data.

	Major axis	Phase	Inclination	Minor axis
T61				
AWAC	2.43	17	116	0.22
Model	2.19 (10%)	8 (9°)	128 (-12°)	0.22 (0%)
T74				
AWAC	1.45	327	139	0.13
Model	1.40 (4%)	326 (-1°)	149 (-10°)	0.17 (-29%)
T75				
AWAC	2.11	17	128	0.25
Model	2.22 (-5%)	14 (3°)	137 (-9°)	0.31 (-23%)

Table 6.2 Comparison of major axis amplitudes, phases, inclinations and minor axis magnitudes of M_2 currents from Telemac model with AWAC measurements at T61, T74 and T75 deployments. Numbers in brackets show the level of agreement with AWAC data.

	Major axis	Phase	Inclination	Minor axis
T61				
AWAC	0.59	45	117	0.03
Model	0.63 (7%)	49 (17°)	127 (-10°)	0.02 (-29%)
T74				
AWAC	0.37	31	142	0.07
Model	0.36 (2%)	40 (-13°)	144 (2°)	0.07 (0%)
T75				
AWAC	0.45	39	127	0.11
Model	0.68 (-53%)	52 (13°)	136 (-9°)	0.07 (34%)

In general results for the S_2 tide were less satisfactory but this can be afforded given that S_2 has a less dominant effect on the overall tide. In comparison with the 2D hydrodynamic model of the English Channel built by Haynes et al. (2015), results presented here show a significant improvement in the accuracy of S_2 major axis amplitudes, whilst the majority of phases and inclinations are within the same error bounds of ±10% or ±10°.

Figure 6.3 compares the depth averaged velocity time series obtained from the AWAC deployments with simulated results. Results from deployments T61 and T74 show good agreement with simulated results, whilst for deployment T74 the dominant ebb tide is under predicted using the 2D hydrodynamic model. This is likely to be a result of the fact that the T74 AWAC was positioned in the path of a large recirculating eddy shed off the North-Eastern tip of Alderney (Haynes 2015), highlighting the importance of analysing both tidal ellipses *and* depth averaged flow velocities directly.

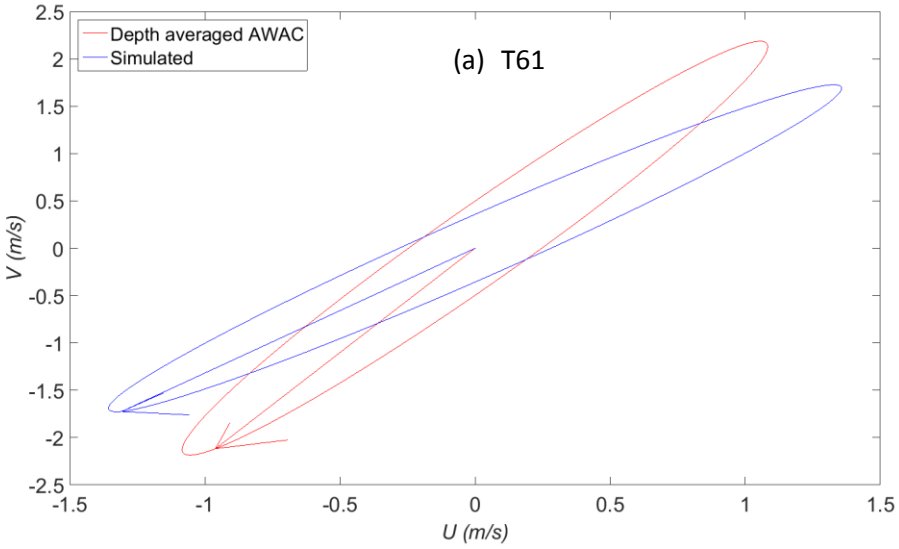

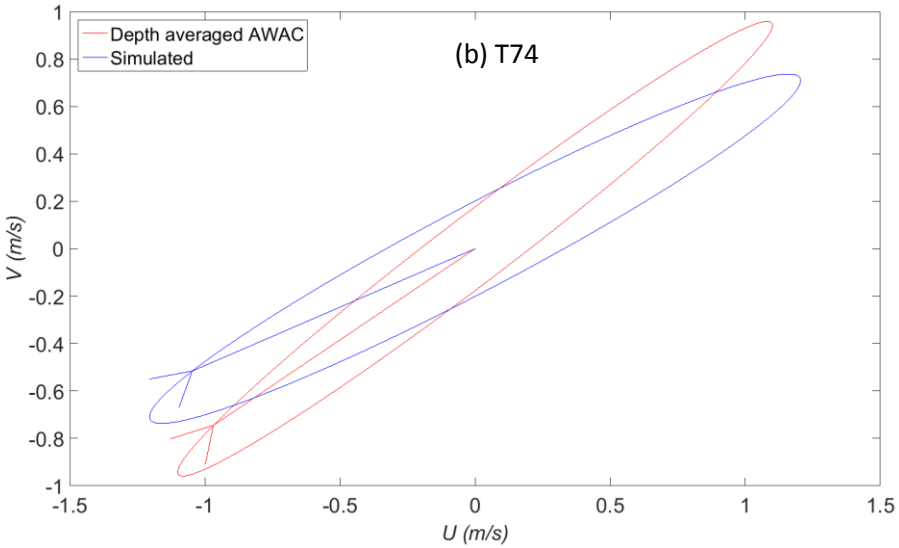

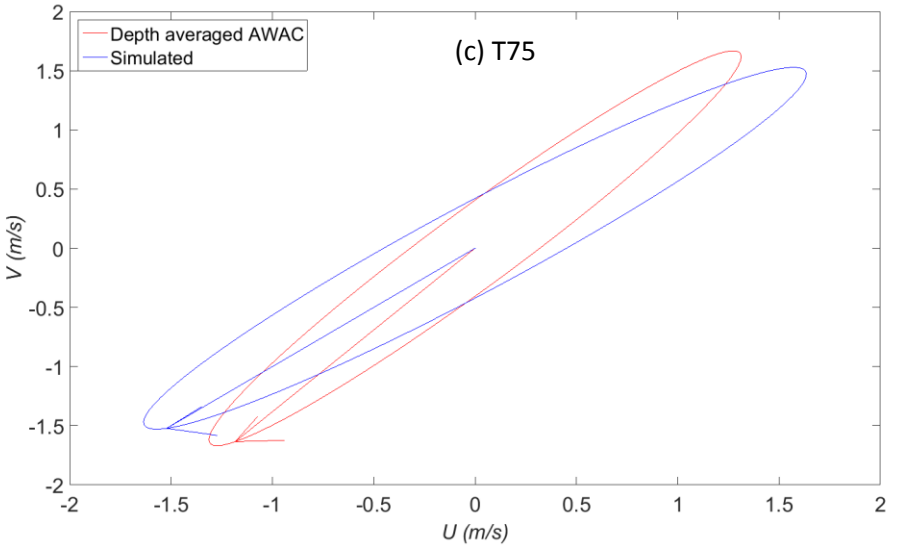

Figure 6.1 M_2 tidal stream ellipses for AWAC deployments in Alderney Race

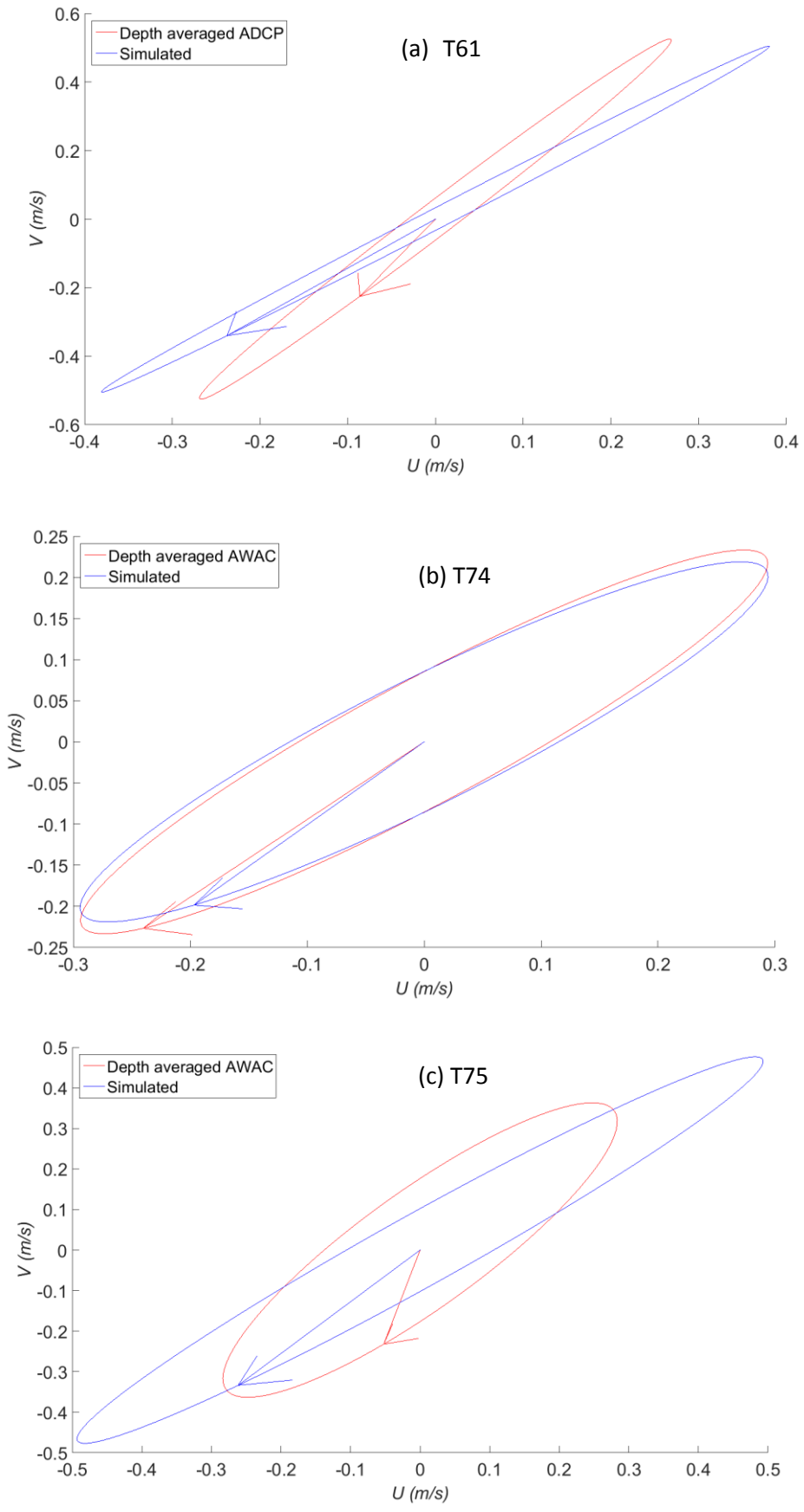

Figure 6.2 S_2 tidal stream ellipses for AWAC deployment in block (a) T61 (b) T74 and (c) T75.

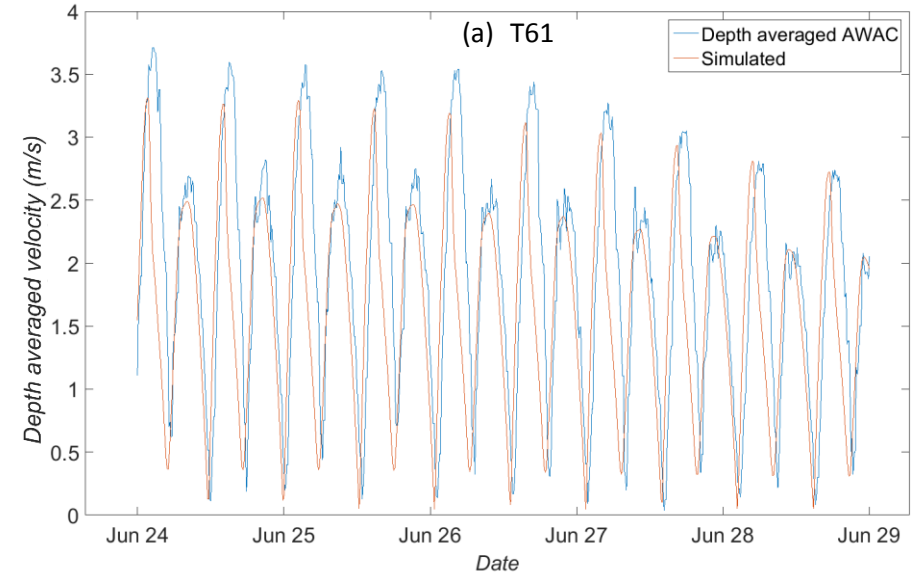

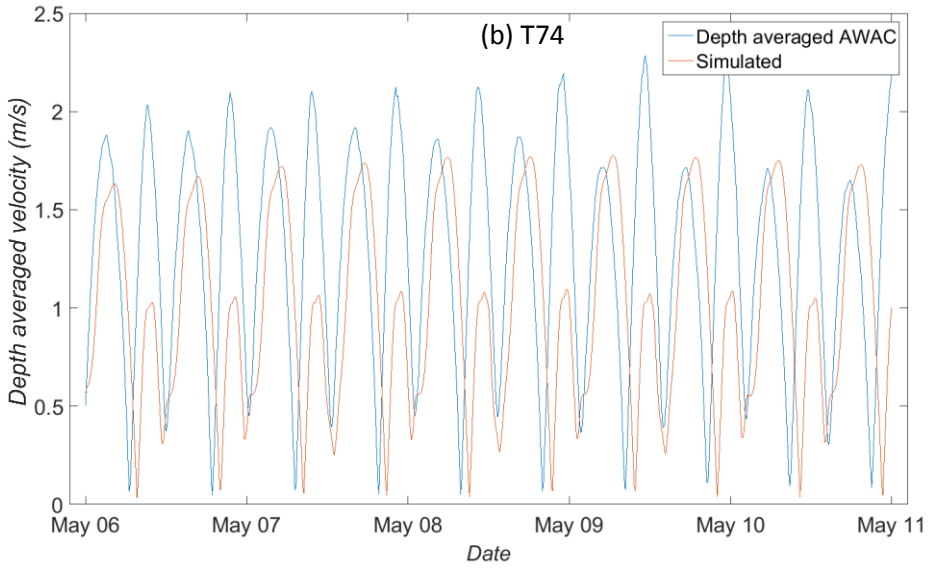

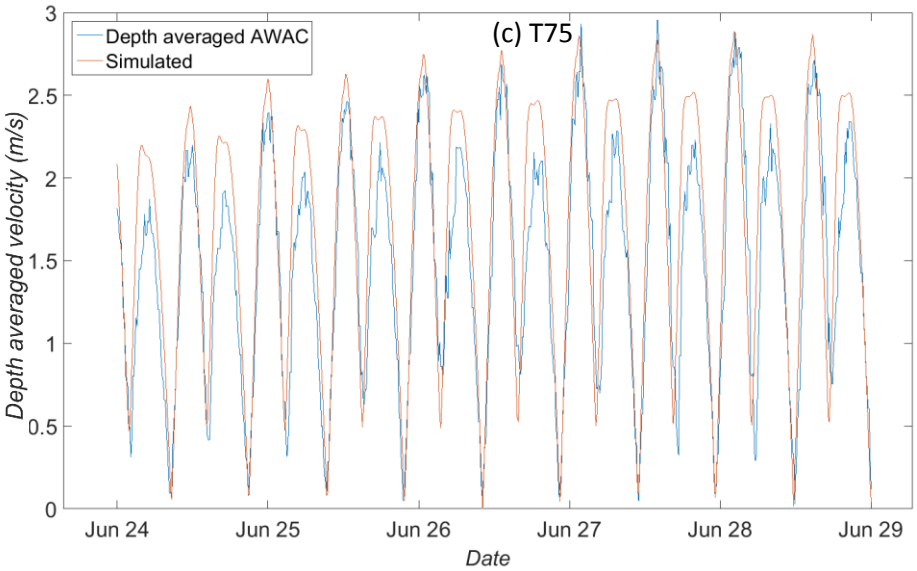

Figure 6.3 Comparison between tidal currents at (a) T61, (b) T74 and (c) T75

6.2.2 Free surface elevations

Table 6.3 compares M_2 and S_2 tidal elevation amplitudes and phases at thirteen ports around the English Channel Model domain. When calibrating the model, emphasis was placed on the ports in and closest proximity to the Channel Islands. Accurately simulating free surface elevations are important for estimating the maximum average power potential of a site, which is dependent on the free surface elevation across a site (i.e. the difference in free surface elevation at either ends of a channel/Race) as described by Equation 2.19. Results show that for a uniform bed drag coefficient of 0.025, eight out of thirteen ports are within 10% of measured amplitudes and 10 degrees of measured phases, including all six ports around the Channel Islands (Alderney, Jersey, Guernsey, Sark, Cherbourg and St. Malo).

Table 6.3 Differences in M_2 & S_2 amplitudes and phases at thirteen ports located throughout the English Channel domain using a bed drag coefficient of 0.025.

Port	Measured values				Model results			
	M_2		S_2		M_2		S_2	
	Amp (m)	Pha (°)	Amp (m)	Pha (°)	Amp (m)	Pha (°)	Amp (m)	Pha (°)
Alderney	1.81	200	0.74	227	1.69 *(7)*	195 *(5)*	0.68 *(8)*	236 *(9)*
Jersey	3.33	180	1.31	231	3.04 *(9)*	180 *(0)*	1.21 *(7)*	226 *(5)*
Guernsey	2.74	181	1.08	230	2.35 *(10)*	175 *(6)*	0.97 *(10)*	224 *(6)*
Sark	2.63	189	0.98	236	2.47 *(9)*	179 *(10)*	0.95 *(3)*	226 *(10)*
Cherbourg	1.87	228	0.62	272	1.83 *(2)*	232 *(-4)*	0.66 *(6)*	269 *(3)*
St. Malo	3.67	177	1.44	227	3.33 *(9)*	177 *(0)*	1.31 *(-5)*	226 *(-1)*
Newlyn	1.72	133	0.58	177	1.83 *(-6)*	124 *(9)*	0.63 *(-8)*	168 *(9)*
Weymouth	0.59	190	0.31	241	0.73*(-23)*	199 *(-9)*	0.35*(-14)*	241 *(0)*
Bournemouth	0.42	273	0.18	292	0.42*(-84)*	259 *(14)*	0.29(-*56)*	288 *(4)*
Newhaven	2.25	321	0.74	10	2.50*(-11)*	300 *(21)*	0.82*(-12)*	348 *(22)*
Dover	2.25	331	0.72	23	2.42 *(-8)*	312 *(19)*	0.79*(-10)*	1 *(22)*
Dunkirk	2.13	22	0.64	75	1.75 *(18)*	339 *(75)*	0.53 *(18)*	24 *(51)*
Le Havre	2.62	285	0.89	333	2.90*(-10)*	279 *(6)*	0.96 *(-7)*	326 *(7)*

The most erroneous region of tidal amplitude is along the South coast of England at Bournemouth and Weymouth. North of Bournemouth an M_2 amphidrome (point of zero M_2 amplitude) is located, alluding to the fact that in this region M_2 and S_2 amplitudes are relatively low. For this reason the error corresponds to a relatively small absolute error, as shown in Table 6.3.

Additionally upon inspection free surface time series were taken in shallower waters for Weymouth and Bournemouth in comparison with other ports, where amplitude is more sensitive to continuity and shallow water processes such as drag due to bottom friction, which Pugh (1996) states removes a larger proportion of the propagating tidal energy than in deeper waters. This suggests that finer tuning of bed friction is required in this region if better accuracy is required, but is not necessary here.

6.2.3 Summary of calibration results

Results presented here were relatively insensitive to small changes in bed roughness coefficient, making it challenging to establish the most suitable bed drag coefficient. For example doubling the bed drag coefifficient from 0.013 to 0.025 resulted in only a 4% change in tidal stream major axis amplitudes. It was concluded that 0.025 gave the overall best fit with calibration data, giving the following accuracies between the model and validation data:

AWAC tidal currents:

- All major axis amplitudes within 10% with the exception of T75 S_2.
- All phases within 10° with the exception of T61 and T74 S_2.
- All inclinations within 10° with the exception of T61 M_2.
- All minor axis amplitudes within 30% with the exception of T75 S_2.

Tidal elevations:

- 9 ports within 10% of validated amplitudes, including all six in and around the Channel Islands.
- 9 ports within 10% of validated phases, including all six in and around the Channel Islands.

The sensitivity of energy extraction to bed roughness coefficient could potentially be much higher than validation data analysed here and for this reason it is investigated further in Chapter 7.

6.2.4 Model validation

To validate the model, simulations were re-run using a start date of 9/11/2014. Constituent free surface elevation amplitudes and phases were then re-analysed. Results indicated that both M_2 and S_2 amplitudes and phases agreed within 4% of results presented in Table 6.3 for simulations using a start date of 1/5/2009.

Given the limited ADCP datasets available at the time, further tidal stream validation was not possible. However, confidence was gained from results presented in 6.2.1 that show good

agreement between ADCP data and model results for the T61 AWAC deployment that starting obtaining readings on 1/5/2009 and the T74 and T75 deployments that started obtaining readings on 17/6/2009.

6.3 Ambient flow characterisation

Figure 6.4 shows the average kinetic power distribution across the Channel Islands, indicating that flows within Alderney Race, Casquets and Big Russel exceed the average kinetic power density distribution of 2.5 kW/m^2 necessary for reasonable project economics(Black and Veatch 2011b) . However, this is not true of North West Guernsey and North East Jersey.

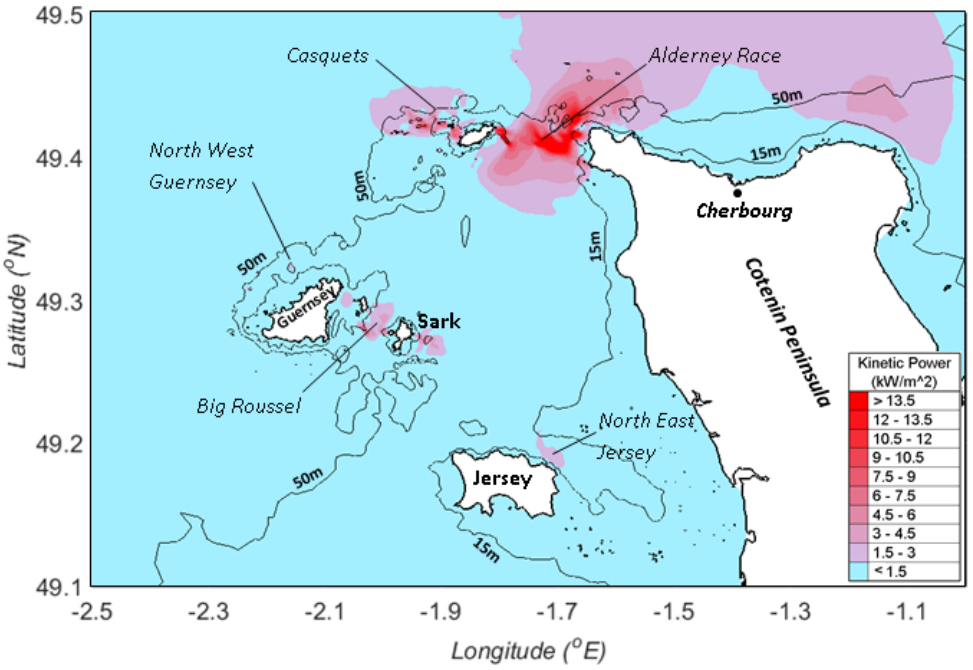

Figure 6.4 Average kinetic power distribution around the Channel Islands, with 50 m and 15 m depth contours shown in red and green respectively.

Table 6.4 summarises the suitable array plan area at each site in Figure 6.4 in comparison to the range of plot areas used in previous studies covered in Chapter 2. In general, the areas identified in Figure 6.4 are significantly smaller than previous studies as a result of higher resolution flow data and a stricter limit on acceptable mean velocities.

Table 6.4 Summary of area over which distribution of kinetic power density exceeds 2.5 kW/m^2 at each site compared with plot areas considered in previous studies.

Site	Plot area exceeding 2.5 kW/m^2 (km^2)	Plot area range in previous studies (km^2)
Alderney Race	93	68 – 102 (Energy Technology Support Unit 1993; Bahaj & Myers 2004; Myers & Bahaj 2005)
Casquets	7	190-215 (Energy Technology Support Unit 1993; European Commission 1996; Black and Veatch 2005)
Big Russel	14	90 (Energy Technology Support Unit 1993)
North West Guernsey	0	221-366 (Energy Technology Support Unit 1993; European Commission 1996; Black and Veatch 2005)
North East Jersey	0	20-58 (Energy Technology Support Unit 1993; European Commission 1996)

6.3.1 Alderney Race

The highest average kinetic power density is seen in Alderney Race, where in the shallower faster waters of the East Race kinetic power density exceeds 13.5kW/m^2. Depths across the majority of Alderney Race exceed 15 m and never go above 50m, making it geometrically suitable to house 1st and 2nd generation devices. There is significant spatial variation in velocities across the Race caused by bathymetric features. For example in the East Race off the North East tip of Alderney, a region of high flow velocity stretches out into Alderney Race. In this region highest mean velocities exceeding 2 m/s are located around Race Rocks, two tower like rock formations in close proximity to one another that accelerate flow through and around them, creating strong jet flows during ebb tide. In the West Race a large region of high velocity flow exceeding 2 m/s is located 2 km off the French coast, where depth decreases with distance from the French coast to around 15 m.

Maximum velocities occur during the stronger ebb tide when flow curves South from above the Contenin Peninsular north of Cherbourg in the English Channel down through Alderney Race towards the Atlantic Ocean.In the East and West Race. Results from the model show that in the East Race flow velocities exceed 4 m/s approximately 25% of the time, reaching magnitudes of up to 5.4 m/s.

6.3.2 Casquets & Big Russel

Both Casquets and Big Russel also exhibit mean power densities greater than 2.5kW/m^2, however the plot area for which this is true is significantly smaller compared to Alderney Race, which contradicts the study areas identified in previous literature significantly. Mean kinetic power density at Casquets and Big Russel was approximately 7kW/m^2 and 5kW/m^2 respectively. There are two small regions either side of Big Russel (between Herm and Guernsey and the opposite side of Sark that also exhibit high kinetic power density, however they occur in shallow waters so are also discarded from this study.

Chapter 7: Results and discussion: Energy extraction at Alderney Race, Casquets and Big Russel

This chapter presents results that expand upon a journal paper published in the Energy journal by Coles et al. (2017).

7.1 Overview

Previous resource assessments of sites in the Channel Islands covered in Chapter 2 were based on low temporal and spatial resolution flow data, often relying on a time series from a single/only a few point(s) to characterise the flow and bathymetry over an entire site (Energy Technology Support Unit 1993; Bahaj & Myers 2004; Myers & Bahaj 2005; Black and Veatch 2005; Turner & Owen 2007). To better characterise the temporal and spatial flow variation, the English Channel hydrodynamic model was used. Results are presented here that estimate available array power from multiple energy extraction scenarios outlined in Chapter 4, including tidal fences spanning the width of each site and sub-arrays in Alderney Race based on the work by Bahaj et al. (2004). Estimates for available power are compared with published data for the output of the London Array, the world's largest offshore windfarm.

7.2 Tidal fences

Using the methodology outlined in Chapter 4, flow was simulated through arrays of turbines spanning the entire width Alderney Race, Casquets and Big Russel using a uniformly distributed area averaged array drag coefficient. The energy extraction cases (Case F1-F7) are outlined in Table 4.2. Commonly these arrays are described as 'tidal fences'. Based on the validation results in Chapter 6, a seabed drag coefficient of 0.025 was implemented.

7.2.1 Alderney Race (Case F1)

Figure 7.1 shows the relationship between the average extracted power over an M_2 tidal cycle at Alderney Race and the area averaged array drag coefficient. Using M_2 forcing only, the maximum average extracted power at Alderney Race was 5.1 GW with an area averaged array drag coefficient of 0.05, causing a reduction in volume flux through the Race of 42%. As the area averaged array drag coefficient is increased (i.e. to simulate the impact of more turbines), the head loss across the fence increases as volume flux through the Race decreases. Since power is the product of head loss and volume flux, a maximum average extracted power is reached at the

point where the decrease in volume flux has a dominating effect over the increase in head drop (Sutherland et al. 2007). This is a significant increase of 300% on the upper bound estimated by Black and Veatch (2011b), which is somewhat unsurprising given claims that discrepancies between flow data sources contain up to +30%/-45% uncertainty.

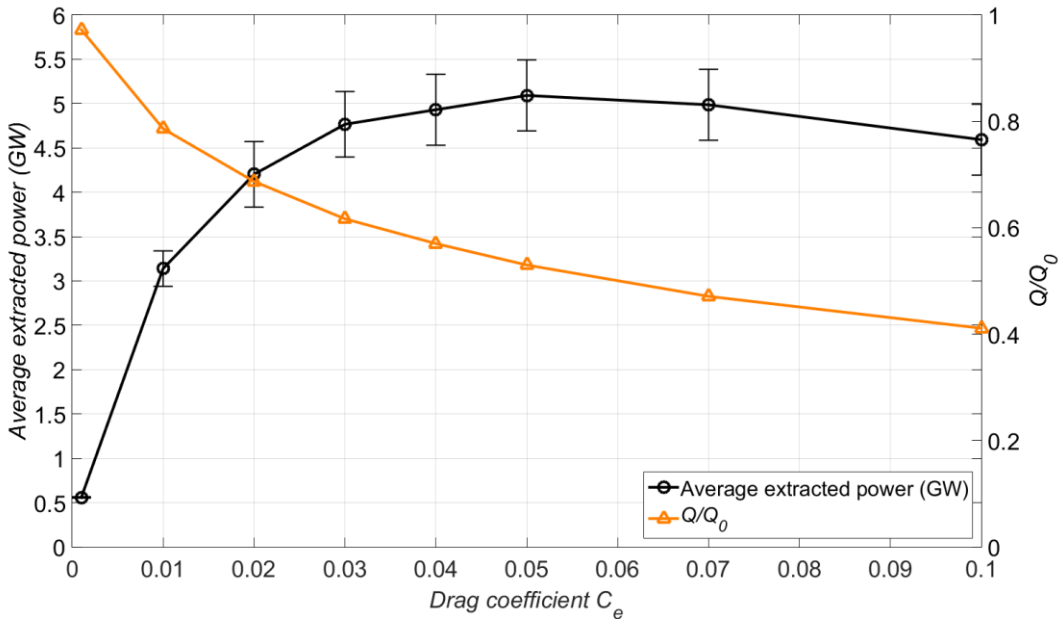

Figure 7.1 Relationship between the area averaged array drag coefficient and the average extracted power from Alderney Race over an M_2 tidal cycle. The change in volume flux through Alderney Race is also plotted. Error bars show the average extracted power within the realistic limits of bed drag coefficient of 0.013-0.052.

Given the uncertainty in seabed drag coefficient, simulations were re-run for seabed roughness coefficients within physically realistic bounds of 0.013-0.052. Error bars in Figure 7.1 show the range in average extracted power results obtained for this range of bed drag coefficients, which for the peak average extracted power is approximately 15%. In general as bed friction coefficient increases, estimates for extracted power decrease as more energy is extracted by the seabed.

To help give confidence to the result, the English Channel model was run for an ambient case without energy extraction to estimate the power potential analytically using Equation 2.19 from theory developed by Garrett et al. (2005). This yielded a maximum average power of 4 GW, using a peak flow in the undisturbed state of 1.08 x10^6 m^3/s, a tidal forcing constant of 0.22 and a head difference of 1.04 m from points taken 25 km from the narrowest constriction of the Race, where the difference in free surface in comparison with the undisturbed state is less than 5% and based on a phase lag of flow rate behind the dynamic head of 48°. The analytical solution agrees within 20% of the estimate from the numerical model. The analytical model does not incorporate important flow features such as exit losses and coriolis. Error in this estimate also arises from the

dynamic head difference across the fence, which in this case does not remain unaffected by energy extraction as assumed in Equation 2.19 (the head difference increased when a tidal fence array density was increased). Additionally the analytical model was developed for a uniform channel so does not incorporate uneven coastlines and bathymetric features that cause variations in ambient velocity across the Race.

Adding the S_2 constituent gives a maximum average potential of approximately 4.4 GW, obtained using the ratio of the amplitude of the dynamic head to the dynamic head of the M_2 constituent as described in 2.7.1.3.

7.2.2 Casquets (Case F2)

The same procedure was carried out for Casquets as Alderney Race. Figure 7.2 shows estimated maximum average power potential was 0.47 GW, approximately 10% of Alderney Race. This was obtained with an area averaged array drag coefficient of 0.025. At this upper bound the reduction in volume flux was 42%, the same fraction reduction as for Alderney Race and in line with analytical results (Sutherland et al. 2007).

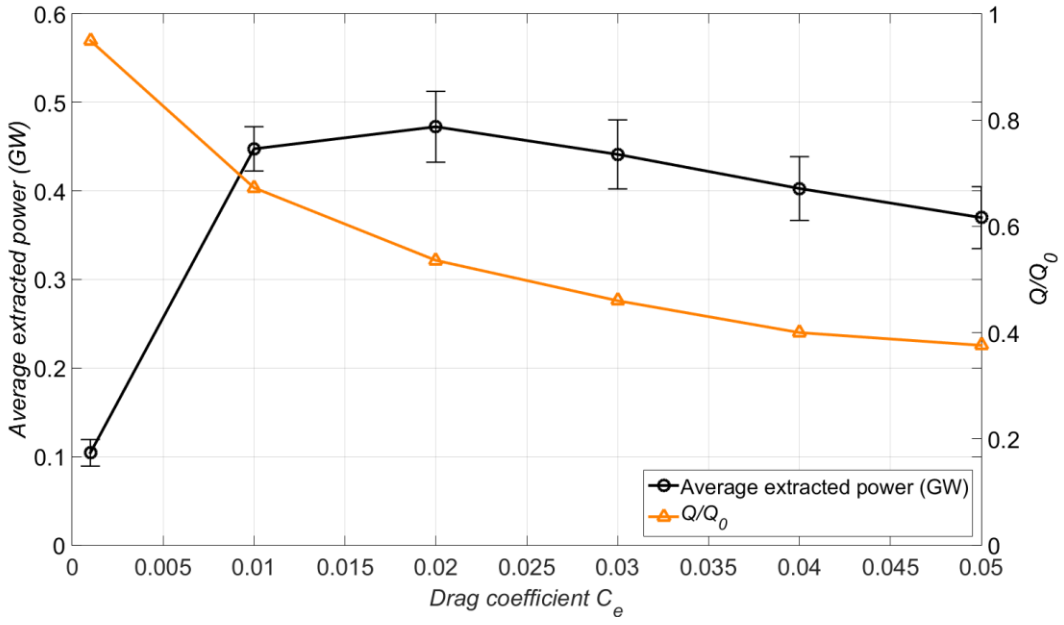

Figure 7.2 Relationship between the area averaged array drag coefficient and the average extracted power from Casquets over an M_2 tidal cycle. The change in volume flux through Alderney Race is also plotted. Error bars show the average extracted power within the realistic limits of bed drag coefficient of 0.013-0.052.

This result is in vast contrast to work by Black and Veatch (2011b), which estimates the maximum average power potential equal to 1.73 GW, close to that of Alderney Race. Since the approach taken used a generic domain to estimate the power potential of many tidal streaming sites it is

likely this caused significant error in results. Furthermore in this previous study a significantly larger plot area was considered, which was determined based on low resolution flow data.

Results presented in Figure 7.2 were obtained from a validated model of the specific site, which is more likely to give a more accurate estimate of the power curve of a tidal fence at Casquets.

The variation in results with seabed roughness coefficient were approximately within the same error bounds as for Alderney Race, where for the maximum average power potential results showed a 13% variation for bed drag coefficient of 0.013-0.052.

7.2.3 Big Russel (Case F3)

Figure 7.3 shows the estimated maximum average power potential of Big Russel was 0.23 GW, approximately 5% of Alderney Race and 50% of Casquets. This was achieved with an area averaged drag coefficient of 0.09, which gave a reduction in volume flux through the channel of 43%. At this upper bound the sensitivity to sea bed friction drag was also 15%.

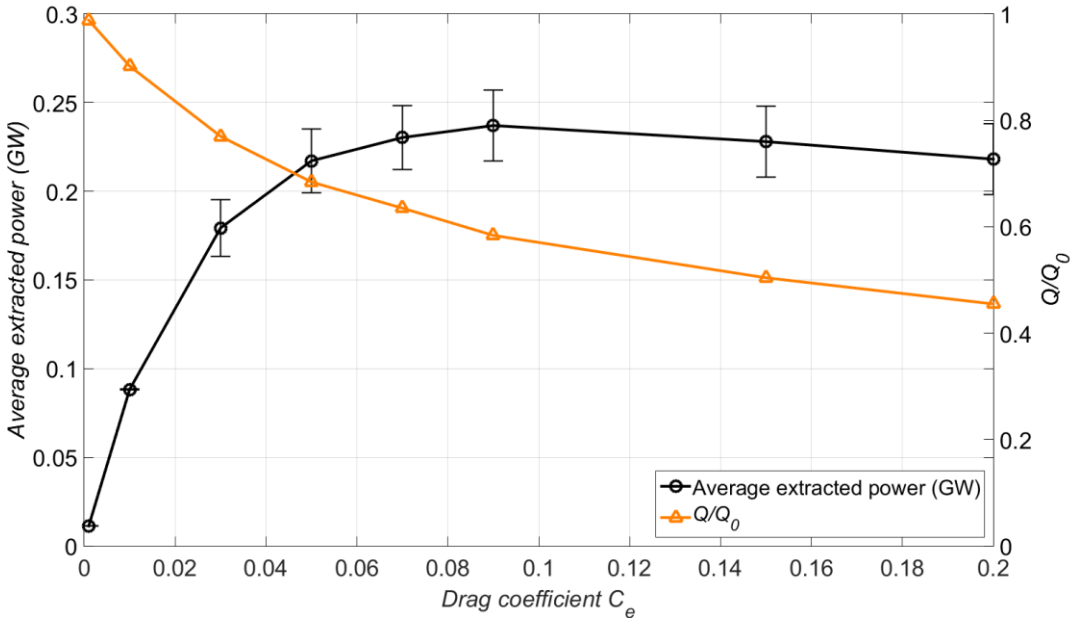

Figure 7.3 Relationship between the area averaged array drag coefficient and the average extracted power from Big Roussel over an M_2 tidal cycle. The change in volume flux through Alderney Race is also plotted. Error bars show the average extracted power within the realistic limits of bed drag coefficient of 0.013-0.052.

In line with resource assessment work carried out for Minas Passage (Walters et al. 2013), for each of the three sites it was found that by varying the fetch of the energy extraction strip (i.e. the longitudinal distance between the site inlet and outlet parallel to the direction of flow where drag was applied), the product of the fetch and the area averaged array drag coefficient required to

achieve the maximum average power potential remained approximately constant (within 5%). Physically this means that if the fetch of the energy extraction strip is increased, the equivalent array drag coefficient must decrease to obtain the maximum average power potential.

7.2.4 Summary of results

For comparison, Table 7.1 summarises the estimated maximum average power potential for the three sites studied here along with four other well-known sites found in literature. Alderney Race has the greatest potential in the Channel Islands which is significant given that it is approximately 136% of the maximum average power potential estimate for the Pentland Firth in Scotland (Draper et al. 2014). Casquets and Big Russel have significantly lower maximum average power potentials, which is unsurprising given that these two sites are considerably smaller and in general have lower distributed power density.

To incorporate more constituent forcings, simulations were run using M_2,S_2,N_2,K_2,K_1,O_1,P_1,Q_1 and M_4 forcings. Results for maximum average power potential are presented in Table 7.2. In general this increases the maximum average power potential at each site by a factor of approximately 1.15. This agrees well with the analytical approach developed in (Garrett & Cummins 2005), which suggests a factor of 1.14. Simulations were run using a seabed roughness coefficient of 0.025.

Table 7.1 Estimated maximum average power potential for an M_2 tidal cycle at different high potential sites for tidal energy development, including the results estimated here for Alderney Race, Casquets and Big Roussel within the realistic bounds of seabed drag coefficient, ranging between 0.013-0.052.

Site	Estimated maximum average power potential (GW)	Boundary forcing
Minas Passage, Canada	5.7 (Walters et al. 2013)	M_2,S_2,N_2,K_2,K_1,O_1,P_1,Q_1
Alderney Race	*4.7-5.5*	M_2 only
Pentland Firth, Scotland	3.75 (Draper et al. 2014)	M_2 only
Johnstone Strait, Canada	1.3 (Sutherland et al. 2007)	M_2 only
Casquets	*0.43-0.51*	M_2 only
Big Russel	*0.22-0.26*	M_2 only
Masset Sound, Canada	0.08 (Blanchfield et al. 2008)	M_2 only

Table 7.2 Estimated maximum average power potential using M_2,S_2,N_2,K_2,K_1,O_1,P_1,Q_1 and M_4 forcings at different high potential sites for tidal energy development, including the results estimated here for Alderney Race, Casquets and Big Roussel.

Site	Estimated maximum average power potential (GW)	Boundary forcing
Alderney Race	*6.1*	M_2,S_2,N_2,K_2,K_1,O_1,P_1,Q_1,$M4$
Minas Passage, Canada	5.7 (Walters et al. 2013)	M_2,S_2,N_2,K_2,K_1,O_1,P_1,Q_1
Pentland Firth, Scotland	3.75 (Draper et al. 2014)	M_2 only
Johnstone Strait, Canada	1.3 (Sutherland et al. 2007)	M_2 only
Casquets	*0.55*	M_2,S_2,N_2,K_2,K_1,O_1,P_1,Q_1,M_4
Big Russel	*0.27*	M_2, S_2,N_2,K_2,K_1,O_1,P_1,Q_1,M_4
Masset Sound, Canada	0.08 (Blanchfield et al. 2008)	M_2 only

7.2.5 Site interaction (Cases F4-F7)

The three sites considered here are in relatively close proximity, especially Alderney Race and Casquets which are separated by only the 4 km wide island of Alderney, whilst Big Russel is approximately 30 km from Alderney Race and Casquets. Therefore energy extraction at each site is likely to affect the surrounding flow dynamics, hence altering the total power potential of the three sites. This was quantified by simulating simultaneous energy extraction scenarios. Initially the upper bound drag coefficient for each of the individual sites was used and simulations were run for all seven combinations, as presented in Table 7.3.

Table 7.3 Maximum average extracted power for all seven combinations using Alderney Race, Casquets and Big Russel with a bed drag coefficient of 0.025.

Case	Site	Alderney Race	Casquets	Big Russel	Total (GW)
F1	Alderney Race	5.10	-	-	5.10
F2	Casquets	-	0.47	-	0.47
F3	Big Russel	-	-	0.24	0.24
F4	Alderney Race +Casquets	5.28	0.84	-	6.12
F5	Alderney Race +Big Russel	5.03	-	0.21	5.24
F6	Casquets+Big Russel	-	0.56	0.23	0.79
F7	Alderney Race+Casquets+Big Russel	5.24	1.02	0.20	6.46

Figure 7.4 shows the change in mean velocity as a result of energy extraction using Cases F2 and F4. Interaction between Alderney Race and Casquets (Case F4) gives a 79% increase in the estimated maximum average extracted power at Casquets and a 10% increase in the overall total power extracted in comparison to Case F 1 and F 2 simulated separately. Energy extraction at Alderney Race (Case F1) caused flow diversion around Alderney through Casquets instead of through Alderney Race, giving a 25 % increase in volume flux through Casquets and an increase in average head drop across Casquets of approximately 0.03 m in comparison with energy extraction at Casquets only (Case F2). For Case F4, this phenomenon works to increase the extracted power at Alderney Race also, but only by 4% since the flow diversion caused by energy extraction at Casquets into Alderney Race has a much less dominating effect, giving only a 1% increase in volume flux through Alderney Race. This flow diversion also effects energy extraction at Big Russel, reducing extracted power by 13% at this site for Case F5 in comparison with Case F3. This is attributed to the fact that on the ebb tide, energy extraction at Alderney Race and Casquets which are both upstream of Big Russel cause flow diversion around the Channel Islands, which gives a 2.5% reduction in volume flux through Big Russel in comparison with the ambient case with no energy extraction.

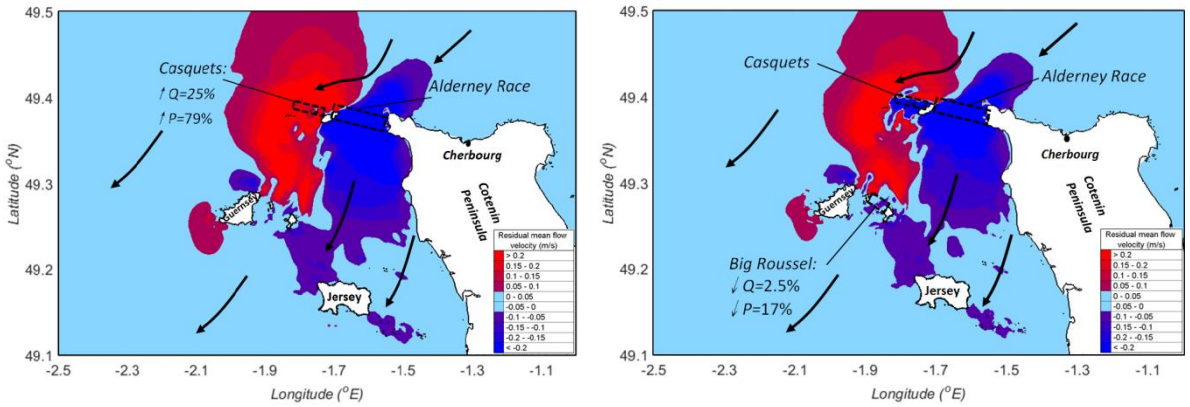

Figure 7.4 Mean velocity distribution difference plot between (a) the case of upper bound energy extraction at Casquets (Case F2) and energy extraction at Alderney Race and Casquets (Case F4), (b) the case of upper bound energy extraction at Big Russel only (Case F3) and energy extraction at Alderney Race, Casquets and Big Russel (Case F7). Arrows show the direction of the dominant ebb tide and flow diversion around Alderney Race into Casquets.

Maximum power was extracted using all three sites (Case 7), giving a total extracted power of 6.46 GW. The results summarised in Table 7.3 highlight the sensitive nature of simultaneous energy extraction at Alderney Race, Casquets and Big Russel, emphasising the likelihood that sites in the Channel Islands must to be developed in tandem to quantify and optimise overall extracted

power. However this phenomenon may reduce as drag at each site is lowered from the upper bound limit. This is now investigated in 7.2.6.

7.2.6 Realistic array drag

7.2.6.1 Extracted power

To achieve the maximum average power potential at Alderney Race and Big Roussel, very high turbine densities are required. For these two sites the flow is constricted due to the positioning of coastlines so that an increase in distributed drag results in an increase in head drop across the zone, resulting in an increase in extracted power. Such high packing densities are unlikely to ever be realised as turbines will be in the near wake of upstream devices, severely diminishing efficiency. The area averaged array drag coefficient from tidal turbines can be estimated by (Walters et al. 2013):

$$C_e = \frac{1}{2}\left(\frac{A_s}{A_p}\right)C_d \qquad 7.1$$

Where C_e=area averaged array drag coefficient, A_s=swept area of the turbine, A_p=array plot area and C_d=turbine drag coefficient. Assuming a drag coefficient of 0.8 (A. S. Bahaj et al. 2007), Table 7.4 gives an approximate longitudinal spacing for the area averaged drag coefficient used to obtain the maximum average power potential at each site using Equation 7.1 and assuming a lateral spacing (tip to tip) between turbines of 2 diameters.

Table 7.4 Estimated equivalent longitudinal and lateral spacing between devices to achieve the maximum average power potential at each individual site

Site	Area averaged array drag coefficient	Eq. lateral spacing (turbine diameters)	Eq. longitudinal spacing (turbine diameters)
Alderney Race	0.05	2	2
Casquets	0.025	2	5
Big Russel	0.1	2	1

Array spacings in Table 7.4 show that to extract maximum power, Casquets requires the least densely packed array. This is because Casquets is open to the English Channel so is the least constricted site, allowing flow to divert around the energy extraction strip more easily with an increase in distributed drag so that the maximum average power potential is achieved with a

relatively small increase in area averaged array drag. For sites where the flow is more constricted due to the positioning of coastlines such as Alderney Race and Big Russel, an increase in distributed drag results in an increase in head drop across the array instead of flow diversion, resulting in an increase extracted power.

Results highlight that to achieve the maximum average power potential at each site an unrealistically high turbine density is required, where turbines will be in the near wake of upstream devices, severely diminishing efficiency (Myers & Bahaj 2010). Simulations were re-run using a value of added drag based on the assumption that turbines have 1 diameter lateral spacing (tip to tip), and 10 diameter longitudinal spacing based on guidelines published by the European Marine Energy Centre (Legrand 2009), giving an area averaged array drag coefficient of 0.016 and array density of 0.04, applied over the same energy extraction area where mean ambient kinetic power exceeds 2.5 kW/m^2. Results are presented in Table 7.5, showing the reduction in estimated maximum average power potential in comparison with the optimum case in parenthesis.

Table 7.5 Average extracted power for all seven combinations using Alderney Race, Casquets and Big Russel with an area averaged array drag coefficient of 0.016. Percentages given in column 5 show the reduction in power potential compared to the optimum cases given in Table 7.3.

Case	Site(s)	Alderney Race	Casquets	Big Russel	Average Extracted Power (GW)	Q/Q_0
F1	Alderney Race	3.86	-	-	3.86 (-24%)	0.73
F2	Casquets	-	0.47	-	0.47 (0%)	0.56
F3	Big Russel	-	-	0.12	0.12(-50%)	0.89
F4	Alderney Race & Casquets	4.05	0.79	-	4.84 (-21%)	0.69 & 0.61
F5	Alderney Race & Big Russel	3.87	-	0.12	3.99 (-23%)	0.75 & 0.90
F6	Casquets & Big Russel	-	0.57	0.12	0.69(-13%)	1.05 & 0.90
F7	Alderney Race & Casquets & Big Russel	4.01	0.78	0.11	4.90 (-24%)	0.71 & 0.60 & 0.85

The reduction in extracted power relative to the maximum case is dependent on each site's sensitivity to the area averaged array drag coefficient. This is illustrated in Figure 7.5.

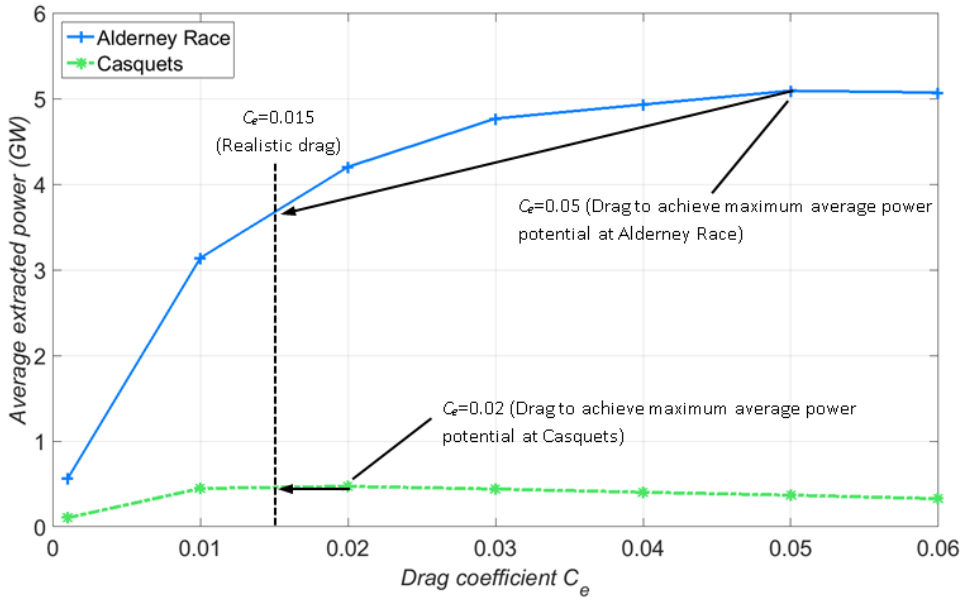

Figure 7.5 Average extracted power from Alderney Race and Casquets over an M_2 tidal cycle as a result of increased area averaged array drag coefficient. Graph illustrates the reduction in mean extracted power when comparing the upper bound cases against a realistic level of drag.

At Alderney Race the maximum average power potential was obtained with a relatively high area averaged array drag coefficient of 0.05 because of the more constricted nature of the site and higher ambient velocities. When area averaged array drag coefficient was reduced to the more realistic there was a 24% reduction in average extracted power.

At Casquets, the maximum average power potential was achieved with a relatively low added drag of 0.02 because flow easily diverted into the English Channel as drag was added. This upper bound drag coefficient used for estimating the maximum average power potential is close to the realistic value. As a result there is no significant change in extracted power between the maximum and realistic cases at Casquets. This is demonstrated in Figure 7.5, which shows the change in average extracted power at Casquets and Alderney Race for the maximum and realistic cases.

The greatest drop in average extracted power was 50% at Big Roussel (Case 3), where the difference between maximum and the realistic average extracted power level applied here is greatest.

Interaction between sites for simultaneous energy extraction show the same trends as was seen in Table 7.3 for the upper bound cases, where the greatest extracted energy occurs using all three sites (Case 7). Constructive interference between Alderney Race and Casquets caused a 12% increase in the total extracted power compared with energy extraction from the individual sites simulated separately. Power extracted at Big Russel remained at 0.12 GW for all energy extraction scenarios with the exception of Case 7, which gave an 8% reduction in extracted power at Big Russel. Maximum extracted power still occurred with energy extraction at all three sites, as was the case for the upper bound simulations case in 7.2.5.

7.2.6.2 Available power

Results for available power are presented in Table 7.6. These results quantify the electrical power that could be generated by positioning turbines within the energy extraction zones located in Alderney Race, Casquets and Big Roussel with the same realistic array drag used in Chapter 7.2.6.1. As would be expected, the available power is significantly lower than the extracted power to account for the coefficient of power. This analysis shows that if the entire width of each site is developed the average available power at all three sites from the M_2 tide is 1.83 GW, with 82% from Alderney Race, 16% from Casquets and 2% from Big Roussel. Column 7 shows the realistic extracted power obtained previously in Chapter 7.2.6.1 for comparison.

Table 7.6 Realistic average available power for Cases 1-7 using Alderney Race, Casquets and Big Roussel with an area averaged array drag coefficient of 0.015. Realistic average extracted power results are shown for comparison.

Case	Site/Site combination	Realistic average available power (GW)				Realistic average extracted power (GW)
		Alderney Race	Casquets	Big Roussel	Total for site(s)	
F1	Alderney Race	1.44	-	-	1.44	3.86
F2	Casquets	-	0.17	-	0.17	0.47
F3	Big Roussel	-	-	0.04	0.04	0.12
F4	Alderney Race & Casquets	1.51	0.29	-	1.80	4.84
F5	Alderney Race & Big Roussel	1.45	-	0.04	1.49	3.99
F6	Casquets & Big Roussel	-	0.18	0.04	0.22	0.69
F7	Alderney Race, Casquets & Big Roussel	1.50	0.29	0.04	1.83	4.90

7.2.6.3 Change in flow dynamics

Figure 7.6a shows the change in mean velocity distribution due to energy extraction at Alderney Race (Case 1) in comparison to the ambient flow. Energy extraction in Alderney Race diverts flow around Alderney and through Casquets, giving an increase in mean flux through Casquets of 9% and a reduction in volume flux through Alderney Race of 27%. Energy extraction at Alderney Race (Case 1) has no significant impact on the velocities at Big Roussel, where velocities match those in the ambient case, giving the same mean volume flux through Big Russel.

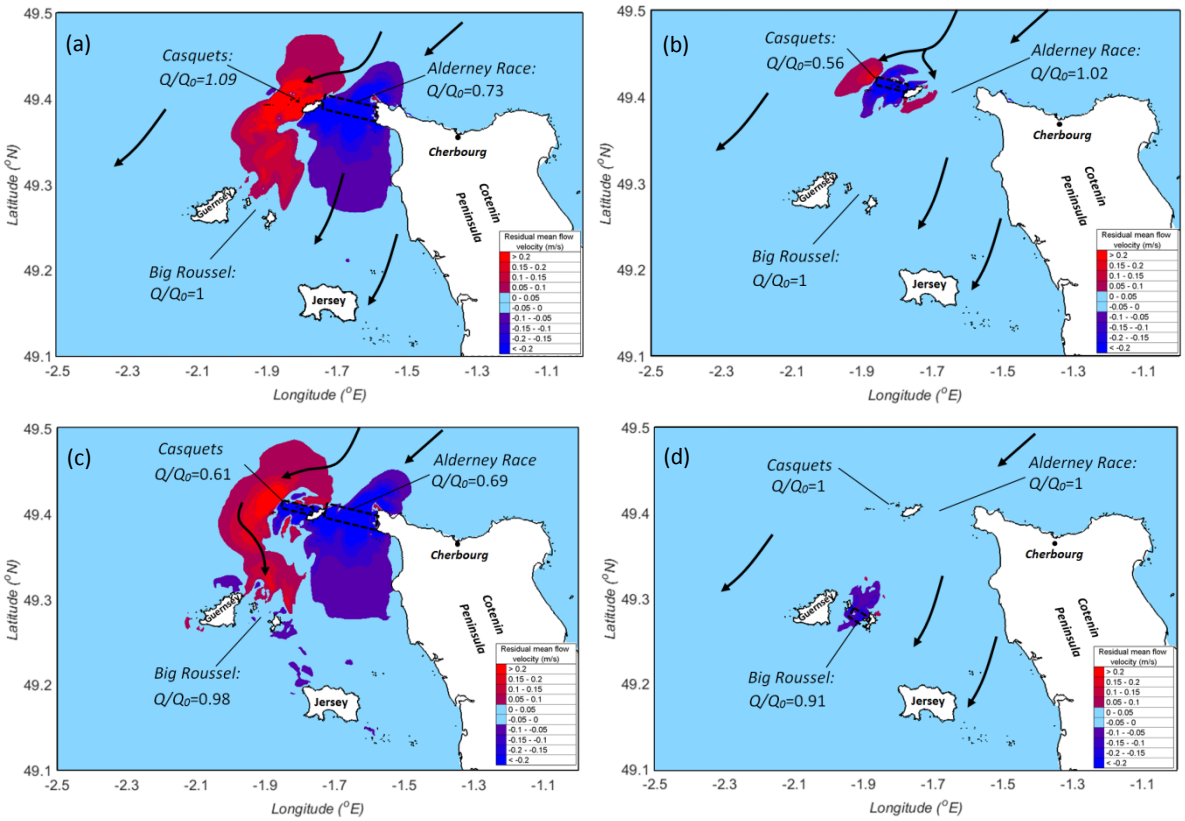

Figure 7.6 Mean velocity distribution difference plots between the ambient case and (a) energy extraction at Alderney Race (Case 1) (b) energy extraction at Casquets (Case 2) (c) energy extraction at Alderney Race and Casquets (Case 4) (d) energy extraction at Big Russel (Case 3). The energy extraction zones at Alderney Race and Casquets are also shown along with the change in flow rate through Big Russel as a result of energy extraction at Alderney Race and Casquets.

This may change with the inclusion of additional boundary forcings as this will increase velocities within the Channel Islands, hence increasing the magnitude of the force exerted on the flow at the energy extraction zone in Alderney Race and increasing the magnitude of bypass velocities around Alderney into Casquets and down into Big Russel.

When energy is extracted at Alderney Race and Casquets together (Case F4), energy extraction at Alderney Race causes an increase in power extracted at Casquets in comparison to energy extracted at Casquets only (Case F2) of 0.32 GW, an increase of 68%. This results in an increase in total extracted power (at both sites) of 12% compared with energy extraction from the individual sites simulated separately (Case F1 and F2). This is a similar finding to the upper bound case, emphasising the need for regulators and developers to account for the constructive impact from dual development at Alderney Race and Casquets when designing turbine layouts, as it will lead to improved energy yield, making it a more attractive proposition.

Figure 7.6b shows the change in mean velocity distribution due to energy extraction at Casquets in comparison to the ambient flow. The increased drag applied uniformly over the energy extraction zone in Casquets diverts flow around into the English Channel and through Alderney Race, shown by regions of enhanced mean velocity. The added drag applied at Casquets gives a small increase in mean flux through Alderney Race of 2% and a reduction in volume flux through Casquets of 44%. This high reduction in volume flux through Casquets is because Casquets is the least constrained site, so flow is easily diverted into the English Channel with the inclusion of added drag in Casquets' energy extraction zone. Energy extraction at Casquets gives no change in mean velocities at Big Roussel.

Figure 7.6c shows the change in mean velocity distribution due to energy extraction at Alderney Race and Casquets together (Case F4) in comparison to the ambient flow. The increased drag applied uniformly over the energy extraction zones at Alderney Race and Casquets diverts flow around Casquets and into the English Channel. This enhanced flow region persists down towards Guernsey, however it does not reach Big Roussel where the mean velocity actually reduces slightly compared with the ambient case, giving a 2% reduction in mean volume flux through Big Roussel and a reduction in mean extracted power of 0.01 GW (8%) compared to energy extraction at Big Roussel only (Case F3). When energy is extracted at Alderney Race and Casquets together, energy extraction at Casquets causes an increase in power at Alderney Race of 0.2 GW, an increase of 5%.

Figure 7.6d shows that energy extraction at Big Russel (Case F3) has a very localised effect on mean velocities compared with the ambient case, so does not affect mean velocities in Alderney Race and Casquets, resulting in no change in mean volume flux through Alderney Race and Casquets. Energy extraction at Big Russel only (Case F3) gives a reduction in average volume flux through Big Russel of 9% in comparison with the ambient case.

Such results have implications for site development. That is, energy extraction planning within these sites will require careful, path-dependent techno-economic analysis. Authorities should

consider what leasing conditions are likely to lead to the fullest and fastest development of tidal power in the region with a view that sites will affect each other.

7.3 Sub arrays in Alderney Race

Table 7.7 summarises estimates for annual available power from sub arrays positioned in the West and East of Alderney Race based on the approach taken by Bahaj et al. (2004), which was outlined in Chapter 4.4.4. The numbers given in parenthesis are the values obtained by Bahaj et al. (2004) using the kinetic flux method with low resolution flow data. In the West Race, results for annual available power using the distributed drag method yields a result 45% higher than that obtained using the kinetic flux method (Bahaj & Myers 2004). Conversely in the East Race the result obtained using the distributed drag method is 34% higher. Coincidentally the total annual power output estimated by the distributed drag method (7.62 TW h) is within 1% of the estimate obtained using the kinetic flux method.

Table 7.7 Summary of results for estimated available power from sub-arrays positioned in the East and West of Alderney Race. Numbers in brackets give the results obtained in (Bahaj & Myers 2004) using the kinetic flux method with low resolution flow data.

No. sub-arrays	Rotor diameter (m)	Available power (TW h)
West Race		
9	14	0.43
19	20	1.59
15	25	1.86
	Total	***3.88 (2.67)***
East Race		
29	14	2.67
4	20	0.59
2	25	0.48
	Total	***3.74 (4.73)***

In obtaining the results presented in Table 7.7 improvements to previous work by Bahaj et al. (2004) have been made. Firstly higher spatial and temporal resolution flow data has been obtained from simulations using the English Channel model. Since turbine power is a function of velocity cubed, poor definition of velocity distribution is likely to have led to a significant error in estimates for available power of individual sub arrays. Secondly the distributed drag method has

been used to simulate energy extraction to account for the change in flow dynamics caused by the sub-arrays. This is something the kinetic flux method does not consider.

To demonstrate the importance of this last point, Figure 7.7 shows the mean velocity difference between the ambient flow (without energy extraction by sub arrays) and the flow with energy extraction by sub arrays. Flow accelerates around each sub-array, creating regions of increased mean velocity through the centre of Alderney Race and within close proximity of Alderney and French coastlines. On the Alderney side this is in close proximity to the Southbanks, a large sand bank running along the South East coast of Alderney. It is unclear from this work what effect the sub-arrays would have on the sediment dynamics of this area, where similar studies to those conducted by Haynes et al. (2013) would be needed to quantify this effect.

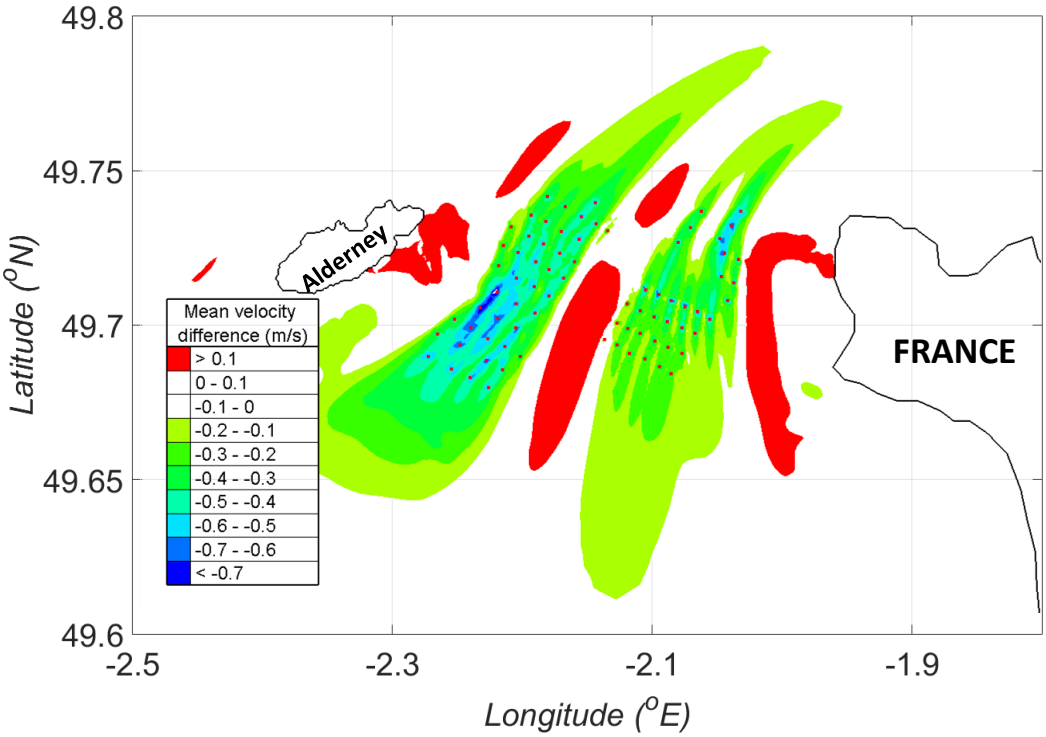

Figure 7.7 Mean velocity difference between the ambient flow and flow with energy extraction in Alderney Race, demonstrating the significant impact of sub arrays on the surrounding flow field. Red points show the location of each sub-array.

The significant discrepancies between results highlight the need for site specific modelling of large tidal turbine arrays to obtain reliable high resolution flow data.

7.4 Large arrays in Alderney Race

Large arrays were simulated in Alderney Race, where array plots were based on the distribution of mean kinetic power, as described in Chapter 4.4.5, Table 4.3 and shown in Figure 7.8. In total 4 arrays were considered; three in Alderney Race (small, medium and large) and one in Casquets. Mean annual power per swept area is used as a metric to compare array performance, based on the approach formerly adopted by Adcock et al. (Adcock et al. 2013).

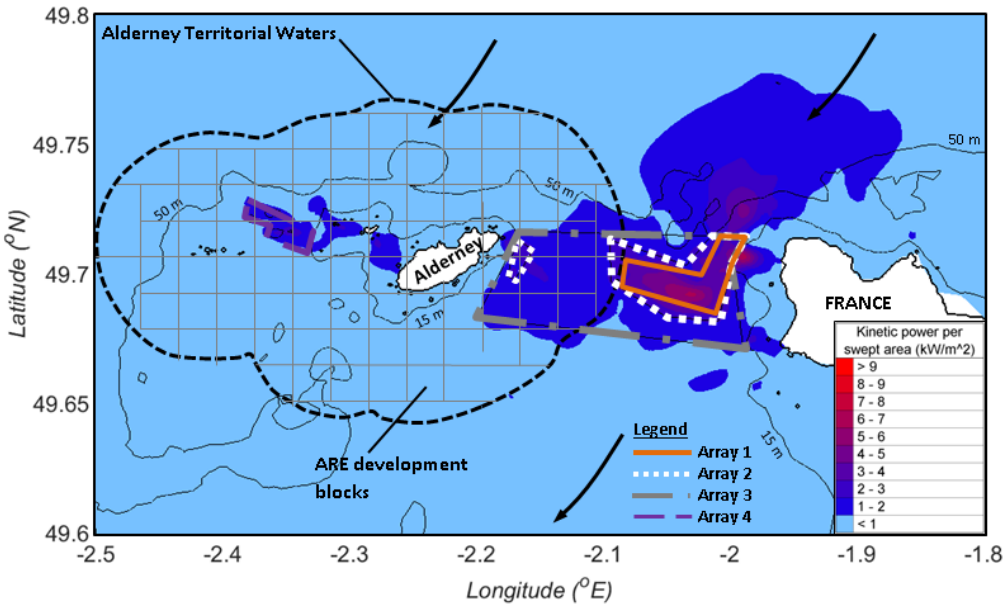

Figure 7.8 Arrays 1,2,3 and 4 located in Alderney Race and Casquets over regions of highest time averaged kinetic power per swept area within depths ranging between 15 m and 50 m. The perimeter of Alderney Territorial Waters is shown by the black dotted line, which contains development blocks set out by Alderney Renewable Energy (ARE). Arrows show the direction of the dominant ebb tide.

7.4.1 Available Power

Figure 7.9 shows the relationship between the array density of Arrays 1: Alderney (small), Array 2: Alderney (medium) and Array 3: Alderney (large) and the available power. Simulations were run for 1 month period to consider the spring-neap variation in the tidal resource and results were averaged over this period. The mean annual power available to Array 3 is far superior to that of Arrays 1 and 2, so much so that its minimum average annual available power of 0.7 GW using an array density of 0.01 exceeds that of the maximum average available power of Array 1 (0.65 GW using an array density of 0.078) by 8%. However, this is somewhat unsurprising given that the plot area of Array 3 is 475% greater than Array 1. For all three arrays, as array density increases, the rate of increase in average annual available power reduces. For example the density of Array 1

increases from 0.01 to 0.02, there is an increase in power of 0.15 GW (60%). However when the density of Array 1 increases from 0.06 to 0.07, there is only a 0.05 GW (8%) increase in power. This is because the increase in array drag reduces the velocities upstream and within the array plot area, and also causes flow to divert around the array, taking a path of less resistance and reducing the available power within the array itself. Flow diversion around the arrays is extremely important when considering such sites and is quantified and discussed in more detail in Chapter 7.4.3.

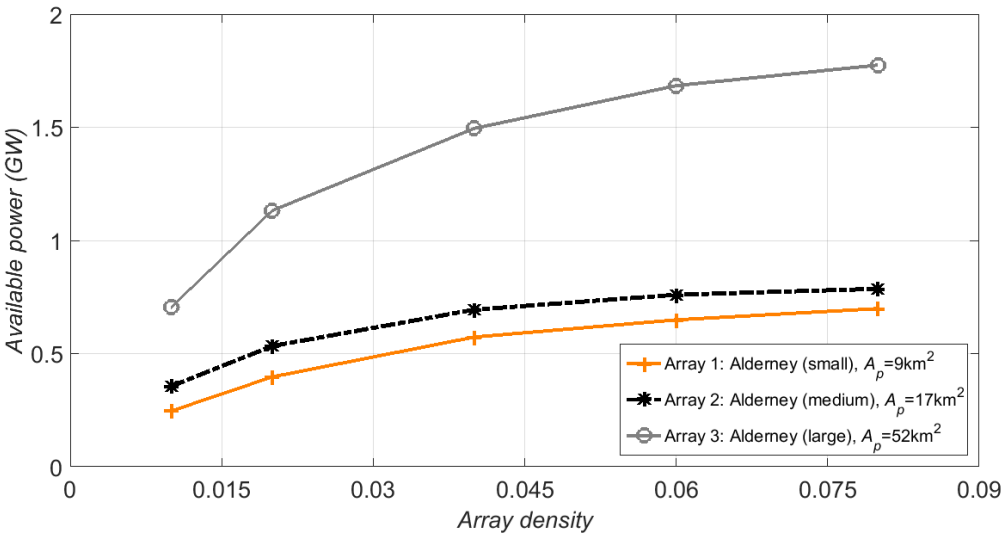

Figure 7.9 Available power of Array plots 1 (small), 2 (medium) and 3 (large) in Alderney Race with increasing array density. Power averaged over 1 month.

Another efficiency indicator is the average annual generated power per swept area. For comparison, the London Array, currently the world's largest offshore windfarm, generated 0.25kW/m^2 during a maximum efficiency period in December 2015 (London Array 2016). **Error! Reference source not found.** shows the power per swept area of Arrays 1, 2 and 3. Since Array 1 is positioned in the most energetic flow, the available power per swept area of Array 1 remains above 1 kW/m^2 (i.e. far exceeding that of the London Array) over the majority of the array density range, only dropping below 1 kW/m^2 for array density greater than 0.075. At this limit the average available power is estimated to be 0.67 GW. Encouragingly, at lower array density this 1 kW/m^2 limit is far exceeded, where for an array density of 0.01, the mean annual power per swept area is 2.75 kW/m^2, over ten times that of the maximum achieved by the London Array . Under this array configuration the tidal array generates an average annual power of 0.25 GW, 4% higher than the average available power of London Array during its maximum efficiency period. Further performance comparisons with the London Array are discussed in Chapter 7.5.

For Array 2 the average available power per swept area exceeds 1 kW/m^2 for array densities less than 0.04, where the average available power reaches 0.69 GW with an array density of 0.04. The maximum acceptable array density to achieve an average available power per swept area greater than 1 kW/m^2 for Array 2 is lower than for Array 1 because Array 2 has some turbines positioned in lower ambient energy flow. Similarly, the maximum acceptable array density to achieve an average available power per swept area of 1 kW/m^2 drops further for Array 3 to 0.02, where for an array density of 0.02 Array 3 generates an average power of 1.1 GW.

Array 3: Alderney (large) has a significantly higher available power over the whole array density range in comparison to Array 1 and 2 (Figure 7.9). The main reason for this is it covers a much larger area than Arrays 1 and 2, so uses significantly more turbines. This is shown in Figure 7.11, which estimates the total number of turbines based on a standard turbine diameter of 20 m. Given the significant variation in depth across Alderney Race, in reality turbines of different sizes would be needed.

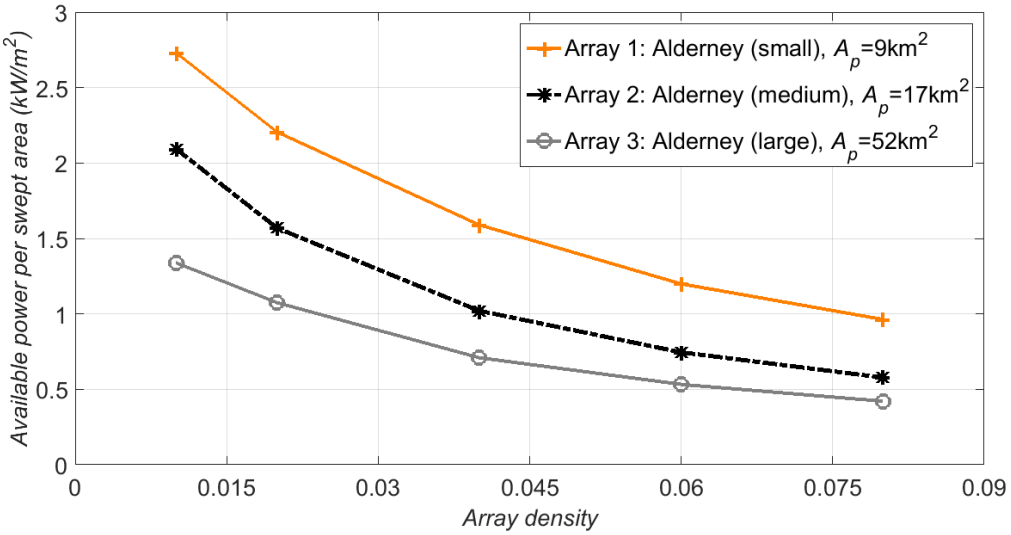

Figure 7.10 Available power per swept area of Array plots 1 (small), 2 (medium) and 3 (large) in Alderney Race with increasing array density. Power averaged over 1 month.

For Array 2 the average available power per swept area exceeds 1 kW/m^2 for array densities less than 0.04, where the average available power reaches 0.69 GW with an array density of 0.04. The maximum acceptable array density to achieve an average available power per swept area greater than 1 kW/m^2 for Array 2 is lower than for Array 1 because Array 2 has some turbines positioned in lower ambient energy flow. Similarly, the maximum acceptable array density to achieve an average available power per swept area of 1 kW/m^2 drops further for Array 3 to 0.02, where for an array density of 0.02 Array 3 generates an average power of 1.1 GW.

Figure 7.11 presents an estimate for the total number of turbines based on a standard turbine diameter of 20 m. The total number of turbines within each array is another important consideration since each individual device will require manufacturing, installation, cabling, commissioning, maintenance, and decommissioning operations to be completed during the project lifetime. A higher number of turbines could increase the number of operations necessary to keep the array generating power, hence increasing the cost of energy. This is especially prevalent given that the diameter of tidal turbines is restricted by depth, meaning that in comparison with a windfarm, a higher number of smaller turbines will be needed to achieve the same total swept area.

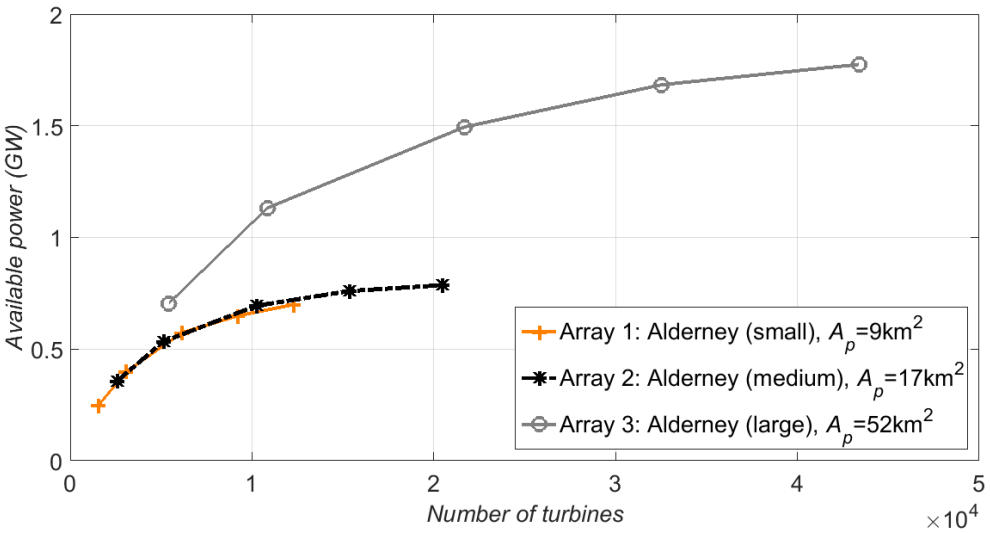

Figure 7.11 Available power of Array plots 1 (small), 2 (medium) and 3 (large) in Alderney Race with increasing array density in terms of equivalent number of 20 m diameter turbines.

The total number of turbines within Arrays 1, 2 and 3 were estimated, where given the considerable spatial variation in depth within each array, it was assumed that each array contains turbines of different diameters. It was further assumed that the centroid height of each turbine (i.e. the hub height) is positioned at mid depth based on mean sea level and that each turbine diameter is equal to one third of the depth (also based on mean sea level). Physically this means that to achieve a predefined uniform array density, in the shallower waters such as within Array 1 a high number of smaller diameter turbines are used whilst in deeper waters such as through the central channel of Alderney Race, a lower number of larger diameter turbines are used.

Parts of Array 1 are positioned in relatively shallow depths, where ambient mean sea level goes as low as 15 m. For this reason Array 1 uses a relatively large number of smaller diameter turbines to generate power. For example, Array 1 with density of0.01 uses 1530 turbines to generate a time

averaged power of 246 MW, equivalent to 0.16 MW/turbine. For comparison, the London Array uses 175 turbines to generate approximately the same time averaged power of 240 MW, equivalent to 1.37 MW/turbine. Array 3 also covers these shallow regions also covered by Array 1, however Array 3 also covers regions of greater depth in the central channel of the Race, up to 74 m. In these deeper regions larger turbine diameters can be adopted so that Array 3 is able to use fewer, larger turbines to achieve the same uniform array density in comparison with the shallow regions covered by Array 1. This means that Array 3 with density of 0.01 generates a time averaged power of 0.71 GW, approximately the same level as Array 1 using the highest array density of 0.08, but with 5425 turbines, 6800 less turbines than Array 1. Whilst velocities in the deeper West Race tend to be lower than the shallower East Race, these deeper waters in the West Race may be a more attractive proposition for developers who wish to minimise the number of turbines within an array, hence minimising the likely number of installation, maintenance and decommissioning operations without compromising on generated power output.

As the array density of Array 3 is increased, the number of turbines increases drastically, where for an array density of 0.08 Array 3 contains over 40,000 turbines to achieve an average annual power generation of 1.8 GW! This seems like an unrealistic number of turbines to be able to install, operate and maintain, adding complication that would inevitably push up the cost of energy.

Adcock (2013) assessed the viability of increasing array density for arrays in the Pentland Firth based on the available power of the *added* turbines only. Results based on this approach are summarised in Table 7.8. Based on the assumption that the added turbines must generate a power per added swept area of at least 1 kW/m^2 to be viable, only Array 1: Alderney (small), with array density up to 0.04 and Array 2: Alderney (medium) with array density up to 0.02 achieves this criteria.

Table 7.8 Incremental increase in mean annual available power and mean annual available power per added swept area using Arrays 1,2 and 3.

Array	Increase in array density	Available power of added turbines (GW)	Available power of added turbines /added swept area of added turbines(kW/m^2)
1	From 0.01 to 0.02	0.15	1.67
1	From 0.02 to 0.04	0.17	0.98
1	From 0.04 to 0.06	0.07	0.42
1	From 0.06 to 0.08	0.05	0.28
2	From 0.01 to 0.02	0.13	0.97
2	From 0.02 to 0.04	0.11	0.43
2	From 0.04 to 0.06	0.04	0.16
2	From 0.06 to 0.08	0.01	0.06
3	From 0.01 to 0.02	0.42	0.81
3	From 0.02 to 0.04	0.36	0.34
3	From 0.04 to 0.06	0.19	0.18
3	From 0.06 to 0.08	0.09	0.08

Array 1: Alderney (small) with density equal to 0.04 gives an estimated power output of 0.55 GW using an equivalent of 1100 x 20m diameter turbines with an available power per swept area of 1.59 kW/m^2. Array 3: Alderney (large) with array density equal to 0.01 provides a greater average annual power output of 0.71 GW but with an inferior available power per swept area of 1.33 kW/m^2 in comparison. As a result Array 3: Alderney (large) uses an equivalent of 1700 x 20m diameter turbines. Comparing this with Array 1: Alderney (small) with array density equal to 0.04, this is a 55% increase in total swept area for a 27% increase in mean annual power output, reducing mean available power per swept area by 16%.

Available power during the dominant spring ebb tide reached a maximum value of 2.7 GW, both for Array 1: Alderney (small) and Array 3: Alderney (large). This maximum is just under the capacity of the FABlink interconnector cable, which will be able to deliver 1.4 GW of electrical power from Alderney to Britain and Alderney to France at the same time, giving a total export capacity of 2.8 GW. However, in the future other regions such as Casquets may also be developed, which could mean this 2.8 GW threshold could be exceeded. Given that Alderney has a peak demand for electricity of only 1.5 MW, it is possible that solutions such as energy storage will be required to allow energy to be stored at spring tide and then exported during times of low available power. The likely level of energy extraction at Casquets is quantified in 7.4.2.

7.4.2 Casquets

Array 4: Casquets covers an area of 3 km^2 over the region of highest ambient velocities. Results in Figure 7.12 show that for array density equal to 0.01, average annual available power was 38 MW with an average available power per swept area of 1.3kW/m^2. Figure 7.13 shows the relationship between the available power per swept area and array density. When array density was increased to an array density of 0.02, the available power of the added turbines reduced to 0.62 kW/m^2, below the limit of 1 kW/m^2 set out in this work.

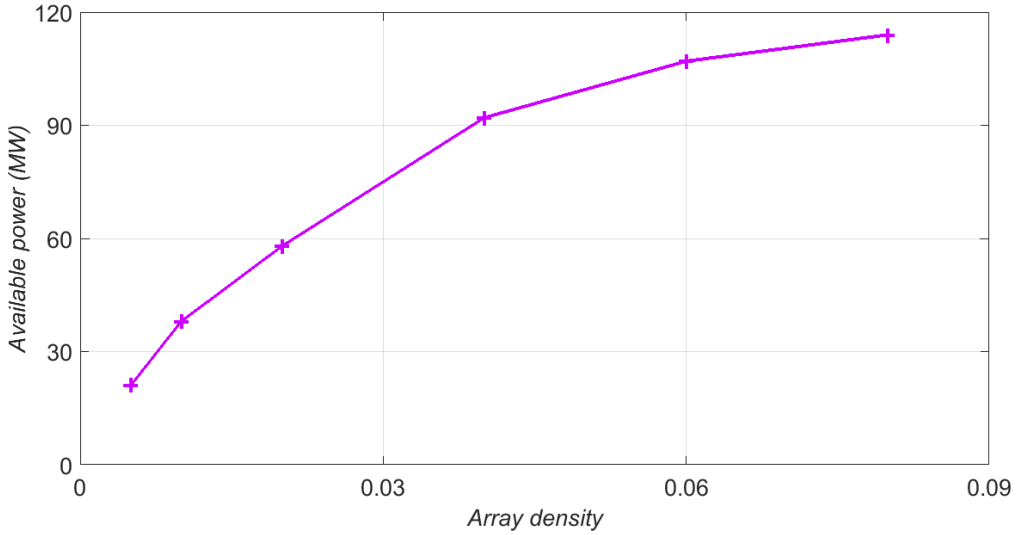

Figure 7.12 Available power for Array plot 4: Casquets in the absence of energy extraction in Alderney Race.

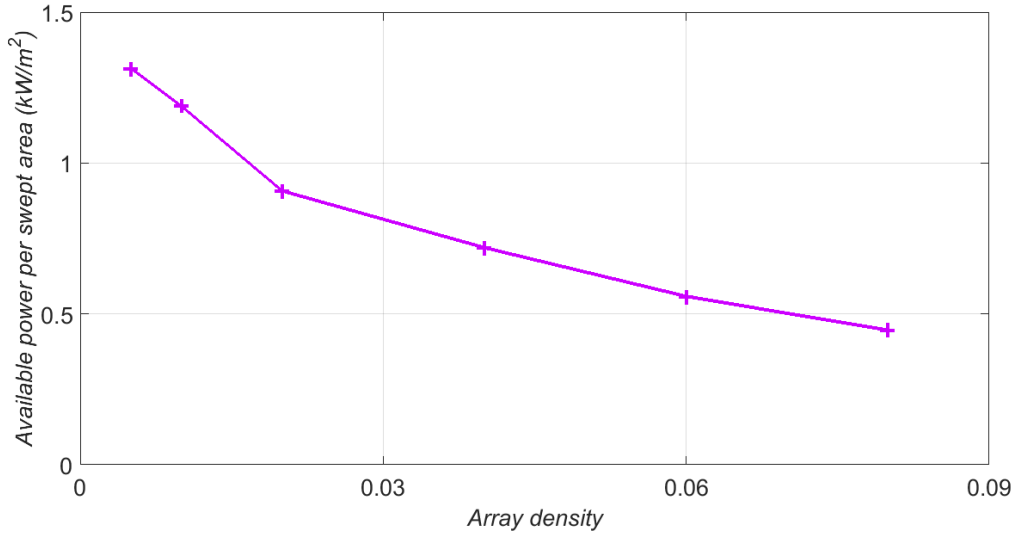

Figure 7.13 Available power per swept area for array plot 4: Casquets with increasing array density in the absence of energy extraction in Alderney Race.

Table 7.9 shows that when energy extraction was simulated using Array 1: Alderney (small) with an array density of 0.04 and Array 4: Casquets with an array density of 0.01 simultaneously, the available power of Array 4: Casquets increased by 6 MW compared with Array 4: Casquets on its own, an increase of 15%. The distributed drag associated with Array 1: Alderney (small) diverts flow around Alderney Race and into Casquets, resulting in a 2% increase in volume flux through the cross section of Array 4: Casquets aligned perpendicular to the flow. This increases the energy available in the flow at Casquets for energy extraction when Array 4: Casquets is added. The available power of Array 1: Alderney (small) remained unchanged with energy extraction at Casquets because the drag associated with Array 4: Casquets is not large enough to cause a significant change in flow through Alderney Race.

Table 7.9 Mean available power using combinations of Array 1: Alderney (small) with array density λ=0.04 and Array 4: Casquets with λ=0.01.

	Alderney	Casquets	Total (MW)
Array 1: Alderney (small)	573	-	573
Array 4: Casquets	-	38	38
Array 1: Alderney (small)+ Array 4: Casquets	572	44	614

This result shows that for the arrays considered here available power at Alderney Race is independent of available power at Casquets, however the reverse is not true. Table 7.9 shows that for Array 1: Alderney (small) and Array 4: Casquets, if Casquets was considered on its own it would lead to a 15% underestimation of available power at Casquets, however this is still less than 1% of the power available to Array 1: Alderney (small).

7.4.3 Changes to ambient flow field

Blockage by large arrays positioned in the flow in Alderney Race will cause an increase in hydraulic resistance in the region covered by the array, causing flow to divert around the array, following a path of less resistance. This is an important consideration when developing sites because such flow diversion will (a) alter the surrounding tidal resource, affecting the performance of other closely located arrays and (b) may cause detrimental environmental impacts such as sediment transport effects within Alderney Territorial Waters. This former point is important given that the Alderney Race is split into French and Alderney territorial waters, meaning that tidal development within French waters could have an impact on the tidal resource within Alderney territorial waters and vice versa.

Figure 7.14a shows that energy extraction using Array 1 with an array density of0.01 causes a large wake region downstream, where the mean velocity distribution shows a region of reduced average velocity stretching 11 km downstream of the array (in both the ebb and flood direction). There are only very small regions where the mean flow shows increased average velocities (in the red regions) compared with the ambient case, located to the East of the array. Therefore the array, which is located in French territorial waters, does not have a significant impact on the flow within Alderney territorial waters to the West, where the volume flux through the cross section within Alderney territorial waters compared with the ambient case. In this case, the maximum increase in velocity reached 1 m/s at times of spring ebb tide in comparison with the ambient case in the region to the East of Array 1.

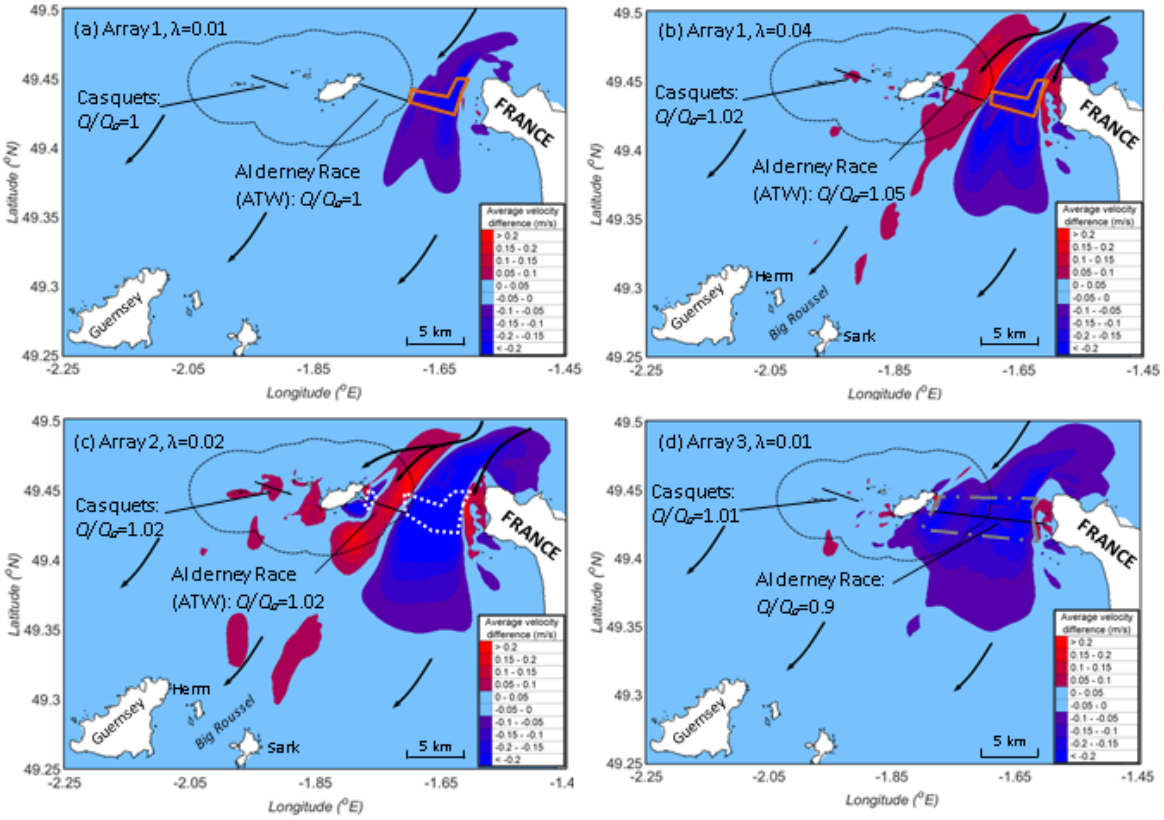

Figure 7.14 Mean velocity difference plot between the ambient case and energy extraction using (a) Array 1 with array density of 0.01 (b) Array 1 with array of 0.04 (c) Array 2 with array density of 0.02 and (d) Array 3 with array density of 0.01. The change on average volume flux through Alderney Territorial Waters (ATW) within Alderney Race, the entire width of Alderney Race and Casquets are also shown, along with the outline of Alderney Territorial Waters. Arrows show the direction of the dominant ebb tide and the general nature of flow diversion caused by energy extraction.

Figure 7.14b shows that when the density of Array 1 was increased to 0.04, there was a significant increase in the velocities within Alderney territorial waters, caused by the increase in hydraulic

resistance from added turbines within Array 1's plot area. This gave a 5% increase in the average volume flux through the cross section within Alderney territorial waters in comparison to the ambient case. The region of enhanced velocity between Array 1 and the French coast (i.e. East of Array 1) also increased in comparison to the previous case (Array 1 with density of 0.01) so that it now covers an area of 1.7 km^2. Within this region there were times when velocities increased to greater than 2 m/s above the ambient case during spring ebb tide.

The wake length downstream of Array 1 also increased as a result of increased array density, so that the region of decreased velocity distribution compared with the ambient case now extends to 15 km (both in the ebb and flood direction). There are also regions of increased average velocity distribution within Casquets on the opposite side of Alderney, increasing the average volume flux through this region to by 2%, improving the resource for energy extraction. There are also regions of increased velocity in the region between Alderney Race and Sark, which is approaching Big Russel, the channel located between the islands of Herm and Sark, which has also been identified as a site suitable for tidal energy development based on suitable depths and velocities.

In general, for energy extraction using Array 1, flow is diverted into the open section of Alderney Race through the central channel, keeping the overall mean volume flux through the entire cross section of Alderney Race within 10% of the natural regime over all array densities (i.e. up to an array density of 0.08).

Figure 7.14c shows that energy extraction using Array 2 with array density of 0.02 causes a significant change in velocities across Alderney Race. Energy extraction using Array 3 with density of 0.01 reduced the average volume flux through the entire cross section of Alderney Race by 10% (Figure 7.14d). Regions of increased average velocities are limited to small patches neighbouring the French coast directly to the East of Array 3, close to the North East tip of Alderney within Alderney Race and within Casquets. Within these regions at times of spring ebb tide, velocities exceeded ambient flow velocities by up to 1.8 m/s. The average volume flux through Casquets increased in comparison with the ambient case by 1%.

7.5 Performance comparisons with offshore windfarms

Table 7.10 summarises the results obtained for fences spanning the width of Alderney Race, Casquets and Big Russel (Chapter 7.2), sub arrays in Alderney Race (Chapter 7.3) and large arrays (Chapter 7.4). Column 1 gives a comparison with performance data from the London Array, the world largest windfarm currently in operation, which was obtained during a maximum efficiency period over December 2015, so gives an upper bound for performance to date. The available power of a wind turbine varies from around 0.25-1kW/m^2 at offshore locations around the UK (DTI 2008).

7.5.1 Array layout 1: Alderney Race (small)

Array 1: Alderney (small) with array density of 0.01 (Table 7.10, column 3) gives a mean available power of 0.25 GW, approximately the same as the London Array. However, Array 1: Alderney (small) achieves this over an array plot area one tenth the size of the London Array and with half the array density. This results in a mean available power per swept area of 2.7 kW/m^2, over ten times that of the London Array. This is achieved with an equivalent of 285 x 20 m diameter turbines, 63% more devices than the London Array. This is because a typical tidal turbine has a rated power of around 1 MW whilst the wind turbines used in the London array are rated at 3.6 MW, so more smaller devices are needed. The capacity factor of the tidal turbine array is 0.28, 26% lower than the London Array. This is because the rated velocity of the simulated tidal turbines is 4 m/s, however the average velocities within Array plot 1: Alderney (small) are around 2.5 m/s so maximum power is rarely reached.

An array density of 0.01 corresponds to a lateral spacing between devices of 3 diameters (tip-to-tip) and longitudinal spacing between rows of 20 diameters. Doubling array density to 0.02 (to the same density as the London Array) gave a 60% increase in mean available power to 0.397 GW. This resulted in a 20% drop in mean annual available power to 2.2 kW/m^2, still approximately nine times that of the London Array. The capacity factor also dropped, by 20% to 0.22 as a result of increased flow diversion around the array plot due to increased drag which resists the flow.

Doubling array density again to 0.04 gave an increase in average available power of 45% to 0.573 GW, reducing mean available power per swept area by 27% to 1.6 kW/m^2. Any further increase in array density reduces turbine performance below the 1 kW/m^2 threshold. Array density of 0.04 corresponds to a lateral spacing between devices of 1 diameter (tip-to-tip) and longitudinal spacing between rows of just 10 diameters. This makes it unlikely that array density will exceed this value in reality as sufficient space is needed between rows to allow wake recover.

Table 7.10 Comparison between estimates for available power using Array 1: Alderney (small) with array densities of 0.04,0.02 and 0.01, sub arrays in Alderney Race and tidal fences spanning the width of Alderney Race, Casquets and Big Russel. For comparison performance data from the London Array, the world's largest offshore windfarm is included in column 2. Results for available power averaged over a period of 1 month of simulation time.

	London array	Array 1, λ=0.04 (Alderney Race)	Array 1, λ=0.02 (Alderney Race)	Array 1, λ=0.01 (Alderney Race)	Sub arrays (Alderney Race)	Tidal fence, λ=0.04 (Alderney Race)	Tidal fence, λ=0.04 (Casquets)	Tidal fence, λ=0.04 (Big Russel)
Array plot area (km^2)	100	9	9	9	70	61	27	4
Turbine swept area (m^2)	11309	314*	314*	314*	154, 314, 490	314*	314*	314*
Array density	0.02	0.04	0.02	0.01	~0.01	0.04	0.04	0.04
No. turbines	175	1150*	575*	285*	2176	3100	1400	200
Available power (MW)	240 **	573	397	246	840	440	54	14
Available power per swept area (kW/m^2)	0.25 **	1.6	2.2	2.7	1.2	0.45	0.13	0.22
Available power per array plot area (MW/km^2)	2.4	63	44	27	12	7.2	2	3.5

*Assumes all turbines have 20 m diameter rotors. **Achieved during maximum efficiency period over December 2015, giving a power output of 369 GW h (London Array 2016).

to ensure array efficiency in terms of available power per swept area is maintained (Legrand 2009).

The maximum available power at spring ebb tide using Array 1: Alderney (small) with array density of 0.04 was 2.7 GW, just under the capacity of the FAB link interconnector cable currently under construction that will export up to 1.4 GW to England and to France at the same time. Any further array development in Alderney Race and Casquets is likely to require accompanying energy storage solutions to capture this power since Alderney has a very low demand for electricity, which peaks at just 1.5 MW.

7.5.2 Sub arrays in Alderney Race

The sub arrays modelled in Alderney Race generated a mean annual power of 840 MW, significantly more than that of Array 1: Alderney (small). This was achieved over a much larger area with many more turbines where sub arrays were positioned in regions with much lower ambient kinetic power, leading to a more modest mean available power per swept area of 1.2 KW/m^2. Nevertheless the performance of subarrays in Alderney Race still far exceeds that of the London Array, where mean available power per swept area and per plot area were both over four times greater.

7.5.3 Tidal fences spanning Alderney Race, Casquets and Big Russel

The main use of tidal fences in this work was to estimate an upper bound for energy extraction at Alderney Race, Casquets and Big Russel to compare against each other and other sites in literature. Table 7.10 shows that whilst a tidal fence at Alderney Race (Case F1) generates a significant level of power, array performance in terms of mean available power per swept area and per plot area is diminished in comparison with Array 1: Alderney (small) and sub arrays within Alderney Race. This is because the fence spans the entire Race, so covers less energetic regions. The same is true for tidal fences at Casquets and Big Russel, where array performance drops below the levels of the London Array.

The estimated mean available power of Array 3: Alderney (large) which spans the majority of Alderney Race (so is representative of a tidal fence) was 1.2 GW using a realistic array density of 0.04, giving a mean annual power per swept area of 1 kW/m^2. This reduced with any further increase in array density. Array 3: Alderney (large) gives the highest estimated extracted power of any array where mean annual power per swept area exceeds 1 kW/m^2. This is achieved with a reduction in volume flux through Alderney Race of 10%.

Tidal fences spanning the entire width of a channel could potentially infringe on other industries such as shipping, so are unlikely to be a viable option in the future. This is especially true of Alderney Race where shipping traffic is considerable on a daily basis. Another reason for not using tidal fences is that they cause a significant reduction in volume flux through a channel as was demonstrated for Array 3: Alderney (large).

Chapter 8: Conclusions and recommendations

8.1 Conclusions

To date, regional scale assessments of the tidal energy resource at sites around the Channel Islands have been limited by poor temporal and spatial resolution flow data and simplistic methods for modelling energy extraction. The objectives of this work were set out in Chapter 1.4 to improve the accuracy of estimates for the available power, thereby reducing uncertainty in energy yield estimates. This work should be of interest to regulators and tidal stream developers looking to develop tidal energy in the Channel Islands region, as well as other sites around the world.

In Chapter 4 a new 2D hydrodynamic model of the English Channel was presented. The model was built using Telemac 2D to simulate tidal flows around the Channel Islands at significantly improved spatial and temporal resolution. Validation results presented in Chapter 6 show that all M_2 velocity amplitudes and phases with the exception of one were within 10%/10° of field measurements, as well as all six free surface elevation amplitudes and phases located around the Channel Islands. This gave confidence in the English Channel model's ability to accurately model tidal flows in the Channel Islands. Results gave a significant improvement in S_2 major axis amplitudes in comparison with a similar model developed by Haynes (2015).

The distribution of mean kinetic power was used to assess the suitability of each site for tidal energy development based on levels used for 'acceptable project economics' (Black and Veatch 2005; Adcock et al. 2013). This work concluded that in general the total area suitable for tidal energy development is approximately 70% smaller than previous studies reviewed in Chapter 2. As highlighted in this thesis Alderney Race has the greatest potential for tidal energy development where the mean ambient kinetic power exceeds 13 kW/m^2, over five times the minimum recommended for 'reasonable project economics' (Black and Veatch 2011b). This was followed by Casquets which exceeded 7 kW/m^2 and then Big Russel, exceeding 5 kW/m^2. Based on results from this study, the suitable development area at Alderney Race actually increased by 35% compared to some studies, whilst at Casquets and Big Russel there was a reduction in area of 95% and 85% respectively as a result of improved spatial and temporal resolution flow data. Sites in North West Guernsey and North East Jersey did not exceed 2 kW/m^2 so were deemed unsuitable for tidal energy development at this stage, which contradicts previous estimates that relied upon lower resolution flow data.

To support the modelling of energy extraction within the English Channel Model and other regional scale models, an experimental campaign was carried out to validate the distributed drag method for modelling arrays of porous fences. Comparison was made between the total array drag obtained empirically using load cell measurements and a parameterisation often used in literature. Results showed the parameterisation of the area averaged array drag coefficient to be robust within the limits of realistic array density. However, the validity of the model was shown to be sensitive to bed topography, where enhanced velocities under the fences caused by the arrays increased the pressure drag acting on the roughness strips on the flume bed, increasing the bed drag by up to 100%.

To the best of the authors knowledge, these experiments are the first to validate the distributed drag method for modelling energy extraction by large tidal turbine arrays. Currently the distributed drag method provides the only feasible option for modelling large scale energy extraction in regional scale models at acceptable computational expense. This makes it an important tool for quantifying large scale energy extraction and the change in flow dynamics considered here, two determining features for determining the feasibility of recently proposed tidal turbine array projects.

The validated distributed drag parameterisation was used to model energy extraction from large tidal stream turbine arrays in the Channel Islands using the English Channel hydrodynamic model. An initial upper bound analysis found that Alderney Race has the greatest potential for energy extraction, giving a maximum average power potential of 5.1 GW, which scales up to 6.1 GW using nine tidal constituents to force the model. This is a significant finding as it shows the power potential at Alderney Race is 35% greater than the Pentland Firth (Draper et al. 2014), the best know site in the UK. The maximum average power potential at Casquets and Big Russel were 0.47 GW and 0.24 GW respectively. A sensitivity study was conducted to investigate the effect of seabed drag coefficient on results. Within the realistic limits of bed drag coefficient the mean annual power potential showed a 15% variation, which could be significant for developers and investors who want to determine the viability of specific array designs.

It was demonstrated that in reality these upper bound limits often rely on unrealistically high array densities, where turbines in close proximity have a detrimental impact on device efficiency due to wake interaction. A more realistic drag coefficient was implemented, resulting in reduced array density to a more realistic level. The analysis showed that for the realistic case, the available power is reduced by 24% (to 3.86 GW) and 50% (to 0.12 GW) at Alderney Race and Big Russel respectively. At Casquets there was no change in extracted power since the level of drag required to achieve the upper bound was relatively low. This is because Casquets is the least constricted

site, meaning that added drag caused greater flow diversion around the site rather than a build-up in head which occurred at the more constricted sites of Alderney Race and Big Russel.

When sites are working simultaneously, the increase in hydraulic resistance caused by added drag in Alderney Race diverts flow around Alderney, hence increasing energy extraction in Casquets by up to 68%. These results have implications for site development strategy, where it has been shown to be beneficial to develop Alderney Race and Casquets together since the more Alderney Race is developed, the better the resource at Casquets becomes. This is good news for simultaneous energy extraction at these sites, and it would be beneficial for developers to work together to strategically position arrays in each site to maximise constructive impact on energy yield.

In Chapter 7, the ambient flow results obtained from the English Channel Model were used to set out large array layouts in regions of highest mean ambient kinetic power. The performance of each array was assessed in comparison with that of an operational large offshore windfarm using metrics that describe the spatial efficiency of each array, such as the mean available power per swept area of rotor and the mean available power per array plot area. In general it was found that in comparison with the windfarm, the tidal turbine arrays in Alderney Race were more spatially efficient, however significantly more, smaller turbines were needed since turbine diameter is limited by depth. For example large scale energy extraction within the most energetic flows in the East Race is capable of generating a time averaged power output of 0.25 GW, 25% greater than that of the London Array, using only 9% of the windfarm's plot area and 20% of the total swept area, albeit with nine times more individual devices.

8.2 Suggestions for further research

8.2.1 Experimental flow characterisation in the hydraulically rough regime

Results in Chapter 5 showed self-similar wake behaviour downstream of a single fence, which for hydraulically rough flow was observed after just eight fence heights. It would be interesting to obtain measurements of wake deficit for more flows within the hydraulically rough regime by further modifying the geometric properties of the added bed roughness to investigate if they show the same behaviour. If so it would suggest that knowledge of the wake downstream of a single row of turbines could be used predict the wake downstream of rows added downstream in a kinematic model similar to the ones presented in Chapter 2.

8.2.2 Porous disk array modelling

Chapter 3.3 discussed the limitations of porous fences, which do not allow lateral spacing between adjacent turbines within the same row, so prohibit staggered array layouts. To quantify the effect of lateral spacing and staggered arrays on the array drag and validity of the distributed drag method, the methodology set out in Chapter 3 should be adopted for porous disk arrays, where load cell measurements are obtained for each individual disk and ADV measurements capture the level of lateral wake mixing in the transition and equilibrium regions of each array. This would provide a useful experimental dataset of wake flow through multi-row arrays to compliment results in Chapter 5 to further validate computational models.

8.2.3 Array optimisation within Alderney Race

Results in Chapter 7 are limited to arrays of uniform array density. In reality it is likely that array density will vary spatially to optimise power generation whilst also minimising environmental impact. To conduct array optimisation, approaches have been developed using machine learning to decide on the most suitable device spacing based on determining factors such as power generation, environmental impact (e.g. magnitude of sediment transport) and minimum cabling routes. This would be especially useful for optimising arrays at Alderney Race and Casquets simultaneously, as is necessary based on results presented in Chapter 7. To add further realism it would also be necessary to introduce the support structure drag into the model.

8.2.4 3D modelling of large arrays

Given the significant limitations of 2D modelling of large arrays discussed in Chapter 2, it would be useful to model the flume experiments using Telemac 3D, which separates the flow into horizontal layers, so that drag could be applied across the vertical extent of the rotor/fence. Results of free surface elevation drop across the arrays and vertical velocity profiles could be compared with results obtained from a 2D model and the experimental flume measurements to investigate any improvement to the distributed drag approach using three dimensional modelling and its ability to account for added bed drag in the high bed roughness cases.

References

A. Crespo, J. Hernandez, S.F., 1999. Survey of Modelling Methods for Wind Turbine Wakes and Wind Farms. *Wind Energy, Wiley*, 24(2), pp.1–24.

ABPmer, 2013. *Alderney Regional Environmental Assessment of Renewable Energy: Scoping Report*, Report no R.2096.

Adcock, T.A.A., Draper, S., Houlsby, G.T., Borthwick, A.G.L. & Serhadlıoğlu, S., 2013. The available power from tidal stream turbines in the Pentland Firth. *Proceedings of the Royal Society A, Royal Society*, 469(2157), pp.72–93.

Adcock, T.A., Draper, S. & Nishino, T., 2015. Tidal power generation - A review of hydrodynamic modelling. *Proceedings of the Institution of Mechanical Engineers, Part A: Journal of Power and Energy, Sage*, 229, pp.755–771.

Ahmadian, R. & Falconer, R.A., 2012. Assessment of array shape of tidal stream turbines on hydro-environmental impacts and power output. *Renewable Energy, Elsevier*, 44, pp.318–327.

Ainslie, J., 1985. Development of an eddy viscosity model for wind turbine wakes. In *Proceedings of the BWEA Wind Energy Conference (British Wind Energy Association)*. pp. 61–66.

Anderson, J.D., 1995. *Computational Fluid Dynamics The Basics with Applications*, Chapter 3, pp. 95-121: McGraw Hill.

Anon, http://noc.ac.uk/using-science/products/tidal-harmonic-analysis. *[Date Accessed: 06/07/2014]*.

Anon, 2016. Sustainable Energy Research Group. Available at: http://www.energy.soton.ac.uk/research/ [Accessed May 20, 2016].

Bahaj, A., Myers, L., Thomson, M. & Jorge, N., 2007. Characterising the wake of horizontal axis marine current turbines. In *Proc. 7th EWTEC*. Porto.

Bahaj, A.S., 2011. Generating electricity from the oceans. *Renewable and Sustainable Energy Reviews, Elsevier*, 15(7), pp.3399–3416.

Bahaj, A.S., Molland, A.F., Chaplin, J.R. & Batten, W.M.J., 2007. Power and thrust measurements of marine current turbines under various hydrodynamic flow conditions in a cavitation tunnel and a towing tank. *Renewable Energy, Elsevier*, 32(3), pp.407–426.

Bahaj, A.S. & Myers, L., 2004. Analytical estimates of the energy yield potential from the Alderney Race (Channel Islands) using marine current energy converters. *Renewable Energy, Elsevier*, 29(12), pp.1931–1945.

Bahaj, A.S. & Myers, L.E., 2003. Fundamentals applicable to the utilisation of marine current turbines for energy production. *Renewable Energy, Elsevier*, 28(14), pp.2205–2211.

Bahaj, A.S. & Myers, L.E., 2013. Shaping array design of marine current energy converters through scaled experimental analysis. *Energy, Elsevier*, 59, pp.83–94.

Balsells, A.S., 2015. *Management of the Electricity Supply in Alderney*. MSc Thesis, Cranfield University.

Barthelmie, R., Frandsen, S., Jensen, L., Mechali, M. & Rethore, P.-E., 2005. Verification of an efficiency model for very large wind turbine clusters. *Copenhagen Offshore Wind 2005 Conference*.

Barthelmie, R.J. & Jensen, L., 2010. Evaluation of wind farm effi ciency and wind turbine wakes at the Nysted offshore wind farm. *Wind Energy, Wiley*, 13, pp.573–586.

Barthelmie, R.J., Larsen, G.C., Folkerts, L., Rados, K.G., Pryor, S.C., Lange, B. & Schepers, G., 2006. Comparison of wake model simulations with offshore wind turbine wake profiles. *Journal of Atmospheric and Oceanic Technology, American Meteorological Society*, 23(7), pp.888–901.

Bastankhah, M. & Porté-Agel, F., 2014. A new analytical model for wind-turbine wakes. *Renewable Energy, Elsevier*, 70, pp.116–123.

Biron, P.M., Robson, C., Lapointe, M.F. & Gaskin, S.J., 2004. Comparing different methods of bed shear stress estimates in simple and complex flow fields. *Earth Surface Processes and Landforms, John Wiley & Sons*, 29(11), pp.1403–1415.

Black and Veatch, 2005. *Phase II UK Tidal Stream Energy Resourse Assessment*, pp. 10-31, Report comissioned by the Carbon Trust.

Black and Veatch, 2011a. *UK Tidal Current Resource & Economics : Appendix C*, pp. 24-52, Report commissioned by the Carbon Trust and npower, Project number 121393.

Black and Veatch, 2011b. *UK Tidal Current Resource and Economics*, pp. 15-45, Report commissioned by the Carbon Trust and npower, Project number 121393.

Blackmore, T., Batten, W.M.J. & Bahaj, A.S., 2013. Turbulence generation and its effect in LES approximations of tidal turbines. In *Proceedings of EWTEC 2013*. Aalborg, Denmark.

Blackmore, T., Batten, W.M.J., Muller, G.U. & Bahaj, A.S., 2014. Influence of turbulence on the drag of solid discs and turbine simulators in a water current. *Experiments in Fluids, Springer*, 55, pp.1–10.

Blanchfield, J., Garrett, C., Rowe, A. & Wild, P., 2008. Tidal stream power resource assessment for Masset Sound, Haida Gwaii. *Proceedings of the Institution of Mechanical Engineers, Part A: Journal of Power and Energy, Sage*, 222(5), pp.485–492.

Blunden, L., 2009. *New approach to tidal stream energy analysis at sites in the English Channel*. PhD thesis, University of Southampton, UK.

Blunden, L. & Bahaj, A., 2007. Tidal energy resource assessment for tidal stream generators. *Journal of Power and Energy, Sage*, 221, pp.137–146.

Blunden, L.S., Batten, W.M.J., Harrison, M.E. & Bahaj, A.S., 2009. Comparison of boundary-layer and field models for simulation of flow through multiple-row tidal fences. In *8th European Wave and Tidal Energy Conference*. pp. 1–10.

Bosanyi, E.A., Maclean, C., Whittle, G.E., Dunn, P.D., Lipman, N.H. & Musgrove, P.J., 1980. The Efficiency of Wind Turbine Clusters. In *Third International Syposium on Wind Energy Systems*. Lyngby, Denmark, p. 401–416.

Bourban, S., Liddiard, M., Durand, N., Cheeseman, S. & Baldock, A., 2013. High Resolution Modelling Of Tidal Resources , Extraction And Interactions Around The UK. In *1st Marine Energy Technology Symposium (METS13)*. Washington D.C, USA.

Bradshaw, P. & Huang, G.P., 1941. The Law of the Wall in Turbulent Flow. *Mathematical and Physical Sciences, Royal Society*, 451, pp.165–188.

Braye, D.I., 1982. Flow resistance in gravel-bed rivers. *Gravel-bed rivers, Fluvial processes, Engineering and Management*, 1, pp.109–137.

Brown, J., Colling, C., Park, D., Phillips, J., Rothery, D. & Wright, J., 1993. Waves, Tides and Shallow-Water Processes. In The Open University & Pergamon Press, pp. 43–52.

Brutto, O.A. Lo, Nguyen, V.T., Guillou, S.S., Gualous, H. & Boudart, B., 2015. Tidal farm analysis using an analytical model for the flow velocity prediction in the wake of a tidal turbine. *Renewable Energy, Elsevier*, In review.

Builtjes, P.J.H., 1979. The interaction of windmill wakes. In *International Symposium on Wind Energy Systems*. Netherlands.

Calaf, M., Meneveau, C. & Meyers, J., 2010. Large eddy simulation study of fully developed wind-turbine array boundary layers. *Physics of Fluids, AIP Publishing*, 22(1), pp.1–16.

Campbell, A.R., Simpson, J.H. & Allen, G.L., 1998. The Dynamical Balance of Flow in the Menai Strait. *Estuarine, Coastal and Shelf Science, Elsevier*, 46(3), pp.449–455.

Cant, R., Castro, I. & Walklate, P., 2002. Plane jets impinging on porous walls. *Experiments in Fluids, Springer*, 32, pp.16–26.

Cebeci, T. & Cousteix, J., 1999. *Modeling and computation of boundary-layer flows*, Horizons Publishing Inc., pg. 239-240.

Cengal, Y.A. & Cimbala, J.M., 2006. *Fluid Mechanics Fundamentals and Applications*, McGraw-Hill, pp. 426-433.

Chamorro, L.P. & Porté-Agel, F., 2011. Turbulent flow inside and above awind farm: A wind-tunnel study. *Energies, MDPI*, 4(11), pp.1916–1936.

Chow, V., 1959. Gradually Varied Flow. In *Open Channel Hydraulics*. New York: McGraw-Hill.

Cleve, J., Greiner, M., Enevoldsen, P., Birkemose, B. & Jensen, L., 2009. Model-based analysis of wake-flow data in the Nysted offshore wind farm. *Wind Energy, John Wiley and Sons*, 12(2), pp.125–135.

Coles, D., Blunden, L. & Bahaj, A., 2015. Energy extraction potential from the Alderney Race. In *11th European Wave and Tidal Energy Conference*. Nantes, France, pp. 1–9.

Coles, D.S., Blunden, L.S. & Bahaj, A.S., 2017. Assessment of the energy extraction potential at tidal sites around the Channel Islands. *Energy, Elsevier*, 124, pp.171–186.

Coles, D.S., Blunden, L.S. & Bahaj, A.S., 2014. Experimental testing for spatially averaged numerical modelling of large marine current energy converter arrays. In *Asian Wave and Tidal Energy Conference*. Tokyo, Japan, pp. 1–4.

Coles, D.S., Blunden, L.S. & Bahaj, A.S., 2016. Experimental validation of the distributed drag method for simulating large marine current turbine arrays using porous fences. *International Journal of Marine Energy, Elsevier*, 16(16), pp.298–316.

Crafoord, C., 1979. Interaction in limited arrays of windmills. In *International Symposium on Wind Energy Systems*. Netherlands, pp. 169–171.

Cruise, J., Sherif, M. & Singh, V., 2007. *Elementary hydralics*, Toronto, Ont., Thomson/Nelson.

Cui, J., Patel, V.C. & Lin, C.-L., 2003. Large-eddy simulation of turbulent flow in a channel with rib roughness. *International Journal of Heat and Fluid Flow*, 24(3), pp.372–388.

Culley, D.M., Funke, S.W., Kramer, S.C. & Piggott, M.D., 2016. Integration of cost modelling within the micro-siting design optimisation of tidal turbine arrays. *Renewable Energy, Elsevier*, 85, pp.215–227.

D.T.Pugh, 1996. *Tides, Surges and Mean Sea-Level* 1st ed., John Wiley & Sons, pp. 59.

Davies, A.M., Hall, P., Howarth, M.J., Knight, P.J. & Player, R.J., 2004. Tidal currents, energy flux and bottom boundary layer thickness in the Clyde Sea and North Channel of the Irish Sea. *Ocean Dynamics*, 54(2), pp.108–125.

Draper, S., Adcock, T.A., Borthwick, A.G.L. & Houlsby, G.T., 2014. Estimate of the tidal stream power resource of the Pentland Firth. *Renewable Energy, Elsevier*, 63, pp.650–657.

DTI, 2008. *Atlas of UK marine renewable energy resources*, Technical report no. R1106. Available at: www.renewables-atlas.info.

DTI, 2007. http://www.renewables-atlas.info/. *[Date Accessed: 25/12/2014]*.

Egbert, G. & Erofeeva, L., 2014. http://volkov.oce.orst.edu/tides/atlas.html. *OSU Tidal Data Inversion, [Date Accessed: 07/06/2014]*.

Egbert, G.D., Erofeeva, S.Y. & Ray, R.D., 2010. Assimilation of altimetry data for nonlinear shallow-water tides: Quarter-diurnal tides of the Northwest European Shelf. *Continental Shelf Research, Elsevier*, 30(6), pp.668–679.

Elliott, A.J., 2002. The Boundary Layer Character of Tidal Currents in the Eastern Irish Sea. *Estuarine, Coastal and Shelf Science, Elsevier*, 55(3), pp.465–480.

Emami, A. & Noghreh, P., 2010. New approach on optimization in placement of wind turbines within wind farm by genetic algorithms. *Renewable Energy, Elsevier*, 35(7), pp.1559–1564.

Energy Technology Support Unit, 1993. *Tidal Stream Energy Review*, Technical report ETSU-T/05/00155/REP, Harwell Laboratory.

Environmental Change Institute, 2005. *Variability of UK marine resources*, pp. 12-13, Report comissioned by the Carbon Trust.

European Commission, 1996. *The exploitation of tidal marine currents, Wave Energy, Project results*, Technical Report EUR 16683 EN.

FAB Link Limited, 2016. FAB France - Alderney - Britain. Available at: http://www.fablink.net/ [Accessed October 15, 2015].

Florens, E., Eiff, O. & Moulin, F., 2013. Defining the roughness sublayer and its turbulence statistics. *Experiments in Fluids*, 54(4).

Frandsen, S., 1992. On the wind speed reduction in the center of large clusters of wind turbines. *Journal of Wind Engineering and Industrial Aerodynamics, Elsevier*, 39(1–3), pp.251–265.

Frandsen, S., Barthelmie, R., Pryor, S., Rathmann, O. & Larsen, S., 2006. Analytical modelling of wind speed deficit in large offshore wind farms. *Wind Energy, John Wiley and Sons*, 9, pp.39–53.

Funke, S.W., Kramer, S.C. & Piggott, M.D., 2015. Design optimisation and resource assessment for tidal-stream renewable energy farms using a new continuous turbine approach. *Renewable Energy*, 99, pp.1046–1061. Available at: http://arxiv.org/abs/1507.05795.

Garrett, C. & Cummins, P., 2004. Generating Power from Tidal Currents. *Journal of Waterway, Port, Coastal and Ocean Engineering, ASCE*, 130(June), pp.114–118.

Garrett, C. & Cummins, P., 2005. The power potential of tidal currents in channels. *Proceedings of the Royal Society A, Royal Society*, 461, pp.2563–2572.

Green, M.O., Hewitt, J.E. & Thrush, S.F., 1998. Seabed drag coefficient over natural beds of horse mussels (Atrina zelandica). *Journal of Marine Research, Yale University Press*, 56(3), pp.613–637.

Hardwick, J., Ashton, I. & Johanning, L., 2015. Field characterisation of currents and near surface eddies in the Pentland Firth. In *4th Oxford Tidal Energy Workshop*. Oxford, UK.

Harrison, M.E., 2008. Comparisons of a Large Tidal Turbine Array Using the Boundary Layer and Field Wake Interaction Models. In *2nd International Conference on Ocean Energy (ICOE 2008)*. Brest, France, pp. 1–9.

Haynes, S.G., 2015. *The Effects of Array Installation upon the Morphology of a Headland Associated Linear Sandbank*, pp 49-55, PhD: Transfer report, University of Southampton, UK.

Haynes, S.G., Blunden, L.S. & Bahaj, A., 2013. *Feasability study of the impacts of a proposed tidal array installation in Alderney South Banks - Final Report*, University of Southampton, UK.

Heathershaw, A.D., 1981. Comparisons of measured and predicted sediment transport rates in tidal currents. *Marine Geology, Elsevier*, 42(1–4), pp.75–104.

Hicks, S.D., 2000. *Tide and current glossary*, U.S. Department of Commerce, National Oceanic and Atmospheric Administration (NOAA), National Ocean Services, Center for Operational Oceanographic Products and Services, pp. 6.

International Panel on Climate Change, 2014. *Climate Change 2014 Mitigation of Climate Change*, IPCC, Fifth Assessment Report.

IT Power, 2011. *Tidal Power for Jersey the Next Steps*, Technical Report ITP/UKP1091.

Jean-Michel Hervouet, 2007. *Hydrodynamics of Free Surface Flows modelling with the finite element method*, Wiley, pp. 89-90.

Jensen, N.O., 1983. *A Note on Wind Generator Interaction*, Riso National Laboratory, Technical report, Ris-M-2411.

Kapoor, D.C., 1981. General bathymetric chart of the oceans (GEBCO). *Marine Geodesy, Taylor and Francis*, 5(1), pp.73–80.

Karsten, R., Swan, A. & Culina, J., 2012. Assessment of arrays of in-stream tidal turbines in the Bay of Fundy. *Proceedings of the Royal Society A, Royal Society*, 371, pp.189–203.

Karsten, R.H., McMillan, J.M., Lickley, M.J. & Haynes, R.D., 2008. Assessment of tidal current energy in the Minas Passage, Bay of Fundy. *Proceedings of the Institution of Mechanical Engineers, Part A: Journal of Power and Energy, Sage*, 222(5), pp.493–507.

Katic, I., Højstrup, J. & Jensen, N.O., 1986. A Simple Model for Cluster Efficiency. In *European Wind Energy Conference and Exhibition*. Rome, Italy, pp. 407–410.

Keogh, B., Myers, L. & Bahaj, A., 2014. Tidal stream turbine performance with changes in channel size and geometry. In *Grand Renewable Energy 2014*. Tokyo, Japan, pp. 1–4.

Knopf, B., Pahle, M., Kondziellab, H. & Joas, F., 2012. *Germany's Nuclear Phase-Out: Impacts on Electricity Prices, CO2 Emissions and on Europe*, Potsdam Institute for Climate Impact Research (PIK), pp. 9.

Krogstad, P.-Å., Antonia, R. a. & Browne, L.W.B., 1992. Comparison between rough- and smooth-wall turbulent boundary layers. *Journal of Fluid Mechanics, Clambridge University Press*, 245, p.599.

Kusiak, A. & Song, Z., 2010. Design of wind farm layout for maximum wind energy capture. *Renewable Energy, Elsevier*, 35(1), pp.685–694.

Lang, P., 2010. *TELEMAC modelling system User Manual*, EDF- R&D, pp. 33-34.

Lang, P. & Desombre, J., 2013. *TELEMAC-2D Software Operating Manual*, Release 6.2.

Legrand, C., 2009. *Assessment of Tidal Energy Resource Marine Renewable Energy Guides*, EMEC Report.

London Array, 2016. Renewable Energy Record Achieved at London Array. Available at: http://www.londonarray.com/project/renewable-energy-record-achieved-at-london-array/ [Accessed May 4, 2016].

Marmidis, G., Lazarou, S. & Pyrgioti, E., 2008. Optimal placement of wind turbines in a wind park using Monte Carlo simulation. *Renewable Energy, Elsevier*, 33(7), pp.1455–1460.

Marriott, M.J. & Jayaratne, R., 2010. Hydraulic roughness - links between Manning's coefficient, Nikuradse's equivelant sand roughness and bed grain size. In *5th Annual Advances in Computing and Technology Conference*. Kochi, India, pp. 27–32.

Milborrow, D.J., 1980. The performance of arrays of wind turbines. *Journal of Wind Engineering and Industrial Aerodynamics, Elsevier*, 5(3–4), pp.403–430.

Milne, I.A., Sharma, R.N., Flay, R.G.J., Bickerton, S. & A, P.T.R.S., 2013. Characteristics of the turbulence in the flow at a tidal stream power site. *Proceedings of the Royal Society, Royal Society*, (371), pp.1–14.

Milne, I. & Sharma, R., 2011. Characteristics of the Onset Flow Turbulence at a Tidal-Stream Power Site. In *Proceedings of the 9th EWTEC Conference*. Upsala, Sweden.

Moore, D.J., 1979. Depletion of available wind power by a large network of wind generators. In *2nd International Conference on Future Energy Concepts*. London, pp. 302–305.

Myers, L. & Bahaj, A.S., 2005. Simulated electrical power potential harnessed by marine current turbine arrays in the Alderney Race. *Renewable Energy, Elsevier*, 30(11), pp.1713–1731.

Myers, L.E. & Bahaj, A.S., 2012. An experimental investigation simulating flow effects in first generation marine current energy converter arrays. *Renewable Energy, Elsevier*, 37(1), pp.28–36.

Myers, L.E. & Bahaj, A.S., 2010. Experimental analysis of the flow field around horizontal axis tidal turbines by use of scale mesh disk rotor simulators. *Ocean Engineering, Elsevier*, 37(2–3), pp.218–227.

Myers, L.E., Bahaj, A.S., Rawlinson-Smith, R.I. & Thomson, M., 2008. The Effect of Boundary Proximity Upon the Wake Structure of Horizontal Axis Marine Current Turbines. In *Proceedings of the ASME 27th International Conference on Offshore Mechanics and Arctic Engineering OMAE2008*. Estoril, Portugal: Asme, pp. 709–719.

Nauclér, C.S., 2016. *FAB France Alderney Britain Interconnector, Project Summary*, FAB Link Ltd.

Newman, B.G., 1977. The spacing of wind turbines in large arrays. *Energy Conversion, Elsevier*, 16(4), pp.169–171.

Nikuradse, J., 1933. *Stomungsgesetze in rauhenRohren, Forshhungsshefte* VDI: NACA.,

Offshore Renewable Energy Catapult, 2015. *Wave and Tidal Energy Yield Uncertainty*, PN000083-SRT-004.

Okamoto, S., Seo, S., Nakaso, K. & Kawai, I., 1993. Turbulent Shear Flow and Heat Transfer Over the Repeated Two-Dimensional Square Ribs on Ground Plane. *Journal of Fluid Mechanics, Cambridge University Press*, 115, pp.7–16.

Owen, A., 2005. *Tidal Stream Resource Assessment for the Channel Islands Area*, Report for Black and Veatch Consiultimg Ltd.

Pawlowicz, R., Beardsley, B. & Lentz, S., 2002. Classical tidal harmonic analysis including werror estimates in MATLAB using T_TIDE. *Computers and Geosciences, Elsevier*, 28(8), pp.929–937.

Pérez-Ortiz, A., Pescatore, J. & Bryden, I., 2013. A Systematic Approach to Undertake Tidal Energy Resource Assessment with Telemac-2D. In *EWTEC 2013*. Aalborg, Denmark.

Perry, A.E., Schofield, W.H. & Joubert, P.N., 1969. Rough wall turbulent boundary layers. *Journal of Fluid Mechanics*, 37(2), pp.383–413.

Plew, D.R. & Stevens, C.L., 2013. Numerical modelling of the effect of turbines on currents in a tidal channel – Tory Channel, New Zealand. *Renewable Energy, Elsevier*, 57, pp.269–282.

Race Tidal, 2014. *Race Tidal Alderney*, http://www.openhydro.com/download/OPENHYDRO-RACE-TIDAL-PROJECT-FACT-SHEET.pdf. Available at: http://www.openhydro.com/download/OPENHYDRO-RACE-TIDAL-PROJECT-FACT-SHEET.pdf.

Rannacher, R., 1999. *Finite Element Methods for the Incompressible Navier-Stokes Equations*, University of Heidelberg, University of Heidelberg, Report, INF 293/294, D-69120.

Raupach, M.R., Antonia, R.A. & Rajagopalan, S., 1991. Rough-wall turbulent boundary layers.

Applied Mechanics Reviews, ASME, 44(1).

Saavedra-Moreno, B., Salcedo-Sanz, S., Paniagua-Tineo, A., Prieto, L. & Portilla-Figueras, A., 2011. Seeding evolutionary algorithms with heuristics for optimal wind turbines positioning in wind farms. *Renewable Energy, Elsevier*, 36(11), pp.2838–2844.

Soulsby, 1997. *Dynamics of Marine Sands* 1st ed., pp. 47-48: Thomas Telford.

Soulsby, R.L.D., 1983. The bottom boundary layer of shelf seas. In B.Johns, ed. *Physical Oceanography of Coastal and Shelf Seas*. Elsevier, pp. 189–266.

Sternberg, R.W., 1968. Friction factors in tidal channels with differing bed roughness. *Marine Geology, Elsevier*, 6(3), pp.243–260.

Sutherland, G., Foreman, M. & Garrett, C., 2007. Tidal current energy assessment for Johnstone Strait, Vancouver Island. *Proceedings of IMechE Part A: Journal of Power and Energy, Sage*, 221(2), pp.147–157.

Swinbank, W.C., 1974. The geostrophic drag coefficient. *Boundary-Layer Meteorology, Springer*, 7(1), pp.125–127.

Tassi, P., 2014. *Sisyphe v6.3 User's Manual*, EDF SA 2014.

TCarta, 2014. http://www.tcarta.com/home/. *[Date Accessed: 16/06/2014]*.

Templin, R.J., 1974. *An estimate of the interaction of windmills in widespread arrays*, Laboratory technical report LTR-LA-171, National Aeronautical Establishment, Ottowa, Canada.

Thiebot, J., Bailly du Bois, P. & Guillou, S., 2015. Numerical modeling of the effect of tidal stream turbines on the hydrodynamics and the sediment transport - Application to the Alderney Race (Raz Blanchard), France. *Renewable Energy, Elsevier*, 75, pp.356–365.

Thom, A.S., 1971. Momentum absorption by vegetation. *Quarterly journal of the Royal Meteorological Society, Wiley*, 97, pp.414–428.

Thomson, J., Polagye, B., Durgesh, V. & Richmond, M.C., 2012. Measurements of turbulence at two tidal energy sites in Puget Sound, WA. *IEEE Journal of Oceanic Engineering, IEEE*, 37(3), pp.363–374.

Townsend, A., 1976. *The structure of turbulent shear flow* G. Batchelor & J. Miles, eds., Cambridge University Press, pp. 140.

Trembanis, A.C., Wright, L.D., Friedrichs, C.T., Green, M.O. & Hume, T., 2004. The effects of

spatially complex inner shelf roughness on boundary layer turbulence and current and wave friction: Tairua embayment, New Zealand. *Continental Shelf Research, Elsevier*, 24(13–14), pp.1549–1571.

Turner, N. & Owen, A., 2007. Development of a Tidal Turbine for Deployment in Areas with Slow Moving Tidal Flows. In *Proceedings of Oceans Conference 2007, IEEE*. Aberdeen, Scotland, pp. 1–3.

U.S. Energy Information Administration, 2014. *International Energy Outlook 2014: World Petroleum and Other Liquid Fuels With Projections to 2040 (IEO2014)*, Washington DC, USA.

UK Hydrographic Office, 2016. *Admiralty Tide Tables United Kingdom English Channel to River Humber (Including Isles of Scilly, Channel Islands and European Channel Ports)*, NP201A, Volume 1A.

Vennell, R., Funke, S.W., Draper, S., Stevens, C. & Divett, T., 2015. Designing large arrays of tidal turbines: A synthesis and review. *Renewable and Sustainable Energy Reviews, Elsevier*, 41, pp.454–472.

Vermeulen, P., Builtjes, P., Dekker, J. & Van Bueren, G.L., 1979. *An experimental study of the wake behind a full scale vertical axis wind turbine*, TNO-report, No. 79-06118.

Walters, R.A., Tarbotton, M.R. & Hiles, C.E., 2013. Estimation of tidal power potential. *Renewable Energy, Elsevier*, 51, pp.255–262.

Zhou Liu, 1999. *Sediment Transport*, Aalborg University publishing, pp. 8-10.

Appendix A Theory

A1. Tidal theory

The behaviour of the tides is influenced by physical phenomena at a vast range of scales, from the relative motion between the Earth, Moon and Sun that causes water motion in the deep oceans, the coastal scale where tides are affected by local topography and the turbine scale for which large arrays operate. This chapter gives an overview of tidal theory to explain how tides are predicted to characterise the environment into which large arrays will be placed, and its applications in numerical modelling.

A1.1 Earth-Moon system

The net force of attraction between the Earth and Moon is described by Newton's law of gravitation (D.T.Pugh 1996):

$$F_{e,m} = \frac{GM_eM_m}{R^2} \qquad 8.1$$

Where $F_{e,m}$=net force of attraction between the Earth and Moon, G=universal gravitational constant equal to 6.672 x 10^{-11} *N* m^2 kg^{-2}, M_e = mass of the Earth, M_m is the mass of the Moon and R =distance between the centre of mass of the Earth and Moon.

Figure 8.1 shows an illustration of the Earth-Moon system. The Earth and Moon revolve about a common point where the centre of mass of the Earth-Moon system is located (known as the barycentre), where the necessary acceleration of each body towards this point is produced by their mutual attraction. This point is labelled *CM* in Figure 8.1. For a particle at point A on the Earth's surface in Figure 2.1, the force it experiences towards the Moon is:

$$F_{A,m} = \frac{GM_AM_m}{(R - r_e)^2} \qquad 8.2$$

Where $F_{A,m}$ = net force of attraction between the particle A and the Moon, M_A=mass of particle at location *A* and r_e=radius of the Earth.

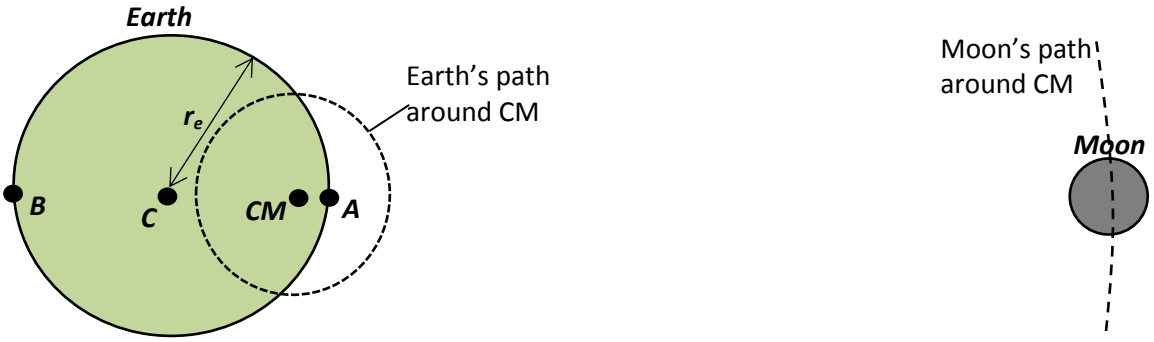

Figure 8.1 The Earth-Moon system showing the distances used to estimate the tide producing forces at different points on the Earth's surface.

The force required for the particle at location *A* with mass M_A to rotate around the centre of mass the Earth-Moon system is the same as any other particle on Earth, since all points follow the dotted path shown in Figure 8.1. This force is expressed for a particle C at the centre of the Earth as:

$$F_{A,CM} = F_{C,CM} = \frac{GM_C M_m}{R^2} \tag{8.3}$$

Where $F_{A,CM}$= Force required for the particle at location *A* with mass M_A to rotate around the centre of mass the Earth-Moon system, $F_{C,CM}$= Force required for the particle at location *C* with mass M_C to rotate around the centre of mass the Earth-Moon system and R=distance between the centre of mass of the Earth and the Moon. The difference between these two forces creates the tide producing force at location *A*:

$$F_{A,m} - F_{A,CM} = \frac{GM_A M_m}{R^2}\left[\frac{1}{\left(1-\frac{r_e}{R}\right)^2} - 1\right] \tag{8.4}$$

Which simplifies assuming the radius of the Erath is significantly smaller than the distance between the centre of mass of the Earth and the Moon to give the net force towards the Moon:

$$F_{A,m} - F_{A,CM} = \frac{2GM_A M_m r_e}{R^3} \tag{8.5}$$

Similarly at point *B* beyond the Earths centre, the net force is of the same magnitude but with opposite sign.

The force that acts to move water is the tractive force, defined as the force acting tangential to the Earth's surface, which is the horizontal component of the tide producing force. This is half the magnitude at points *A* and *B* in Figure 8.1, creating tidal bulges aligned with the equatorial plane through the Earth and Moons centres. As the Earth completes one full rotation in approximately 24 hours, this creates semi diurnal tides at point *S* (Figure 8.2). When the Moon is outside of the equatorial plane, diurnal tides occur, for example at point *T*.

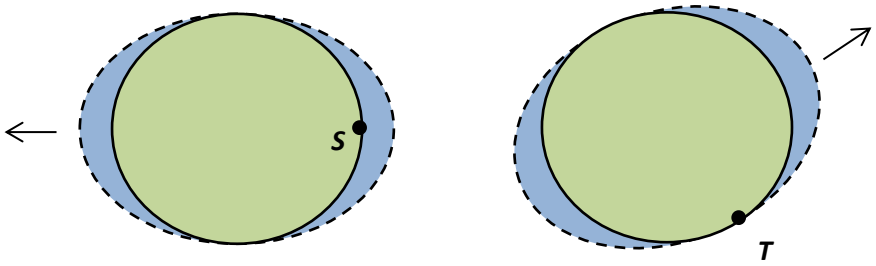

Figure 8.2 Tidal bulges on Earth caused by the orientation of the Moon's equatorial plane. Arrows show the direction of the Moon.

Variation in the tide producing force occurs for multiple reasons, for example the orbit of the Moon around the Earth is not circular but elliptical, with the Earth not at the centre of this ellipse. Hence there is a variation in distance between the Earth and Moon over time. Whilst it is assumed the Moon's orbit around the Earth is circular, in reality it is elliptical and the distance between the two bodies varies between 356,400km and 406,700km at the extreme perigees, (a variation of approximately 12%) however this simplification allows us to assume that the centrifugal force acting on the Earth is constant at all points.

A1.2 Earth-Moon system

The Sun also applies a tide producing force on the Earth and is dependent on the gravitational force it exerts on the Earth. The mass of the Sun is approximately 332,946 times greater than that of the Moon, however the distance between the Earth and Sun is approximately 360 times further (than between the Earth and Moon). The magnitude of the tide producing force from the Sun is approximately 0.46 times that of the Moon (Table 8.1). As with the orbit of the Moon around the

Earth, the Earth's orbit around the Sun is elliptical, however the radius of orbit only varies by approximately 4%.

Table 8.1 Characteristics of tidal components

Tidal component	Notation	Period (solar hours)	Coefficient ratio (%)
Semi diurnal:			
Principal lunar	M_2	12.42	100
Principal solar	S_2	12	46.6
Larger lunar elliptic	N_2	12.66	19.2
Luni-solar	K_2	11.97	12.1
Diurnal:			
Luni-solar	K_1	23.93	58.4
Principal lunar	O_1	25.82	41.5
Principal solar	P_1	24.07	19.4
Longer period:			
Lunar fortnightly	M_f	327.86	17.2
Lunar fort monthly	M_m	661.30	9.1

A1.3 Interaction between systems

The relative motion of the Sun, Earth and Moon create constantly varying tide producing forces that combine to produce varying tides. As the Moon orbits the Earth, positive/negative interaction between the tide producing forces of the Sun and Moon causes different tidal ranges, defined as the elevation difference between succeeding high and low tide. When the tidal range is greater than average, spring tides occur, as when the Sun and Moon are in conjunction or in opposition, i.e. they are aligned with the Earth so the tide producing forces from the Sun and Moon reinforce each other. When this occurs, the Moon is said to be in syzygy. Conversely, when the Moon is at first or third quarter relative to the Earth and Sun, the tide producing forces partially cancel each other out, causing the tidal range to be lower than average, also known as neap tides. As the Moon orbits the Earth, the Earth rotates on its axis so that the time taken for the Moon to complete one full rotation relative to a point on the Earth is 24 hours and 50 minutes, making the lunar day slightly longer than a day as we know it. The interval between consecutive high (and low) tides is approximately 12 hours 25 minutes and the interval between high and low tide is approximately 6 hours 12 minutes for semi-diurnal tides.

A1.4 Harmonic analysis

It is predominantly the relative cyclic motions of the Earth, Moon and Sun that causes tidal dynamics in the deep ocean. Such motions include the Moon's orbit around the Earth and the obliquity (tilt angle) of the Earth's equator. The effect of each cyclic motion gives rise to a partial tide, also known as a tidal constituent, which defines the influence of that specific motion on the overall tidal behaviour such as free surface elevation at a specific location with respect to time. Summing each partial tide together gives a true representation of the real tidal behaviour. As many as 390 tidal constituents exist, however there are several principal constituents that contribute the most significant proportion to the overall tide, based on the magnitude of their amplitudes as shown in Table 8.1, where the coefficient ratio describes amplitudes as a percentage of the M_2 amplitude.

The period or angular frequency of each tidal constituent describes the time between successive high elevation levels. Semi diurnal tides are denoted with subscript 2 and have two cycles per day and a tidal range that typically increases and decreases cyclically over a 14 day period, where the maximum (spring tides) ranges occur a few days after both new and full moons, when the Earth, Moon and Sun are in syzergy. The minimum ranges (neap tides) occur shortly after the first and last quarters (lunar quadrature). Diurnal tides have one cycle per day and so are denoted with subscript 1.

Tidal harmonic analysis defines the tidal elevation at a point as:

$$z = \sum_{j=1}^{N} A_j f_j cos\left(\omega_j t + V_j - G_j + u_j\right) \qquad 8.6$$

Where z = free surface elevation, j= index representing tidal constituent 1,2,…N where N=total number of tidal constituents, A = amplitude of tidal constituent , f=nodal amplitude correction factor, ω=angular speed of tidal constituent, t = time given in fractional hours, V=equilibrium phase, G=constituent phase and u= nodal phase correction factor.

The amplitude gives half the tidal range of the tidal constituent. The phase is the phase lag of the observed tidal constituent relative to the theoretical equilibrium tide, which is a hypothetical tide caused due to the tide producing forces under equilibrium theory (also known as the gravitational tide). Equilibrium theory is a model that assumes the water covering the Earth instantly responds to the tide producing forces of the Moon and Sun to form a surface of equilibrium. The model disregards friction, inertia and the irregular distribution of land mass.

Nodal correction factors are used to account for the variation about the plane of motion of the Moon orbiting the Earth. This variation is approximately 0.053 degrees per mean solar day and completes a revolution every 18.6 years. The angular speed of a constituent is the rate of change of phase that can be calculated based on five basic astronomical speeds, namely the rotation of Earth on its axis with respect to the Sun (15 degrees/hour), the rotation of Earth about the Sun, (0.4106864 degrees/hour), the rotation of the Moon about Earth (0.54901653 degrees/hour), the precession of the Moon's perigee, where perigee is the closest distance the Moon gets to the Earth (0.00464183 degrees/hour) and the precession of the plane of the Moon's orbit (-0.0220641 degrees/hour).

The equilibrium phase (also called the equilibrium argument or astronomical argument) is the theoretical phase of a tidal constituent of the equilibrium tide. It can be viewed as the angular position of a fictitious star relative to a longitude at time t, where the fictitious star travels around the equator with the same angular speed as the corresponding constituent's angular speed, so is the phase offset to bring you to time t. Put another way, it is the phase of the tidal potential (tidal bulge) at Greenwich longitude at a given time, t. If the equilibrium phase is zero, this means the tidal potential is a maximum at Greenwich longitude at time t. Each constituent has a different equilibrium phase that varies in time but not space.

A1.5 Tidal currents

Tidal currents have the same periodicities as vertical oscillations in surface elevation. Figure 8.3 shows the variation in flow velocity and direction at a point, described with a tidal ellipse that represents a rotary current with radial vectors to show magnitude and phase. The inclination is the direction of the tide at maximum major axis amplitude. A cycle is completed in half a day for semi-diurnal tides or a whole day for diurnal tides (Hicks 2000).

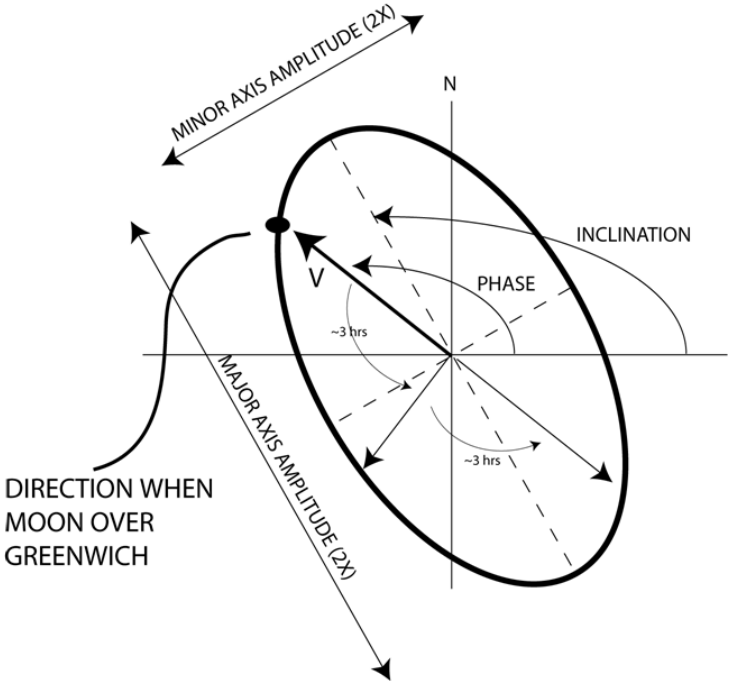

Figure 8.3 Semi diurnal tidal ellipse schematic.

A1.6 Coriolis

Coriolis causes objects in motion such as bodies of water to deflect their path from their original direction of motion in a stationary reference frame due to the rotation of the Earth around its axis. The Coriolis Effect deflects currents clockwise in the northern hemisphere and anticlockwise in the southern hemisphere when viewed from the original direction of movement due to the rotation of the Earth. Bodies moving either directly east or directly west along the equator (i.e. at 0 degrees latitude) do not experience the Coriolis Effect. The effect of the Coriolis Effect can be defined using the Rossby number, which is the ratio of inertial to Coriolis forces;

$$Ro = \frac{U}{2L\Omega sin\varphi} \qquad 8.7$$

Where Ro = Rossby number, U = streamwise velocity, L= characteristic length scale, Ω= angular speed of rotation of the Earth and φ = latitude. When the Rossby number is small, the system is heavily influenced by the Coriolis Effect because the Coriolis force is of the same or higher magnitude with respect to the inertial force. At the scale of tidal turbine arrays, a typical flow travelling at 1m/s would travel over 11 km in a quarter of the period of the principal M_2 semi-diurnal tide, giving a Rossby number of approximately 0.01, indicating that the Coriolis Effect has a dominating effect in changing the direction of motion of a body of water, so must be considered with respect to energetic flows for energy extraction.

A1.7 Shallow water dynamics

Shallow water constituents describe the effect of near shore physical characteristics such as bottom friction, local topography and coastal configuration on tidal harmonics in waters where elevation is no longer insignificant compared to depth. Variation in bottom topography and irregular coastlines causes tidal currents to follow coastal contours, where pressure gradients across the direction of the streamlines cause changes in direction of the current flow. Assuming the sea surface well away from the coast to be level, the effect at a headland will be a reduced elevation close to the headland and increased elevations at the bays in comparison to those offshore.

Drag due to bottom friction creates an opposing force that removes energy from tidal flows causing a reduction in current magnitude in the benthic boundary layer. The relationship between drag and flow rate is of the form:

$$\tau_b = -C_b \rho Q|Q| \qquad 8.8$$

Where τ_b= bed shear stress, C_b = bed drag coefficient, ρ =water density and Q = volume flux. Energy loss is proportional to the square of current velocity, so more energy is lost at times of maximum flood and ebb. This results in the generation of a higher harmonic shallow water constituent, or overtide, M_6 with a period one third that of M_2. Another overtide occurs because friction takes greater effect in shallower water, so slows down a trough more than a crest, which gives rise to the asymmetric shallow water constituent M_4, with a period of one half that of M_2.

This relationship between energy loss and velocity can also lead to 'compound tides' due to the interaction of different parent tides. For example, tidal constituents M_2 and N_2 go in and out of phase every 27.6 days. Energy dissipation from bed drag is proportional to the square of velocity, so the increased energy loss when M_2 and N_2 are in phase is greater than the decreased energy loss when they are out of phase.

A1.8 Turbulent boundary layer flow

The power performance of tidel turbines is dictated by the velocity and turbulence statistics incident on the turbine (Blackmore et al. 2013; Blackmore et al. 2014). It is therefore important to characterise the velocity and turbulence distribution in the vertical plane, and their dependency on the roughness geometry of the boundary surface.

Equation 8.9 is known as the law of the wall and describes the mean velocity distribution in the vertical plane for turbulent flows over flat boundary surfaces such as the sea bed. The velocity is a

function of the shear stress at the boundary surface and the fluid density, which are both contained within the friction velocity term in Equation 8.9 (Cebeci & Cousteix 1999). The friction velocity is given by Equation 2.11, and is used to express the shear stress in the units of velocity. The shear stress is transmitted to the boundary surface by a combination of tangential viscous stresses and normal pressures generated at the boundary surface (Townsend 1976). The velocity is also a function of the vertical distance from the bed and the dynamic viscosity (Bradshaw & Huang 1941).

$$U(z) = \frac{u_*}{\kappa} ln\left(\frac{z}{z_0}\right) \tag{8.9}$$

$$u_* = \sqrt{\frac{\tau}{\rho}} \tag{8.10}$$

Where U =streamwise velocity, u_*=friction velocity, κ=Von Karman constant, z=vertical distance above the bounding surface, z_0=roughness length, τ= shear stress and ρ =the fluid density. The roughness length is the elevation above the bed at which the velocity theoretically becomes zero based on the logarithmic flow distribution (Brown et al. 1993). This is illustrated in

Figure 8.4. The magnitude of the bed shear stress and roughness length are influenced by the bed roughness geometry of the boundary surface, such as the physical roughness element height (Soulsby 1983) and roughness element spacing (Perry et al. 1969; Raupach et al. 1991).

The roughness sub layer typically extends from the boundary surface to between two and five physical roughness heights above the boundary surface (Florens et al. 2013). The velocity and turbulence within the roughness sub layer are also influenced by the length scales of individual roughness elements, such as the physical roughness height and roughness element spacing. Measurements of the mean velocity profile within the roughness sub-layer for flow over bluff bodies such as cubes have been fitted to an empirical exponential profile, making the law of the wall invalid within the roughness sub layer. It should be noted that the accuracy of experimental velocity measurements is challenging within close proximity to the boundary surface (Florens et al. 2013) so the flow in this region is difficult to characterise.

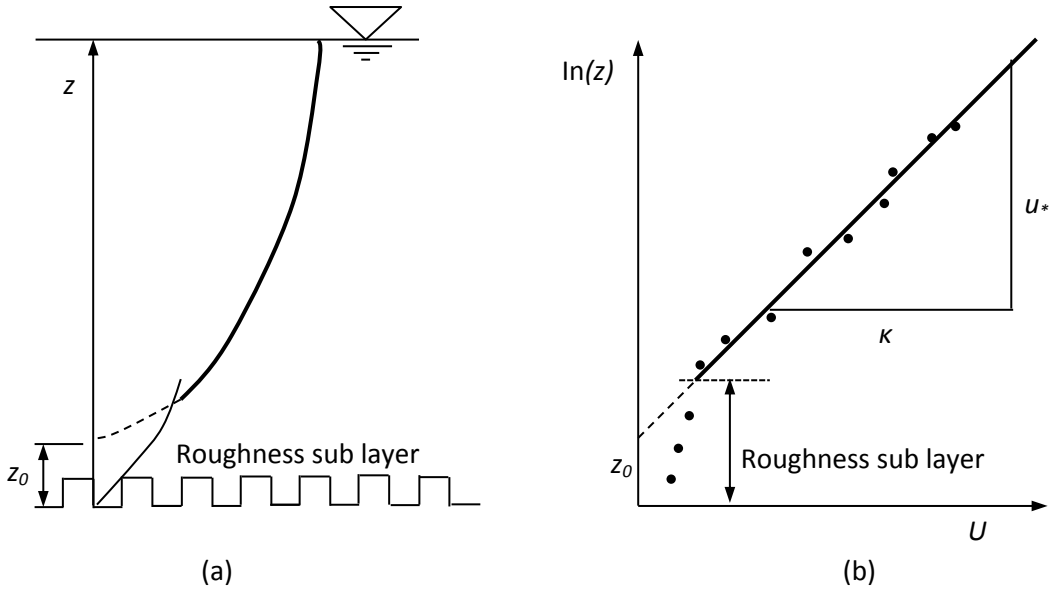

Figure 8.4 (a) Illustration of turbulent boundary layer flow over a rough surface, the law of the wall is valid over the bold velocity profile (b) Semi-logarithmic velocity profile illustrating how friction velocity and roughness length can be derived.

For tidal flows the law of the wall has been shown to extend up to the free surface (Sternberg 1968). Assuming the roughness sub layer thickness is relatively small in comparison to the depth, the law of the wall (Equation 2.10) is a good approximation of the velocity throughout the whole water column. For any logarithmic profile distributed over the depth, the depth averaged velocity occurs at a depth above the boundary surface of z/h=0.4 (Raupach et al. 1991).
Another important use of the law of the wall is to estimate the bed shear stress and roughness length from measured velocity data. This is carried out by plotting the velocity distribution in the vertical plane (obtained experimentally) using a semi logarithmic plot.

Figure 8.4b shows a semi-logarithmic plot of velocity data, where the law of the wall applies over the linear region of velocity data points shown by the bold filled line of best fit. The roughness height is the theoretical intercept of the linear section (shown by the dashed line) with the y-axis and the friction velocity can be found from the gradient of the linear section. The roughness sub layer thickness is also shown, which extends to an elevation above the boundary surface where velocity data points no longer fit the linear trend of the law of the wall. In Chapter 5 this method is used to quantify the roughness length and friction velocity of flows within flume experiments to make comparisons with measurements at offshore tidal sites from literature.

The roughness Reynolds number defined by Equation 8.11 gives an approximate measure for the influence the surface roughness has in augmenting the turbulence intensity of the flow.

$$Re_r = \frac{u_* l_r}{\mu}$$

8.11

Where Re_r=Roughness Reynolds number, u_*=friction velocity, l_r=physical roughness height and μ=dynamic viscosity. Tidal flows are in the hydraulically rough regime where the roughness Reynolds number exceeds 70 (Nikuradse 1933). In the hydraulically rough regime flow separation occurs off the roughness geometry to directly influence the turbulent properties of the bulk flow (Raupach et al. 1991).

For regular roughness element spacing, the ratio of the physical roughness height to the roughness element spacing, known as the pitch ratio, also influences the turbulent properties of the flow. For a pitch ratio less than 4 (known as d-type roughness), eddy separation is confined to the gaps between roughness elements so that the bulk flow 'rides' over the roughness elements, minimising the influence roughness elements have on the bulk flow velocity and turbulence (Cui et al. 2003). For a pitch ratio greater than 4 (known as k-type roughness) separation and reattachment occurs between roughness elements, causing larger eddies to shed off the leading edge of the roughness elements and emanate into the outer flow, enhancing ambient turbulence intensities (Perry et al. 1969). This is an area of ongoing research and findings from literature. K-type roughness is implemented in flume experiments to augment turbulence intensities, friction velocity and roughness length to magnitudes more representative of tidal flows.

A2. Numerical modelling of tidal flows

The shallow water equations are a set of partial differential equations used in 2D hydrodynamic numerical modelling to describe fluid flow for cases where vertical dynamics can be neglected when compared with horizontal effects, hence the term 'shallow'. They are derived from the conservation of mass, momentum and energy.

A2.1 Mass continuity

Mass continuity requires that for an incompressible fluid, the mass flux into a control volume is equal to the mass flux out for the mass to remain constant as descried in Equation 8.12.

$$\frac{\partial U}{\partial x} + \frac{\partial V}{\partial y} + \frac{\partial W}{\partial z} = 0$$

8.12

Where U=streamwise velocity component, V=lateral velocity component, W=vertical velocity component.

A2.2 Momentum

The Navier-Stokes equations are used to describe fluid motion in 3 dimensions. They are derived from Newton's second law, which states that the acceleration of a body (such as the control volume) is directly proportional to the net force acting on it and inversely proportional to its mass:

$$F = ma$$

8.13

Where F=force acting on the control volume, m=mass of control volume, a=acceleration of the control volume. The forces acting on the control volume are the body forces caused by gravity, coriolis, centrifugal force and the tide producing force, and surface forces that act on the surfaces of the control volume such as viscous forces, pressure and surface tension).

The resultant net force per unit volume acting on the control volume in the *x* direction gives the x axis momentum equation shown by Equation 8.14:

$$\rho \frac{\partial U}{\partial t} = -\frac{\partial p}{\partial x} + \frac{\partial \tau_{xx}}{\partial x} + \frac{\partial \tau_{yx}}{\partial y} + \frac{\partial \tau_{zx}}{\partial z} + B_x$$

8.14

Where ρ=fluid density, U=streamwise velocity, t=time, p=pressure, τ_{xx}= normal stress on the x plane due to the force acting in the streamwise x direction, τ_{yx}=shear stress on the y plane due

to the force acting in the streamwise x direction, τ_{zx}= shear stress on the z plane due to the force acting in the streamwise x direction and B_x=body forces acting in the x direction. Similarly for the y and z axis:

$$\rho\frac{\partial V}{\partial t} = -\frac{\partial p}{\partial y} + \frac{\partial \tau_{xy}}{\partial x} + \frac{\partial \tau_{yy}}{\partial y} + \frac{\partial \tau_{zy}}{\partial z} + B_y$$

8.15

$$\rho\frac{\partial W}{\partial t} = -\frac{\partial p}{\partial z} + \frac{\partial \tau_{xz}}{\partial x} + \frac{\partial \tau_{yz}}{\partial y} + \frac{\partial \tau_{zz}}{\partial z} + B_z$$

8.16

Where V=lateral velocitycomponent, B_y= body forces acting in the y direction, W=vertical velocity component and B_z= body forces acting in the z direction. Also note that shear stresses are symmetric, i.e. τ_{xy}=τ_{yx}, τ_{xz}=τ_{zx} and τ_{yz}=τ_{zy}.

A2.3 Navier-Stokes equations

Assuming the flow is isothermal, the dynamic and kinematic viscosities remain constant. Additionally, for an incompressible Newtonian fluid the stress tensor is linearly proportional to the strain rate. These assumptions lead to the nine components of the viscous stress tensor given by Equation 8.17.

$$\begin{pmatrix} \tau_{xx} & \tau_{xy} & \tau_{xz} \\ \tau_{yx} & \tau_{yy} & \tau_{yz} \\ \tau_{zx} & \tau_{zy} & \tau_{zz} \end{pmatrix} = \begin{pmatrix} 2\mu\frac{\partial U}{\partial x} & \mu\left(\frac{\partial U}{\partial y} + \frac{\partial V}{\partial x}\right) & \mu\left(\frac{\partial U}{\partial z} + \frac{\partial w}{\partial x}\right) \\ \mu\left(\frac{\partial V}{\partial x} + \frac{\partial U}{\partial y}\right) & 2\mu\frac{\partial V}{\partial y} & \mu\left(\frac{\partial V}{\partial z} + \frac{\partial W}{\partial y}\right) \\ \mu\left(\frac{\partial W}{\partial x} + \frac{\partial U}{\partial z}\right) & \mu\left(\frac{\partial W}{\partial y} + \frac{\partial V}{\partial z}\right) & 2\mu\frac{\partial W}{\partial z} \end{pmatrix}$$

8.17

Where μ=dynamic viscosity. Substituting Equation 8.14 into Equation 8.17 for the *x* axis gives:

$$F_x = -\frac{\partial p}{\partial x} + 2\mu\frac{\partial^2 U}{\partial x^2} + \mu\frac{\partial}{\partial y}\left(\frac{\partial V}{\partial x} + \frac{\partial U}{\partial y}\right) + \mu\frac{\partial}{\partial z}\left(\frac{\partial W}{\partial x} + \frac{\partial U}{\partial z}\right) + B_x$$

8.18

Where F_x=resultant force acting on the control volume in the x direction. Rearranging and simplifying using mass continuity gives:

$$\rho\frac{\partial U}{\partial t} = -\frac{\partial p}{\partial x} + \mu\left[\frac{\partial}{\partial x}\left(\frac{\partial U}{\partial x} + \frac{\partial V}{\partial y} + \frac{\partial W}{\partial z}\right) + \frac{\partial^2 U}{\partial x^2} + \frac{\partial^2 U}{\partial y^2} + \frac{\partial^2 U}{\partial z^2}\right] + B_x$$

$$= -\frac{\partial p}{\partial x} + \mu\left[\frac{\partial^2 U}{\partial x^2} + \frac{\partial^2 U}{\partial y^2} + \frac{\partial^2 U}{\partial z^2}\right] + B_x$$

8.19

Similarly for the y and z axis:

$$\rho\frac{\partial V}{\partial t} = -\frac{\partial p}{\partial y} + \mu\left[\frac{\partial^2 V}{\partial x^2} + \frac{\partial^2 V}{\partial y^2} + \frac{\partial^2 V}{\partial z^2}\right] + B_y$$

8.20

$$\rho\frac{\partial W}{\partial t} = -\frac{\partial p}{\partial z} + \mu\left[\frac{\partial^2 W}{\partial x^2} + \frac{\partial^2 W}{\partial y^2} + \frac{\partial^2 W}{\partial z^2}\right] + B_z$$

8.21

Which together along with the mass continuity equation give the Navier Stokes equations for incompressible flow. The Navier Stokes equations contain 4 unknowns (3 velocity components and pressure, so solutions to unsteady turbulent flows are virtually impossible due to the complex, non-linear nature of turbulence.

A2.4 Reynolds averaged Navier-Stokes equations

Time averaging of the Navier Stokes equation is undertaken to simulate turbulent flows, where the instantaneous velocity is decomposed into a time averaged term and fluctuating term given by:

$$U = \langle U\rangle + U'$$

8.22

Where $\langle U\rangle$=time averaged streamwise velocity and U'=fluctuation in streamwise velocity. Similarly for the lateral and vertical directions:

$$V = \langle V\rangle + V'$$

8.23

$$W = \langle W\rangle + W'$$

8.24

The Reynolds Averaged Navier Stokes (RANS) equations time average the Navier Stokes equations (Equations 8.19 - 8.21) with the inclusion of the decomposed velocity components to give:

$$\rho\frac{\partial U}{\partial t} = -\frac{\partial p}{\partial x} + \mu\nabla^2\langle U\rangle + B_x - \left[\frac{\partial\langle U'^2\rangle}{\partial x} + \frac{\partial\langle U'V'\rangle}{\partial y} - \frac{\partial\langle U'W'\rangle}{\partial z}\right]$$

8.25

$$\rho\frac{\partial V}{\partial t} = -\frac{\partial p}{\partial y} + \mu\nabla^2\langle V\rangle + B_y - \left[\frac{\partial\langle U'V'\rangle}{\partial x} + \frac{\partial\langle V'^2\rangle}{\partial y} - \frac{\partial\langle U'W'\rangle}{\partial z}\right]$$

8.26

$$\rho\frac{\partial W}{\partial t} = -\frac{\partial p}{\partial z} + \mu\nabla^2\langle W\rangle + B_z - \left[\frac{\partial\langle U'W'\rangle}{\partial x} + \frac{\partial\langle V'W'\rangle}{\partial y} - \frac{\partial\langle W'^2\rangle}{\partial z}\right]$$

8.27

The bracketed terms on the right hand side consist of Reynolds stresses that arise due to the eddy motion of fluid particles that cause momentum flux in/out of the control volume. The RANS equations are used along with a model for turbulence by numerical models to describe fluid dynamics.

A2.5 Shallow water equations

The basic two-dimensional unsteady open channel equations are derived by applying continuity and conservation of momentum in a similar way to the derivation of the Navier-Stokes equations, assuming flow is two-dimensional in the horizontal plane, hydrostatic pressure distribution and constant water density. The hydrostatic pressure is:

$$\frac{\partial p}{\partial z} = -\rho g$$

8.28

$$p = -g\rho\int_z^h dz + p_a$$

8.29

Where p=pressure, ρ=fluid density, g=acceleration due to gravity, h=depth and p_a=atmospheric pressure.

Assuming a constant water density in the vertical (z axis), the pressure gradient in the x and y axis is:

$$\frac{\partial p}{\partial x} = \rho g\frac{\partial S}{\partial x}$$

8.30

$$\frac{\partial p}{\partial y} = \rho g\frac{\partial S}{\partial y}$$

8.31

Where S=free surface slope. Shallow water flow is defined for flow where the wavelength is much greater than the depth so that vertical acceleration can be neglected (Equation 8.32) and streamwise and lateral velocities are independent of z, i.e (Equation 8.33 and 8.34):

$$\frac{\partial W}{\partial t} = 0 \tag{8.32}$$

$$\frac{\partial U}{\partial z} = 0 \tag{8.33}$$

$$\frac{\partial V}{\partial z} = 0 \tag{8.34}$$

Along with Equation 8.31, these simplify the mass and momentum equations, which in conservative form give the shallow water equations:

$$\frac{\partial}{\partial t}(h) + \frac{\partial}{\partial x}(hU) + \frac{\partial}{\partial t}(hV) = 0 \tag{8.35}$$

$$\frac{\partial}{\partial t}(hU) + \frac{\partial}{\partial x}\left(hU^2 + \frac{1}{2}gh^2\right) + \frac{\partial}{\partial y}(hUV) = -gh\frac{\partial B}{\partial x} \tag{8.36}$$

$$\frac{\partial}{\partial t}(hV) + \frac{\partial}{\partial x}(hUV) + \frac{\partial}{\partial y}\left(hV^2 + \frac{1}{2}gh^2\right) = -gh\frac{\partial B}{\partial y} \tag{8.37}$$

A2.6 Finite element method

The finite element method is a numerical technique for finding approximate solutions to the three velocity components and pressure (assuming isothermal flow) from the shallow water equations. The differential equations are converted into a variational form approximated by linear trial functions (Rannacher 1999) using techniques such as the method of characteristics, which converts the hyperbolic Partial Differential RANS equations into a set of ordinary differential equations, each with one unknown (Anderson 1995). The variables are approximated at each node through an iterative procedure on a typically unstructured grid generated to discretize the spatial domain into a grid of discrete points. The simulation is also discretized in time by definition of a time step.

A3. Experimental modelling of tidal flows

Manufacturing a full scale tidal turbine and deploying it offshore for testing comes at a significant cost for tidal stream turbine developers. Along with numerical modelling, scaled down experimental modelling can provide a cost effective intermediary step between concept design and full scale deployment to inform the design of full scale tidal stream turbines and the positioning of turbines within arrays. Theory is presented here that outlines the methods for scaling a physical model based on a full scale tidal stream turbine array.

A3.1 Scaling

In this description of scaling, a full scale tidal stream turbine is referred to as the prototype. Typically the prototype is scaled down to the experimental model (referred to as the model from now on). Models and prototypes can be scales in different ways.

Geometric similarity refers to shape. Geometric similarity exists if the ratio of all corresponding dimensions are equal. This ratio is known as the scale ratio and is defined by Equation 8.38.

$$s = \frac{L_M}{L_P} \tag{8.38}$$

Where s=scale ratio, L_M = model dimension and L_P = prototype dimension. Currently full scale tidal turbines have a diameter up to 20 m, whereas the typical diameter of a model turbine used in experimental tank testing is 0.8 m. In this case the scale factor is 0.04.

Kinematic similarity refers to fluid motion and requires dimensions and time scales at any two corresponding points between the prototype and model to be the same. For example the ratio of the velocities at the same corresponding point between the prototype and model. Kinematic similarity requires the shape of the streamlines at any two corresponding points to be the same in the model and prototype. For this to be true, geometric similarity must also be assured.

Dynamic similarity refers to the similarity of forces acting in two kinematially similar (and therefore geometrically similar) systems. For dynamic similarity the actions of the forces in the system, which accelerate, decelerate and maintain velocity must be the same. This means that the ratio of the gravitational, inertial and viscous forces must be the same, as demonstrated by Equation 8.39.

$$\frac{(F_g)_M}{(F_g)_P} = \frac{(F_I)_M}{(F_I)_P} = \frac{(F_v)_M}{(F_v)_P} = Constant$$

8.39

Where F_g, F_I and F_v are the gravitational, inertial and viscous forces respectively and subscript M and P refer to the model and prototype respectively.

In open channel sub critical flows, gravitational forces dominate over inertial and viscous forces (Cruise et al. 2007). In this case the ratio of the inertial to gravitational forces must be equal for the prototype and model to achieve dynamic similarity, as described in Equation 8.40 (Cengal & Cimbala 2006). This ratio is known as Froude similarity;

$$\left(\frac{U}{gh}\right)_M = \left(\frac{U}{gh}\right)_P$$

8.40

Where U= streamwise velocity, g =acceleration due to gravity, h=depth and subscript M and P refer to the model and prototype respectively.

For flow around submerged bodies such as tidal stream turbines, the flow is dominated by viscous forces, where the ratio of inertial to viscous forces is given by the Reynolds number, Re:

$$Re = \frac{\rho U L}{\mu}$$

8.41

Where ρ = fluid density, U= streamwise velocity, L= characteristic length scale and μ =dynamic viscosity. For comparison, velocities at typical offshore tidal sites reach 4 m/s whilst velocities in laboratory flumes are typically around 0.5 m/s. Using the turbine diameter as the characteristic length, full scale tidal turbines have a diameter of 20 m whilst experimental model turbines are typically 0.8 m in diameter. Therefore Reynolds similarity is not possible without changing the working fluid density or viscosity.

Appendix B English Channel Model calibration results

Table B1 and B2 summarise the tidal stream velocity validation results obtained from the Telemac model of the English Channel. These give a comparison between simulated results using a range of realistic uniform bed roughness coefficients and field data obtained from AWAC measurements.

Table A1 Summary of results comparing major axis amplitudes, phases, inclinations and minor axis magnitudes of M_2 currents from Telemac model with AWAC measurements from T61, T74 and T75 deployments with varying bed friction coefficient. Numbers in brackets show the level of agreement with AWAC data. Green is for values within 10%/10°, orange for values within 20%/20° and red for values greater than 20%/20°.

		Model results					
AWAC	AWAC data	C_b=0.13	C_b=0.091	C_b=0.052	C_b=0.035	C_b=0.025	C_b=0.013
Major axis (m/s)							
T61	2.43	2.01 *(-17)*	2.04 *(-16)*	2.11 *(-13)*	2.15 *(-11)*	2.19 *(10)*	2.23 *(-8)*
T74	1.45	1.30 *(10)*	1.32 *(9)*	1.36 *(7)*	1.38 *(5)*	1.40 *(4)*	1.43 *(2)*
T75	2.11	1.79 *(15)*	2.08 *(1)*	2.15 *(-2)*	2.19 *(-4)*	2.22 *(-5)*	2.26 *(-7)*
Phase (°)							
T61	17	2 *(15)*	2 *(15)*	7 *(10)*	7 *(10)*	8 *(9)*	8 *(9)*
T74	327	326 *(-1)*	326 *(-1)*	326 *(-1)*	326 *(-1)*	326 *(-1)*	326 *(-1)*
T75	17	2 *(15)*	13*(4)*	14 *(3)*	14 *(3)*	14 *(3)*	14 *(3)*
Inclination (°)							
T61	116	129 *(-13)*	128 *(-12)*	128 *(-12)*	128 *(-12)*	128 *(-12)*	128 *(-12)*
T74	139	149 *(-10)*	149*(-10)*	145 *(-10)*	149 *(-10)*	149 *(-10)*	139*(-10)*
T75	128	141 *(-13)*	137 *(-9)*	137 *(-9)*	137 *(-9)*	137 *(-9)*	137 *(-9)*
Minor axis (m/s)							
T61	0.22	0.21 *(-6)*	0.21 *(-6)*	0.21 *(-4)*	0.22 *(-1)*	0.22 *(0)*	0.23 *(3)*
T74	0.13	0.12 *(8)*	0.14 *(-6)*	0.16 *(-19)*	0.17 *(-25)*	0.17 *(-29)*	0.18*(-34)*
T75	0.25	0.23 *(8)*	0.28 *(-11)*	0.30 *(-17)*	0.30 *(-20)*	0.31 *(-23)*	0.32*(-27)*

Table A2. Summary of results comparing major axis amplitudes, phases, inclinations and minor axis magnitudes of S_2 currents from Telemac model with AWAC measurements from T61, T74 and T75 deployments with varying bed friction coefficient.. Numbers in brackets show the level of agreement with AWAC data. Green is for values within 10%/10°, orange for values within 20%/20° and red for values greater than 20%/20°.

		Model results					
AWAC	AWAC data	C_b=0.13	C_b=0.091	C_b=0.052	C_b=0.035	C_b=0.025	C_b=0.013
Major axis (m/s)							
T61	0.59	0.57 *(-4)*	0.58 *(-2)*	0.60 *(2)*	0.62 *(5)*	0.63 *(7)*	0.65 *(10)*
T74	0.37	0.34 *(8)*	0.34 *(7)*	0.35 *(5)*	0.36 *(4)*	0.36 *(2)*	0.37 *(1)*
T75	0.45	0.51 *(-14)*	0.62 *(-39)*	0.65 *(-45)*	0.67 *(-50)*	0.68 *(-53)*	0.70 *(-57)*
Phase (°)							
T61	45	45 *(21)*	44 *(22)*	49 (17)	49 *(17)*	49 (17)	50 *(16)*
T74	31	31 *(-4)*	31*(-4)*	37 *(-10)*	38 *(-11)*	40 (-13)	41 *(-14)*
T75	39	39 *(22)*	52 *(9)*	52 *(9)*	52 *(9)*	52 *(9)*	52 *(9)*
Inclination (°)							
T61	117	128 *(-11)*	128 *(-11)*	127 *(-10)*	127 *(-10)*	127 *(-10)*	127 *(-10)*
T74	142	147 *(5)*	147 *(5)*	145 *(3)*	145 *(3)*	144 *(2)*	143 *(1)*
T75	127	141 *(-14)*	136 *(-9)*	136 *(-9)*	139 *(-9)*	136 *(-9)*	136 *(-9)*
Minor axis (m/s)							
T61	0.03	0.03 *(0)*	0.03 *(11)*	0.02 *(-21)*	0.02 *(-25)*	0.02 *(-29)*	0.02 *(-35)*
T74	0.07	0.05 *(22)*	0.06 *(9)*	0.07 *(0)*	0.07 *(-3)*	0.07 *(-3)*	0.07 *(-1)*
T75	0.11	0.07 *(38)*	0.07 *(34)*	0.07 *(35)*	0.07 *(34)*	0.07 *(34)*	0.07 *(34)*

Appendix C Matlab boundary condition generation code

Matlab code written to extract boundary point coordinates from 'Boundary_conditions.bc2' file generated in Blue Kenue and generate amplitude and phase data at each point from the Tide Model Driver (TMD) Matlab package.

```
%%%%%%%%%%%%%%%%%%%%%%%%%%%%%%%%%%%%%%%%%%%%%%%%%%%%%%%%%%%%%%%%%%%%%%%%%%%%%%%
% Read in Boundary node numbers from Boundary conditions file (.bc2) - M
% is a vector with all global node numbers for nodes on the liquid
% boundary, O is a vector with the liquid node numbers

[O,M,y]=litcount('Boundary_conditions.bc2','5 4 4')

%%%%%%%%%%%%%%%%%%%%%%%%%%%%%%%%%%%%%%%%%%%%%%%%%%%%%%%%%%%%%%%%%%%%%%%%%%%%%%%
% Clear the new13.txt file
filename = 'new13.txt'; %Clear the new13.txt file
fid = fopen(filename,'wt','a');
fclose(fid);

%%%%%%%%%%%%%%%%%%%%%%%%%%%%%%%%%%%%%%%%%%%%%%%%%%%%%%%%%%%%%%%%%%%%%%%%%%%%%%%
% Find liquid boundary node coordinates from the Boundaryconditions.bc2
% file and using M from above

fid = fopen('Boundary_conditions.bc2');
count = 0;
while feof(fid) == 0
count = count +1;
tline = fgetl(fid);
matches = findstr(tline, 'BeginNode');
num = length(matches);
if num > 0
q=count; %Count gives the line number in Boundaryconditions.bc2 at which
%the node coordinates begin.
end
end

C=zeros(42,1);
for i = 1:length(M)
C(i,:)=M(i,:)+q; %C gives the lines in Boundaryconditions.bc2 where the
%liquid boundary nodes are. Note: This may not include bathymetry!
end

fileID = fopen('Boundary_conditions.bc2'); %Read in the text file
T = textscan(fileID,'%s','Delimiter','\n');
v=size(M);
v=v(1,1); %v is the number of liquid nodes


L=cell(v,2); %L is a cell where the coordinates will go in as strings
%into each row
for i=1:v

a=T{1}{C(i,:)};
a = char(a);
a=strsplit(a); %Split the strings up
L{i,1}=a(1,1);
```

```
L{i,2}=a(1,2); %L is a cell containing coordinates of all the liquid
%boundary nodes
end

r=zeros(length(M),2); % Converts L from a cell to a matrix, r

for i=1:length(M)
e=L{i,1};
f=L{i,2};
e_num=cell2mat(e);
e_num=str2num(e_num);
% r is a matrix containing all liquid node coordinates to use in the next
%section!
f_num=cell2mat(f); %Where the coordinates have been shifted -4300000
%already in Blue Kenue and given in the .bc2 file, this must be accounted
%for when converting to latitudes and longitudes (below)
f_num=str2num(f_num);
r(i,1) = e_num;
r(i,2)=  f_num;
end

%%%%%%%%%%%%%%%%%%%%%%%%%%%%%%%%%%%%%%%%%%%%%%%%%%%%%%%%%%%%%%%%%%%%%%%%%%%
% Convert liquid node coordinates to lat lon

mstruct = defaultm('mercator');
mstruct.origin = [0 0 0];
mstruct = defaultm(mstruct);
mstruct.geoid = [6371000 0];
xc=r(:,1);
yc=r(:,2)+4300000;
[lat,lon]=minvtran(mstruct,xc,yc);

%%%%%%%%%%%%%%%%%%%%%%%%%%%%%%%%%%%%%%%%%%%%%%%%%%%%%%%%%%%%%%%%%%%%%%%%%%%
% Input these coordinates into tmd_get_coeff.m to get A (Amplitudes) and
% P (Phases) matrices to use

Model='Model_ES2008'; %Defines name of Tide model driver model file name
%in directory
conlist=['M2';'S2';'N2';'K2';'K1';'O1';'P1';'Q1';'M4']; %Constituent list

A=zeros((length(lon)),length(conlist)); %Creates amplitude matrix A
P=zeros((length(lon)),length(conlist)); %Creates amplitude matrix A

AF=A;
PF=P;
for j=1:length(conlist);
        cons=conlist(j,:);
        [x,y,amp,phase]=tmd_get_coeff(Model,'z',cons); %tmd_get_coeff
%gives each individual constituents amplitude and phase
         XY=ap2reim(amp,phase,'f');
    A(:,j)=interp2(x,y,XY.x,lon,lat);
    P(:,j)=interp2(x,y,XY.y,lon,lat);
    AP=ap2reim(A(:,j),P(:,j),'b');
    AF(:,j)=AP.x(:);
    PF(:,j)=AP.y(:);
end

figure(10); clf;
subplot(2,2,1);
plot(AF,lat); ylabel('Latitude'); xlabel('Amplitude')
subplot(2,2,2);
plot(PF,lat); xlabel('Phase')
```

```
subplot(2,2,3);
plot(AF,lon); ylabel('Longitude'); xlabel('Amplitude')
subplot(2,2,4);
plot(PF,lon); ylabel('Longitude'); xlabel('Phase')

MAP=[O M AF PF]; %Concatenate and reorder matrices


MAP2=sortrows(MAP);

%%%%%%%%%%%%%%%%%%%%%%%%%%%%%%%%%%%%%%%%%%%%%%%%%%%%%%%%%%%%%%%%%%%%%%%%%%%%%%%
% Generate FORTRAN code to use in BORD subroutine

filename = 'new13.txt';
fid = fopen(filename,'wt','a');
fclose(fid);

n_nodes = length(M);
n_cons = 9;
B=cell(1,8); % Distinction of different nodes
C=cell(n_cons,6); % Corrected amplitudes and phases

for i=1:n_nodes;
C1='A('; %A is an array to go into FORTRAN containing all amplitudes for
%each liquid boundary
C2=num2str(MAP2(i,1));
C3=',1:10)';
C4='=(/';
C5=num2str(MAP2(i,1));
C6='.,';
C7=num2str(MAP2(i,3));
C8=',';
C9=num2str(MAP2(i,4));
C10=',';
C11=num2str(MAP2(i,5));
C12=',';
C13=num2str(MAP2(i,6));
C14=',';
C15=num2str(MAP2(i,7));
C16=',';
C17=num2str(MAP2(i,8));
C18=',';
C19=num2str(MAP2(i,9));
C20=',';
C21=num2str(MAP2(i,10));
C22=',';
C23=num2str(MAP2(i,11));
C24='/)';

C=[C1 C2 C3 C4 C5 C6 C7 C8 C9 C10 C11 C12 C13 C14 C15 C16 C17 C18 C19 C20
C21 C22 C23 C24]

E1='P('; %P is an array to go into FORTRAN containing all phases for each
liquid boundary
E2=num2str(MAP2(i,1));
E3=',1:9)';
E4='=(/';
E5=num2str(MAP2(i,12));
E6=',';
E7=num2str(MAP2(i,13));
E8=',';
E9=num2str(MAP2(i,14));
```

```
E10=',';
E11=num2str(MAP2(i,15));
E12=',';
E13=num2str(MAP2(i,16));
E14=',';
E15=num2str(MAP2(i,17));
E16=',';
E17=num2str(MAP2(i,18));
E18=',';
E19=num2str(MAP2(i,19));
E20=',';
E21=num2str(MAP2(i,20));
E22='/)';

E=[E1 E2 E3 E4 E5 E6 E7 E8 E9 E10 E11 E12 E13 E14 E15 E16 E17 E18 E19 E20
E21 E22]

filename = 'new13.txt'; %Write amplitudes to text file
%Write amplitudes to tex
fid = fopen(filename,'a');
fprintf(fid,'\n');
fprintf(fid, C);
fclose(fid);

filename = 'new13.txt'; %Write phases to text file
fid = fopen(filename,'a');
fprintf(fid,'\n');
fprintf(fid, E);
fclose(fid);

end
```

Appendix D Telemac Steering File

Example steering file used to run the English Channel hydrodynamic model in Telemac 2D. Comments are added for each line to give a brief description of its purpose, which begin with a forward slash.

```
/FILE MANAGEMENT////////////////////////////////////////////////////////////////////////////////////////////////
GEOMETRY FILE                    = Geometry.slf              /Binary mesh file containing mesh coordinates
BOUNDARY CONDITIONS FILE         = Boundary_conditions.cli   /Formatted boundary conditions file
FORTRAN FILE                     = Fortran.f90               /Fortran file containing all subroutines
RESULTS FILE                     = Results.slf               /Binary results file
PARALLEL PROCESSORS              =128                        /Number of parallel processors for simulations
                                                             /using  IRIDIS supercomputer
VARIABLES FOR GRAPHIC PRINTOUTS  = 'U,V,H,W,S'               /U,V=Flow velocities, H=Depth, W =Free surface,
                                                             /S=  Bottom friction
GRAPHIC PRINTOUT PERIOD          = 10                        /Period between output to results file (time steps)
LISTING PRINTOUT PERIOD          = 60                        /Period between listing file output (time steps)
/INITIAL SETUP//////////////////////////////////////////////////////////////////////////////////////////////////
TIME STEP                        = 60                        /(Seconds)
NUMBER OF TIME STEPS             = 48960                     /Total duration of simulation (time steps)
ORIGINAL DATE OF TIME            = 2014;11;9                 /Date at initial state of simulation
                                                             /(year;month;day)
LONGITUDE OF ORIGIN POINT  = 0.0                             /Used to determine tide-generating potential
LATITUDE OF ORIGIN POINT         = 36.0305                   /For spherical coordinates and , which calls the
                                                             /'Latitu' subroutine
SPHERICAL COORDINATES            = YES                       /Spherical Mercator coordinates for simulations
                                                             /over large domains
/PHYSICAL PARAMETERS////////////////////////////////////////////////////////////////////////////////////////////
CORIOLIS                         = YES                       /Includes the effect of the Coriolis force
TIDE GENERATING FORCE            = YES                       /Includes astral forces that produce tides in large
/domains
TURBULENCE MODEL                 = 1                         /Constant turbulent viscosity throughout the
                                                             /domain
TIDAL FLATS                      = YES                       /Enables wetting and drying in shallow regions
VERTICAL STRUCTURES              = YES                       /Enables 'Dragfo' subroutine to parameterise drag
                                                             /from tidal turbine arrays
/BOUNDARY CONDITIONS////////////////////////////////////////////////////////////////////////////////////////////
LAW OF BOTTOM FRICTION           = 5                         /Nikuradse friction law used to model bed friction
                                                             /over the whole domain
FRICTION COEFFICIENT             = 0.03                      /Friction coefficient relating to Nikuradse friction
                                                             /law applied uniformly over the domain
PRESCRIBED ELEVATIONS            = 0                         /Defines elevation of open boundaries
OPTION FOR LIQUID BOUNDARIES     = 2                         /Thompson method to find unknown boundary
                                                             /velocities
/INITIAL CONDITIONS/////////////////////////////////////////////////////////////////////////////////////////////
INITIAL ELEVATION                = 'CONSTANT ELEVATION'      /Constant elevation across domain
```

```
INITIAL ELEVATION                    = 4.0                  /Magnitude of initial elevation (m)
/SOLVER SETUP////////////////////////////////////////////////////////////////////////////////////////////////////////
SOLVER                               = 1                    /Conjugate gradient method for the
                                                            /hydrodynamic propagation step
SOLVER ACCURACY                      = 1.E-3                /Accuracy during propagation step
DISCRETIZATIONS IN SPACE             = 12 ;11               /Quasi bubble triangle (4 node triangle) velocity
                                                            /and linear depth
SUPG OPTION                          = 1;1                  / Upwind scheme
TYPE OF ADVECTION                    = 1;5                  / Type of upwind scheme: Upwind scheme with
                                                            /classic SUPG method
TREATMENT OF THE LINEAR SYSTEM       = 2                    /Uses velocity from momentum equation rather
                                                            /than continuity equation to improve
                                                            /computational efficiency
PRECONDITIONING                      = 2                    /Diagonal preconditioning (default) to speed up
                                                            /convergence
INITIAL GUESS FOR H                  = 1                    /Initial value of DH equal to value of DH at the
                                                            /previous time step (default), used to speed up
                                                            /convergence when solving propagation step
INITIAL GUESS FOR U                  = 2                    /Same as above but for U rather than H
FREE SURFACE GRADIENT COMPATIBILITY= 0.5                    /Relaxes continuity to remove free surface wiggles
IMPLICITATION FOR DEPTH              = 0.55                 /To account for semi-implicit discretization of time
IMPLICITATION FOR VELOCITY           = 0.55                 /To account for semi-implicit discretization of time
&FIN                                                        /End of Steering file
```

Appendix E BORD subroutine

Example BORD subroutine used to run the English Channel hydrodynamic model in Telemac 2D, written in FORTRAN. Constituent amplitudes and phases at each open boundary node obtained from the Matlab boundary condition generation code (Appendix A) are input into BORD, which are used to describe the temporal and spatial variation in free surface elevation to drive flow in and out of the domain through the open boundaries. Comments are added for each line to give a brief description of its purpose, which begin with an exclamation mark.

```
    SUBROUTINE BORD
(HBOR,UBOR,VBOR,TBOR,U,V,H,ZF,NBOR,TRA05,TRA06,LIHBOR,LIUBOR,LITBOR,&

XNEBOR,YNEBOR,NPOIN,NPTFR,NPTFR2,TEMPS,NDEBIT,NCOTE,NVITES,NTRAC,NTRACE,NFRLIQ,NUMLI
Q,KENT,KENTU,PROVEL,MASK,MESH,EQUA,NOMIMP)



  USE BIEF

  USE DECLARATIONS_TELEMAC2D, ONLY: BOUNDARY_COLOUR

  IMPLICIT NONE

! Variables

  INTEGER
LNG,LU,K,NPTFR,NDEBIT,NCOTE,NVITES,NTRACE,MSK1,NTRAC,NPTFR2,NPOIN,NFRLIQ,IFRLIQ,
KENT,KENTU, NBOR(NPTFR), LIHBOR(NPTFR),LIUBOR(NPTFR),
PROVEL(100),NUMLIQ(NPTFR),P_IMAX,I,KK, K_DC,L,S,SECOND,DAYS,SECDAY,DAYINC,HOURS

  INTEGER, SAVE, DIMENSION (NPTFRL) :: BDY_IDX

  INTEGER, SAVE, DIMENSION (4,NCONSTIT) ::DOOD   ! Four Doodson integers for each
const.

  INTEGER, PARAMETER :: DAY = 313

  INTEGER, PARAMETER :: YEAR = 2014

  INTEGER, PARAMETER :: NPTFRL=1202              !Number of liquid boundary nodes

  INTEGER, PARAMETER :: NCONSTIT = 9             ! Number of constituents

  DOUBLE PRECISION HBOR(NPTFR),UBOR(NPTFR,2),VBOR(NPTFR,2), ZF(NPOIN),
XNEBOR(NPTFR),YNEBOR(NPTFR), TEMPS,Z, Q,SL,VIT,TR, PI, sel,hel,per,pprime,
N_DC,NA,NP

  DOUBLE PRECISION, SAVE, DIMENSION (NPTFRL,NCONSTIT+1) :: A

  DOUBLE PRECISION, SAVE, DIMENSION (NPTFRL,NCONSTIT) :: A_PRIME

  DOUBLE PRECISION, SAVE, DIMENSION (NPTFRL,NCONSTIT) :: P

  DOUBLE PRECISION, SAVE, DIMENSION (NPTFRL,NCONSTIT) ::FREQ

  DOUBLE PRECISION, DIMENSION (NPTFRL,NCONSTIT) :: V_eq,NodAmp,NodPhase

  DOUBLE PRECISION, DIMENSION (NPTFRL) ::HEIGHT_DC
```

```
  DOUBLE PRECISION, DIMENSION (NCONSTIT) :: ConConst = (/ 0., 0., 0., 0.,
90.,270.,270.,270.,0. /)   ! M2,S2,N2,K2,K1,O1, P1, Q1, M4 (deg/hr)

  COMMON/INFO/LNG,LU

  CHARACTER(LEN=20) EQUA

  CHARACTER(LEN=144) NOMIMP

  TYPE(BIEF_MESH) :: MESH

  TYPE(BIEF_OBJ)  :: MASK,H,U,V,TRA05,TRA06,LITBOR,TBOR

  EXTERNAL Q,SL,VIT,TR ,P_IMAX

  INTRINSIC MAX

  logical, SAVE :: BORD_CALLED_ALREADY = .FALSE.


  IF (.NOT.BORD_CALLED_ALREADY) then        ! Start time-invariant assignments

     BORD_CALLED_ALREADY=.TRUE.

     A=-999.                                ! Initialize all values in A

     P=-999.                                ! Initialize all values in P

! Amplitude and phase data obtained from Matlab boundary condition generation code
(Appendix C) inserted below, typically Matrices A and P have hundreds of rows:

A(1,1:10)=(/1.,1.1292,0.36865,0.22908,0.099271,0.04286,0.020331,0.007818,0.0083436,0
.031794/)

P(1,1:9)=(/129.5901,163.022,107.229,162.1935,72.0488,339.3083,82.4531,284.8258,269.4
1)

…

A(1202,1:10)=(/1202.,1.1693,0.41065,0.20995,0.11375,0.049729,0.054904,0.022855,0.019
575,0.0067257/)

P(1202,1:9)=(/155.88,206.1995,136.5164,207.876,172.1716,34.8893,160.7234,340.7632,88
.6204/)

     A_PRIME=A(1:NPTFRL,2:NCONSTIT+1)


     YEARS=YEAR-2000                            ! Defines year in y2k epoch

     DAYSTART=(365*YEARS)+(DAY-1) + (YEARS -1)/4 ! Defines initial day

     PI = 3.141592653589793D0

     FREQ=SPREAD( & ! (deg/hr)

          (/28.9841042,& !M2

          30.0000000,& !S2

          28.4397295,& !N2

          30.0821373, & !K2

          15.0410686, & !K1
```

```
          13.9430356,& !O1
          14.9589314,& !P1
          13.3986609, & !Q1
          57.4238337/),& !M4
          1,NPTFRL)

     DOOD=RESHAPE((/-2, 2, 0, 0,& !M2
          0, 0, 0, 0,& !S2
          -3, 2, 1, 0,& !N2
          0, 2, 0, 0,& !K2
          0, 1, 0, 0,& !K1
          -2, 1, 0, 0,& !O1
          1,-2, 0, 0,& !P1
          -2, 0, 1, 0,& !Q1
          -4, 4, 0, 0/),& !M4
          SHAPE(DOOD))
     BDY_IDX=-1                                   ! Initialize boundary index
     N_BDY_PTS=0
     DO KK=1,NPTFRL                               ! Loop over the full mesh's
boundary nodes
        inner_loop: DO K_DC=1,NPTFR               ! Loop over the sub-meshes boundary
nodes
           IF (LIHBOR(K_DC).EQ.KENT) THEN
              IF(BOUNDARY_COLOUR%I(K_DC)==KK) THEN
                 BDY_IDX(K_DC)=KK                 ! Assign boundary index.
                 N_BDY_PTS=N_BDY_PTS+1            ! Increment number of bdy. pts
                 EXIT inner_loop
              END IF
           END IF
        END DO inner_loop
     END DO
     write(LU,*) "number of bdy pts: ",N_BDY_PTS
  END IF                                          ! End of time-invariant assignment

  MSK1 = 1
  IF (N_BDY_PTS.GT.0) then
```

```
      DAYS=DAYSTART+idint((TEMPS)/86400.)         ! Increase DAYS at start of each
day

      HOURS =(DMOD( TEMPS,86400.))/3600.          ! Increase HOURS in decimal hours

      sel= 218.3164 +(13.17639648 * (DAYS+0.5))

      hel= 280.4661 +  (0.98564736 * (DAYS+0.5))

      per= 83.3535 +  (0.11140353 * (DAYS+0.5))

      pprime=282.94

      N_DC=125.0445-(0.05295377*DAYS)

      NA=1.0004-(0.0373*COSD(N_DC))+(0.0002*COSD(2*N_DC))

      NP=(-2.14)*SIND(N_DC)

      V_eq = &

           SPREAD( &

           DMOD (&

           DOOD(1,1:NCONSTIT)*sel + &

           DOOD(2,1:NCONSTIT)*hel + &

           DOOD(3,1:NCONSTIT)*per + &

           DOOD(4,1:NCONSTIT)*pprime + &

           ConConst , 360.), &

           1,NPTFRL)


      DO L=1,9                                    ! Loop over all constituents

         if (L==1) then !M2

            NodAmp(1:NPTFRL,L)=NA

            NodPhase(1:NPTFRL,L)=NP

         else if (L==2) then !S2

            NodAmp(1:NPTFRL,L)=1.0

            NodPhase(1:NPTFRL,L)=0.0

         else if (L==3) then !N2

            NodAmp(1:NPTFRL,L)=NA

            NodPhase(1:NPTFRL,L)=NP

         else if (L==4) then !K2

            NodAmp(1:NPTFRL,L)= 1.0241 + 0.2863*dcosd(N_DC) + 0.0083*dcosd(2*N_DC) +
0.0015*dcosd(3*N_DC)

            NodPhase(1:NPTFRL,L)=-17.74*dsind(N_DC) + 0.68*dsind(2*N_DC) -
0.07*dsind(3*N_DC)

         else if (L==5) then !K1
```

```
           NodAmp(1:NPTFRL,L)=1.006 + 0.115*dcosd(N_DC) - 0.0088*dcosd(2*N_DC) +
0.0006*dcosd(3*N_DC)

           NodPhase(1:NPTFRL,L)=-8.86*dsind(N_DC) + 0.68*dsind(2*N_DC) -
0.07*dsind(3*N_DC)

        else if (L==6) then !O1

           NodAmp(1:NPTFRL,L)=1.0089 + 0.1871*dcosd(N_DC) - 0.0147*dcosd(2*N_DC) +
0.0014*dcosd(3*N_DC)

           NodPhase(1:NPTFRL,L)=10.8*dsind(N_DC) - 1.34*dsind(2*N_DC) +
0.19*dsind(3*N_DC)

        else if (L==7) then !P1

           NodAmp(1:NPTFRL,L)=1.0

           NodPhase(1:NPTFRL,L)=0.0

        else if (L==8) then !Q1

           NodAmp(1:NPTFRL,L)=0.0

           NodPhase(1:NPTFRL,L)=0.0

        else if (L==9) then !M4

           NodAmp(1:NPTFRL,L)=NA**2

           NodPhase(1:NPTFRL,L)=2*NP

        end if

     END DO


     HEIGHT_DC=0.                                  ! Initialize all values in Z to
zero

     HEIGHT_DC = 4.0 + sum ( NodAmp*A_PRIME*DCOSD( FREQ*HOURS+V_eq-P+NodPhase) , 2 )

                                                    !NOTE: Mean sea level is
                                               introduced above

     DO I=1,NPTFR

        IF (BDY_IDX(I).GT.-1) then

           HBOR(I) = HEIGHT_DC(BDY_IDX(I)) - ZF(NBOR(I))

        END IF

     END DO

  END IF


  RETURN

  END SUBROUTINE BORD
```

Appendix F LATITU subroutine

Example LATITU subroutine used to run the English Channel hydrodynamic model in Telemac 2D, written in FORTRAN. LATITU is used to convert t spherical coordinates, prompted by the keyword "SPHERICAL COORDINATES=YES" in the Steering file (Appendix D). The Cartesian coordinate of each point is obtained from the geometry file and converted to spherical coordinates using the latitude of origin point defined in the Steering file. Comments are added for each line to give a brief description of its purpose, which begin with an exclamation mark.

```
SUBROUTINE LATITU (COSLAT,SINLAT,LAMBD0,Y,NPOIN)
      IMPLICIT NONE
     ! Variables
      INTEGER LNG,LU,I
      INTEGER, INTENT(IN) :: NPOIN
      DOUBLE PRECISION LB2RAD,SURR,PISUR4,PISUR2,XLAMB
     DOUBLE PRECISION, INTENT(IN) :: Y(NPOIN)
      DOUBLE PRECISION, INTENT(INOUT) :: COSLAT(NPOIN),SINLAT(NPOIN)
      DOUBLE PRECISION, INTENT(IN) :: LAMBD0
      COMMON/INFO/LNG,LU
       INTRINSIC TAN,ATAN,SIN,COS,EXP
      SURR = 1.D0 / 6371000.D0   ! Earths radius
      PISUR4 = ATAN(1.D0)
      PISUR2 = PISUR4 + PISUR4
      LB2RAD = LAMBD0 * PISUR4 / 90.D0
      DO 10 I = 1 , NPOIN
        XLAMB = 2.D0* ATAN(EXP(Y(I)*SURR)*TAN(LB2RAD+PISUR4))-PISUR2
        COSLAT(I) = COS(XLAMB)
        SINLAT(I) = SIN(XLAMB)
10    CONTINUE
      RETURN
       END
```

Appendix G DRAGFO subroutine

Example DRAGFO subroutine used to parameterise turbine array drag in the English Channel hydrodynamic model in Telemac 2D, written in FORTRAN. DRAGFO is prompted by the keyword "VERTICAL STRUCTURES=YES" in the Steering file (Appendix D). Comments are added for each line to give a brief description of its purpose, which begin with an exclamation mark.

```
      SUBROUTINE DRAGFO (FUDRAG,FVDRAG)
      USE BIEF
      USE DECLARATIONS_TELEMAC2D
      IMPLICIT NONE

     ! Variables
      INTEGER LNG,LU,IELEM,I,I4,NSOM,DISCLIN,m,j,n_inpoly
     DOUBLE PRECISION
UNORM,AIRE,SOM,XSOM(4),YSOM(4),X4,Y4,A,N,D,AIRE,P,ASWEPT,P_DSUM
      COMMON/INFO/LNG,LU
      TYPE(BIEF_OBJ), INTENT(INOUT) :: FUDRAG,FVDRAG
      EXTERNAL         P_DSUM
      real(8) UDRAG,depth,fdrag
      real(8), parameter :: CD = 0.8        ! Turbine thrust coefficient
      real(8), parameter :: U_design=4      ! Turbine rated speed (m/s)
      real(8), parameter :: DENSITY=0.02    ! Array density

!     COMPUTE THE MASSE INTEGRALS:
      CALL VECTOR (T1,'=','MASBAS          ',UN%ELM,1.D0, &
                  S,S,S,S,S,S,MESH,.FALSE.,S)
      CALL CPSTVC(UN,FUDRAG)
      CALL CPSTVC(VN,FVDRAG)
      CALL OS('X=C     ',FUDRAG,FUDRAG,FUDRAG,0.D0)
      CALL OS('X=C     ',FVDRAG,FVDRAG,FVDRAG,0.D0)

      NSOM = 4                              ! Number of vertices in array plot
perimeter
      XSOM(1) =  -229849.D0                 ! Coordinates of vertices
      XSOM(2) =  -230171.D0
```

```
      XSOM(3) =  -222482.D0
      XSOM(4) =  -220047.D0
      YSOM(1) =  2064793.D0
      YSOM(2) =  2062599.D0
      YSOM(3) =  2060465.D0
      YSOM(4) =  2066765.D0
!-----------------------------------------------------------------

      AIRE=0.D0                          ! Array plot area, initiated to zero
      n_inpoly=0                         ! Number of nodes within array plot area

      DO I=1,BIEF_NBPTS(11,MESH)         ! Loop to calculate AIRE and n_inpoly
        IF(INPOLY(X(I),Y(I),XSOM,YSOM,NSOM)) THEN
          AIRE = AIRE + T1%R(I)
          n_inpoly=n_inpoly+1
        ENDIF
      ENDDO

!     QUASI-BUBBLE POINTS
      IF(FU%ELM.EQ.12) THEN              ! Accounts for quasi-bubble
discretization
        DISCLIN=11
        CALL CHGDIS(FUDRAG,DISCLIN,12,MESH)
        CALL CHGDIS(FVDRAG,DISCLIN,12,MESH)
        DO IELEM = 1 , NELEM
          I4=IKLE%I(IELEM+3*NELMAX)
          X4=(X(IKLE%I(IELEM         ))+ &
             X(IKLE%I(IELEM+  NELMAX))+ &
             X(IKLE%I(IELEM+2*NELMAX)))/3.D0
          Y4=(Y(IKLE%I(IELEM         ))+ &
             Y(IKLE%I(IELEM+  NELMAX))+ &
             Y(IKLE%I(IELEM+2*NELMAX)))/3.D0
          IF(INPOLY(X4,Y4,XSOM,YSOM,NSOM)) THEN
          AIRE = AIRE + T1%R(I4)
          END IF
```

```
        ENDDO
      ENDIF
!     IN PARALLEL THE AREA MAY BE SPLIT INTO SEVERAL SUB-DOMAINS:
      IF(NCSIZE.GT.0) AIRE=P_DSUM(AIRE)
      ASWEPT = (AIRE/n_inpoly) * DENSITY    ! Calculate total swept area of all
turbines


      DO I=1,BIEF_NBPTS(11,MESH)            ! Loop to calculate array drag
        IF(INPOLY(X(I),Y(I),XSOM,YSOM,NSOM)) THEN
          depth=max(H%R((I)), 0.01)
          UNORM = MAX((SQRT(UN%R(I)**2+VN%R(I)**2)),1.D-4)
          UDRAG = min(UNORM,U_design)
          FUDRAG%R(I) = (-0.5 * UDRAG**2 * CD * DENSITY) / (UNORM * depth)
          FVDRAG%R(I) = FUDRAG%R(I)
        ENDIF
      ENDDO
      RETURN
      END
```

Appendix H IJOME journal paper

Journal paper published in the International Journal of Marine Energy (IJOME). The paper gives an in depth presentation of results from experimental flume testing to validate a method for parameterising drag using the distributed drag method. Results are presented in Chapter 5.

Experimental validation of the distributed drag method for simulating large marine current turbine arrays using porous fences

D. S. Coles[1], L. S. Blunden, A. S. Bahaj

Energy and Climate Change Division, Sustainable Energy Research Group (www.energy.soton.ac.uk)

Faculty of Engineering and the Environment, University of Southampton, UK

[1]d.coles@soton.ac.uk

Abstract

Marine current energy conversion can provide significant electrical power from resource-rich sites. However, since no full scale arrays of conversion technologies currently exist, validation of methods used for simulating energy extraction by large marine current turbine arrays relies upon model scale down laboratory experiments. We present results from an experiment using porous fences spanning the width of a recirculating flume to simulate flow through large, regular, multi-row marine current turbine arrays. Measurements of array drag, free surface elevation drop and velocity distribution were used to validate a method for parameterising equivelant array drag in the distributed drag approach, which is typically implemented in regional scale models. The effect of array density was also investigated by varying the spacing between fences and the number of fences within a pre-defined plot area. Two different inflow conditions were used, the first used the flume bed in its natural state, giving a logarithmic flow distribution in the vertical plane that agreed within 5% of measurements at real tidal sites. The second used roughness strips on the flume bed to significantly enhance ambient turbulence intensity to levels similar to those recorded in the Pentland Firth. For realistic array densities (<0.07), a depth-averaged formulation of effective array drag coefficient agreed within 10% of that derived from experimental results for both inflow conditions. The validity of the distributed drag approach was shown to be dependent on longitudinal row spacing between porous fences and ambient turbulence intensity, two features that determine the level of wake recovery downstream of each porous fence. Finally a force balance analysis was used to quantify the change in bed drag as a result of the presence of porous fence arrays. Adding arrays to the flow gave an increase in bed drag coefficient of up to 95%, which was 20% of the total added bed and array drag coefficient. Results have implications for regional scale marine current turbine array modelling, where array layout along with site specific characteristics such as turbulence intensity and bed profile determine the validity of the distributed drag approach for simulating energy extraction.

Keywords

Tidal energy, marine current turbine arrays, porous fence, distributed drag method, regional scale modelling of large arrays

Nomenclature

A_t Rotor area (m^2)

A_P Array plot area (m^2)

A_i Flume inlet cross sectional area (m^2)

A_o Flume outlet cross sectional area (m^2)

C_b Bed drag coefficient

C_e Equivelant added array drag coefficient

C_t Fence drag coefficient

$C_{t,a}$ Array drag coefficient

ε Blockage ratio

$\bar{F}_a$ Depth-averaged array force (N)

F_b Bed drag force (N)

F_f Porous fence drag force (N)

F_w Weight force (N)

g Acceleration due to gravity (m/s^2)

h_i Inlet depth (m)

h_o Outlet depth (m)

k Physical roughness height (m)

l_a Longitudinal porous fence array length (m)

l_f Porous fence row spacing (m)

l_z Porous fence height (m)

n Porous fence number

p Pitch between roughness strips (m)

ρ Density of water (kg/m^3)

Re Reynolds number

Re_b Boundary Reynolds number

τ_a Array shear stress (Pa)

θ Flume bed slope angle (°)

$\overline{U}$ Depth-averaged flow velocity (m/s)

$U_{f,n}$ Flow velocity through fence *n* at fence centroid height (m/s)

$U_{0,f}$ Upstream flow velocity at fence centroid height (m/s)

u_* Friction velocity (m/s)

$u'w'$ Shear stress (m^2/s^2)

ν Kinematic viscosity of water (m^2/s)

z_0 Roughness length (m)

1. Introduction

For marine current turbines to make a significant contribution to electricity generation, methods for simulating large arrays must be validated to build confidence in performance predictions (Bahaj 2011). Only then will it be possible to justify array design such as the longitudinal row spacing required to maximise energy extraction, minimise array footprint whilst also minimising environmental impact at specific sites.

The task of modelling the performance of turbines in arrays is a multi-scale problem, adding significant complexity. These scales are outlined in (Adcock et al. 2015), namely blade, turbine, array, site and regional scales. This work focuses on the distributed drag method for simulating large arrays in regional scale models. In this approach, a drag is applied uniformly over the array plot area A_p and

individual turbines are not modelled, allowing arrays to be simulated at acceptable computational expense. Assuming mesh independence for energy extraction is achieved, no further mesh preparation is required, meaning the same mesh can be used to investigate array size, positioning and density rather than having to adapt the mesh for any change in array layout. Array density is defined as the ratio of total swept area of turbines A_s to the array plot area A_p. This method is typically used in the early stage of resource assessment to quantify far field effects (Bourban et al. 2013), optimise array shape (Ahmadian & Falconer 2012), quantify array-array interaction (Draper et al. 2014), quantify sediment dynamics (Thiebot et al. 2015) and quantify energy extraction (Draper et al. 2014; Walters et al. 2013; Plew & Stevens 2013; Karsten et al. 2012; Karsten et al. 2008; Blanchfield et al. 2008; Sutherland et al. 2007).

Since no full scale arrays currently exist, validation of methods used for simulating energy extraction by large marine current turbine arrays rely upon model scale laboratory experiments. To date these have mainly focused on single devices (Myers & Bahaj 2010; A. S. Bahaj et al. 2007; A. Bahaj et al. 2007) and interactions between only a few devices (Myers & Bahaj 2012; Bahaj & Myers 2013), often with no consideration to modification of ambient flow properties such as turbulence intensity to values observed at tidal sites. For these reasons further experimental work is needed to validate large array models (Blunden & Bahaj 2007).

The performance of individual turbines in a large array is complicated by the co-existence of multiple superimposed wakes, ambient flow velocity and turbulence, wake added turbulence, local bathymetry, and the effect of the boundary layer. Such complex interactions limit our ability to correctly predict the performance of individual turbines in a large array. This work addresses this problem experimentally through a coherent set of measurements that characterise the flow through arrays of porous fences, which are used to simulate the far wake effects downstream of densely packed rows of marine current turbines at laboratory scale (Figures 1 and 2).

The paper structure is as follows; first an overview of the distributed drag approach for simulating large arrays and highlights the potential sources of error (§2). The experimental setup is then presented, outlining the procedure taken to quantify array drag, free surface elevation, bed drag and flow distribution within arrays of varying density (§3). Characterisation of the two different ambient flows used for each array is presented along with the thrust and wake characteristics of a single fence in both flows (§4). Flow is then characterised through arrays of porous fences with varying array density, λ. Analysis of flume discharge, free surface elevation, flow and fence load was used to quantify the accuracy of the distributed drag method in quantifying array drag. This was done by comparing experimental results with estimates from a depth-averaged formulation. Finally the effect

of arrays on flume bed drag was quantified using experimental measurements and a simple force balance is presented (Figure 1).

2. Regional scale modelling of large arrays
    a. Distributed drag method

Observations from windfarms (Barthelmie et al. 2005) and scaled down wind and tidal farm experiments (Chamorro & Porté-Agel 2011; Harrison 2008; Blunden et al. 2009; Coles et al. 2014) show that flow within large arrays with more than four rows exhibit equilibrium conditions, where the flow dynamics between each row repeat and the wake recovers to the same magnitude by the time it reaches the next row downstream. This creates an even distribution in drag amongst rows in the equilibrium region, allowing the windfarm to be modelled using a uniform drag distributed over the array area. In the case of windfarms, energy loss from devices, the ground and turbulent dissipation is replenished by vertical energy transport from the boundary layer above the farm, creating an energy balance (Frandsen 1992). In the case of marine current turbine arrays, the longitudinal pressure gradient driving the flow (F_i-F_o) and the weight component (F_w) is in balance with the opposing drag from porous fences, $F_{f,n}$ where n is the number of porous fences and the bed, F_b. This is demonstrated in Figure 1, which shows the control volume used for the experiments carried out in this work. The force balance is given by Equation 1 where the first two terms give the hydrostatic force at the inlet and outlet of the flume respectively where A_i and A_o are cross sectional areas at the inlet and outlet respectively.

$$\int_{z=0}^{h_i} \rho g z \, dA_i - \int_{z=0}^{h_o} \rho g z \, dA_o + F_w sin\theta - F_b - \sum_{i=1}^{n} F_{f,i} = 0 \qquad (1)$$

The distributed drag approach is well suited for modelling this equilibrium flow state as it assumes a spatially averaged balance between momentum input and drag forces. Individual turbines are not modelled and instead an effective array drag ($\sum_{i=1}^{n} F_i$) is applied uniformly over the whole array plot area.

Flow must transition to equilibrium conditions which for windfarms has been shown to take up to 3 rows (Chamorro & Porté-Agel 2011). This could potentially create an uneven drag distribution amongst fences in this region if the flow through fences 1, 2 and 3 is such that $U_1 \neq U_2 \neq U_3$ (shown in §4, Figure 10b). This is quantified in this work using load cell measurements on each fence in arrays of varying density.

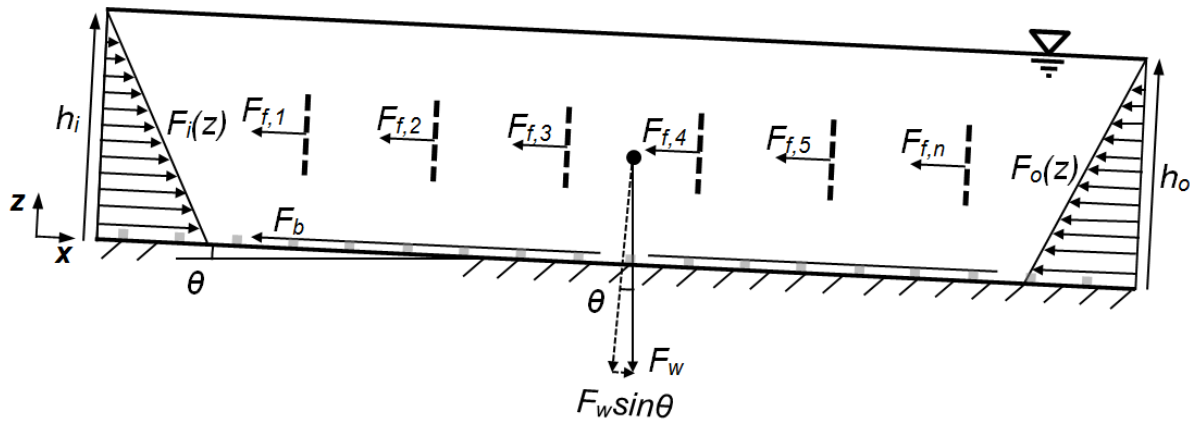

Figure 1. Elevation view of recirculating flume experiment, showing the force balance between the hydrostatic forces F_i and F_o at inlet and outlet, the drag force from the flume bed, F_b, the weight component, $F_w sin\ \theta$ and the opposing force from each porous fence, $F_{f,n}$ where n is the number of porous fences. In the case of this experiment, bed slope angle, θ=0.09°, so is exaggerated for demonstrative purposes. Square grey blocks on the flume bed are roughness strips used to enhance ambient turbulence intensity and modify flow distribution in the vertical plane.

For this work, an array is defined as 'large' if it has more than three equally spaced rows to investigate equilibrium conditions as flow develops through each row. Assuming the lateral and longitudinal spacing between devices does not exceed realistic values for spatially efficient array development of approximately 5 and 20 diameters respectively, this also satisfies another definition where turbines no longer perform as isolated turbines due to influences of the array on the flow dynamics (Vennell et al. 2015). Furthermore, multi-row array layouts will enable significant levels of energy extraction to contribute towards power generation whilst respecting the spatial constraints at specific sites. This is of particular relevance at locations where other industries such as fishing and passenger ferries operate (ABPmer 2013), as well as the potential environmental impact of large arrays such as enhanced levels of sediment transport depending on the proximity of turbines to sandbanks (Haynes 2015). These considerations make it unlikely that single row arrays spanning the width of a channel can realistically be implemented, as has been considered in the past (Garrett & Cummins 2005; Blanchfield et al. 2008; Draper et al. 2014; Walters et al. 2013). Finally, given that there is often an uneven spatial distribution in ambient kinetic energy flux over a site, such as has been shown for Alderney Race for example, multi-row arrays will enable only the most energy dense plots to be developed to increase array performance. For these reasons there is a need to understand the flow dynamics through multi row array layouts to estimate energy extraction and its environmental impact.

b. Parameterisation of effective array drag

The depth-averaged force, $\overline{F_a}$ exerted on the flow by n turbines each with swept area A_t is given by (Jean-Michel Hervouet 2007; Walters et al. 2013; Plew & Stevens 2013):

$$\overline{F_a} = \frac{1}{2}\rho|\overline{U}|\overline{U}nA_tC_t \quad (2)$$

Where $\overline{U}$ is the depth-averaged flow velocity within the array and C_t is the thrust coefficient of a single turbine. Typically for marine current turbines the thrust coefficient used is C_t=0.8 based on experiments of a scaled down device (A. S. Bahaj et al. 2007), which assume turbine thrust is a function of upstream hub height flow velocity, $U_{0,f}$. Depending on the vertical inflow distribution incident on a turbine or fence, it is conceivable that $\overline{U} \neq U_{0,f}$ as depth-averaged models do not define the flow distribution in the vertical plane. If this is the case, the estimated turbine or fence drag using a depth-averaged formulation (Equation 2) will be erroneous, given that C_t is derived from a hub height inflow. In a large array, where the slower moving wake from upstream turbines (or fences) impedes on downstream turbines, it is possible that $\overline{U} > U_{f,n}$ given that $\overline{U}$ is approximately constant throughout the array assuming the free surface slope is not significant. This is demonstrated in Figure 2, which illustrates the vertical flow distribution of three flows all with the same depth-averaged flow velocity, $\overline{U}$. Each profile is based on results using Acoustic Doppler Anemometer (ADV) measurements taken upstream and within porous fence arrays in this work. The green profile shows a typical wake flow seen between fences in an array of porous fences.

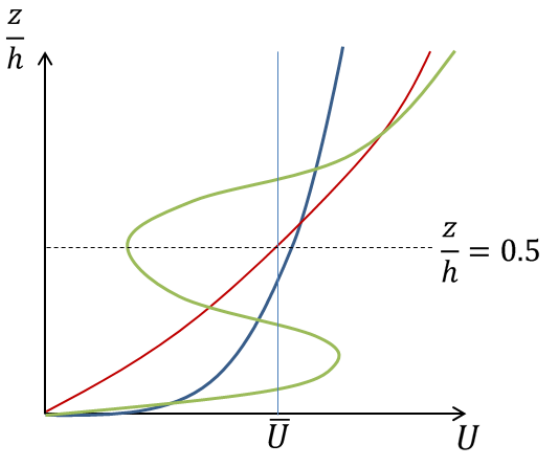

Figure 2. Illustration of typical flow distribution in the vertical plane of three flows within an array of porous fences, all with the same depth-averaged flow velocity, $\overline{U}$. Dotted horizontal line intercepts each flow profile at the centroid height of the fences, *z/h*=0.5.

The stress induced by the array over the array plot area, A_p is:

$$\tau_a = \frac{\overline{F_a}}{A_p} \tag{3}$$

This stress is added to the momentum equations in the form $\frac{\tau_a}{\rho h}$ where *h* is the flow depth, giving an extra depth-averaged source term:

$$\frac{\tau_a}{\rho h} = \frac{\lambda C_{t,a}}{2h}|\overline{U}|\overline{U} = \frac{C_e}{h}|\overline{U}|\overline{U} \tag{4}$$

Where $C_{t,a}$ is the total array drag coefficient and C_e is the effective array drag coefficient:

$$C_e = \frac{1}{2}\lambda C_{t,a} \tag{5}$$

C_e is added to the bed drag coefficient C_b to give the 2D formulation of combined drag as a shear force:

$$\frac{\tau}{\rho h} = \left(\frac{C_e + C_b}{h}\right)|\overline{U}|\overline{U} \tag{6}$$

In most cases it is assumed that the presence of a marine current turbine array has no impact on the bed drag coefficient C_b. However for windfarm modelling different approaches have been taken, such as the assumption that bed drag increases due to flow diversion in the region under the turbines (Moore 1979). The change in bed drag will be quantified using the force balance described by Equation 1.

The depth-averaged array drag is estimated from Equation 7, which will be compared with experimental values for array drag obtained from load cell measurements on each fence.

$$\overline{F_a} = \iint_{A_p} \frac{1}{2}\rho C_e\, \overline{U}^2\, dA \tag{7}$$

To summarise doubts over the accuracy of the distributed drag approach for simulating large arrays arise from three main potential sources of error. In the first, the drag force of turbines exerted on the flow is parameterised based on the assumption that turbine thrust is dependent on upstream, hub height flow velocity, $U_{0,f}$.However in depth-averaged formulations such as Equation 2, turbine drag is estimated based on a depth-averaged flow velocity $\overline{U}$. Depending on the flow distribution in the vertical plane, it is conceivable that $\overline{U} \neq U_{0,f}$, which would lead to an error in the estimated array drag. This discrepancy between $\overline{U}$ and $U_{0,f}$ will be made worse within an array where the drag of downstream fences are affected by the slower moving wake flow created by upstream fences. This can be quantified experimentally by measuring the thrust force on each fence using load cells with two different vertical inflow distributions, as outlined in §3.

Second in the transition region at the front of the array flow is developing to equilibrium conditions, creating an uneven drag distribution over the first few fences, which cannot be modelled by an evenly distributed drag. The consequence of this on the accuracy of the distributed drag approach was quantified for different array densities, again using load cell measurements on each fence.

Third it is plausible that the presence of an array could affect the bed drag coefficient, C_b in comparison with bed drag for ambient flow. This is quantified using a force balance (Equation 1) where the bed drag, F_b in the absence of turbines was compared with bed drag for flow through arrays of fences.

The effect of local blockage on the total array drag is another contributing source of error in the distributed drag method. However, it was not considered here as the effect of row blockage on fence thrust is taken into account directly through load cell measurements for each fence. Experimental analysis of the effect of local blockage on device thrust is covered in (Keogh et al. 2014).

3. Experimental method
    a. Experimental setup

A recirculating flume with 19 m working section, width w =1.37 m and depth h=0.3 m was used with porous fences positioned perpendicular to the flow (Figures 3 and 4). The fences had height, l_z=0.1 m and width w=1.34 m and were placed at centroid height z_h=0.15 m (mid depth, giving each fence a blockage ratio, ϵ=1/3. The fences had 5 x 5 mm square perforations positioned at 8 mm centres, giving a porosity β=0.39. A low porosity was chosen to ensure a significant change in elevation, flow velocity and thrust to be observed. Additionally, previous experiments using fences with higher porosity (greater open area) exhibited deformation when incident on high flow.

K-type roughness with a pitch ratio of p/k=10 was used to alter the vertical flow distribution in the vertical plane and enhance ambient turbulence intensity, where p is the pitch between roughness elements (p=0.3m) and k is the roughness height (k=0.03m). This geometry was chosen based on results in (Cui et al. 2003), which show greatest interaction between the flow in the roughness layer and the outer flow for p/k=10.

Experiments were run with seven different arrays (Table I). The first fence in each array was positioned at x=6m downstream of the flow straightener at the flume inlet. Fences were then positioned downstream at different spacings, l_f, with the last fence a distance l_a downstream of the first. Six spacings between fences were used at l_f=7l_z, 10l_z, 13l_z, 16l_z, 19l_z *and* 60l_z. This was seen as a sensible range to ensure varying degrees of interaction between fences and the wake of upstream fences so that this behaviour on the overall array drag could be investigated. The number of fences, n, was reduced with increasing row spacing, l_f, so that each array took up approximately the same plot area and length, l_a.

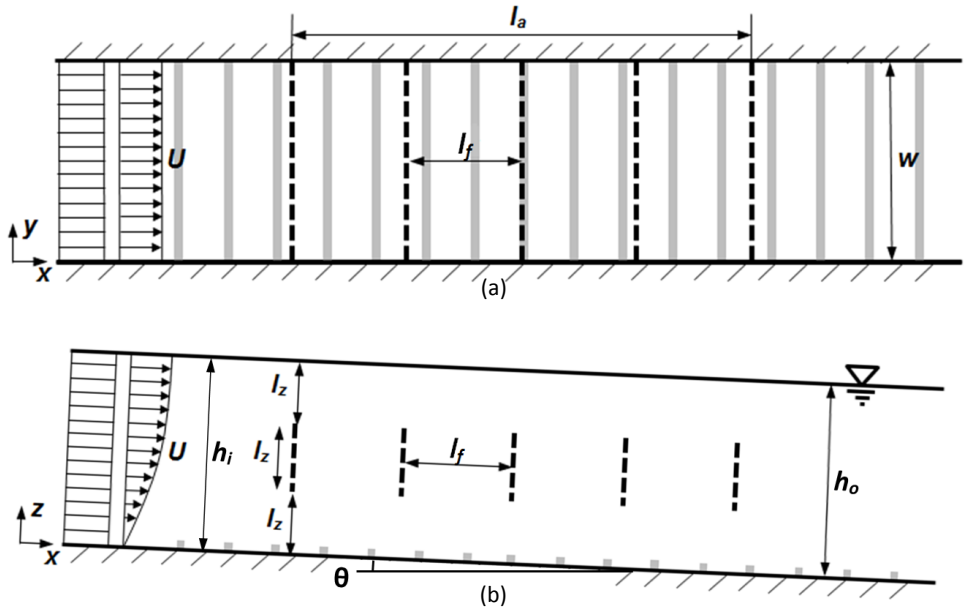

Figure 3. Experimental setup showing (a) Plan view and (b) Elevation view of porous fences positioned in the recirculating flume with flow straighteners at the inlet and bed roughness attached to the flume bed shown by grey strips. In the case of this experiment, bed slope angle, θ=0.09°, so is exaggerated for demonstrative purposes.

Initially the flume was run without porous fences to characterise the ambient flow. Centreline measurements of vertical flow distribution were obtained and the head drop between inlet and outlet was measured. Flow distribution was measured across the flume (along the y-axis) to quantify the boundary layer from the flume side walls.

Table I. Characteristics of 7 different arrays used in the experiment

Case	Array density, λ	No. fences	Spacing, l_f (l_z)	Array length, l_a (l_z)	Measurements
1	→0	1	-	-	Upstream mid depth flow velocity, $U_{0,hh}$, vertical flow velocity distribution within each array $U(x,z)$, flume discharge, Q, load on each fence, F_i, elevation drop across the array, Δz.
2	0.033	2	60	60	
3	0.070	4	19	57	
4	0.078	5	16	64	
5	0.092	6	13	65	
6	0.117	7	10	60	
7	0.159	10	7	63	

Each fence was positioned in the flow using two narrow vertical bars (2 mm) connected 0.42 m from the centre of the fence. It was assumed these had no effect on the flow along the centreline of the flume where measurements were taken.

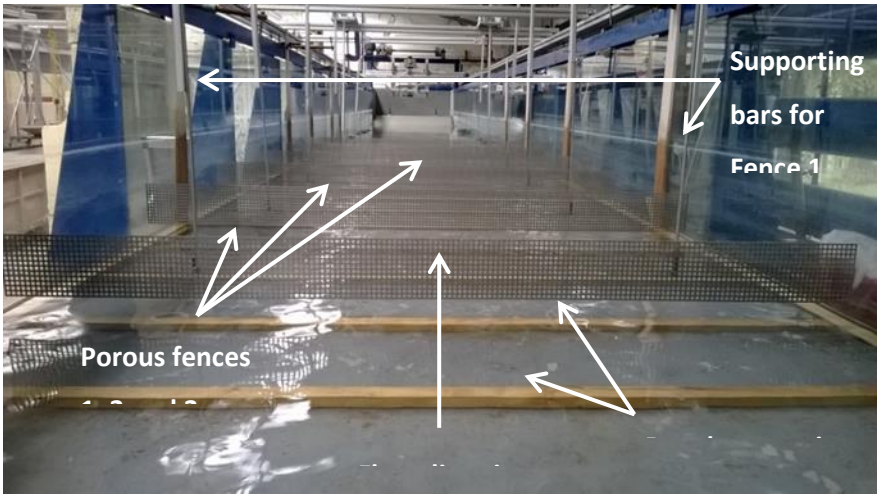

Figure 4. Porous fences positioned in the flume with row spacing, $l_f=7l_z$. Bed roughness positioned on the flume bed. Flume outlet with raised weir shown at the far end. Porous fences held in position using 2 thin vertical supporting bars.

Initially results were obtained without the added roughness on the flume bed (referred to as Case A: without roughness from now on). Once results were obtained for all experiments listed in Table I, the added bed roughness was secured to the bed and the experiments were repeated (referred to as Case B: with roughness from now on).

b. Measurements

A downward looking Acoustic Doppler Velocimeter (ADV) with 150 mm^3 sampling volume was used to measure the upstream velocity, $U_{0,f}$ at x=4m downstream of the flow straightener. The flume was adjusted to ensure a constant Froude number (based on $U_{0,f}$) of Fr= 0.13. This corresponds to an upstream mid-depth flow velocity at the centroid height of the fences, $U_{0,f}$=0.23 m/s, giving a full scale tidal velocity of approximately 2.5 m/s by scaling flow velocity with channel Froude number. A sampling frequency of 200 Hz was used to capture turbulence properties of the flow. Flow velocity profiles and turbulence intensity profiles between fences were obtained using a sideways looking ADV along the centerline of the flume at 0.1l_z, 0.3l_z, 0.6l_z, 0.9l_z, 1.2l_z, 1.5l_z, 1.8l_z, 2.2l_z and 2.7l_z above the flume bed. Three profiles between each fence were obtained, with the longitudinal spacing between profiles depending on the fence spacing, x_f. Profiles were obtained at 1l_z upstream of each fence (the closest the ADV could be positioned upstream of a fence), 3l_z downstream of each fence and one profile halfway in-between these positions to obtain the widest range in between fences.

Two load cells positioned 0.355 m either side of the centerline of each fence were used to measure the reaction on the supporting structure of each fence. An ultrasonic distance sensor (Senix Toughsonic TSPC-30 series) was used to measure flow depth along the centreline of the flume. With prior knowledge of the flume bed level, which drops almost linearly from inlet to outlet by 25mm, the free surface elevation drop across each array was obtained. A discharge meter (Sonteq IQ Plus) positioned at the flume outlet measured discharge for each case. Measurements were used alongside flow depths to obtain depth-averaged flow velocities.

c. Porous fences

At laboratory scale static porous disks/fences have been shown to reproduce the axial velocity flow field in the far wake (distances greater than approximately 5 diameters) downstream of a rotor (A. Crespo, J. Hernandez 1999) when the thrust coefficient of the disk is matched to the turbine it is simulating. Porous disks/fences dissipate energy in the wake through turbulence generation. No mechanical energy is extracted from the flow as with real turbines, so the energy contained in the near wake will be different. Additionally there is no turbine rotation which causes vortex sheets to shed from the trailing edge of the rotor blades and blade tips, generating blade vortices, however this phenomenon is also confined to the near wake region. Therefore porous fences have been chosen as a suitable method to simulate the far wake effects of turbines in large arrays, with a minimum spacing between rows of 7 diameters.

In (Cant et al. 2002) experiments were conducted to characterise jet flow through porous fences with porosity, β=0.41, 0.5, 0.57 and 0.65. The jet flow velocity U_0=40 m/s and jet width, b_0 gave a jet

Reynolds number of approximately 15,000. It was expressed that if the porosity scale is small relative to the jet scale, the flow through the fence should be independent of the details of the porosity (e.g. hole width/shape) and only on the value of porosity itself. Given that w_f is only 5% of fence height l_z, and less than 2% of the flow depth h, it was assumed that only the porosity itself was a significant parameter in determining the wake flow, not the porous geometry, however this was not investigated further. Using fence height l_f as the characteristic length scale gives a Reynolds number of 23,000. Alternatively, using the width of the square holes in each fence w_f=0.5cm as the characteristic length scale gives a Reynolds number of 1,150.

4. Results and discussion
    a. Ambient flow characterisation

Figure 5a shows data obtained experimentally of the ambient centreline vertical flow distribution using Case A: without roughness and Case B: with roughness, plotted alongside the depth-averaged flow in each case. Flow using Case A: without roughness exhibits a logarithmic boundary layer in the bottom half of the water column up to approximately z/h=0.6 above the bed, where all flow data points fit within 10% of a logarithmic distribution (Figure 5b) with roughness length, z_0=0.0002m. Based on results in (Heathershaw 1981) this is equivalent to a bed similar to sand/broken shell (z_0=0.0003). Flow distribution in the vertical plane compares well with flow data obtained in the Irish Sea (Elliott 2002), where ship mounted ADCP measurements in depths of approximately 50 m show a logarithmic profile in the lower 50-60% of the water column except at times of slack tide. Friction velocity was obtained from the gradient of the logarithmic flow distribution in the vertical plane, giving u_*=0.014 m/s, agreeing within 7% of the friction velocity measured at Colvos Passage tidal site in Washington State, USA of 0.015 m/s (Sternberg 1968). The influence bed roughness has on the turbulent properties of the outer flow was determined using the boundary Reynolds number Re_b (Equation 8).

$$Re_b = \frac{u_* k}{\nu} \tag{8}$$

Where k is the physical roughness height and ν is the kinematic viscosity of water (1.3x10^{-6} m^2/s). For hydraulically rough flow separation occurs off the bed roughness geometry to directly influence the turbulent properties of the bulk flow, as is the case in real tidal flows. Based on Re_w>70 for hydraulically rough flow, Case A: without roughness requires a minimum roughness, k_s=6.5 mm assuming u_*=0.014 m/s. Measurements of flume roughness were obtained using ultrasonic distance measurements, showing a 2 mm variation in bed surface elevation over multiple randomly selected

regions of the flume, where typically this variation occurred over a 10 mm length, therefore it is unlikely that the flow is hydraulically rough using Case A: without roughness.

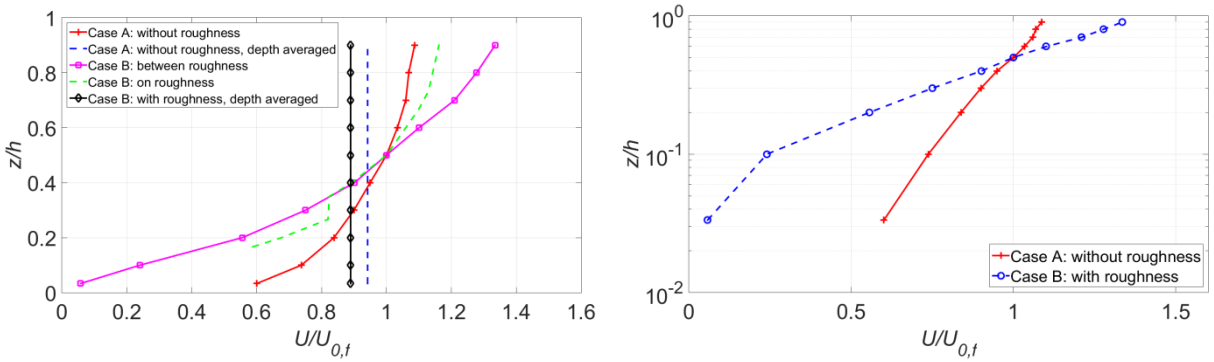

(a) (b)

Figure 5. Vertical distribution of ambient streamwise flow for flow using Case A: without roughness and Case B: with roughness with depth-averaged flow velocity, $\overline{U}$ to demonstrate the discrepancy between $\overline{U}$ and U_f. (b) Logarithmic distribution in ambient streamwise flow using Case A: without roughness and Case B: with roughness. Results are normalised by the mid depth flow velocity, $U_{0,f}$.

The fully developed vertical flow distribution using Case B: with roughness was quasi-steady, where at each roughness strip flow accelerates due to increased blockage and then slows in the cavity between each roughness strip, giving a variation in the flow profile (Figure 5a). The friction velocity was estimated as u_*=0.036 m/s, which is in close agreement with measurements In the Irish Sea of 0.031 m/s (Elliott 2002). Figure 5b shows the vertical distribution in flow is logarithmic above z/h=0.1, where the flow is displaced vertically by the roughness a distance equal to the summation of the displacement height d and roughness length z_0 in the roughness sub layer (Raupach et al. 1991). The criteria for hydraulically rough flow is met easily for Case B: with roughness according to Equation 8 given that k=0.03 m in this case.

Figure 5a shows that for both Case A: without roughness and Case B: with roughness, at $z/h \approx 0.4 \approx e^{-1}$ the depth-averaged flow velocity $\overline{U}$ is equal to the mid-fence height ambient flow velocity $U_{0,f}$. It is interesting to note that this would be expected to be the case if the flow profile was logarithmic over most of the depth [32]. This is an important point when considering the validity of the distributed drag method for modelling large multi-row arrays. If we assume the row spacing is sufficient for wakes to recover completely before reaching the next downstream row, the numerical formulation for array drag described by Equation 2 will underestimate array drag because $\overline{U} < U_{f,0}$. However if row spacing is insufficient for complete wake recovery to occur, this may indirectly improve Equation 2's accuracy of array drag if the depth-averaged flow $\overline{U}$ becomes a closer representation of the flow velocity at porous fence centroid height U_f. The depth-averaged flow velocity recorded using Case A: without roughness was $\overline{U}$=0.215 m/s, 6% lower than the mid depth (z/h=0.5) streamwise flow velocity, $U_{f,0}$= 0.225 m/s. Similarly using Case B: with roughness, $\overline{U}$ was approximately 10% lower than $U_{f,0}$. Therefore the drag from the first fence, $F_{f,1}$ will be underestimated using Equation 2, given that $F_{f,1} = f(|\overline{U}|\overline{U})$. This assumes the approach taken in (Plew & Stevens 2013), where the depth-averaged flow is used to calculate the force on a turbine (or fence in this case) using Equation 2, and that the force on a fence is related to flow at hub height (mid depth) only. This error is quantified in §4 by comparing the estimated array drag from the experiment obtained from load cell measurement on each porous fence with results from Equation 2.

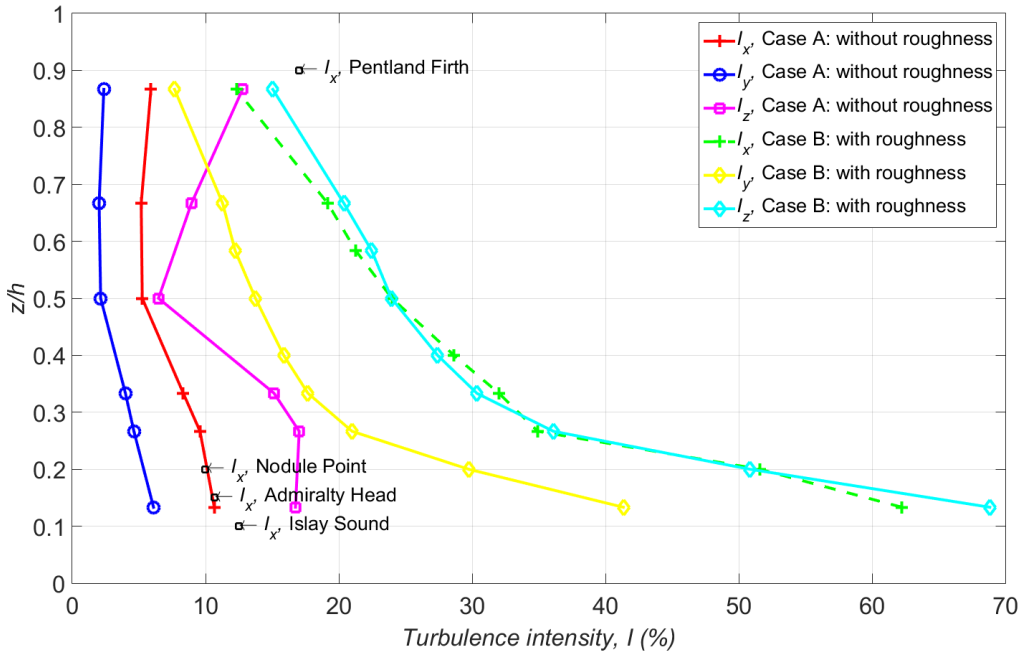

Figure 6. Vertical distribution of ambient streamwise (x), transverse (y) and vertical (z) turbulence intensity using Case A: without roughness and Case B: with roughness obtained experimentally from ADV measurements.

Figure 6 shows the ambient centreline streamwise, transverse and vertical turbulence intensity distribution in the vertical plane using Case A: without roughness and Case B: with roughness, using Equation 9, where U_i is the mean velocity and u_i' is the fluctuating velocity component where *i=x, y, z*, correspond to the longitudinal, lateral and vertical directions respectively.

Results for flow using Case A: without roughness agree within 5% of measurements taken at Nodule Point, Admiralty Head (Thomson et al. 2012) and the Sound of Islay (Milne et al. 2013) in the lower 20% of the water column.

$$I_i = 100\sqrt{\frac{\langle u_i'^2 \rangle}{U_i^2}} \tag{9}$$

Maximum recorded flow velocitys of 1.8 m/s at *z/h*=0.2 and 3.2 m/s at *z/h*=0.14 were obtained at Nodule Point and Admiralty Head respectively whilst in the Sound of Islay the mean flow reached 2.5 m/s at *z/h*=0.1. Transverse and vertical turbulence intensities compare less well, with (Milne et al. 2013) observing approximately 9-10 % and 7-8% turbulence intensities in the transverse and vertical directions respectively, giving a ratio of streamwise turbulence intensity to transverse and vertical intensities of 1:0.75:0.56 for the Sound of Islay. Flume measurements give the same ratio as 1:0.57:1.57, showing significantly higher turbulence intensity in the vertical relative to the streamwise and transverse directions.

Case B: with roughness significantly enhanced turbulence intensity in the streamwise, transverse and longitudinal directions. Eddies shed off the leading edge of each roughness strip increased turbulence intensity to enhance mixing between the flow in the roughness layer and the outer flow, augmenting momentum exchange (Cui et al. 2003). This was found in (Trembanis et al. 2004), where energetic vortices shed by pronounced ripples over a rough surface enhanced vertical transfer of momentum. Values observed here are more representative of higher energy sites such as the Pentland Firth, where streamwise turbulence intensities of 17% were recorded close to the free surface (Hardwick et al. 2015).

Both Case A: without roughness and Case B: with roughness demonstrated a relatively flat lateral flow profile across the flume, measured at height *z/h*=0.5. The boundary layer on either wall extends no further than 0.15m so does not encroach on centreline measurements.

Table II shows experimental results used to estimate the ambient bed drag, $F_{b,0}$ from Equation 1 using Case A: without roughness and Case B: with roughness. Bed drag $F_{b,0}$ using Case A: without

roughness was very low; within the same order as the precision of depth measurements h_i and h_o (±1 mm) making $F_{b,0}$ highly sensitive to the magnitude of the resultant hydrostatic force F_i-F_o. Case B: with roughness increases bed drag significantly as would be expected.

Table II. Experimental measurements of inlet depth h_i taken at x=5m, outlet depth h_o taken at x=13m, depth-averaged inlet and outlet flow velocity U_i and U_o, hydrostatic forces F_i and F_o, the weight component F_w and bed drag force F_b using the force balance described by Equation 1.

Roughness case	h_i **(m)**	h_o **(m)**	U_i **(m/s)**	U_o **(m/s)**	F_i **(N)**	F_o **(N)**	$F_w sin\vartheta$ **(N)**	$F_{b,0}$ **(N)**
A : without roughness	0.295	0.310	0.249	0.237	585	646	63	2
B: with roughness	0.289	0.301	0.223	0.209	559	607	61	14

b. Single fence

Observations of wake flow downstream of a single fence using Case A: without roughness (Figure 7a) demonstrate that momentum transfer between the wake and bypass flow above and below the fence was insufficient to recover the flow downstream of the fence, where at a distance of $18l_z$ downstream of the fence, U_f=0.82$U_{0,f}$. As a consequence of this, additional fence(s) positioned downstream of the first will be subjected to this type of change in incident velocity. Based on previous experimental results of the wake downstream of a porous disk (Myers & Bahaj 2010) where wakes were shown to persist over twenty diameters downstream, it is highly likely that this will be a feature of full-scale arrays, as has been shown to be the case from full scale windfarm measurements (Barthelmie et al. 2005).

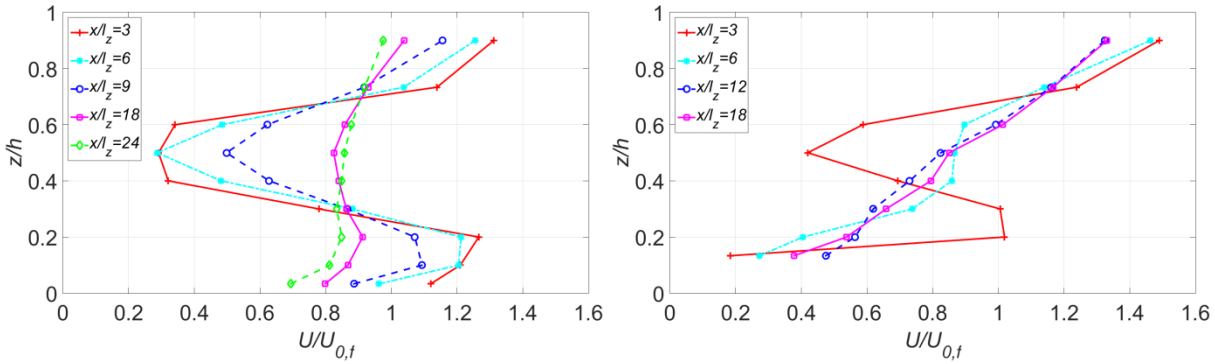

Figure 7. Vertical flow distribution at positions downstream of a single fence positioned perpendicular to the flow using (a) Case A: without roughness (b) Case B: with roughness. Results normalised by the hub height flow velocity, $U_{0,f}$ 20l_z upstream of the fence.

For Case B: with roughness, higher ambient turbulence intensity enhanced momentum transfer between the wake and bypass flow to improve near wake recovery in comparison with flow over Case A: without roughness. This is shown in Figure 7b and Figure 8, where at a distance of 5l_z downstream of the fence the mid depth flow velocity had recovered to approximately the same magnitude as the flow in Case A: without roughness by 18l_z downstream. The consequence of this is that for arrays with row spacing l_f<15l_z, the force incident on downstream fences is likely to be higher in comparison with flow in Case A: without roughness, giving a greater total array force, $\bar{F}_a$ from Equation 2, assuming the same upstream hub height flow velocity, $U_{0,f}$ and number of fences n.

In the far wake where x>20l_z, flow using Case A: without roughness and Case B: with roughness converge to a similar value of flow velocity within 5%, giving U_f=0.87$U_{0,f}$. Therefore when x>20l_z the wakes are independent of ambient turbulence intensity (Figure 8). Coincidentally the far wake deficit shown in Figure 8 is approximately the same magnitude as the difference between ambient depth-averaged flow velocity $\bar{U}$ and ambient flow velocity at porous fence centroid height $U_{f,0}$ shown in Figure 7. This may improve the accuracy of the depth-averaged formulation of array drag given by Equation 2 when modelling a multi row array (as opposed to a single isolated fence) because depth-averaged flow velocity $\bar{U}$ becomes a better representation of flow velocity in the far wake of a porous fence U_f where the next downstream fence is positioned.

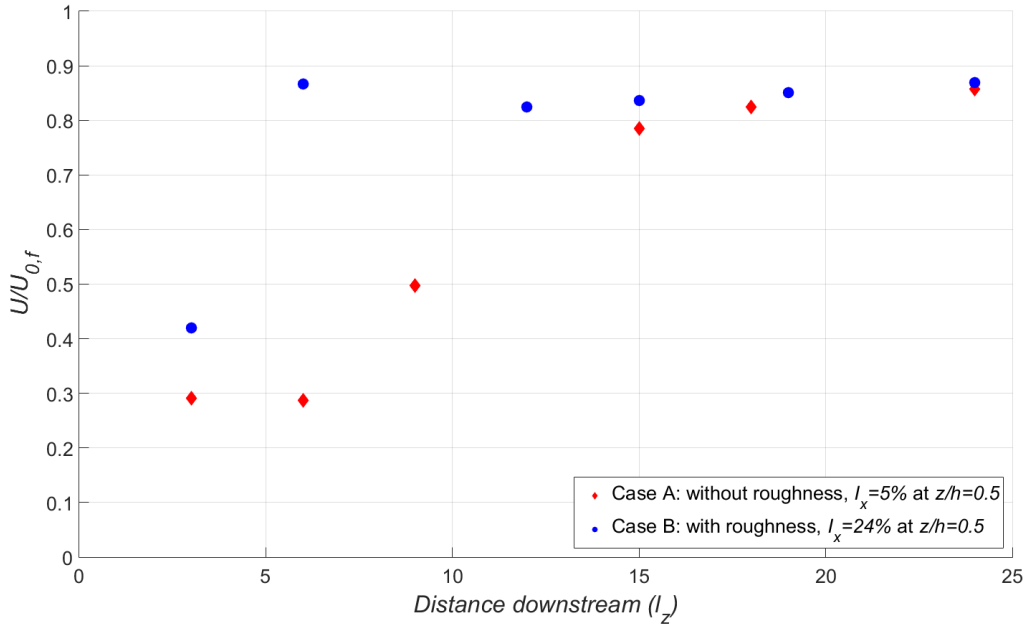

Figure 8. Mid depth wake recovery downstream of a single fence using Case A: without roughness and Case B: with roughness, normalised by hub height flow velocity, $U_{0,f}$ 20I_z upstream of the fence.

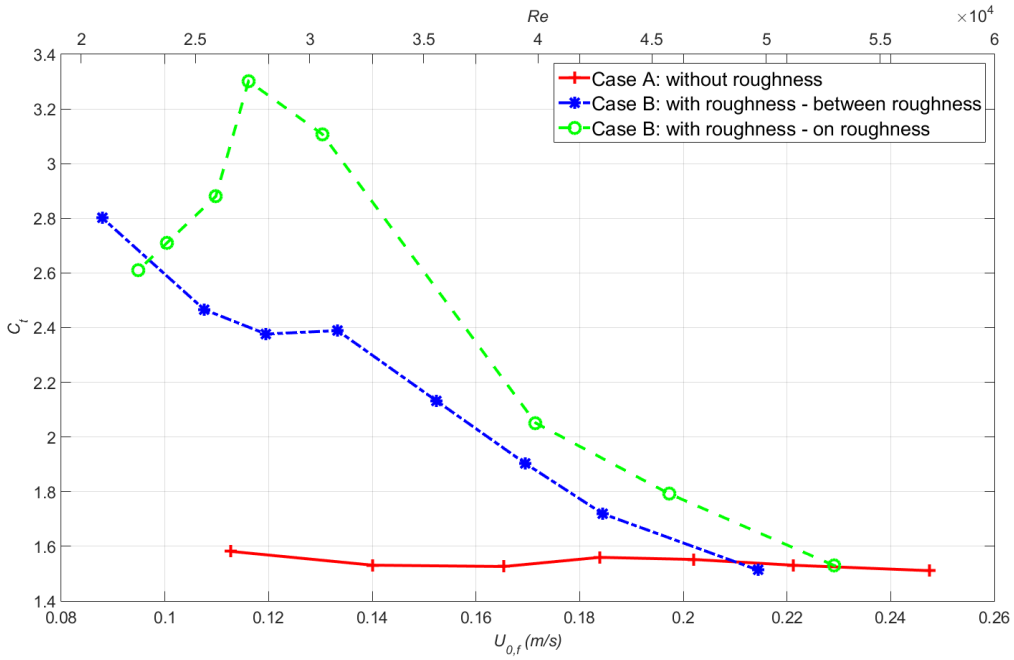

Figure 9. Variation in thrust coefficient, C_t of a single fence with upstream Reynolds number (using hydraulic radius as the characteristic length scale and $U_{0,f}$ as the characteristic velocity scale) using Case A: without roughness and Case B: with roughness. Upstream flow velocity $U_{0,f}$ is plotted on the second x axis.

The thrust coefficient of a single fence, C_t remained approximately constant with upstream flow velocity, $U_{0,f}$ for flow over Case A: without roughness (Figure 9). In contrast C_t reduced significantly for flow over Case B: with roughness with increasing upstream flow velocity, both when the fence was positioned half way between roughness strips and directly above a roughness strip in more constrained flow. This is likely to be related to the eddies shed off the roughness, which are a function of $U_{0,f}$.

For Case B: with roughness, with $U_{0,f}$>0.15 m/s the thrust coefficient, C_t reduced linearly with $U_{0,f}$. For numerical estimates of array drag in §4d, an average linear relationship between flow and C_t was used based on $\overline{U} > 0.15$ m/s, giving a linear decrease in C_t with increasing Reynolds number for Re>4 x 10^4:

$$C_t = 3.5 - \frac{Re}{2.5 \times 10^4} \tag{10}$$

c. Array flow characterisation

Figure 10a shows the flow distribution in the vertical plane 6l_z downstream of fences 1-5 using Case A: without roughness with array 7 (λ=0.155, l_f=7l_z). Out of all fences in the array, flow at centroid height (z/h=0.5) through Fence 1, $U_{f,1}$ was highest as it was not in the wake of any upstream fences, so was positioned in ambient flow. As a result the reduction in flow momentum through Fence 1 was also greatest, creating a high wake flow deficit directly downstream of the fence so that the flow velocity at mid depth hitting Fence 2 was significantly reduced (i.e. $U_{f,2}$<$U_{f.1}$). The bypass flow above and below the fence bottom edge where z/h<0.33 and z/h>0.66 respectively increased to satisfy continuity.

In the region between Fence 1 and 3, the flow was transitioning to an equilibrium state where the drag from fences and the bed is in balance with the longitudinal pressure gradient and weight component that drives flow through the array, as described by Equation 1. In this transition region at Fence 2 the depth-averaged flow, $\overline{U}$ was approximately 250% greater than the mid depth flow velocity, U_f because of the presence of the wake from Fence 1. This would incur a significant error in the depth-averaged force attributed to Fence 2 in a depth-averaged drag formulation such as Equation 2 using high density porous Fence arrays. For array 7 this is also true in the equilibrium region downstream of Fence 3, where the depth-averaged flow velocity $\overline{U}$ overpredicts the flow velocity through each porouce fence at z/h=0.5 by 25%.

By Fence 3 the flow reached an equilibrium described by Equation 1 where the opposing forces on the flow (the thrust on Fence *n*, $F_n = f(C_t, \overline{U}^2, A_t)$ and bed drag, $F_b = f(\overline{U}^2, \lambda, z_0)$) were closely balanced against the longitudinal pressure gradient and weight component, F_w driving the flow so that the wake downstream of successive fences recovers to approximately the same magnitude, $U_{f,n}$.

$$U_{f,n} - \sum U_{f,n} < \Delta U \tag{11}$$

For all arrays, equilibrium conditions were reached after three rows (Figure 10b, 11b), where the flow velocity through each remaining downstream equilibrium fence (downstream of the three transition fences) was within ±2.5% of the flow speed through the final fence. This is referred to as the equilibrium flow velocity, $U_{f,\infty}$ from now on.

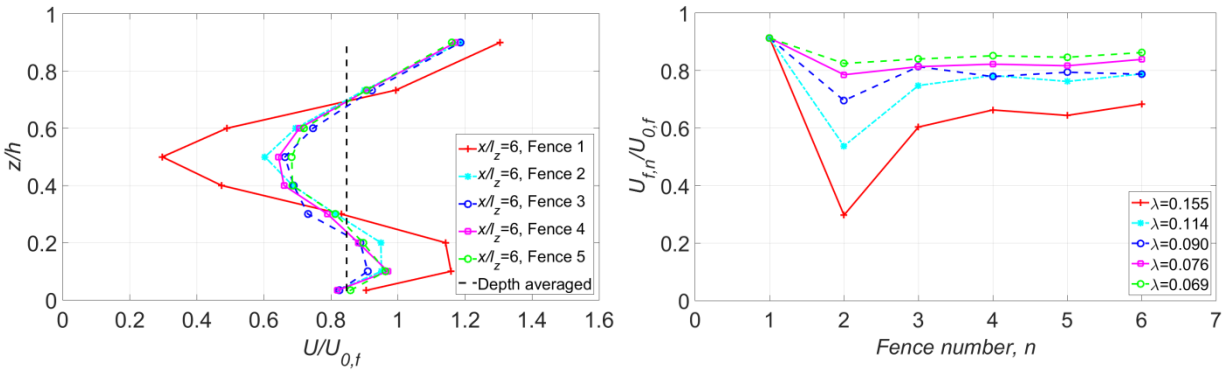

(a) (b)

Figure 10. (a) Vertical flow distribution $1l_z$ upstream of fences *n*=1,2,3,4,5, using array 5 (λ=0.155, x_f=7l_z) with Case A: without roughness b) Mid depth flow through successive fences for all 5 arrays using Case A: without roughness. All results normalised by the mid depth flow velocity, $U_{0,f}$ 20l_z upstream of Fence 1.

For each array the highest flow was through Fence 1, $U_{f,1}$ as it was not obstructed by upstream fences (Figure 10b). Downstream of Fence 1 the greatest velocity deficit occurs, so that the lowest flow is through Fence 2, $U_{f,2}$. The wake deficit downstream of Fence 1 is most noticeable for high array density cases where row spacing l_f is small, reducing the longitudinal distance available for wake recovery. To limit the reduction in drag and therefor increase the generated power from row 2, it would be beneficial to increase the row spacing between Fence 1 and 2, with further rows added with gradually reduced row spacing. This was not investigated further here but is the subject of ongoing work.

Since the wake flow is not modelled in depth-averaged numerical models (as shown in Figure 2), the distributed drag approach cannot be expected to accurately predict the drag on fences within the transition region when an uneven distribution in drag between fences occurs. However, analysis of load cell measurements on each fence shows that the average force on fences within the transition region (fences 1-3) (Equation 12) is within 10% of the average force on each fence in the equilibrium region (fence 4 onwards) (Equation 13) and within 5% of the average force on each fence in the whole array (Equation 14) over all array densities (Table III). Therefore, even within the transition zone where there is a highly uneven distribution of drag amongst the first three fences, the average force amongst porous fences within this region was still representative of the total array average.

$$\bar{F}_{trans} = \frac{1}{3}\sum_{i=1}^{3} F_{f,i} \tag{12}$$

$$\bar{F}_{eq} = \frac{1}{n-3}\sum_{i=4}^{n} F_{f,i} \tag{13}$$

$$\bar{F}_{array} = \frac{1}{n}\sum_{i=1}^{n} F_{f,i} \tag{14}$$

Table III. Average force amongst fences in the transition region (Equation 12), equilibrium region (Equation 13) and whole array (Equation 14) for arrays usingCase A: without roughness.

$\boldsymbol{\lambda}$	$\boldsymbol{\bar{F}_{trans}}$	$\boldsymbol{\bar{F}_{eq}}$	$\boldsymbol{\bar{F}_{array}}$
0.069	5.69	5.44	5.57
0.076	5.22	5.00	5.10
0.090	4.93	4.59	4.73
0.114	4.89	4.47	4.63
0.155	4.24	4.17	4.19

The magnitude of $U_{f,\infty}$ increased with increased row spacing, l_f (reduced array density, λ) for Case A: without roughness and Case B: with roughness as shown in Figure 10b and Figure 11b respectively

due to greater wake recovery between fences. $U_{f,\infty}$ also increases with increased ambient turbulence intensity (for flow over Case B: with roughness), which enhanced mixing between the wake and bypass flow hence improving wake recovery (Blackmore et al. 2013) (Figure 11b and 12). The magnitude of $U_{f,\infty}$ was also effected by other features such as fence drag coefficient, C_t and ambient turbulent length scales, however these were not varied in the experiments due to time constraints.

For lower array densities and/or higher ambient turbulence intensity, the difference between $U_{f,1}$,$U_{f,2}$ and $U_{f,3}$ in the transition zone was less pronounced because of greater wake recovery (Figure 10b and 11b). For Case B: with roughness, the flow recovered to approximately the same magnitude by the point it reached each successive fence, hence removing the transition zone completely so that the flow incident on each fence was equal (Figure 11b). This resulted in an even distribution in drag amongst all fences apart from Fence 1 which was out of the wake of upstream fences.

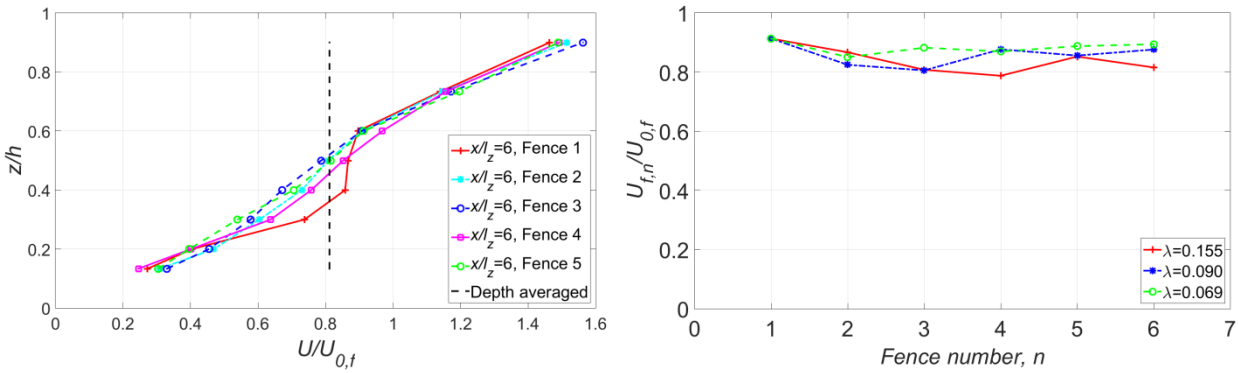

(a) (b)

Figure 11. (a) Vertical flow distribution $6l_z$ upstream of fences 1,2,3,4,5 using array 5 (λ=0.155, l_f=7l_z) with Case B: with roughness (b) Mid depth flow through successive fences for all 5 arrays using Case B: with roughness. All results normalised by the hub height flow velocity, $U_{0,f}$ $20l_z$ upstream of the fence.

Figure 12 shows that for high ambient turbulence intensity flow using Case B: with roughness, there was a 6% reduction in equilibrium velocity $U_{f,\infty}$ as array density was increased from λ=0.07 to λ=0.16. Over the same array density range, porous fence arrays in the lower ambient intensity flow using Case A: without roughness gave a 23% reduction in equilibrium velocity$U_{f,\infty}$. To determine whether it is beneficial to add an additional row to a marine current turbine array in a pre-defined plot area, the power generated by the added row must be greater than the reduction in power generated by the existing rows due to the reduction in equilibrium flow velocity with increased array density. This can only be understood with site specific array optimisation given that wake recovery is dependent on ambient turbulence intensity.

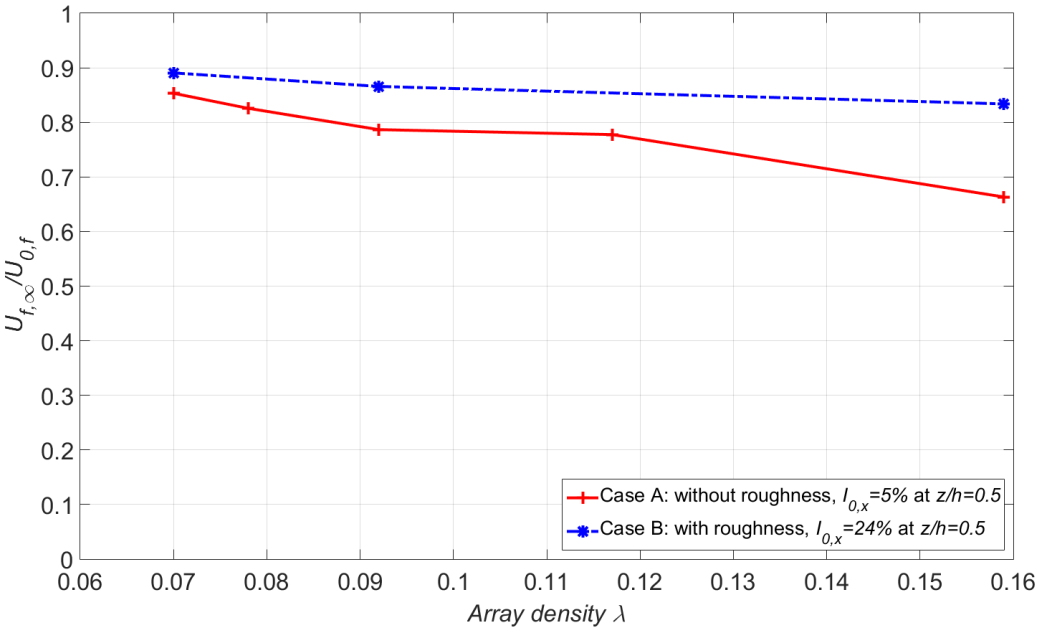

Figure 12. Variation in equilibrium flow velocity $U_{f,\infty}$ with array density and ambient turbulence intensity using Case A: without roughness and Case B: with roughness. Results normalised by upstream mid depth flow velocity $U_{0,f}$.

d. Force balance

Ultrasonic distance measurements along the centreline of the flume show that flow depth upstream of any given array was less than the flow depth downstream so that depth increased across the array. Since the flume bed elevation drops approximately linearly with distance downstream of the inlet (S_0=0.0015), free surface elevation also dropped across the arrays. As fences were added, the total array drag opposing the flow increased. This resulted in an increase in upstream depth with array density, whilst downstream depth was independent of array density so remained constant for all cases. This led to an increase in the hydrostatic force driving flow in the *x* direction with increasing array density, λ to counter the increase in array drag, F_a. Results from the force balance (Equation 1) are shown in Table IV and V for Case A: without roughness and Case B: with roughness respectively. For Case A: without roughness, the estimated bed drag was very low, as was the case for the ambient flow regime in §4a. The force balance implies that the bed drag is insignificant in comparison to hydrostatic and weight component force terms. In some cases, F_b<0 which is physically incorrect. Given that F_b was so close to zero in all cases and highly sensitive to small error in inlet and outlet depth measurements h_i and h_o, it is thought that this is the reason for this inconsistency.

Table IV. Experimental measurements with Case A: without roughness of inlet depth h_i taken at x=5m, outlet depth h_o taken at x=13m, depth-averaged inlet and outlet flow velocity U_i and U_o, hydrostatic forces F_i and F_o, the weight component F_w, array force F_a and bed drag force F_b using a force balance (Equation 1).

Case	**λ**	h_i **(m)**	h_o **(m)**	$\overline{U}_i$ **(m/s)**	$\overline{U}_o$ **(m/s)**	F_i **(N)**	F_o **(N)**	$F_w sin\vartheta$ **(N)**	F_a **(N)**	F_b **(N)**
1	→0	0.295	0.310	0.242	0.231	585	646	63	6	~0
2	0.032	0.297	0.310	0.242	0.231	593	646	63	12	~0
3	0.069	0.299	0.310	0.228	0.220	601	646	63	22	~0
4	0.076	0.301	0.310	0.235	0.229	609	644	64	25	~0
5	0.090	0.303	0.311	0.238	0.232	615	648	64	29	~0
6	0.114	0.303	0.310	0.248	0.242	617	646	64	33	~0
7	0.155	0.305	0.310	0.235	0.232	625	646	64	46	~0

Table V. Experimental measurements with Case B: with roughness of inlet depth h_i taken at x=5m, outlet depth h_o taken at x=13m, depth-averaged inlet and outlet flow velocity U_i and U_o, hydrostatic forces F_i and F_o, the weight component F_w, array force F_a and bed drag force F_b using a force balance (Equation 1).

Case	**λ**	h_i **(m)**	h_o **(m)**	$\overline{U}_i$ **(m/s)**	$\overline{U}_o$ **(m/s)**	F_i **(N)**	F_o **(N)**	$F_w sin\vartheta$ **(N)**	F_a **(N)**	F_b **(N)**
1	→0	0.290	0.300	0.234	0.226	565	605	61	6	16
2	0.032	0.292	0.300	0.228	0.222	573	605	62	11	19
3	0.069	0.295	0.300	0.226	0.222	583	605	62	19	21
4	0.076	0.296	0.300	0.219	0.216	587	605	62	24	20
5	0.090	0.297	0.301	0.239	0.236	593	609	62	32	14
6	0.114	0.298	0.300	0.212	0.210	595	605	62	32	21
7	0.155	0.296	0.295	0.212	0.213	589	585	62	49	16

In Figure 12 empirical array drag is plotted using the array drag coefficient, $C_{t,a}$, defined as:

$$C_{t,a} = \frac{F_a}{\frac{1}{2}\rho|\overline{U}|\overline{U}A_a}$$

(15)

Where A_a is the total frontal area of all fences in the array and F_a is the array force obtained from load cell measurements. This was compared with a numerical estimate for array drag coefficient using Equation 2 with C_t obtained from the performance of an individual fence (Figure 9) as is commonly done in literature for individual turbines (Plew & Stevens 2013; Karsten et al. 2012). For Case A: without roughness , $C_{t,a}$=1.54 was used. For Case B: with roughness, $C_{t,a}$ was defined using Equation 10.

For Case A: without roughness numerical array drag coefficient was predicted within 10% of experimental results for array density, λ<0.07 (Figure 13). This is in part due to the fact that depth-averaged flow velocity underestimates the mid –depth flow (Figure 5), so that within the array where fence flow reduces due to upstream wakes (as was seen downstream of a single fence in Figure 8), a depth-averaged flow velocity becomes a reasonable representation of the flow through each fence. In the region where λ<0.07, increasing array density gives a linear increase in array drag. As array density exceeds this value, numerical array drag starts to overestimate experimental results. This is caused by the slow moving wake from upstream fences which impedes on downstream fences, reducing the equilibrium flow velocity, so hence reducing fence drag. Depth-averaged flow velocity does not account for this so that $\overline{U} > U_f$, as was shown in Figure 10a for array case 7.

For Case B: with roughness (Figure 13) experimental and numerical results agreed within 10% over the whole array density range. This was due to enhanced wake recovery as a result of augmented ambient turbulence intensity in the near wake as was shown in Figure 8 for the wake downstream of a single porous fence. In this case wake flow impeded less on downstream fences so that $\overline{U} \approx U_f$, as was seen in Figure 11a for array case 7. Under these conditions there is an even distribution in drag over all fences, eliminating the transition region at the front of the arrays (Figure 11b) with the exception of Fence 1.

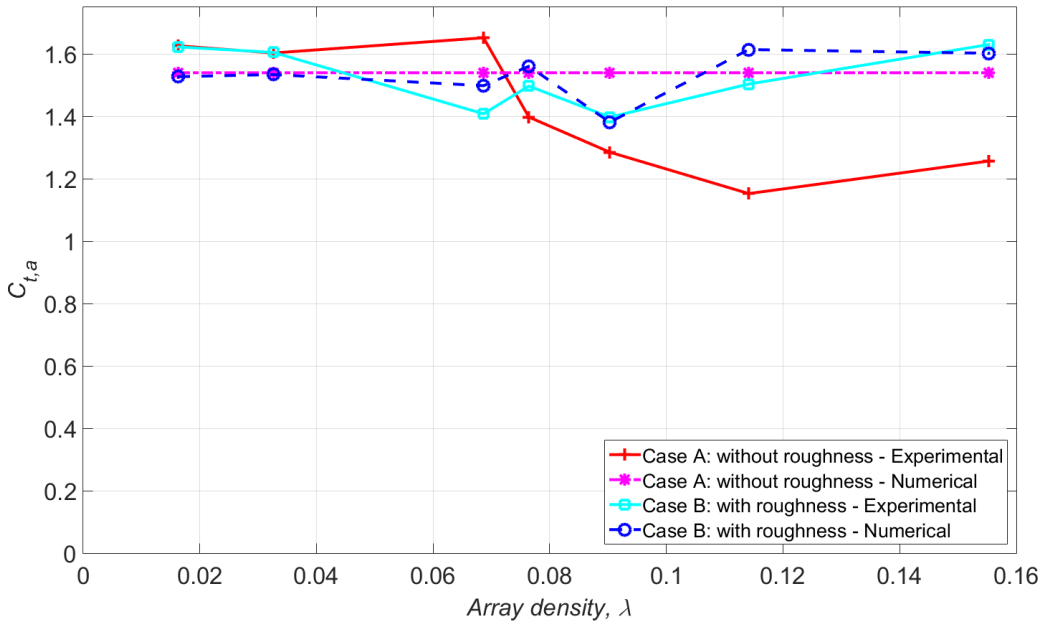

Figure 13. Variation in total array drag coefficient, $C_{t,a}$ with array density using Case A: without roughness and Case B: with roughness. Experimental and numerical expression for $C_{t,a}$ given by Equation 10 and §4b respectively.

A depth-averaged numerical estimate for effective array drag coefficient, C_e was calculated using Equation 5 for all array cases. Results for C_e were then compared with experimental data, where $C_e = \frac{1}{2}\lambda C_{t,a}$ and $C_{t,a}$is the array thrust coefficient plotted in Figure 13 using Equation 15. Results (Figure 14) show the same trend as in Figure 13 where for Case A: without roughness and array density λ<0.07, estimated numerical array drag using Equation 2 and 5 agreed within 7% of experimental results. Any further increase in λ resulted in an error exceeding 10%, where numerical array drag was overestimated because the depth-averaged flow, $\overline{U}$ within the array does not account for the variation in flow velocity in the vertical plane caused by fence wake, so that $\overline{U} > U_f$.

For flow using Case B: with roughness (Figure 14) reasonable agreement between experimental and numerical results within 5% was observed for all array densities with the exception of λ=0.07. This is thanks in part to the depth-averaged approach, which for ambient logarithmic boundary layer flow under-predicts the flow velocity at fence centroid height, as was shown in Figure 5a. Since in the arrays wakes impede on downstream porous fences hence reducing the flow velocity through each fence, the depth-averaged flow speed becomes a closer representation of fence flow velocity inside the arrays when array density λ<0.07. Since depth-averaged flow velocity $\overline{U}$ is used in Equation 2 to estimate array drag numerically, this gives better agreement with load cell measurements obtained experimentally. Nevertheless the parameterisation of array drag described by Equation 2 appears to be robust within the realistic array density range of λ<0.07, which corresponds to a lateral and

longitudinal spacing between turbines of just 1 and 5.5 diameters respectively (excluding support structure drag). Caution should be taken when the inflow is not logarithmic, and when porous fences/disks/turbines are positioned at different heights, as this will alter the level of agreement between the depth-averaged flow velocity and the flow velocity through the centroid height of the fence/disk/turbine.

Importantly, the change in depth between the porous array inlet and outlet results in a change in depth-averaged flow velocity through the array. In the most extreme case of array 1 using Case A: without roughness, there is a 3.5% change in $\overline{U}$, which is significant for approximations of numerical array drag, C_e as already discussed. This was accounted for by averaging $\overline{U}^2$ over array length by assuming a linear free surface elevation drop across each array. This assumption has been verified using the backwater curves method (Chow 1959) and a simple 2D numerical model that simulates the linear rate of change of free surface elevation over a distributed drag for flow in an open channel with the same input parameters as the experiment.

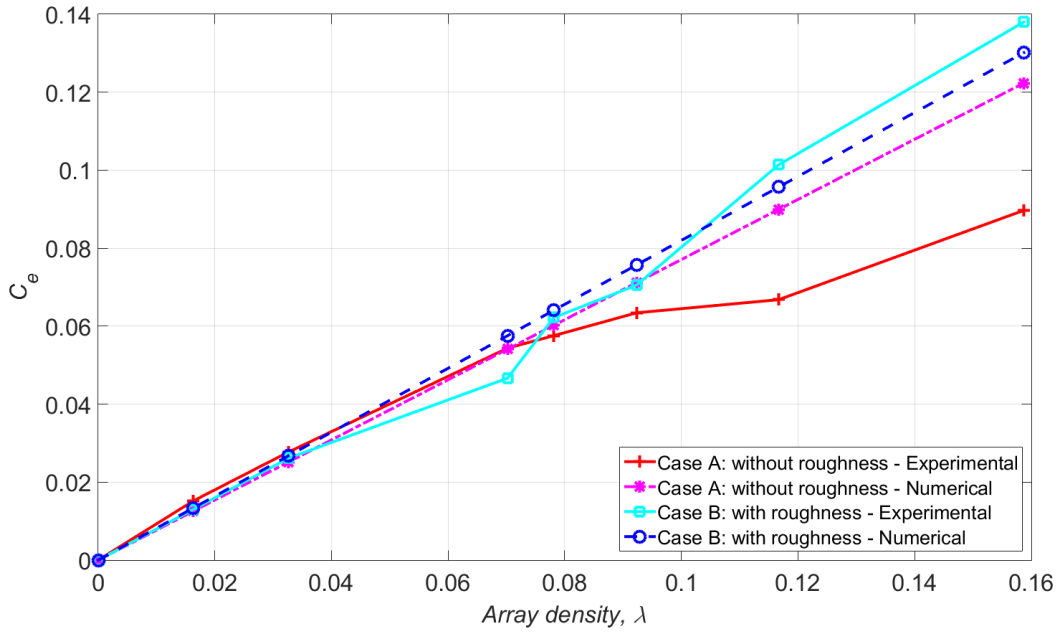

Figure 14. Experimental and numerical variation in effective array drag coefficient, C_e for all arrays using Case A: without roughness. and Case B: with roughness.

e. Bed drag

Experimental results from Table II and V were used with the force balance described by Equation 1 to estimate the change in bed drag opposing the flow as a result of the presence of arrays (F_b-$F_{b,0}$). Results obtained for Case A: without roughness were not used in this analysis as bed drag was very low, causing some unphysical cases where F_b <0. This was due to the sensitivity of the force balance,

where any small error in upstream or downstream depth h_i and h_o resulted in the hydrostatic force F_i-F_o being under/overestimated significantly relative to the small level of bed drag F_b. Results for Case B: with roughness show that over the realistic array density range (λ<0.07), increasing array density increases bed drag coefficient C_b significantly (Figure 15), where by porous array case 3 (λ=0.07) the new bed drag coefficient C_b was 150% of the ambient bed drag coefficient $C_{b,0}$.

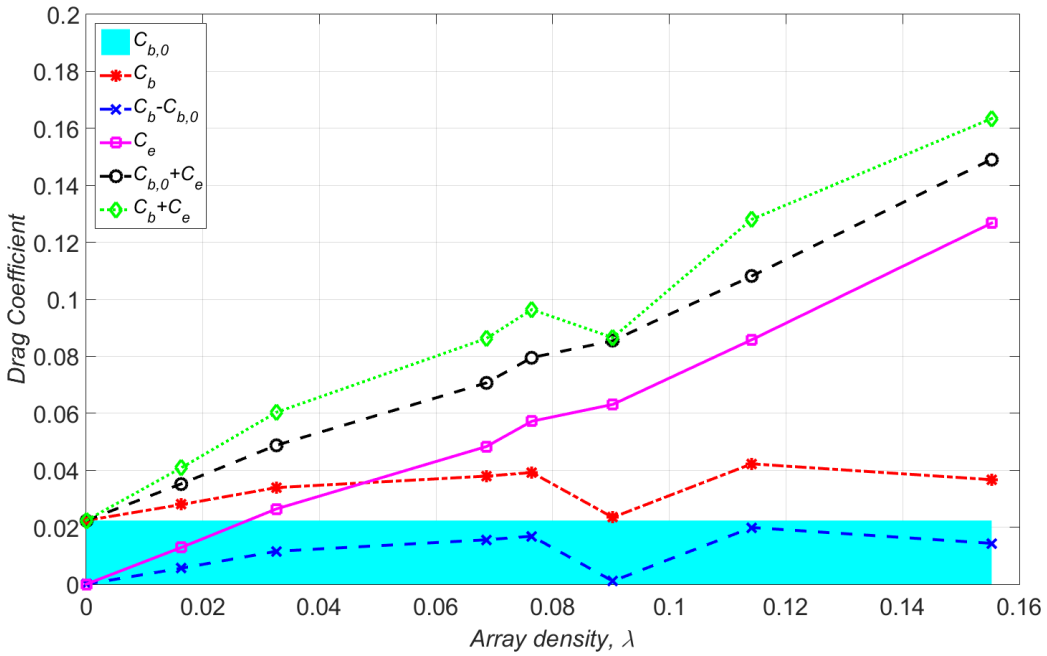

Figure 15. Change in bed drag C_b, array drag C_e, total drag coefficient C_b+C_e, added bed drag coefficient C_b-$C_{b,0}$, total added drag coefficient $C_{b,0}$+C_e (neglecting change in bed drag) and total added drag coefficient C_b+C_e as a result of increasing array density using Case B: with roughness . Ambient bed drag coefficient $C_{b,0}$ is also shown for comparison.

The added bed drag coefficient C_{b+}=C_b-$C_{b,0}$ due to the presence of the porous fence arrays was a significant proportion of the ambient bed drag coefficient $C_{b,0}$, especially at high array density where for λ>0.07, C_{b+} was of the same magnitude as $C_{b,0}$ (Figure 15). Added bed drag coefficient C_{b+} was also a significant proportion of array drag coefficient C_e, especially at low array density when C_e was low relative to the ambient bed drag $C_{b,0}$ (Figure 15). The error in total added drag (due to the presence of porous fence arrays) $C_{b,0}$+ C_e incurred by not accounting for the increase in bed drag C_{b+} ranged between 10-20% over the porous fence array densities used. As a consequence neglecting the added bed drag C_{b+}=C_b-$C_{b,0}$ will lead to array drag and therefore estimates for array power being underestimated. Additionally this will lead to a misrepresentation of the change in surrounding flow dynamics and array wake that could have a knock on effect when quantifying the environmental impact of arrays at a specific site using regional scale depth-averaged hydrodynamic modellingThe added bed drag coefficient C_{b+} is attributed in part to an increase in bed shear in the bottom third of

the water column directly below the bottom edge of each fence (z/h<0.33) close to the bed. Figure 16 shows the difference in spatially averaged shear profile $u'w'$ for porous fence array case 7 (λ=0.159, l_f=7l_z), 5 (λ=0.092, l_f=13l_z) and 3 (λ=0.070, l_f=19l_z) for both Case A: without roughness and Case B: with roughness where the profiles are an average of measurements between each equilibrium (out of the transition region). For both roughness cases as array density increased, the spatially averaged shear stress $u'w'$ directly below the fence and close to the bed (z/h<0.33) also increased, which is commonly used to estimate bed drag (Biron et al. 2004).

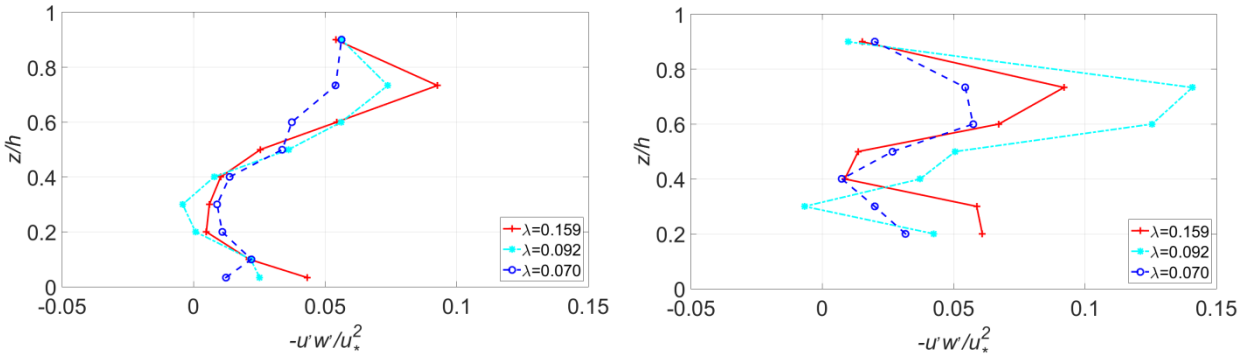

Figure 16. Vertical distribution of shear stress $u'w'$ downstream of equilibrium fences using (a) Case A: without roughness and (b) Case B: with roughness. Results are normalised by ambient friction velocity squared.

The presence of the roughness strips reduced the open area under each fence, causing greater flow acceleration in this region compared to flows over Case A: without roughness (Figure 7). The interaction between this accelerated flow and the frontal area of each roughness strip increased the contribution of bed form drag opposing the flow (also called pressure drag) given by the difference in pressure between the front and back faces of each roughness element. Large Eddy Simulations (LES) of flow over k-type roughness show that pressure drag is significantly greater than the frictional drag component acting on roughness surface, where recirculation downstream of each roughness element causes the frictional drag to act in the flow direction (Cui et al. 2003). Form drag was less significant using Case A: without roughness as the frontal face of the roughness is significantly smaller, so protrudes far less into the oncoming flow.

For Case B: with roughness measurements of shear stress directly above the roughness strips at z/h=0.133 varied greatly, where roughness strips come up to z/h=0.1. This is likely to be because of the highly complex flow close to the roughness strips, where separation and reattachment occurs between adjacent roughness strips, throwing large eddies out into the outer flow (Cui et al. 2003), causing a local maximum in shear stress. Given that ADV measurements were obtained at different

longitudinal positions relative to the roughness strips between each fence (some in closer proximity to the roughness strips than others depending on the phasing of roughness strips to fences), high variability in shear stress was observed. For this reason *u'w'* at *z/h*=0.133 was discarded in Figure 15b.

As an aside, Figure 16 shows a region of high shear above the fence top edge height (*z/h*=0.75) where the slow moving wake meets the fast moving bypass flow. At high array density the spatially averaged shear at this height is relatively high because there are many fences causing this interaction. To reduce array density the number of fences *n* within the plot area was reduced, causing this interaction to occur less frequently, resulting in a reduction in spatially averaged shear stress between the upper wake and bypass flow. For Case B: with roughness array case 5 needs repeating as unexpectedly it does not follow this trend (Figure 15b). This could be the consequence of Reynolds number as upstream flow velocity was slightly higher in this case.

Results indicate that when modelling arrays, the added bed drag C_{b+} must be accounted for, otherwise the total drag C_b+C_e in Equation 6 will be underestimated. This will reduce the impact the array has on the flow dynamics in terms of flow reduction inside the array, making it likely that extracted array power will be overestimated. Results in Figure 15 show the error in total added drag coefficient (C_b+C_e) could be as high as 20% for very rough beds when form drag is significant as was seen for Case B: with roughness used here. For smoother beds (with lower z_0 and u_*) this error is likely to reduce because the bed drag is a smaller proportion of the overall drag (C_b+C_e), as was seen for Case A: without roughness, so any change in bed drag C_{b+} will have a less significant effect.

Further work is required to confirm these relationships given the scattered nature of some data points, such as the decrease in bed drag coefficient for array case 5 (λ=0.092) shown in Figure 15, which could be linked to the drop in array drag coefficient shown in Figure 13. Work is ongoing to develop a better physical grounding based also on the hydrodynamic characteristics of the bed (z_0), the vertical spacing between the bed and the turbine rotor and the ambient inflow conditions.

5. Conclusions

The validity of the distributed drag method for simulating energy extraction by large, regular, multi-row arrays of marine current turbines has been investigated. This was done by quantifying three potential sources of error using flume experiments with arrays of porous fences to simulate the wakes downstream of densely packed marine current turbine rows.

The first source of error is the discrepancy between the depth-averaged flow velocity $\overline{U}$ and the flow velocity at the centroid height of each fence/turbine U_f, which is typically used to determine

fence/turbine drag using Equation 2. For the two ambient inflows used in the flume experiments, each had a different logarithmic distribution in flow velocity in the vertical plane (Figure 5) that agreed well with measurements taken at real tidal sites in the Irish Sea (Elliott 2002)and Covos Passage, USA (Sternberg 1968). For these cases and any other logarithmic flow velocity distribution, the flow speed at height *z/h*=0.4 is equal to the depth-averaged flow velocity $\overline{U}$. This meant that the depth-averaged flow velocity under predicted flow speed at fence centroid height (*z/h*=0.5) by 6-10%. This observation also means that when simulating single devices/rows (out of the wake of other devices/fences) using the distributed drag approach in logarithmic boundary layer flow, the validity of force estimates using Equation 2 is dependent on the turbine/fence height, where if the centroid height is *z/h*=0.4, the depth-averaged flow speed obtained in a 2D hydrodynamic model is an accurate representation of the flow at turbine/fence centroid height.

Multi-row arrays of porous fences were positioned in the flume and load cell measurements of the drag on each fence were compared with a numerical formulation for array drag (Equation 2) used in the distributed drag method. In the low ambient flow case (Case A: no roughness), experimental results for array drag coefficient using the load cell measurements showed agreement with results from the numerical formulation of array drag (Equation 2) within 10% for arrays with density $\lambda<0.07$ (Figure 13). For these lower array densities, the depth-averaged flow velocity was a reasonable representation of the average flow through fences in each array.

As the row spacing between porous fences was reduced to increase array density further, the wake from upstream fences encroached significantly on downstream fences, reducing the flow speed through each fence U_f. Since there was no significant change in depth-averaged flow velocity $\overline{U}$ through the arrays, the depth-averaged approach over-predicted the flow velocity through each fence, in the highest density case by 250% (Figure 10a). This led to the array drag being over-predicted by the numerical formulation of array drag.

In the high ambient turbulence case (Case B: with roughness), roughness strips spanning the flume width were secured to the bed to enhance turbulence intensity to levels similar with those observed at high energy sites such as the Pentland Firth (Figure 6). This enhanced wake recovery downstream of the porous fences significantly by augmenting momentum exchange between the wake and bypass flow. For these cases load cell measurements of array drag showed agreement with results from the numerical formulation of array drag (Equation 2) within 10% over all array densities (Figure 13). ADV measurements of flow velocity within each array showed that over all array densities, the flow within porous fence rows never recovered to its upstream value. Since the depth-averaged flow speed under-predicted the ambient flow velocity at fence centroid height, the depth-

averaged flow speed became a better representation of the flow velocity through each fence, therefore improving accuracy in results for the numerical formulation of array drag using Equation 2.

The second source of error was the uneven distribution in drag amongst porous fences within the transition region covering the first three rows of each array. This was most prevalent for high density arrays, where row spacing was insufficient for reasonable wake recovery, causing an initially high drag on Fence 1 and then a significant drop in drag on Fence 2 (Figure 10b). The distributed drag method is unable to simulate this as it requires an even distribution in drag amongst all fences, which only occurs in the equilibrium region downstream of the third fence. Nevertheless, load cell measurements show that the average force on transition fences was still closely matched with the average drag on equilibrium fences, meaning that the error in drag on Fence 1 and 2 is effectively cancelled out.

The third source of error investigated was the change in bed drag that may occur as a result of positioning an array in the flow. Results from a simple force balance (Equation 1) show that for Case B: with roughness, adding porous fence arrays gave an increase in bed drag coefficient relative to the ambient case of up to 95%, which is equivalent to an error in the total added drag coefficient (including array drag coefficient C_e) of 20% (Figure 15). This increase in bed drag was attributed to the enhanced flow below the porous fences which increased the pressure drag on the roughness strips on the flume bed. In Case A: without roughness there was no noticeable change in bed drag because a smooth bed was used, making pressure drag insignificant.

Overall results are encouraging given that in reality array density would not be expected to exceed λ=0.07, the limit for which experimental results agreed with the numerical formulation of array drag within 10%. This gives confidence in depth-averaged resource scale hydrodynamic modelling and the ability of the distributed drag method to accurately model energy extraction from large marine current turbine arrays, which is a useful tool for regulators, developers and investors to develop specific sites. However care must be taken in quantifying the ambient vertical distribution in flow velocity to understand the level of agreement between the depth-averaged velocity $\overline{U}$ and the flow velocity at fence/turbine centroid height U_f that determines drag. Additionally for rough beds there is likely to be a significant increase in bed pressure drag with the inclusion of large arrays which must be accounted for.

Acknowledgements

This work is part of the activities of the Energy and Climate Change Division and the Sustainable Energy Research Group at the University of Southampton (www.energy.soton.ac.uk). It is also supported by ESPRC under the Supergen Marine research programme.

References

[1] A. S. Bahaj, “Generating electricity from the oceans,” Renew. Sustain. Energy Rev., vol. 15, no. 7, pp. 3399–3416, Sep. 2011.
[2] T. A. Adcock, S. Draper, and T. Nishino, “Tidal power generation - A review of hydrodynamic modelling,” Proc. Inst. Mech. Eng. Part A J. Power Energy, vol. 229, pp. 755–771, 2015.
[3] S. Bourban, M. Liddiard, N. Durand, S. Cheeseman, and A. Baldock, “High Resolution Modelling Of Tidal Resources , Extraction And Interactions Around The UK,” in 1st Marine Energy Technology Symposium (METS13), 2013, p. 8.
[4] R. Ahmadian and R. A. Falconer, “Assessment of array shape of tidal stream turbines on hydro-environmental impacts and power output,” Renew. Energy, vol. 44, pp. 318–327, 2012.
[5] S. Draper, T. A. Adcock, A. G. L. Borthwick, and G. T. Houlsby, “Estimate of the tidal stream power resource of the Pentland Firth,” Renew. Energy, vol. 63, pp. 650–657, Mar. 2014.
[6] J. Thiebot, P. Bailly du Bois, and S. Guillou, “Numerical modeling of the effect of tidal stream turbines on the hydrodynamics and the sediment transport e Application to the Alderney Race (Raz Blanchard), France,” vol. 75, pp. 356–365, 2015.
[7] R. A. Walters, M. R. Tarbotton, and C. E. Hiles, “Estimation of tidal power potential,” Renew. Energy, vol. 51, pp. 255–262, Mar. 2013.
[8] D. R. Plew and C. L. Stevens, “Numerical modelling of the effect of turbines on currents in a tidal channel – Tory Channel, New Zealand,” Renew. Energy, vol. 57, pp. 269–282, Sep. 2013.
[9] R. Karsten, A. Swan, and J. Culina, “Assessment of arrays of in-stream tidal turbines in the Bay of Fundy,” Proc. R. Soc. A, vol. 371, pp. 189–203, 2012.
[10] R. H. Karsten, J. M. McMillan, M. J. Lickley, and R. D. Haynes, “Assessment of tidal current energy in the Minas Passage, Bay of Fundy,” Proc. Inst. Mech. Eng. Part A J. Power Energy, vol. 222, no. 5, pp. 493–507, Aug. 2008.
[11] J. Blanchfield, C. Garrett, A. Rowe, and P. Wild, “Tidal stream power resource assessment for Masset Sound, Haida Gwaii,” Proc. Inst. Mech. Eng. Part A J. Power Energy, vol. 222, no. 5, pp. 485–492, Aug. 2008.
[12] G. Sutherland, M. Foreman, and C. Garrett, “Tidal current energy assessment for Johnstone Strait, Vancouver Island,” Proc. IMechE Part A J. Power Energy, vol. 221, no. 2, pp. 147–157, Jan. 2007.
[13] L. E. Myers and A. S. Bahaj, “Experimental analysis of the flow field around horizontal axis tidal turbines by use of scale mesh disk rotor simulators,” Ocean Eng., vol. 37, no. 2–3, pp. 218–227, Feb. 2010.
[14] A. S. Bahaj, A. F. Molland, J. R. Chaplin, and W. M. J. Batten, “Power and thrust measurements of marine current turbines under various hydrodynamic flow conditions in a cavitation tunnel and a towing tank,” Renew. Energy, vol. 32, no. 3, pp. 407–426, Mar. 2007.
[15] A. Bahaj, L. Myers, M. Thomson, and N. Jorge, “Characterising the wake of horizontal axis marine current turbines,” in Proc. 7th EWTEC, 2007.
[16] L. E. Myers and A. S. Bahaj, “An experimental investigation simulating flow effects in first generation marine current energy converter arrays,” Renew. Energy, vol. 37, no. 1, pp. 28–36, Jan. 2012.
[17] A. S. Bahaj and L. E. Myers, “Shaping array design of marine current energy converters through scaled experimental analysis,” Energy, vol. 59, pp. 83–94, 2013.

[18] L. Blunden and A. Bahaj, “Tidal energy resource assessment for tidal stream generators,” … , Part A J. Power Energy, 2007.
[19] R. Barthelmie, S. Frandsen, L. Jensen, M. Mechali, and P.-E. Rethore, “Verification of an efficiency model for very large wind turbine clusters,” Copenhagen Offshore Wind 2005 Conf., 2005.
[20] L. P. Chamorro and F. Porté-Agel, “Turbulent flow inside and above awind farm: A wind-tunnel study,” Energies, vol. 4, no. 11, pp. 1916–1936, 2011.
[21] M. E. Harrison, “Comparisons of a Large Tidal Turbine Array Using the Boundary Layer and Field Wake Interaction Models,” in 2nd International Conference on Ocean Energy (ICOE 2008), 2008, no. October, pp. 1–9.
[22] L. S. Blunden, W. M. J. Batten, M. E. Harrison, and A. S. Bahaj, “Comparison of boundary-layer and field models for simulation of flow through multiple-row tidal fences,” in 8th European Wave and Tidal Energy Conference, 2009, pp. 1–10.
[23] D. S. Coles, L. S. Blunden, and A. S. Bahaj, “Experimental testing for spatially averaged numerical modelling of large marine current energy converter arrays,” in Asian Wave and Tidal Energy Conference, 2014.
[24] S. Frandsen, On the wind speed reduction in the center of large clusters of wind turbines, vol. 39, no. 1–3. 1992, pp. 251–265.
[25] R. Vennell, S. W. Funke, S. Draper, C. Stevens, and T. Divett, “Designing large arrays of tidal turbines: A synthesis and review,” Renew. Sustain. Energy Rev., vol. 41, pp. 454–472, 2015.
[26] ABPmer, “Alderney Regional Environmental Assessment of Renewable Energy : Scoping Report Alderney Commission for Renewable Energy Alderney Regional Environmental Assessment of Renewable Energy : Scoping Report,” 2013.
[27] S. G. Haynes, “The Effects of Array Installation upon the Morphology of a Headland Associated Linear Sandbank,” pp 49-55, PhD: Transfer report, 2015.
[28] C. Garrett and P. Cummins, “The power potential of tidal currents in channels,” R. Soc. A, vol. 461, pp. 2563–2572, 2005.
[29] D. S. Coles, L. S. Blunden, and A. S. Bahaj, “The potential for electricity generation using large tidal stream turbine arrays in Alderney Race (Raz Blanchard),” to be submitted to Energy, 2016.
[30] Jean-Michel Hervouet, Hydrodynamics of Free Surface Flows modelling with the finite element method. pp. 89-90: WILEY, 2007.
[31] D. J. Moore, “Depletion of available wind power by a large network of wind generators,” in 2nd International Conference on Future Energy Concepts, 1979, pp. 302–305.
[32] B. Keogh, L. Myers, and A. Bahaj, “Tidal stream turbine performance with changes in channel size and geometry,” in Grand Renewable Energy 2014, 2014, pp. 1–4.
[33] J. Cui, V. C. Patel, and C.-L. Lin, “Large-eddy simulation of turbulent flow in a channel with rib roughness,” Int. J. Heat Fluid Flow, vol. 24, no. 3, pp. 372–388, 2003.
[34] S. F. A. Crespo, J. Hernandez, “Survey of Modelling Methods for Wind Turbine Wakes and Wind Farms,” Wind Energy, vol. 24, pp. 1–24, 1999.
[35] R. Cant, I. Castro, and P. Walklate, “Plane jets impinging on porous walls,” vol. 32, pp. 16–26, 2002.
[36] A. D. Heathershaw, “Comparisons of measured and predicted sediment transport rates in tidal currents,” Mar. Geol., vol. 42, no. 1–4, pp. 75–104, 1981.
[37] A. J. Elliott, “The Boundary Layer Character of Tidal Currents in the Eastern Irish Sea,” Estuar. Coast. Shelf Sci., vol. 55, no. 3, pp. 465–480, Sep. 2002.
[38] R. W. Sternberg, “Friction factors in tidal channels with differing bed roughness,” Mar. Geol., vol. 6, no. 3, pp. 243–260, 1968.
[39] M. R. Raupach, R. A. Antonia, and S. Rajagopalan, “Rough-wall turbulent boundary layers,” Appl. Mech. Rev., vol. 44, no. 1, p. 1, 1991.
[40] J. Thomson, B. Polagye, V. Durgesh, and M. C. Richmond, “Measurements of turbulence at two tidal energy sites in Puget Sound, WA,” IEEE J. Ocean. Eng., vol. 37, no. 3, pp. 363–374, 2012.

[41] I. A. Milne, R. N. Sharma, R. G. J. Flay, S. Bickerton, and P. T. R. S. A, “Characteristics of the turbulence in the flow at a tidal stream power site,” R. Soc., no. January, 2013.
[42] A. C. Trembanis, L. D. Wright, C. T. Friedrichs, M. O. Green, and T. Hume, “The effects of spatially complex inner shelf roughness on boundary layer turbulence and current and wave friction: Tairua embayment, New Zealand,” Cont. Shelf Res., vol. 24, no. 13–14, pp. 1549–1571, 2004.
[43] J. Hardwick, I. Ashton, and L. Johanning, “Field characterisation of currents and near surface eddies in the Pentland Firth,” in 4th Oxford Tidal Energy Workshop, 2015.
[44] T. Blackmore, W. M. J. Batten, and A. S. Bahaj, “Turbulence generation and its effect in LES approximations of tidal turbines,” in EWTEC 2013, 2013.
[45] V. Chow, “Open-channel hydraulics,” New York: McGraw-Hill, 1959.
[46] P. M. Biron, C. Robson, M. F. Lapointe, and S. J. Gaskin, “Comparing different methods of bed shear stress estimates in simple and complex flow fields,” Earth Surf. Process. Landforms, vol. 29, no. 11, pp. 1403–1415, 2004.

Appendix I Energy journal paper

Journal paper submitted to the Energy journal in January 2017. The paper gives an in depth presentation of results from hydrodynamic modelling using the English Channel model to quantify the maximum average power potential of Alderney Race, Casquets and Big Russel, along with a study of simultaneous energy extraction scenarios at each site to quantify the level of interaction (i.e. destructive/ beneficial interference) between the three sites. Results are presented in Chapter 7.

Assessment of the energy extraction potential from tidal sites within the Channel Islands

D. S. Coles[1], L. S. Blunden and A. S. Bahaj

Energy and Climate Change Division, Sustainable Energy Research Group, (www.energy.soton.ac.uk)
Faculty of Engineering and the Environment, University of Southampton, UK
[1]d.coles@soton.ac.uk

Tidal flows around the Channel Islands contain a significant energy resource that if harnessed could provide electrical power to the Channel Islands, the UK and France. We have developed a new 2D hydrodynamic model of the English Channel which gives an improvement to the temporal and spatial resolution of the ambient flow in comparison with previous regional scale resource assessments. The ambient flow was characterised to identify suitable sites, resulting in a reduction in total development area of up to 80% compared with previous studies. Estimates for upper bound energy extraction confirm that Alderney Race contains the majority of the Channel Islands resource, giving a maximum potential of 5.1 GW, which exceeds a previous estimate for the Pentland Firth by 35%. This is followed by Casquets (0.47 GW) and then Big Roussel (0.24 GW). Our work shows that energy extraction at Alderney Race has a constructive impact on the resource at Casquets, and that the sensitivity to added drag at each site with respect to energy extraction is highly dependent on bathymetry and the proximity of coastlines. These results have implications for the overall resource development within the Channel Islands, where care is needed to account for site-site interaction.

Keywords
Tidal power, marine currents, Alderney Race, Casquets, Big Roussel, Channel Islands

1. Introduction

The Channel Islands are a collection of five main islands located to the west of the Cotenin Peninsula in Normandy, France (Figure 1). In reports commissioned by the Carbon Trust (Environmental Change Institute 2005; Black and Veatch 2005) five sites were identified as suitable for tidal energy development based on tidal current velocities (mean neap peak and mean spring peak velocities), bathymetry and available area. These include three main sites of medium to high potential (Alderney Race, Casquets and Big Roussel) and two low potential sites off the North West coast of Guernsey and off the North East coast of Jersey.

Estimates for energy extraction at these sites vary significantly depending on the method used and the scheme areas and array design considered. This is demonstrated in Table I, which summarises the range of results from previous assessments of Alderney Race, Casquets and Big Roussel. In general, past studies have relied on low spatial and temporal resolution flow data, which may have impacted on the derived results. Additionally methods such as the farm and kinetic flux approaches adopted in the past (Energy Technology Support Unit 1993; European Commission 1996), (Black and Veatch 2005) assume no change to the ambient flow field with the inclusion of turbines (i.e. no consideration into blockage effects), bringing into question the validity of these results. Other studies assume a 5% wake deficit within turbine arrays (Bahaj & Myers 2004), yet they still do not consider the array scale blockage caused by the added array drag. For further information on the farm and kinetic flux methods we recommend the reader consults the references given in Table I.

We recognise that previous studies have provided a knowledge enhancement for estimating the potential from the Channel Islands sites. However, the varied approach to site characterisation, energy extraction model and scarcity of reliable flow data makes it difficult to make direct comparisons of the resource at each location. To address this problem a well-established method

for quantifying an upper bound for energy extraction (termed the maximum average power potential) was implemented here for sites in the Channel Islands, as has been conducted in literature for the Pentland Firth in Scotland (Draper et al. 2014) and Minas Passage (Karsten et al. 2008; Walters et al. 2013), Johnstone Strait (Sutherland et al. 2007) and Masset Sound (Blanchfield et al. 2008) in Canada.

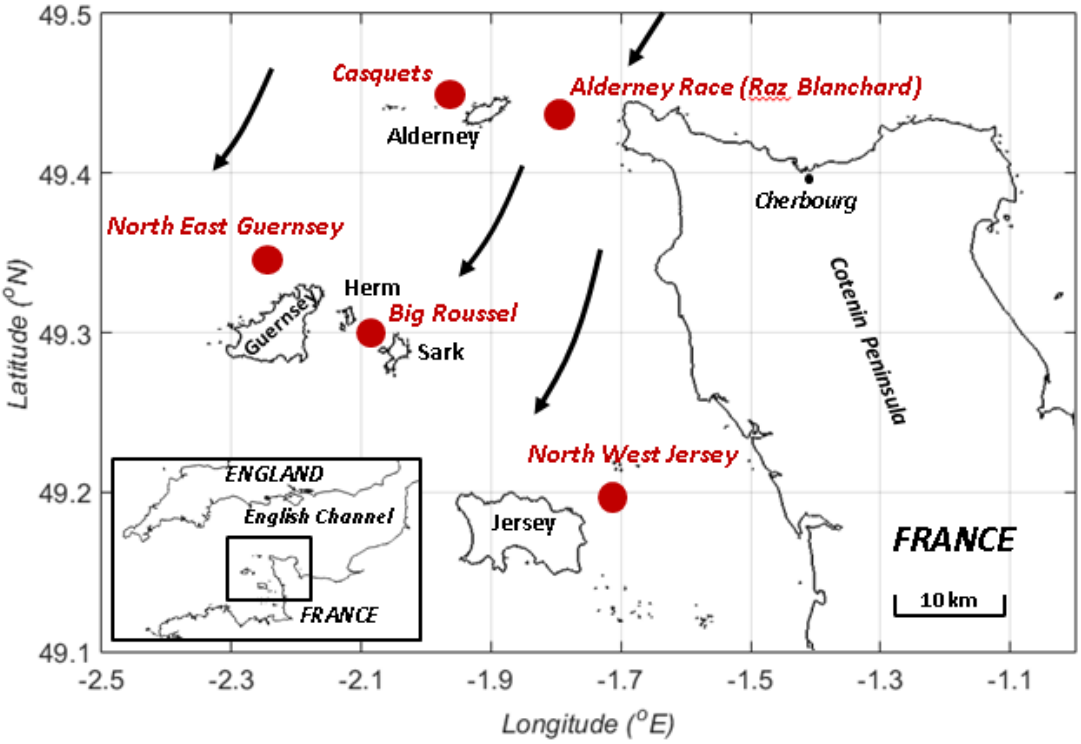

Figure 1. Location of potential sites for tidal energy development in the Channel Islands (Environmental Change Institute 2005), located off the west coast of Normandy, France. Arrows show the direction of dominant ebb tide. The relative location of the Channel Islands to the UK and France is shown inset.

The maximum average power potential gives an upper bound for the total energy extracted at a given site (2007). This is not to be confused with the *available* power, which is the fraction of the extracted power that can be removed by the turbines (which is used directly for electricity generation) (Draper et al. 2014). To simplify the problem, drag is distributed uniformly over regions called 'energy extraction zones' to extract momentum at each site. The energy extraction zone spans the entire width of each site. To simulate the effect of adding more turbines, the drag distributed over the energy extraction zone is increased, resulting in an increase in the hydrostatic pressure force driving the flow through the zone, seen as an increase in the difference between free surface elevation upstream and downstream of the energy extraction zone. The added drag reduces the volume flux through the energy extraction zone. Assuming alternative flow paths exist, the increase in hydraulic resistance of the turbines causes flow to divert around the area of added drag, taking the path of least resistance. The energy dissipated by the array is the product of the head loss across the array and the volume flux through the energy extraction zone. Initially when drag is added the increase in head drop has a dominating effect over the decrease in volume flux, causing the dissipated energy to increase. As further drag is added, the reduction in volume flux has an increasingly significant effect, where at the upper bound it suppresses the increase in head drop, causing the dissipated power to decrease, hence giving an upper bound for power potential.

The information in the paper is organised as follows: in §2 a new 2D hydrodynamic model of the English Channel is presented, which allows simulation of flow around the Channel Islands at significantly improved spatial and temporal resolution compared with previous regional scale studies summarised in Table I. Model validation results are presented in §3 using elevation data at 13 ports around the domain, as well as flow data obtained from Acoustic Wave and Current Profiler (AWAC) deployments in Alderney Race. Such combination of validation datasets gives confidence in the model's ability to accurately recreate tidal flows around the Channel Islands.
Ambient flow distribution results are presented in §4a, which were used to quantify the distribution in mean kinetic power density at Alderney Race, Casquets, Big Roussel, North West Guernsey and North East Jersey. In §4b estimates for the power potential at suitable sites are given, where

Table I. Results from literature showing methods used, array capacity and energy generation from Alderney Race, Casquets and Big Roussel.

Method	Studies	Array scheme area or cross section	Array capacity (GW)	Annual electricity generation (TWh/year)
Alderney Race				
Farm	ETSU (Energy Technology Support Unit 1993), European Commission (European Commission 1996), Bahaj *et al.* [10], Myers *et al.* [11]	65 km^2 - 102 km^2	0.84-2.4	1.35-7.4
Kinetic energy flux	Black and Veatch, Phase I (Black and Veatch 2005), Black and Veatch, Phase II (Black and Veatch 2005), Owen (Owen 2005)	3.3 km – 5.5 km wide cross sections	NA	0.37-1.37
Power potential	Black and Veatch, Phase III (Black and Veatch 2011b)	5 km wide cross section	NA	2.25
Casquets				
Farm	ETSU (Energy Technology Support Unit 1993), European Commission (European Commission 1996)	190 km^2 -215 km^2	0.37-2.5	1.3-2.9
Kinetic energy flux	Black and Veatch, Phase I (Black and Veatch 2005), Black and Veatch, Phase II (Black and Veatch 2005), Owen (Owen 2005)	8 km wide cross section	NA	0.4-1.6
Power potential	Black and Veatch, Phase III (Black and Veatch 2011b)	61 km^2	NA	1.9
Big Roussel				
Farm	ETSU (Energy Technology Support Unit 1993)	90 km^2	2.5	2
Kinetic energy flux	Black and Veatch, Phase I (Black and Veatch 2005), Owen (Owen 2005)	2.7 – 4 km wide cross section	NA	0.16-0.3

comparison is made with estimates for the maximum average power potential at the Pentland Firth in Scotland (Draper et al. 2014), Minas Passage (Karsten et al. 2008; Walters et al. 2013), Johnstone Strait (Sutherland et al. 2007) and Masset Sound (Blanchfield et al. 2008) in Canada (Table VI). In §4c the level of interaction between each site was investigated by simulating simultaneous energy extraction scenarios. In §4d results are presented that consider more realistic levels of array drag

based on the physical constraints of turbine spacing. Energy extraction from these more realistic simulations are compared with the upper bound solutions from §4b and §4c to comment on the viable level of tidal energy development at each site.

2. English Channel Model

a. Domain

Telemac 2D (Lang & Desombre 2013) was used to build a new 2D hydrodynamic model of the English Channel. The domain covers the whole of the English Channel with open boundaries in the Atlantic Ocean, Irish Sea and the North Sea (Figure 2). The location of the three boundaries overlay validated elevation gauge measurements used to drive the model from the European Shelf 2008 (Egbert et al. 2010). Reducing the size of the domain gave unsatisfactory validation results and was therefore not pursued further. The closest boundary to the Channel Islands is the Atlantic Ocean boundary (approximately 350km away). A preliminary study was conducted to investigate the far field effects of energy extraction at Alderney Race, Casquets and Big Roussel on the open boundaries. It was found that this did create back effects on the open boundaries, however changes in velocity at the boundaries were limited to below 0.01% which was deemed acceptable. Figure 2 also shows the average energy flux E_f through each of the three open boundaries due to the M_2 tide, which was calculated using Equation 1 (Davies et al. 2004), where ρ is water density, g is acceleration due to gravity, h is water depth, u is the depth averaged velocity perpendicular to the boundary, ζ is free surface elevation and Γ denotes the line drawn by each open boundary, segmented by length s. The overbar denotes time average over the period of the M_2 tidal cycle.

$$E_f = \rho g \int_\Gamma h\overline{u\zeta}\, ds \qquad (1)$$

The arrows and phase G of the M_2 tide through each boundary (shown in Figure 2) indicate the phase lag of the M_2 wave entering the domain in the Celtic Sea (Boundary 1) and leaving the domain through the Irish Sea (Boundary 2) and the North Sea (Boundary 3).

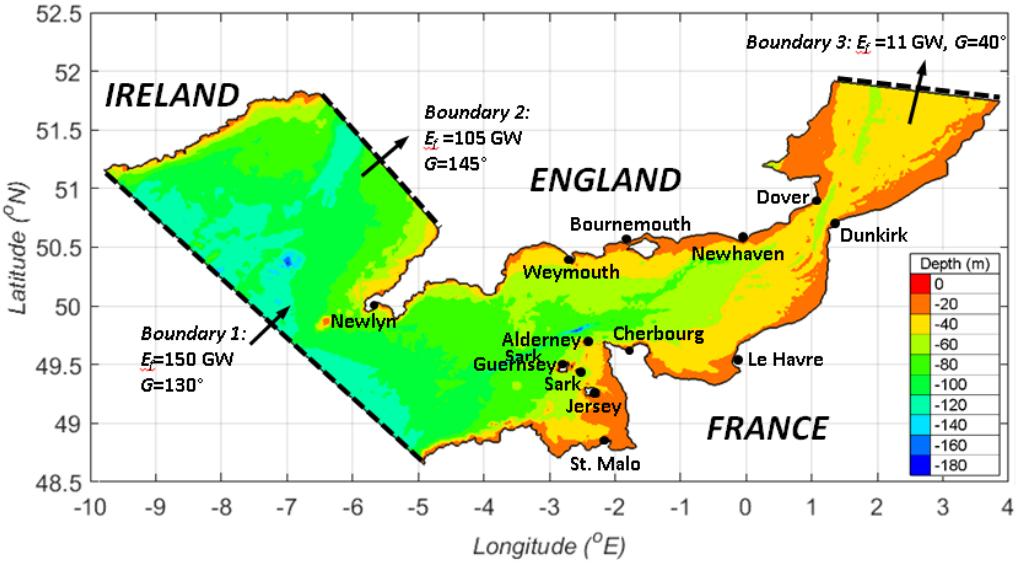

Figure 2. English Channel Model domain in Universal Transverse Mercator (UTM) projection, showing the location of three open boundaries and depth in metres. The location of thirteen ports used for validation in §3a are also shown. G is the phase of the M_2 tide and E_f is the time averaged energy flux through each open boundary.

b. Governing equations

The model solves the shallow water equations using the finite element method. The shallow water equations are applicable for cases where the horizontal length scale is greater than the vertical length scale, such that the vertical velocities are negligible and the pressure can be treated as hydrostatic. Under this assumption, and neglecting other forcing such as wind and buoyancy, depth integration of the Navier-Stokes equations for an incompressible fluid reduces to the shallow water equations solved simultaneously by Telemac 2D (Lang 2010):

Continuity:
$$\frac{\partial h}{\partial t} + u.\vec{\nabla}(h) + h\nabla.(\vec{u}) = S_h \quad (2)$$

Momentum along x:
$$\frac{\partial(u)}{\partial t} + \vec{u}.\vec{\nabla}(u) = -g\frac{\partial Z}{\partial x} + S_x + \frac{1}{h}\nabla(h\nu_t\vec{\nabla}u) \quad (3)$$

Momentum along y:
$$\frac{\partial(v)}{\partial t} + \vec{u}.\vec{\nabla}(v) = -g\frac{\partial Z}{\partial y} + S_y + \frac{1}{h}\nabla.(h\nu_t\vec{\nabla}v) \quad (4)$$

Where *u* and *v* are the horizontal depth averaged velocity components aligned with the *x* and *y* axis, Z is the free surface elevation, *h* is depth, ν_t is the momentum diffusion and $S_h/S_x/S_y$ are fluid source/sink terms that include Coriolis acceleration, bottom friction and/or a momentum sink applied in the energy extraction zones. Equations 2, 3 and 4 are a function of spatial position, *x* and *y* as well as time, *t* as a result of direct tidal forcing boundary conditions.

c. Pre-processing

Over the majority of the domain TCarta 90 m resolution bathymetry data was used. In regions where the TCarta bathymetry did not cover the domain in the deeper Celtic Sea in close proximity to Boundary 1 (see Figure 2), bathymetry was obtained from the General Bathymetric Chart of the Oceans (GEBCO) (Kapoor 1981) at approximately 900 m resolution. The bathymetry was mapped onto an unstructured mesh (Figure 3), where mesh independence studies were conducted to ensure free surface elevations at 13 ports around the domain (Figure 2) were independent of mesh resolution.

Three regions were allocated within the domain based on their likely mesh resolution requirement to capture the necessary scales of flow. Region 1 covers the open sea stretching throughout the majority of the domain where depth is high relative to local changes in bathymetry so that flow gradients are relatively low. In this region free surface elevation amplitudes and phases within the Channel Islands were relatively insensitive to mesh resolution so was kept low at 5 km to improve computational efficiency.

Region 2 incorporates the perimeter of the Channel Islands which roughly follows the 50m depth contour shown in Figure 3, the maximum approximate depth for turbines to be installed. Any further decrease in element size below 1 km gave no change in tidal elevation amplitudes and phases so 1 km elements were adopted for this study.

Region 3 covers the five areas of interest for energy extraction within the Channel Islands. The mesh within this region was resolved to 250 m mesh resolution, with any further mesh refinement showing no change in free surface elevations or energy extraction.

Once the model was reproducing the flow physics of the English Channel, bed friction was used as a tuning parameter to give improved agreement with free surface elevations and flow velocity data from Acoustic Wave and Current Profiler (AWAC) deployments within Alderney (see §3 Model validation).

A realistic range of bed drag coefficient values were estimated based on measurements of hydraulically rough river flow over gravel beds, where Bray (Braye 1982) gives an expression for the Nikuradse grain roughness height k_s in terms of the diameter of the roughness d_{90}, with 90% finer by weight:

$$k_s \approx 3d_{90} \qquad (5)$$

The bed drag coefficient C_b is approximated as (Tassi 2014):

$$C_b = 2\left(\frac{\kappa}{\log\left(\frac{12h}{k_s}\right)}\right)^2 \qquad (6)$$

Where κ is Von Karman constant and h is depth. Alternatively for a flat bed of sediment k_s is related to the median grain diameter (d_{50}) as approximately $k_s=2.5d_{50}$ (Soulsby 1997), whilst Liu (Zhou Liu 1999) suggests $k_s=mH_r$ for bed with sand ripples where H_r is the ripple height and m varies from 0.5-1.0. Based on Equation 6 tuning of C_b was restricted to values less than 0.052, which corresponds to a roughness diameter d_{90} which is 2% of the flow depth h.

To characterise the ambient flow, the dominant M_2, S_2, N_2, K_2, K_1, O_1,P_1,P_1, Q_1 and M_4 amplitudes and phases were extracted from the Atlantic Ocean Atlas (Egbert & Erofeeva 2014) to drive elevations along the three open boundaries shown in Figure 2. Non-reflective boundary conditions were applied along the liquid boundaries to allow waves to leave the domain with little or no reflection (Lang & Desombre 2013).

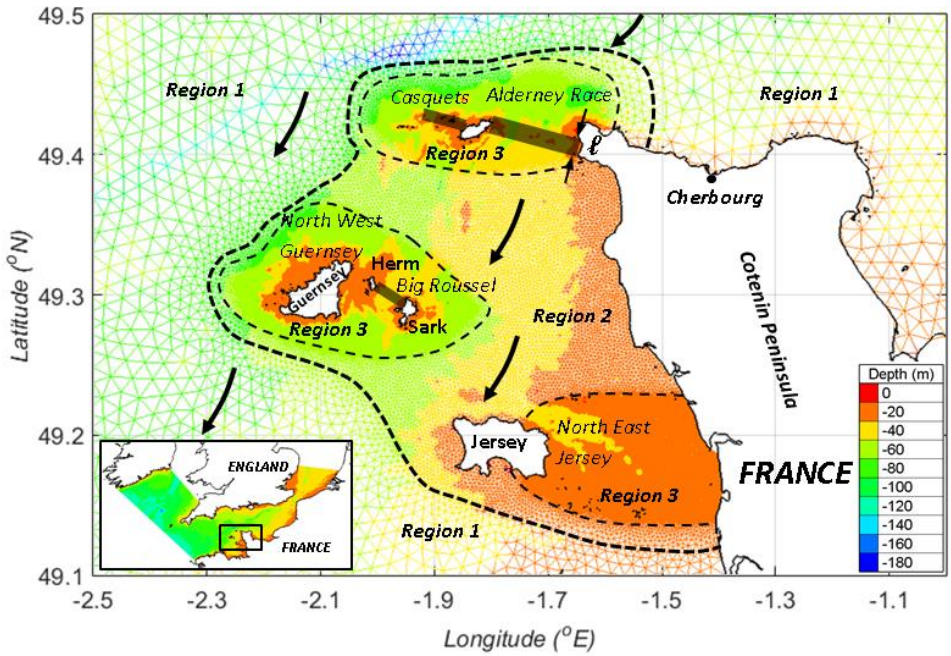

Figure 3. Mesh resolution in and around the Channel Islands, showing 250 m mesh resolution around Alderney Race, Casquets, Guernsey, Herm and Sark and North East Jersey (Regions 3), 1 km mesh resolution around the Channel Islands (Region 2) and 5 km mesh resolution elsewhere (Region 1). The 3 shaded (grey) regions at Alderney Race, Casquets and Big Roussel show the location of the energy extraction zones where added drag is applied, ℓ is the fetch of the energy extraction zone spanning shown for the Alderney Race only. Arrows show the direction of the dominant ebb tide. The model domain is inset.

The model detects shallow areas where the sea bed becomes exposed due to the high tidal range. The model then corrects free surface gradients in these regions to prevent spurious driving forces occurring on semi-wet elements. A constant turbulent viscosity of 10^{-4} Ns/m^2 was used as

implementing turbulence models did not lead to significant improvement of results but did add significantly to computation time. A time step of 1 minute was implemented. A total of 152643 elements and 77301 nodes were used in the domain. The accuracy of the propagation step was set to 0.001, which was deemed acceptable without incurring excessive computational cost. The steering file used to run the simulations is included as Appendix A. The geometry file and subroutines and are available from the University of Southampton Sustainable Energy Research Group (SERG) website (Anon 2016).

d. Simulating energy extraction

Turbines were simulated by applying an equivalent added drag coefficient C_e to the existing parameterisation of bed friction, applied uniformly over the area of the energy extraction zone, A_z. C_e is parameterised using Equation 7 and 8 [5], where array density λ is defined as the total swept area of n turbines within the energy extraction zone area A_z. A_s is the swept area of an individual rotor and C_D is the turbine drag coefficient which is assumed to remain constant at C_D=0.8 based on turbine thrust measurements from scaled down laboratory testing (A. S. Bahaj et al. 2007). This method has recently been validated experimentally for arrays of porous fences (Coles et al. 2016). Porous fences were used to simulate the wake downstream of densely packed turbine rows. Experimental load cell measurements of the total fence drag agreed within 10% of the numerical formulation of array drag given by Equations 7, 8 and 9.

$$\lambda = nA_s/A_z \qquad (7)$$

$$C_e = \frac{1}{2}\lambda C_D \qquad (8)$$

C_e is added to the bed drag coefficient C_b to give the 2D formulation of combined drag as a shear force, where u is the depth-averaged velocity:

$$\frac{\tau}{\rho} = (C_e + C_b)u^2 \qquad (9)$$

The method used here takes the same approach as previous assessments of the Pentland Firth (Draper et al. 2014) and Vancouver Island (Sutherland et al. 2007), so as to make a direct comparison of the estimated power potential with these sites (see Table VI). To adopt the same approach as these studies, energy extraction zones spanned the entire width of each site to prevent flow diversion around the arrays within the site itself and only M_2 forcing was used when simulating energy extraction.

The fetch of each energy extraction zone ℓ (i.e. the longitudinal distance between the site inlet and outlet parallel to the direction of flow over which added drag was applied – shown in Figure 3) was determined based on the distribution of mean ambient kinetic power to cover the most energetic regions where tidal energy development is most likely to be carried out. The average extracted power was calculated by integrating over the zone area and with respect to time t, where T is the duration of the repeating M_2 tidal cycle equal to 12.41 hours (Draper et al. 2014):

$$P = \frac{1}{T}\int_0^T \left(\iint_{A_z} \rho C_e |u|^3 dA\right) dt \qquad (10)$$

The equivalent added drag coefficient was increased incrementally to simulate more turbines (i.e. to increase array density defined as the ratio of total swept area of all turbines to the array plot area) until the total energy dissipated by the added drag reached a maximum and any further increase in

drag caused a reduction in average extracted power. A summary of the simulations undertaken to validate the model and quantify energy extraction are summarised in Table II.

Table II. Summary of the 8 cases simulated using the English Channel model. Scenario 1 is for validation quantifying the distribution of mean flow speeds and kinetic power. Scenarios 2-8 are the energy extraction cases considered at sites in the Channel Islands.

Scenario	Energy extraction location	Objective
1	Not applicable, ambient flow only	Model validation/Quantify distribution of mean flow velocities and kinetic power at sites around the Channel Islands/Obtain elevation data to input into an analytical model (Equation 12) for power potential.
2	Alderney Race	Quantify the maximum average power potential, as well as a realistic level of energy extraction and array density described by Equations 7 and 8.
3	Casquets	As above (Scenario 2).
4	Big Roussel	As above (Scenario 2).
5	Alderney Race + Casquets	Quantify level of interaction between sites based on upper bound levels of energy extraction and realistic levels of energy extraction and array density described by Equations 7 and 8 for the 2 sites.
6	Alderney Race + Big Roussel	As above (Scenario 5) for the 2 sites.
7	Casquets + Big Roussel	As above (Scenario 5) for the 2 sites.
8	Alderney Race + Casquets + Big Roussel	As above (Scenario 5) for the 3 sites.

3. Model Validation

a. Tidal elevations

Driven by M_2, S_2, N_2, K_2, K_1, O_1,P_1, Q_1 and M_4 forcings, a 30 day simulation was run to generate validation datasets for M_2 and S_2 elevations and flow speeds. Surface elevation time series were extracted from 13 locations around the domain (Figure 2) including six locations around the Channel Islands (Alderney, Guernsey, Jersey, Sark, Cherbourg and St. Malo). Tidal harmonic analysis was conducted using the Matlab package T-tide (Pawlowicz et al. 2002) to estimate the amplitude and phase of the M_2 and S_2 constituent at each location from the free surface elevation time series', which was then compared with data from the Tidal Analysis Software Kit (TASK) (Anon n.d.) and Admiralty Tide Chart data (UK Hydrographic Office 2016).

The results from the simulation undertaken to validate the model are shown in Table III. These show that nine out of thirteen ports were within 10% of real M_2 and S_2 amplitudes and 10° of real M_2 and S_2 phases, including all six ports around the Channel Islands. The region with the greatest discrepancy in tidal amplitude is along the south coast of England, where amplitudes are significantly smaller than at other ports. For example, tidal amplitudes at Bournemouth and Weymouth are 0.42 m and 0.59 m respectively, in comparison with 1.87 m at Cherbourg and 1.72m at Newlyn. In these shallower regions the amplitude is a greater proportion of the total depth, making free surface elevation more sensitive to drag due to bottom friction, which removes a greater proportion of the propagating tidal energy, causing a reduction in amplitude (D.T.Pugh 1996). Furthermore, any small absolute error will be most noticeable in shallower regions where the error is a greater proportion of the total depth. Amplitude and phase results shown in Table III were obtained with a uniform Nikuradse drag coefficient over the domain of C_b=0.025. Further refinement of the model in this region was not deemed necessary since the significant distance to the Channel Islands meant it had little to no impact on the validation results in the area of interest.

Table III. Percentage differences between modelled and real-world (admiralty chart (UK Hydrographic Office 2016)) *M_2 and S_2* amplitudes and phases at 13 ports around the English Channel Model domain (locations shown in Figure 2) using tidal harmonic analysis.

Port	Amplitudes		Phases	
	M_2 error (m)	S_2 error (m)	M_2 error (°)	S_2 error (°)

Alderney	-0.12 (-7%)	-0.06 (-8%)	+5	+9
Jersey	-0.29 (-9%)	+0.01 (+7%)	0	+5
Guernsey	-0.4 (-10%)	-0.11 (-10%)	+6	+6
Sark	-0.16 (-9%)	+0.03 (+3%)	+10	+10
Cherbourg	-0.04 (-2%)	+0.04 (+6%)	-4	+3
St. Malo	-0.34 (-9%)	-0.13 (-5%)	0	-1
Newlyn	+0.11 (+6%)	-0.05 (-8%)	+9	+9
Weymouth	+0.14 (+23%)	+0.04 (+14%)	-9	0
Bournemouth	+0.35(+84%)	+0.11 (+56%)	+14	+4
Newhaven	+0.25 (+11%)	+0.08 (+12%)	+21	+22
Dover	+0.17 (+8%)	+0.07 (+10%)	+19	+22
Dunkirk	-0.38 (-18%)	+0.11 (18%)	+75	+19
Le Havre	+0.28 (+10%)	+0.07 (+7%)	+6	+7

b. Tidal stream velocities

Data from three AWAC deployments (locations shown in Figure 4) commissioned by the Alderney Renewable Energy (ARE) in 2009 were used to validate tidal stream velocities in Alderney Race. The AWACs were deployed for a minimum period of 30 days.

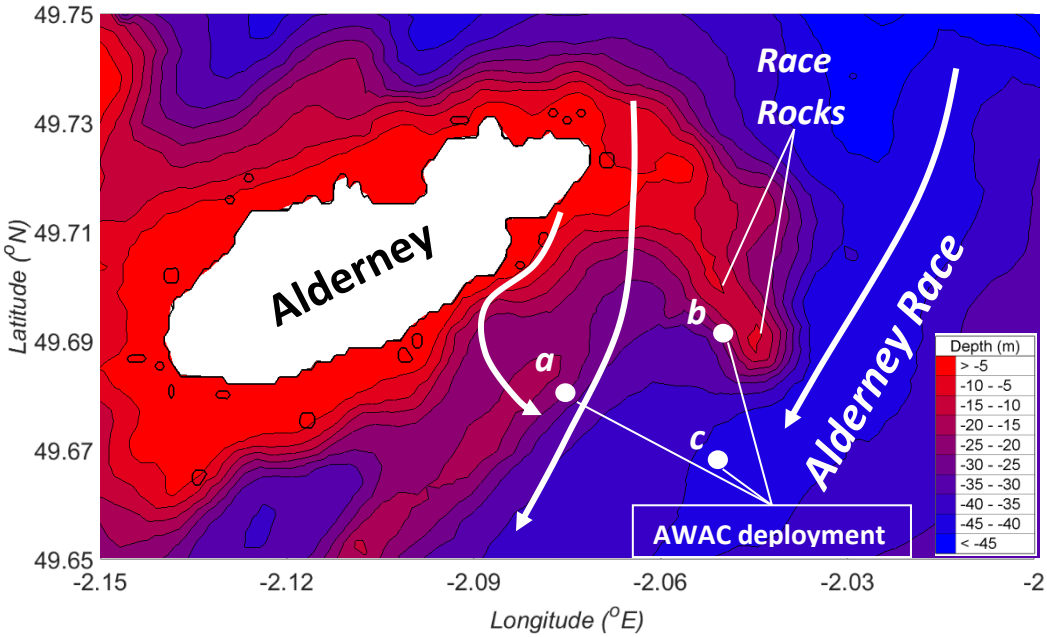

Figure 4. Location of three AWAC deployments (*a,b* and *c*) in Alderney Race. Arrows show the direction of the dominant ebb tide and the eddy shed off the North East tip of Alderney. The location of Race Rocks is also shown.

Figure 5 shows results for M_2 and S_2 constituent major axis amplitudes, phases and inclinations obtained from the English Channel model compared with field measurements.

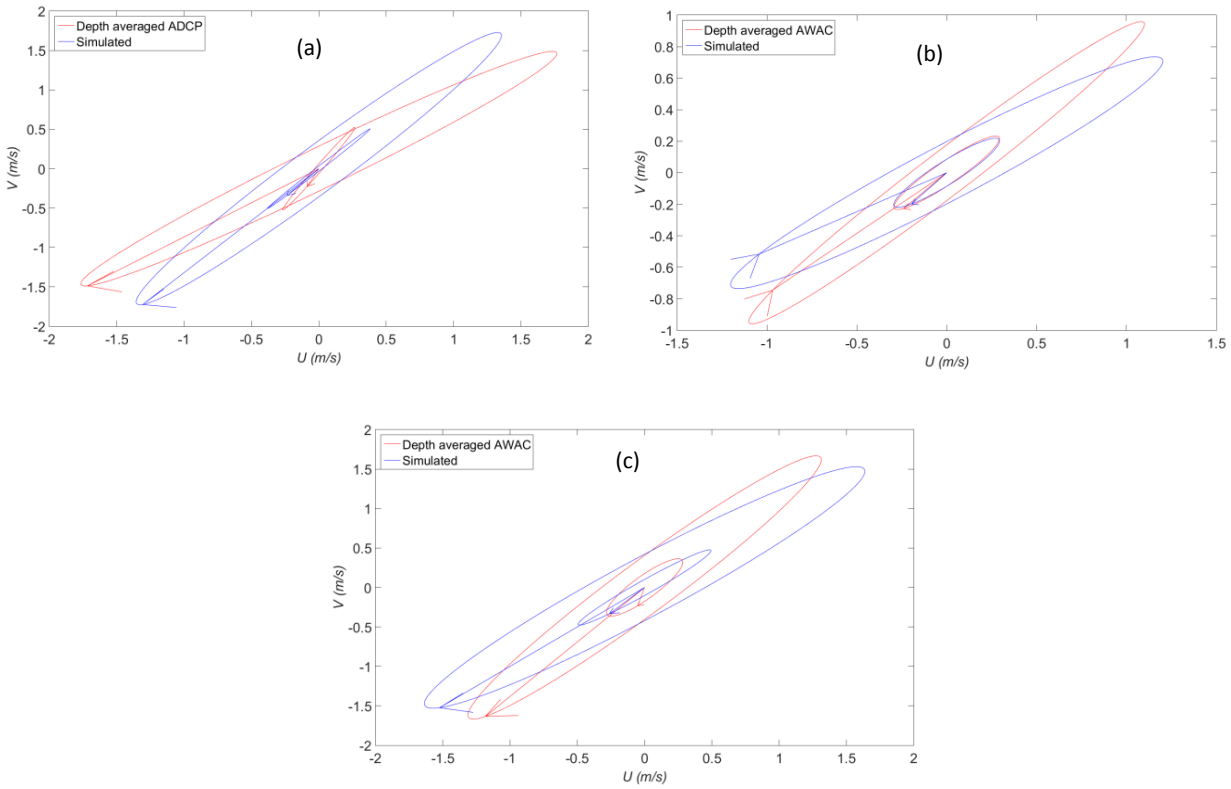

Figure 5. M_2 and S_2 tidal stream ellipses for (a) AWAC deployment a (b) AWAC deployment b and (c) AWAC deployment c. Locations of AWAC deployments shown in Figure 4.

Errors at locations *a* (Figure 5a) and *c* (Figure 5c) are likely to be caused by the large clockwise eddies shed off the North East tip of Alderney during the ebb tide (shown in Figure 4), creating a complex flow pattern in this region. It was shown in (Haynes 2015) that the angular velocity and directional propagation of this eddy is sensitive to the magnitude to sea bed drag coefficient C_b.
AWAC *b* is in close proximity to Race Rocks (shown in Figure 4), two tower like rock formations in close proximity to one another that accelerate flow through and around them, creating strong jet flows during ebb tide. Results from Figure 5b (summarised in Table IV) show that the model is capturing the flow dynamics in this region well, where the M_2 and S_2 major axis amplitudes show agreement within 5%, phases within 13% and inclinations within 10%.

Validation results are summarised in Table IV, showing all M_2 and S_2 constituent major axis amplitudes, phases and inclinations obtained from the English Channel model compared with field measurements. With the exception of the S_2 major axis amplitude at location *c*, all M_2 and S_2 major axis amplitudes and phases lie within 15% of field measurements. Phases and inclinations also show reasonable agreement, with all results excluding the S_2 phase at location *a* lying within 15° of the true values.

Table IV. Differences in M_2 and S_2 major axis, phases and inclination between simulated results and AWAC data at three locations in Alderney Race

AWAC	Major axis amplitude difference (%)	Phase difference (°)	Inclination difference (°)
a	10/7	9/17	-12/-10
b	4/2	-1/-13	-10/2
c	-5/-53	3/9	-9/-9

4. Results and Discussion

a. Ambient flow

The model was run in the ambient case for 31 days, plus 24 hours to allow the model to spin up from still water conditions. In total nine tidal constituents were used to force each open boundary (M_2, S_2, N_2, K_2, K_1, O_1, P_1, Q_1 and M_4). Ambient flow results were used to estimate the distribution in mean kinetic power, a metric commonly used for quantifying a resource (Black and Veatch 2011b; Pérez-Ortiz et al. 2013):

$$P = \frac{1}{T}\sum_{i=1}^{T}\frac{1}{2}\rho U_i^3 \qquad (11)$$

Figure 6 shows the contour plot of mean kinetic power density distribution, which was used for approving/discarding sites in the Channel Islands based on assumptions used in (Black and Veatch 2011b) where it is estimated that for 'reasonable project economics' using first generation turbine devices, mean kinetic power density should exceed 2.5 kW/m^2. In our simulation, the highest kinetic power density is seen in Alderney Race, where in the shallower faster waters of the East Race kinetic power density exceeds 13.5kW/m^2 and the mean flow exceeds 2.5 kW/m^2 over an area of 93 km^2. Depths across the majority of Alderney Race exceed 15 m and never go above 50m, making it geometrically suitable to house 1st and 2nd generation devices such as floating turbines.

As shown in Figure 6, both Casquets and Big Roussel also exhibit mean power densities greater than 2.5kW/m^2, however in both cases the area over which this is true is 7km^2 and 14km^2 respectively, significantly smaller compared to that of the Alderney Race (summarised in Table V). Maximum kinetic power density at Casquets and Big Roussel was approximately 7kW/m^2 and 5kW/m^2 respectively.

In Figure 6 we show a 10 km^2 region where mean kinetic power density exceeds 1.5 kW/m^2 in North East Jersey, potentially making it a viable option in the future as costs related to aspects such as manufacturing, installation and operation and maintenance reduce. However the mean kinetic power density at sites around North West Guernsey and North East Jersey identified in (Environmental Change Institute 2005) do not exceed 2.5kW/m^2 and are therefore not considered further in this study.

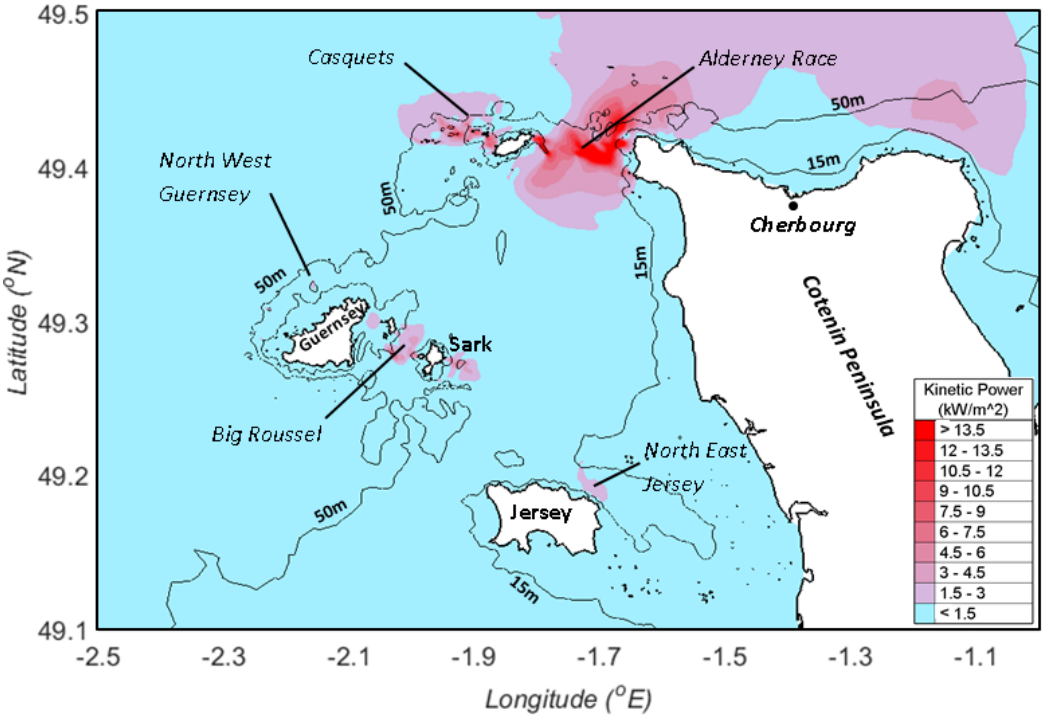

Figure 6. Mean kinetic power density distribution around the Channel Islands, with 50 m and 15 m depth contours also shown.

These result are in contrast to past assessments covered in Table I ((Energy Technology Support Unit 1993; Bahaj & Myers 2004; Myers & Bahaj 2005; Black and Veatch 2005)) that assume the flow velocities are high enough for tidal energy development over areas of up to 58 km^2 in North East Jersey, 366 km^2 in North West of Guernsey, 90 km^2 in Big Roussel and 215 km^2 in Casquets. In Table V we summarise the areas over which the mean kinetic power exceeds 2.5 kW/m^2 within depths of 15-50 m at each site and also give a comparison with previous studies. In general, the areas identified in our work are significantly smaller than previous studies.

We feel these results are more robust as, unlike previous studies, we have used higher resolution flow data and imposed stricter limits on the acceptable mean flow speeds. For the same data and limits, the exception to this is Alderney Race, where the estimated potential development area is approximately 30% greater than previously estimated (Bahaj & Myers 2004; Myers & Bahaj 2005). There are two small regions either side of Big Roussel that also exhibit high kinetic power density, however they occur in shallow waters and are therefore not consider further in this study.

Table V. Summary of area considered in this study over which distribution of mean kinetic power density exceeds 2.5 kW/m^2 at Alderney Race, Casquets, Big Roussel, North West Guernsey and North East Jersey in comparison with previous studies (in Table I.

Site	This Study	Previous studies	
	Area exceeding 2.5 kW/m^2 in depths of 15 -50m (km^2)	Area considered to be energetic (km^2)	Sources
Alderney Race	93	65-102	ETSU [8], European Commission [9], Bahaj *et al.* [10], Myers *et al.* [11]
Casquets	7	61-215	ETSU [8], European Commission [9], Black and Veatch Phase I [13]
Big Roussel	14	90	ETSU [8]
North West Guernsey	0	221-366	ETSU [8], European Commission [9]
North East Jersey	0	20-58	ETSU [8], European Commission [9], Black and Veatch Phase I [13]

b. Maximum average power potential

In estimating the maximum average power potential, drag was applied uniformly to the energy extraction zones shown in Figure 3. These zones were sized and positioned to overlay regions where the mean kinetic power density exceeds 2.5 kW/m^2. In regions close to coastlines, the energy extraction zones cover shallow waters unsuitable for energy extraction by turbines. This was included in our analysis to limit flow acceleration around the energy extraction zones, and follows the same methodology as in literature for the Pentland Firth (Draper et al. 2014), Minas Passage (Walters et al. 2013) and Masset Sound (Blanchfield et al. 2008). This allows direct comparison between sites (see Table VI). The model was run with M_2 boundary forcing for 36.41 hours, made up of 24 hours for spin up and one semi diurnal tidal cycle for analysis.

i. Alderney Race

As the drag coefficient C_e applied uniformly over the energy extraction zone in Alderney Race is increased from zero, the average elevation difference across the energy extraction zone (Z_{in}-Z_{out}) increases, as shown in Figure 7. This increases the hydrostatic force driving flow through the energy extraction zone to oppose the added drag from C_e. The increase in drag coefficient C_e also results in a reduction in the average volume flux through the energy extraction zone (also shown in Figure 7) due to the enhanced hydraulic resistance from C_e so that flow diverts away from Alderney Race (this flow diversion is discussed further in §4c and §4d). Since extracted power is the product of the elevation drop across the energy extraction zone (Z_{in}-Z_{out}) and the volume flux through the energy extraction zone (Q), as C_e increases, the level of extracted power is dependent on the rate of change of both Q and Z_{in}-Z_{out} with respect to C_e. I.e. As C_e increases, if the increase in elevation drop dominates the reduction in volume flux, extracted power will increase, but if the reduction in volume flux supresses the increase in elevation drop, extracted power will decrease. For the case of Alderney Race the maximum average power potential was 5.1 GW, as shown in Figure 8.

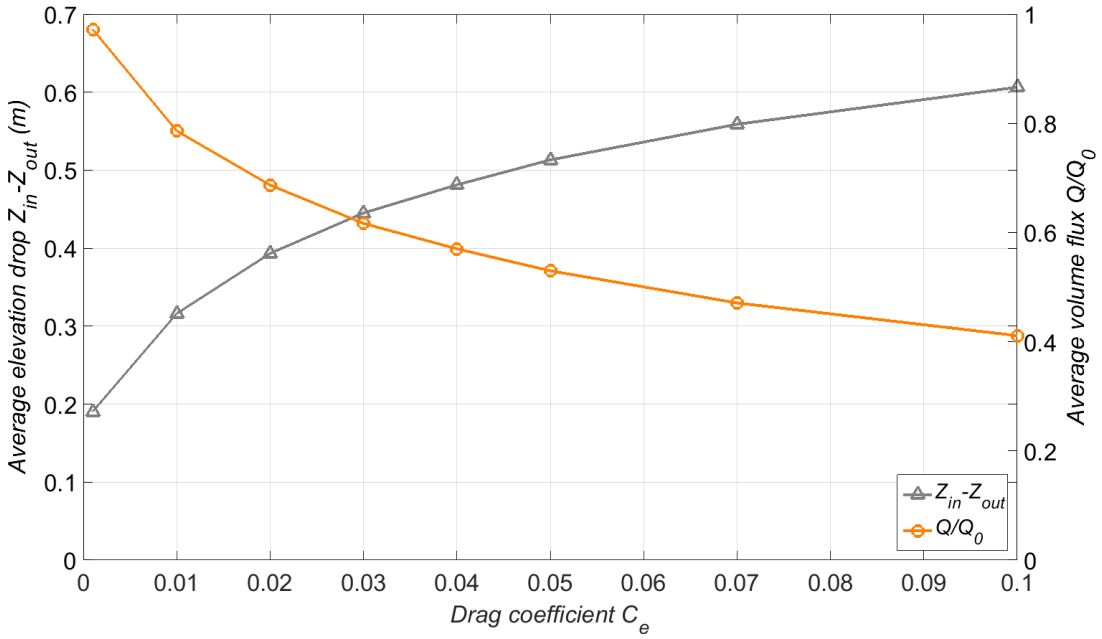

Figure 7. Reduction in average volume flux (Q/Q_0) through Alderney Race and increase in elevation difference across Alderney Race (Z_{in}-Z_{out}) as a result of increased drag coefficient, C_e applied uniformly over the energy extraction zone.

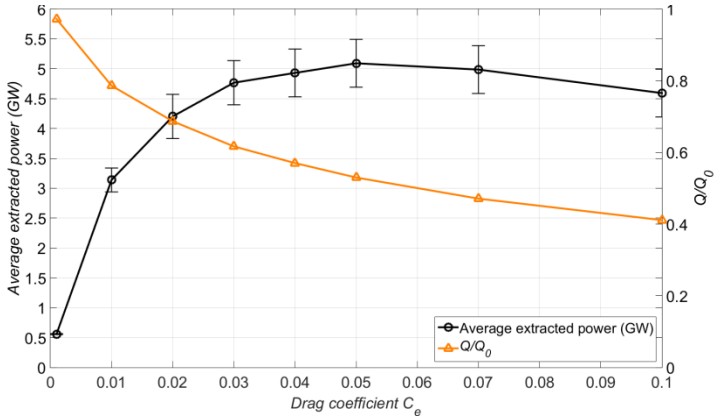

Figure 8. Average extracted power from Alderney Race over an M_2 tidal cycle with decreasing flow rate as a result of increased drag coefficient, C_e applied uniformly over the energy extraction zone. Error bars show the average extracted power within the realistic limits of C_b=0.013-0.052.

To validate the English Channel model a uniform seabed roughness coefficient C_b=0.025 was applied over the whole domain, as discussed in §3. However, in reality seabed roughness coefficient C_b varies both spatially (due to spatial distribution of bed roughness properties throughout the domain) directionally (due to the bi-directional nature of the tides) and temporally (due to changes to bed morphology from scour and sediment dynamics). In (Adcock et al. 2013) it was shown that the level of energy extraction from tidal turbines is sensitive to small changes in sea bed roughness coefficient C_b, where if seabed drag coefficient is increased, more energy is extracted by the bed, reducing the energy extracted by the turbines. For this reason, simulations were re-run for seabed roughness coefficients within physically realistic bounds by assuming the roughness height d_{90} (Equation 6) does not exceed 2% of the depth h but is greater than 0.005% of the flow depth, resulting in a range of C_b of 0.013-0.052 obtained from Equations 5 and 6. Error bars in Figure 8 show the sensitivity of extracted power to sea bed drag coefficient C_b, which for the peak average extracted power is approximately 15%. In general, as bed friction coefficient was increased to C_b=0.052, the extracted power decreased because more energy is extracted by the seabed.

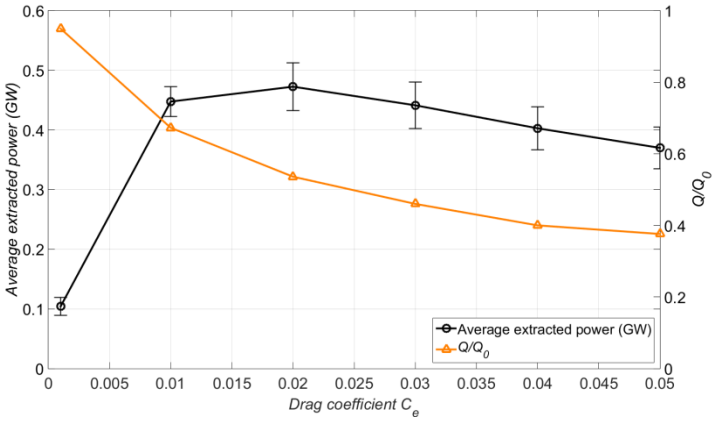

Figure 9. Average extracted power from Casquets over an M_2 tidal cycle with decreasing flow rate as a result of increased drag coefficient C_e applied uniformly over the energy extraction zone. Error bars show the average extracted power within the realistic limits of C_b=0.013-0.052.

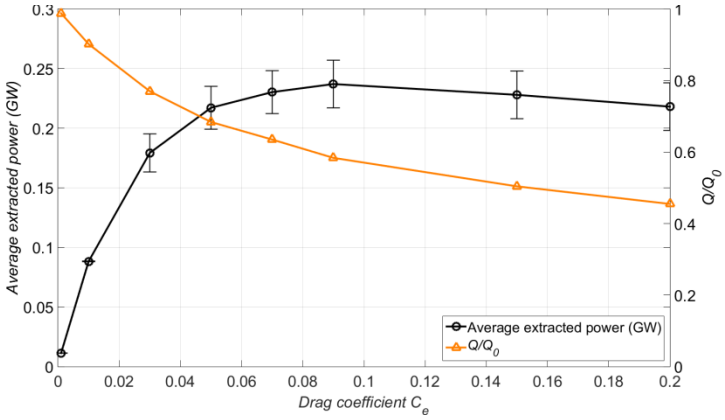

Figure 10. Average extracted power from Big Roussel over an M_2 tidal cycle with decreasing flow rate as a result of increased drag coefficient C_e applied uniformly over the energy extraction zone. Error bars show the average extracted power within the realistic limits of C_b=0.013-0.052.

To provide more resilience in the results, the English Channel model was run for an ambient case without energy extraction with M_2 forcing. Using Equation 12, an estimate of the maximum average power potential was obtained from the theory developed in (Garrett & Cummins 2005), where γ is a coefficient ranging between 0.16 – 0.24 depending on the phase difference between the flow rate and the driving head [26], ρ is water density, g is acceleration due to gravity, a_0 is the amplitude difference between the two ends of the channel and Q_{max} is the maximum volume flux through the channel in the undisturbed case.

$$P_{max} = \gamma \rho g a_0 Q_{max} \qquad (12)$$

This yielded a maximum average power of 4 GW, using a peak flow in the undisturbed state, Q_{max}=1.08 x10^6 m^3/s, γ=0.22 and a head difference a_0=1.13 m. The head difference was taken from points located 25 km from the narrowest constriction of the Race (i.e. so that the two points were located 50 km apart from each other). The phase lag of flow rate behind the dynamic head was 48°.

The estimate for the maximum average power potential obtained using Equation 4 was within 20% of the estimate from the numerical model using the distributed drag approach. Error in this analytical estimate arises from the dynamic head difference a_0, which does not remain unaffected by energy extraction as assumed by Equation 12 (a_0 increases when a drag is applied over the energy extraction zones). Closer agreement would be possible using points located further than 25 km away from Alderney Race to estimate the head drop given that it was found that energy extraction did have an effect on free surface elevations at the locations used, however the difference was found to be less than 5%. This was deemed to be acceptable given that other simplifications in the analytical approach are likely contribute a significant error to the maximum average power potential result. For example important flow features such as exit losses (resulting from flow separation) and Coriolis are not considered.

To add more constituents, (Garrett & Cummins 2005; D.T.Pugh 1996) provide a solution with amplitudes $a_1, a_2..,a_i$, where the solution to Equation 12 is multiplied by $x = 1 + \alpha\left(r_1^2 + r_2^2 + \cdots + r_i^2\right)$, where α is a fraction between 9/16 and 1 depending on the basic dynamic balance and $r_i=a_i/a$ is the ratio of the amplitude of the dynamic head of constituent *i* to the dynamic head of the dominant constituent. To add the S_2 constituent, x=1.1 based on r_1=0.45 obtained from the numerical model, giving a maximum average power potential of approximately 4.4 GW.

ii. Casquets

The same procedure was carried out for Casquets, giving an estimated maximum average power potential with C_e=0.02 of 0.47 GW, which is approximately 10% of Alderney Race (Figure 9). At this upper bound, the reduction in volume flux was 42%, the same fraction reduction as for Alderney Race and in line with analytical results (Sutherland et al. 2007). Our estimated result of 0.47 GW is approximately double the value obtained in (Black and Veatch 2011a) where a 2D hydrodynamic models of generic tidal regimes such as tidal streams were developed to simulate the large scale impact of hypothetical levels of energy extraction. However Casquets is unlikely to be fully representative of the idealised case, especially as bathymetry varies significantly across the site and there are alternative channels for the flow to take into the English Channel and into Alderney Race. The variation in the results with seabed roughness coefficient C_b were approximately within the same error bounds as for Alderney Race, where for the maximum average power potential showed a 13% variation.

iii. Big Roussel

The estimated maximum average power potential of Big Roussel was 0.24 GW, approximately 5% of that of the Alderney Race and 50% of Casquets. This gave a reduction in volume flux through the channel of 43% with C_e=0.09 (Figure 10). At this upper bound the sensitivity to sea bed friction drag C_b was also 15%.

For comparison, Table VI summarises our estimated maximum average power potential for the three sites considered here along with four other well-known studies at other tidal sites in literature. These results should also be compared with outcomes from previously published work undertaken for the Channel Islands sites given in Table 1. Our results indicate that Alderney Race has the greatest potential in the Channel Islands which is significant given that it is approximately 136% that of the maximum average power potential estimated for the Pentland Firth in Scotland (Draper et al. 2014). Casquets and Big Roussel are significantly lower, which is unsurprising given that these two sites are considerably smaller and in general have lower distributed range of power density, as was shown in Figure 6.

The effect of varying the fetch ℓ of each energy extraction zone on the magnitude of the maximum average power potential was investigated. It was found that by increasing the zone fetch ℓ, the drag coefficient C_e required to obtain the maximum average power potential decreased. However, the magnitude of the maximum average power potential did not change (within 5%). This was also found to be the case for a considered narrow zone of turbines spanning the width of the entrance to Minas Passage compared with a drag distributed over the entire area of the channel (Walters et al. 2013). In their work it was shown that for a given geometry and forcing, the product of the energy extraction zone fetch ℓ and the effective added array drag coefficient C_e used to obtain the maximum average power potential remains constant [5].

Table VI. Comparison between this work and published data of the estimated of maximum average power potential of different high potential sites for tidal energy extraction. The table includes our results for Alderney Race, Casquets and Big Russel within the realistic bounds of seabed roughness coefficient C_b=0.013-0.052. Our results for these sites should also be compared with those given in Table 1 above.

Site	Estimated maximum average power potential (GW)	Boundary forcing
Past assessments of other sites		
Minas Passage, Canada (Walters et al. 2013)	5.7	M_2,S_2,N_2,K_2,K_1,O_1,P_1,Q_1,M_4
Pentland Firth, Scotland (Draper et al. 2014)	3.75	M_2 only
Johnstone Strait, Canada (Sutherland et al. 2007)	1.3	M_2 only
Masset Sound, Canada (Blanchfield et al. 2008)	*0.08*	M_2 only
	4.7-5.5	M_2 only
This work	0.43-0.51	M_2 only
Alderney Race	0.22-0.26	M_2 only
Casquets		
Big Roussel		

c. Interaction

The three sites considered here are in relatively close proximity, especially Alderney Race and Casquets, separated only by the 3 km wide island of Alderney, whilst Big Roussel is approximately 40 km from Alderney Race and Casquets. Therefore, energy extraction at each site is likely to affect the surrounding flow dynamics, hence altering the total power potential of each neighbouring site. Such interactions were quantified using the methodology originally adopted by Draper at al. (Draper et al. 2014) in which simultaneous energy extraction scenarios were simulated (scenarios listed in Table VII). For all scenarios, the upper bound (optimum value) drag coefficient C_e for each of the individual sites was used.

Table VII. Maximum average extracted power for all seven scenarios (scenarios first presented in Table II) using Alderney Race with C_e=0.05, Casquets with C_e=0.02 and Big Roussel with C_e=0.09 and seabed drag coefficient C_b=0.025.

		Power potential (GW)			
Scenario	Combinations	Alderney Race	Casquets	Big Roussel	Total (GW)
2	Alderney Race	5.10	-	-	5.10
3	Casquets	-	0.47	-	0.47
4	Big Roussel	-	-	0.24	0.24
5	Alderney Race + Casquets	5.28	0.84	-	6.12
6	Alderney Race + Big Roussel	5.03	-	0.21	5.24
7	Casquets + Big Roussel	-	0.56	0.23	0.79
8	Alderney Race + Casquets + Big Roussel	5.24	1.02	0.20	6.46

Simultaneous energy extraction at Alderney Race and Casquets (Scenario 5) gives a 79% increase in the estimated maximum average extracted power at Casquets and a 10% increase in the overall total power extracted in comparison to energy extraction at Alderney Race and Casquets simulated

separately (Scenarios 2 and 3). Energy extraction at Alderney Race (Scenario 2) causes flow diversion around Alderney giving a 25% increase in volume flux through Casquets and an increase in average head drop across Casquets of 0.03 m in comparison with energy extraction at Casquets only (Scenario 3). The increase in mean velocities through Casquets due to energy extraction at Alderney Race is shown in Figure 11a. The figure shows the residual mean flow velocity distribution for energy extraction at Alderney Race and Casquets together (Scenario 5) and energy extraction at Casquets only (Scenario 3). Red regions show areas of enhanced mean flow velocities due to energy extraction in Alderney Race, which occurs in and around the Casquets energy extraction zone.
The results in Figure 11a highlight the inter-dependent nature of energy extraction when both Alderney Race and Casquets are exploited, where energy extraction at the Alderney Race has a significant impact on the resource at Casquets. This is encouraging as it means that the greater the development in Alderney Race, the more energetic the resource at Casquets becomes.

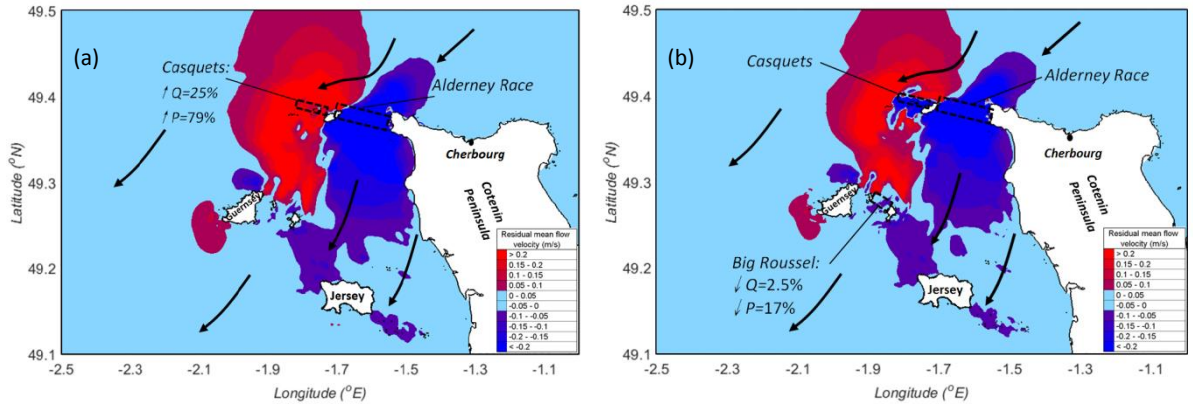

Figure 11. Mean velocity distribution difference plot between (a) the case of upper bound energy extraction at Casquets (Scenario 3 described in Table VII) and energy extraction at Alderney Race and Casquets (Scenario 5 described in Table VII) (b) the case of upper bound energy extraction at Big Roussel only (Scenario 4 described in Table VII) and energy extraction at Alderney Race, Casquets and Big Roussel (Scenario 8 described in Table VII). Arrows show the direction of the dominant ebb tide and flow diversion around Alderney Race into Casquets.

The reduction in mean flow speeds through Big Roussel as a result of energy extraction at Alderney Race and Casquets is shown in Figure 11b. This corresponds to a 17% reduction in extracted power at Big Roussel as a result of energy extraction at Alderney Race and Casquets (Scenario 8) when compared to that at the Big Roussel in isolation (Scenario 4). This is attributed to the fact that on the dominant ebb tide, energy extraction at Alderney Race and Casquets, which are both upstream of Big Roussel, cause flow diversion around the Channel Islands, giving a 2.5% reduction in volume flux through Big Roussel in comparison with the case of energy extraction at Big Roussel only (Scenario 4).

The dependencies listed in Table VII have major implications for the exploitation of the sites. For a developer that leases a plot in Casquets or Big Roussel, failing to consider the effects of energy extraction at Alderney Race (the neighbouring inter-dependant site) on flow within the leased plot will ultimately lead to an over/under estimation of energy yield. Regulators and developers should be aware of this so that a coherent development is planned for to account for such impacts. However, currently to the authors knowledge, there is no clear regulation that takes into account such dependency. We hope that this work will provide the evidence to support the development of regulations that take into account the interdependencies between neighbouring tidal sites.

d. <u>Realistic array drag and power from sites</u>

In reality the zone drag coefficient C_e is limited by the physical constraints of the turbines and turbine spacing. The equivalent added drag from tidal turbines can be estimated using Equations 7 and 8. Table VIII gives an approximate longitudinal spacing for the optimum effective zone drag coefficient C_e used to obtain the maximum average power potential at each site using Equations 7 and 8 and assuming a lateral spacing (tip to tip) of 1 diameter. This lateral spacing was chosen as it is likely to be close to the limit for which devices can physically be installed next to each other. In Equation 8 a turbine drag coefficient of C_D=0.8 was used (A. S. Bahaj et al. 2007).

Table VIII. Estimated equivalent longitudinal and lateral (tip to tip) spacing between devices to achieve maximum average power potential at each individual site, with corresponding array density obtained using Equations 7 and 8.

Site	Optimum C_e	Corresponding array density λ	Equivalent lateral spacing in device diameters (D)	Equivalent longitudinal spacing in device diameters (D)
Alderney Race	0.05	0.125	1	4
Casquets	0.02	0.050	1	10
Big Roussel	0.09	0.225	1	2

To achieve the maximum average power potential at Alderney Race and Big Roussel, very high turbine densities are required. For these two sites the flow is constricted due to the positioning of coastlines so that an increase in distributed drag results in an increase in head drop across the zone, resulting in an increase in extracted power. Such high packing densities are unlikely to ever be realised as turbines will be in the near wake of upstream devices (Myers & Bahaj 2010), severely diminishing efficiency. For the device spacing shown in Table VIII, to extract maximum power in Casquets requires the least densely packed array. This is because Casquets is open to the English Channel so is the least constricted site, allowing flow to divert around the energy extraction zone more easily with an increase in distributed drag, resulting in a reduction in volume flux through the energy extraction zone. A longitudinal spacing of ten diameters is a more realistic packing density that will allow wake recovery between each row.

Further simulations were conducted using a value of added drag based on the assumption that turbines have one diameter lateral spacing (tip to tip), and ten diameter longitudinal spacing, giving C_e= 0.015 and a uniform array density λ=0.038 (using Equations 7 and 8). This drag was applied over the same energy extraction zones used before, where mean ambient kinetic power exceeds 2.5 kW/m^2 (Figure 6). The results are presented in Table IX, showing the reduction in estimated maximum average power potential in comparison with the maximum average power potential at each site from §4b (column 8).

The results show that the reduction in extracted power relative to the maximum (upper bound) average power potential differs for each site. For Casquets, the maximum average power potential (P=0.47 GW) was achieved with a relatively low added drag of C_e= 0.02 because flow easily diverted into the English Channel as drag was added. This upper bound drag coefficient C_e= 0.02 used for estimating the maximum average power potential is close to the realistic value of C_e= 0.015 used to obtain the results in Table IX. For added drag in the range 0.01<C_e<0.03, Casquets power curve shown in Figure 9 is relatively flat so that there is no change in extracted power between the maximum and realistic case. This is demonstrated in Figure 12, which shows the change in average extracted power at Casquets and Alderney Race for the maximum and realistic cases.

Table IX. Average extracted power for Scenarios 2-8 (first presented in Table II) using Alderney Race, Casquets and Big Roussel with an added drag coefficient, C_e=0.015. Column 6 gives the average extracted power for the revised C_e, column 7 gives the maximum average power potential for the optimum C_e given in Table VII and column 8 shows the % reduction in

power potential between the two cases. Column 9 shows the change in mean volume flux through each site for the realistic cases, given as a ratio of the volume flux with energy extraction (Q) and without energy extraction from the ambient flow using Scenario 1 (Q_0).

Scenario	Sites and sites combinations	Realistic average extracted power (GW)				Maximum extracted power (GW) (from Table VII)	Change %	Q/Q_0
		Alderney Race	Casquets	Big Roussel	Total for site(s)			
(1)	(2)	(3)	(4)	(5)	(6)	(7)	(8)	(9)
2	Alderney Race	3.86	-	-	3.86	5.10	- 24%	0.73
3	Casquets	-	0.47	-	0.47	0.47	- 0%	0.56
4	Big Roussel	-	-	0.12	0.12	0.24	- 50%	0.89
5	Alderney Race & Casquets	4.05	0.79	-	4.84	6.12	- 21%	0.69 & 0.61
6	Alderney Race & Big Roussel	3.87	-	0.12	3.99	5.24	- 23%	0.75 & 0.90
7	Casquets & Big Roussel	-	0.49	0.12	0.69	0.79	- 13%	1.05 & 0.90
8	Alderney Race, Casquets & Big Roussel	4.01	0.78	0.11	4.90	6.45	- 24%	0.71 & 0.60 & 0.85

At Alderney Race the maximum average power potential (upper bound; P=5.1 GW) was obtained with a significantly higher added drag coefficient C_e=0.05 (Figure 8), because of the more constricted nature of the site and higher ambient flow velocities. Therefore when C_e was reduced to the more realistic case (C_e= 0.015, Figure 13), the reduction in extracted power was significant (-24%). The greatest drop in average extracted power was 50% at Big Roussel (Scenario 4), where the difference between optimum C_e (=0.09) and the realistic level applied here (C_e=0.015) is greatest.

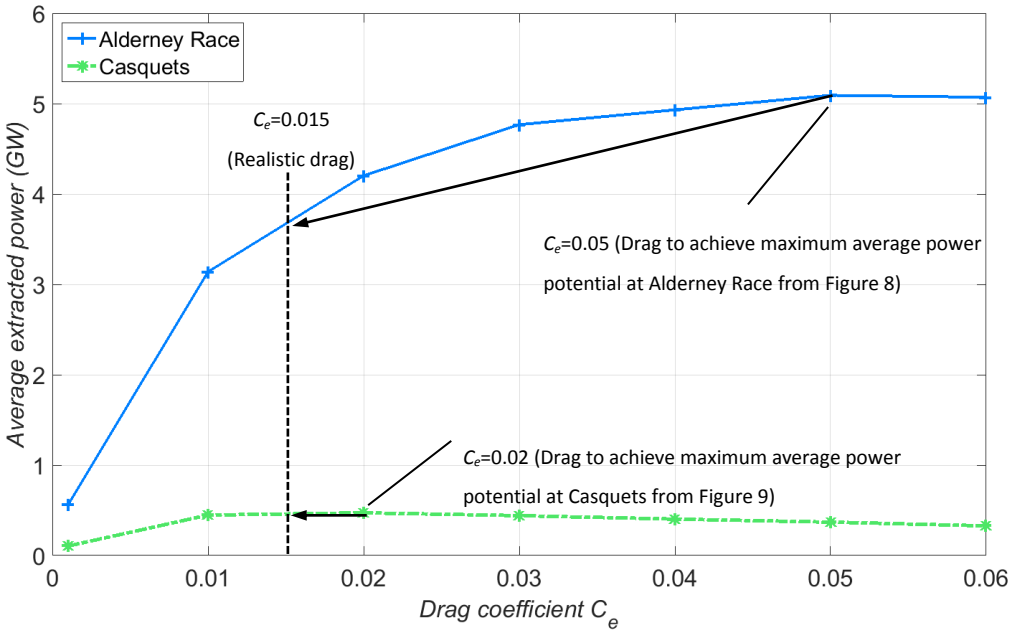

Figure 12. Average extracted power from Alderney Race and Casquets over an M_2 tidal cycle as a result of increased drag coefficient C_e applied uniformly over each energy extraction zone. Graph illustrates the reduction in mean extracted power when comparing the upper bound cases against a realistic level of C_e=0.015 at both sites.

Site interdependencies using the realistic value of C_e are also quantified in Table IX (Scenarios 5-8), and these should be compared with Table VII for the upper bound cases (results repeated in column 7 of Table IX).

e. Available power

The available power for electrical power production was estimated based on a power coefficient C_p=0.3 using Equation 12.

$$P = \frac{\lambda}{2}\frac{1}{T}\int_0^T \left(\iint_{A_z} \rho C_p |u|^3 dA\right) dt \qquad (12)$$

Results for available power, obtained using Equation 12, are presented in Table X. These results quantify the electrical power that could be generated by positioning turbines within the energy extraction zones located in Alderney Race, Casquets and Big Roussel with a uniform array density λ=0.0375, corresponding to C_e=0.015. As would be expected, the available power is significantly lower than the extracted power to account for the coefficient of power in Equation 12. This analysis shows that if the entire width of each site is developed the total average generated power at all three sites from the M_2 tide is 1.83 GW, with 82% from Alderney Race, 16% from Casquets and 2% from Big Roussel. Column 7 shows the realistic extracted power obtained previously in §4d for comparison. Given that results presented here were obtained with M_2 forcing only, the inclusion of additional constituent forcings would increase estimates for extracted and available power, which is the subject of ongoing work.

Table X. Realistic average available power for Scenarios 2-8 (first presented in Table II) using Alderney Race, Casquets and Big Roussel with an added drag coefficient, C_e=0.015. Column 7 shows the realistic average extracted power from Table IX for comparison.

Scenario	Site/Site combination	Realistic average available power (GW)				Realistic average extracted power (GW) (from Table IX)
		Alderney Race	Casquets	Big Roussel	Total for site(s)	
(1)	(2)	(3)	(4)	(5)	(6)	(7)
2	Alderney Race	1.44	-	-	1.44	3.86
3	Casquets	-	0.17	-	0.17	0.47
4	Big Roussel	-	-	0.04	0.04	0.12
5	Alderney Race & Casquets	1.51	0.29	-	1.80	4.84
6	Alderney Race & Big Roussel	1.45	-	0.04	1.49	3.99
7	Casquets & Big Roussel	-	0.18	0.04	0.22	0.69
8	Alderney Race, Casquets & Big Roussel	1.50	0.29	0.04	1.83	4.90

f. Change in flow dynamics

Figure 13a shows the change in mean velocity distribution due to energy extraction at Alderney Race (Scenario 2) in comparison to the ambient flow (Scenario 1). The increased drag applied uniformly over the energy extraction zone in Alderney Race diverts flow around Alderney and through Casquets, giving an increase in mean flux through Casquets of Q/Q_0=1.09 and a reduction in volume flux through Alderney Race of Q/Q_0=0.73. Energy extraction at Alderney Race (Scenario 2) has no significant impact on the flow velocities at Big Roussel, where flow velocities match those in the ambient case, giving the same mean volume flux through Big Roussel (i.e. Q/Q_0=1). This may change with the inclusion of additional boundary forcings as this will increase flow velocities within the Channel Islands, hence increasing the magnitude of the force exerted on the flow at the energy

extraction zone in Alderney Race and increasing the magnitude of bypass flow velocities around Alderney into Casquets and down into Big Roussel.

When energy is extracted at Alderney Race *and* Casquets together (Scenario 5), energy extraction at Alderney Race causes an increase in power extracted at Casquets in comparison to energy extracted at Casquets only (Scenario 3) of 0.32 GW, an increase of 68%. This results in an increase in total extracted power (at both sites) of 12% compared with energy extraction from the individual sites simulated separately (Scenarios 2 and 3). This is a similar finding to the upper bound case, emphasising the need for regulators and developers to account for the constructive impact from dual development at Alderney Race and Casquets when designing turbine layouts, as it will lead to improved energy yield, making it a more attractive proposition.

Figure 13b shows the change in mean velocity distribution due to energy extraction at Casquets in comparison to the ambient flow. The increased drag applied uniformly over the energy extraction zone in Casquets diverts flow around into the English Channel and through Alderney Race, shown by regions of enhanced mean flow velocity in Figure 13b. The added drag applied at Casquets gives a small increase in mean flux through Alderney Race of Q/Q_0= 1.02 and a reduction in volume flux through Casquets of Q/Q_0=0.56 . This high reduction in volume flux through Casquets is because Casquets is the least constrained site, so flow is easily diverted into the English Channel with the inclusion of added drag in Casquets' energy extraction zone. Energy extraction at Casquets gives no change in mean flow velocities at Big Roussel.

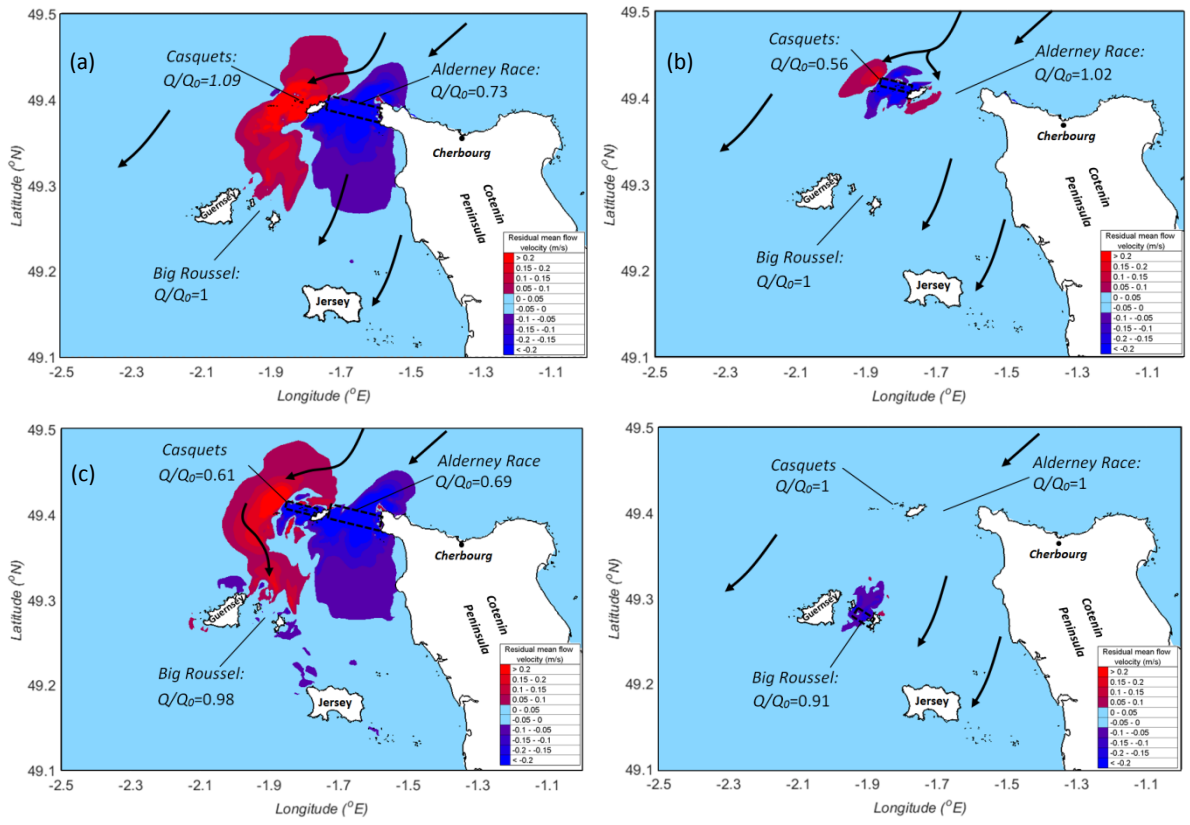

Figure 13. Mean velocity distribution difference plots between (a) the ambient case (Scenario 1) and flow with energy extraction at Alderney Race (Scenario 2) (b) the ambient case (Scenario 1) and flow with energy extraction at Casquets (Scenario 3) (c) the ambient case (Scenario 1) and flow with energy extraction at Alderney Race and Casquets (Scenario 5) (d) the ambient case (Scenario 1) and flow with energy extraction at Big Roussel (Scenario 4). A realistic level of energy extraction (C_e=0.015) applied to the energy extraction zones. Arrows show the direction of the dominant ebb tide and flow diversion around Casquets. The energy extraction zones at Alderney Race and Casquets are also shown along with the change in flow rate through Big Roussel as a result of energy extraction at Alderney Race and Casquets.

Figure 13c shows the change in mean velocity distribution due to energy extraction at Alderney Race and Casquets together (Scenario 5) in comparison to the ambient flow. The increased drag applied uniformly over the energy extraction zones at Alderney Race and Casquets diverts flow around Casquets and into the English Channel. This enhanced flow region persists down towards Guernsey, however it does not reach Big Roussel where the mean flow velocity actually reduces slightly compared with the ambient case (Scenario 1), giving a 2% reduction in mean volume flux through Big Roussel and a reduction in mean extracted power of 0.01 GW (8%) compared to energy extraction at Big Roussel only (Scenario 4). When energy is extracted at Alderney Race *and* Casquets together, energy extraction at Casquets causes an increase in power at Alderney Race of 0.2 GW, an increase of 5%.

Figure 13d shows that energy extraction at Big Roussel (Scenario 4) has a very localised effect on mean flow velocities compared with the ambient case, so does not effect mean flow velocities in Alderney Race and Casquets, resulting in no change in mean volume flux through Alderney Race and Casquets. Energy extraction at Big Roussel only (Scenario 4) gives a reduction in average volume flux through Big Roussel of 9% in comparison with the ambient case (Scenario 1).

Of all seven energy extraction scenarios investigated (Table IX) using realistic C_e, the maximum extracted power still occurred with energy extraction at all three sites as was the case for the upper bound simulations in §4c (Table VII). Using realistic C_e the mean total extracted power for the three sites working simultaneously is 4.9 GW, compared to 6.45 GW for the upper bound in Table VII. This was made up mainly at Alderney Race (4 GW) and Casquets (0.78 GW), with Big Roussel only contributing 0.11 GW, 2% of the total extracted power.

As indicated earlier, such results have implications for site development. That is, energy extraction planning within these sites will require careful, path-dependent techno-economic analysis. Authorities should consider what leasing conditions are likely to lead to the fullest and fastest development of tidal power in the region with a view that sites will affect each other.

5. Conclusions

A new 2D hydrodynamic model of the English Channel was developed to simulate tidal flows around the Channel Islands at significantly improved spatial and temporal resolution than previous work. Using this model, we have carried out a systemic analysis of energy extraction around the Channel Islands focussing on three sites – Alderney, Casquets and Big Roussel. The results provide estimates of the maximum average power potential at these sites which show large potential for power generation, especially at Alderney Race. We estimate that the maximum average power potential at Alderney Race is approximately 5.1 GW, which is 35% greater than that of the Pentland Firth (Draper et al. 2014), the best known site for tidal energy development in the UK. The maximum average power potential at Casquets and Big Roussel were lower but still significant at 0.47 GW and 0.24 GW respectively (Table VI).

The above results were established using upper bound limits to energy extraction. However, we have demonstrated that these upper bound limits often rely on unrealistically high array packing densities, where turbines in close proximity have a detrimental impact on device efficiency due to wake interaction. In this work we have implemented a more realistic drag coefficient C_e, resulting in reduced array density to a more realistic level. The analysis indicted that for the realistic case, the power that can be extracted is reduced by 24% (to 3.86 GW) and 50% (to 0.12 GW) at Alderney Race and Big Roussel respectively (Table IX) compared with the upper bound limits (Table VI). At Casquets there was no change in extracted power since the level of drag required to achieve the upper bound was relatively low. This is because Casquets is the least constricted site, meaning that added drag caused greater flow diversion around the site rather than a build-up in head which occurred at the

more constricted sites of Alderney Race and Big Roussel. For these realistic cases the available power for electrical power generation was also calculated. At Alderney Race, Casquets and Big Roussel the average available power was 1.44 GW, 0.17 GW and 0.04 GW respectively, in total 63% lower than the total extracted power from the three sites.

This work also investigated simultaneous energy extraction scenarios (Table IX). Using realistic C_e, the maximum total energy extracted still occurred when energy extraction was applied at all three sites as was the case for the upper bound simulations (Table VII). Using realistic C_e the mean total extracted power for the three sites working simultaneously is 4.9 GW, compared to 6.45 GW for the upper bound in Table VII. Even in the more realistic case, the Alderney Race has a higher power potential than any site in the UK.

Furthermore, when sites are working simultaneously and at more realistic levels of array drag, the increase in hydraulic resistance caused by added drag in Alderney Race diverts flow around Alderney, hence increasing energy extraction in Casquets by 68%. These results have implications for site development strategy, where it has been shown to be beneficial to develop Alderney Race and Casquets together, where the more Alderney Race is developed, the better the resource at Casquets becomes. This is good news for simultaneous energy extraction at these sites, and it would be beneficial for developers to work together to strategically position arrays in each site to maximise constructive impact on energy yield.

The above mentioned dependencies have major implications for the exploitation of such sites. That is, energy extraction planning within these sites will require careful, path-dependent techno-economic analysis. Regulators and developers should be aware of this so that a coherent development is planned for to minimise negative/account for positive impacts. In essence, authorities / regulators should consider what leasing conditions are likely to lead to the fullest and fastest development of tidal power in the region with a view that sites will affect each other. However, currently to the authors knowledge, there is no clear regulation that take into account such dependency and we hope that this work will provide the evidence to support the development of regulations that take into account the interdependencies between close tidal sites in the Channel Islands.

Acknowledgements
This work is part of the activities of the Energy and Climate Change Division and the Sustainable Energy Research Group at the University of Southampton (www.energy.soton.ac.uk). It is also supported by ESPRC under the Supergen Marine research programme. We also wish to extend our thanks to Alderney Commission for Renewable Energy (ACRE) and Alderney Renewable Energy Ltd (ARE) for the supply of bathymetry data in Alderney Race and AWAC flow data, which were used for validating the English Channel Model.

Data, code and material

The steering file used to run English Channel Model simulations using Telemac 2D is included in Appendix A. The other run files required to conduct the Telemac 2D simulations are the geometry, boundary conditions and subroutines files, which are all available on the University of Southampton Sustainable Energy Research Group website (http://www.energy.soton.ac.uk/).

Authors' contribution

Daniel Coles built and validated the English Channel Model and carried out all ambient and energy extraction simulations. He also conducted all post processing of computational results and drafted

the manuscript. Luke Blunden assisted in building and validating the English Channel Model, and provided input in analysing the computational results data and drafting the manuscript. AbuBakr Bahaj assisted in drafting the manuscript and supervising the research.

References

[1] Environmental Change Institute, "Variability of UK marine resources," pp. 12-13, Comissioned by the Carbon Trust, 2005.
[2] Black and Veatch, "Phase II UK Tidal Stream Energy Resourse Assessment," pp. 10-31, Comissioned by the Carbon Trust, 2005.
[3] Energy Technology Support Unit, "Tidal Stream Energy Review," Technical report ETSU-T/05/00155/REP, Harwell Laboratory, 1993.
[4] European Commission, The exploitation of tidal marine currents, Wave Energy, Project results. Technical Report EUR 16683 EN, 1996.
[5] A. S. Bahaj and L. Myers, "Analytical estimates of the energy yield potential from the Alderney Race (Channel Islands) using marine current energy converters," Renew. Energy, vol. 29, no. 12, pp. 1931–1945, Oct. 2004.
[6] S. Draper, T. A. Adcock, A. G. L. Borthwick, and G. T. Houlsby, "Estimate of the tidal stream power resource of the Pentland Firth," Renew. Energy, vol. 63, pp. 650–657, Mar. 2014.
[7] R. H. Karsten, J. M. McMillan, M. J. Lickley, and R. D. Haynes, "Assessment of tidal current energy in the Minas Passage, Bay of Fundy," Proc. Inst. Mech. Eng. Part A J. Power Energy, vol. 222, no. 5, pp. 493–507, Aug. 2008.
[8] R. A. Walters, M. R. Tarbotton, and C. E. Hiles, "Estimation of tidal power potential," Renew. Energy, vol. 51, pp. 255–262, Mar. 2013.
[9] G. Sutherland, M. Foreman, and C. Garrett, "Tidal current energy assessment for Johnstone Strait, Vancouver Island," Proc. IMechE Part A J. Power Energy, vol. 221, no. 2, pp. 147–157, Jan. 2007.
[10] J. Blanchfield, C. Garrett, A. Rowe, and P. Wild, "Tidal stream power resource assessment for Masset Sound, Haida Gwaii," Proc. Inst. Mech. Eng. Part A J. Power Energy, vol. 222, no. 5, pp. 485–492, Aug. 2008.
[11] A. Owen, "Tidal Stream Resource Assessment for the Channel Islands Area," 2005.
[12] Black and Veatch, "UK Tidal Current Resource and Economics," pp. 15-45, Commissioned by the Carbon Trust and npower, Project number 121393, 2011.
[13] P. Lang and J. Desombre, "TELEMAC-2D Software Operating Manual," Release 6.2, 2013.
[14] G. D. Egbert, S. Y. Erofeeva, and R. D. Ray, "Assimilation of altimetry data for nonlinear shallow-water tides: Quarter-diurnal tides of the Northwest European Shelf," Cont. Shelf Res., vol. 30, no. 6, pp. 668–679, 2010.
[15] A. M. Davies, P. Hall, M. J. Howarth, P. J. Knight, and R. J. Player, "Tidal currents, energy flux and bottom boundary layer thickness in the Clyde Sea and North Channel of the Irish Sea," Ocean Dyn., vol. 54, no. 2, pp. 108–125, 2004.
[16] P. Lang, "TELEMAC modelling system User Manual," EDF- R&D, pp. 33-34, 2010.
[17] D. C. Kapoor, "General bathymetric chart of the oceans (GEBCO)," Mar. Geod., vol. 5, no. 1, pp. 73–80, 1981.
[18] D. I. Braye, "Flow resistance in gravel-bed rivers," Gravel-bed rivers, Fluv. Process. Eng. Manag., vol. 1, pp. 109–137, 1982.
[19] P. Tassi, "Sisyphe v6.3 User's Manual," EDF SA 2014, 2014.
[20] Soulsby, Dynamics of Marine Sands, 1st ed. pp. 47-48: Thomas Telford, 1997.
[21] Zhou Liu, Sediment Transport, 1st ed. pp. 8-10: Aalborg Univeristy, 1999.
[22] G. Egbert and L. Erofeeva, "http://volkov.oce.orst.edu/tides/atlas.html," OSU Tidal Data Inversion, [Date Accessed: 07/06/2014], 2014. .

[23] “Sustainable Energy Research Group,” 2016. [Online]. Available: http://www.energy.soton.ac.uk/research/. [Accessed: 20-May-2016].
[24] A. S. Bahaj, A. F. Molland, J. R. Chaplin, and W. M. J. Batten, “Power and thrust measurements of marine current turbines under various hydrodynamic flow conditions in a cavitation tunnel and a towing tank,” Renew. Energy, vol. 32, no. 3, pp. 407–426, Mar. 2007.
[25] D. S. Coles, L. S. Blunden, and A. S. Bahaj, “Experimental validation of the distributed drag method for simulating large marine current turbine arrays using porous fences,” Int. J. Mar. Energy, no. In review, 2016.
[26] R. Pawlowicz, B. Beardsley, and S. Lentz, “Classical tidal harmonic analysis including werror estimates in MATLAB using T_TIDE,” Comput. Geosci., vol. 28, no. 8, pp. 929–937, 2002.
[27] “http://noc.ac.uk/using-science/products/tidal-harmonic-analysis,” [Date Accessed: 06/07/2014]. .
[28] UK Hydrographic Office, “Admiralty Tide Tables United Kingdom English Channel to River Humber (Including Isles of Scilly, Channel Islands and European Channel Ports),” NP201A, Volume 1A, 2016.
[29] D.T.Pugh, Tides, Surges and Mean Sea-Level, 1st ed. pp. 59: John Wiley & Sons, 1996.
[30] S. G. Haynes, “The Effects of Array Installation upon the Morphology of a Headland Associated Linear Sandbank,” pp 49-55, PhD: Transfer report, 2015.
[31] A. Pérez-Ortiz, J. Pescatore, and I. Bryden, “A Systematic Approach to Undertake Tidal Energy Resource Assessment with Telemac-2D,” in EWTEC 2013, 2013.
[32] European Commission, “The exploitation of tidal marine currents,” pp. 20-25, ISBN 92-827-5658-0, Report EUR 16683 EN, 1996.
[33] L. Myers and A. S. Bahaj, “Simulated electrical power potential harnessed by marine current turbine arrays in the Alderney Race,” Renew. Energy, vol. 30, no. 11, pp. 1713–1731, Sep. 2005.
[34] T. A. A. Adcock, S. Draper, G. T. Houlsby, A. G. L. Borthwick, and S. Serhadlıoğlu, “The available power from tidal stream turbines in the Pentland Firth,” Proc. R. Soc. A, vol. 469, no. 2157, pp. 72–93, 2013.
[35] C. Garrett and P. Cummins, “The power potential of tidal currents in channels,” R. Soc. A, vol. 461, pp. 2563–2572, 2005.
[36] Black and Veatch, “UK Tidal Current Resource & Economics : Appendix C,” pp. 24-52, Commissioned by the Carbon Trust and npower, Project number 121393, 2011.
[37] L. E. Myers and A. S. Bahaj, “Experimental analysis of the flow field around horizontal axis tidal turbines by use of scale mesh disk rotor simulators,” Ocean Eng., vol. 37, no. 2–3, pp. 218–227, Feb. 2010.

Appendix J Applied Energy journal paper

Journal paper submitted to Applied Energy in January 2017. The paper presents results from the English Channel hydrodynamic model that estimate the mean annual generated power from arrays within Alderney Race and Casquets. Comparisons are made with the output of the London Array, the world's largest offshore windfarm to highlight the significantly higher mean generated power per array plot area and total swept area that can be achieved with large tidal turbine arrays. Results are presented in Chapter 7.

Assessment of power generation from large tidal turbine arrays within Alderney Race

D. S. Coles[1], L. S. Blunden, A. S. Bahaj
Energy and Climate Change Division, Sustainable Energy Research Group, (www.energy.soton.ac.uk)
Faculty of Engineering and the Environment, University of Southampton, UK
[1]d.coles@soton.ac.uk

Abstract

Large tidal turbine arrays deployed in the energetic tidal flows at Alderney Race were highlighted as having a significant and predictable power that could supply the Channel Islands, with export to Britain and France. In order to provide a thorough appraisal of this, we have developed a 2D hydrodynamic model of the English Channel to simulate multiple energy extraction scenarios in both the Alderney Race as well as the neighbouring site of Casquets. The work takes a holistic approach by considering site scale energy extraction to account for global blockage affects, which to date has received limited attention in the literature. Estimated power production was compared with that of the London Array, the world's largest offshore windfarm to assess the likely level of tidal energy development that is feasible in the region. The results demonstrate that large scale energy extraction within the most energetic flows in the East Race is capable of generating a time-averaged power output of 0.25 GW, 25% greater than that of the London Array, using only 9% of the windfarm's plot area and 20% of the total swept area, albeit with nine times more individual devices. It is shown that energy extraction causes a significant change to the surrounding flow dynamics, which affects the performance of tidal energy developments in Casquets. Regulators and developers from both France and Alderney must consider these effects to plan the most effective overall tidal energy development.

Keywords

Tidal energy, Alderney Race, power generation, hydrodynamic modelling.

1. Introduction

Alderney Race (also known as Raz Blanchard) is situated between the Cotentin Peninsula, Normandy, France and the island of Alderney in the Channel Islands (Figure 1). Spring tides flow in a North Westerly and South Easterly direction at rates of approximately 5 m/s and 3.5 m/s respectively, with depths ranging between 15 to 50 m over the majority of the narrowest section of the Race. These characteristics are within the suitable ranges to extract energy using large tidal turbine arrays for electricity production.

Currently the island of Alderney is self-reliant in generating its own electricity. This is done predominantly using diesel generators to meet a peak electricity demand of just 1.5 MW and annual consumption of approximately 6.6 MWh (Balsells 2015). The other two largest Channel Islands of Jersey and Guernsey import approximately 500 GWh of electricity a year from mainland France through sub-sea interconnecting cables that runs from France to Jersey then on to Guernsey, as illustrated in Figure 2. Approximately 430 GWh is used on Jersey which accounts for 86% of the total electricity imported from France to the two islands. Based on results from previous studies reviewed in §2 ((Energy Technology Support Unit 1993; Bahaj & Myers 2004; Myers & Bahaj 2005; Black and Veatch 2005; Black and Veatch 2011b)), there is potential for electricity generation by large tidal stream turbine arrays in Alderney Race to far exceed the combined demand of Alderney, Jersey and Guernsey. However, given that previous estimates of energy extraction in Alderney Race vary significantly depending on (a) resource consideration (flow data), (b) array size and position considered and (c) method used to model energy extraction, there is still a high degree of

uncertainty as to the achievable electricity generation potential. Sources of error from previous estimates include the use of low spatial and temporal resolution flow data and less robust approaches for simulating energy extraction, (see detailed discussion in in §2). In order to address these limitations in this work we propose the use of a 2D hydrodynamic model that accurately simulates the depth-averaged flow dynamics around the Channel Islands at improved spatial and temporal resolution. This also allows energy extraction to be simulated using the distributed drag method (outlined in §3d) which has been validated experimentally using arrays of porous fences (Coles et al. 2016).

Given the relatively low demand for electricity amongst the Channel Islands, there are proposals for a new 220 km, 1.4 GW capacity high voltage direct current (HVDC) interconnecting sub-sea cable between England, Alderney and France to export electricity generated by tidal turbines in Alderney Race (Nauclér 2016). The interconnector will also be used to deliver electrical power from other sources between the UK and France. At this stage it is unclear how much capacity will be available for exporting electricity generated by the tidal turbines and this work will provide an indication of this potential and any implications to cable export capacity. This is an important consideration as it is conceivable that at times of spring tide, the electrical power generated by tidal turbines in Alderney Race could exceed the available interconnector capacity, leaving no route to market for excess electricity.

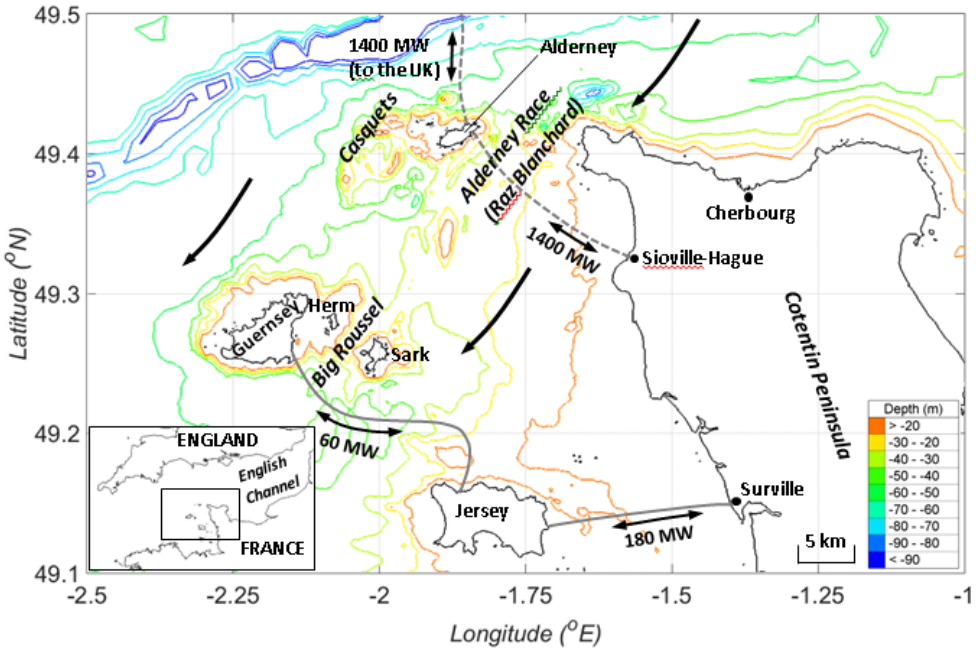

Figure 1. Location of Alderney Race and Casquets in the Channel Islands off the West coast of Normandy, France. Arrows show the direction of the dominant ebb tide. Solid grey lines show the route and capacity of interconnector cables currently in operation (solid line) and proposed in the future (dashed line). Arrows show the direction of the dominant ebb tide. The location of the Channel Islands is shown inset.

The island of Alderney is a constituent part of the Bailiwick of Guernsey and is governed by the States of Alderney. Alderney territorial waters cover over ninety square nautical miles, which stretch three nautical miles into Alderney Race from the Islands South East coastline. Within these territorial waters, Alderney Commission for Renewable Energy (ACRE) has set out 94 x 1 NM^2 development plots for tidal energy development, which are shown in Figure 2. Of these 94 development blocks, 19 blocks have been initially earmarked for tidal energy development within Alderney Race. A further 15 blocks have been assigned in Casquets and a further 14 blocks in the Ortac Channel (ABPmer 2013). These assigned development blocks are shaded blue in Figure 2. The first proposed development within Alderney's territorial waters is a 300 MW array, consisting of 150 x 2 MW

devices with subsea gravity bases, with installation expected to begin in 2020 (Race Tidal 2014). For this array a spacing between turbines of 40 x 200 m has been proposed, which assumes no interaction between adjacent turbines (ABPmer 2013).

The East side of Alderney Race is situated within French territorial waters. In this region, there are plans to install a 7 x 2 MW array as part of the NORMANDIE HYDRO project, a joint venture between Open Hydro DCNS and EDF Energies Nouvelles. There are also plans for a 5.6 MW pilot tidal array consisting of 4 x 1.4 MW devices as part of the NEPTHYD (Normandie Energuie PiloTe HYDrolien) project. It is conceivable that as tidal energy development within French territorial waters increases (i.e. within the East Race), the added hydraulic resistance caused by the turbines will divert flow into the West Race (i.e. into Alderney territorial waters). This is likely to modify the flow dynamics within French territorial waters, impacting on the resource located in the West Race. This is known as the global or array scale blockage effect (Funke et al. 2015). The reverse could also be true. Such effects have been shown to be an important consideration for the other Channel Island site of Casquets, which lies to the West of Alderney (but still within Alderney territorial waters as shown in Figure 2), where it has been shown that tidal arrays within Alderney Race enhance flow velocities within Casquets, improving the resource at Casquets (Coles et al. 2016).

The thrust of this work is to tackle some of the unanswered questions regarding the strategy for developing tidal energy in Alderney Race, such as; how much electrical power can realistically be harnessed within acceptable spatial constraints? How does energy extraction by large tidal turbine arrays effect the surrounding flow dynamics within Alderney Race and Casquets? How spatially efficient is electrical power generation from large tidal turbine arrays within Alderney Race compared with that of typical large windfarms currently in operation around the UK? Will there be times when electrical power generation exceeds the export capacity of the new FABlink interconnector? And how will tidal array sites at Alderney Race and Casquets be developed to avoid/account for site-site interaction?

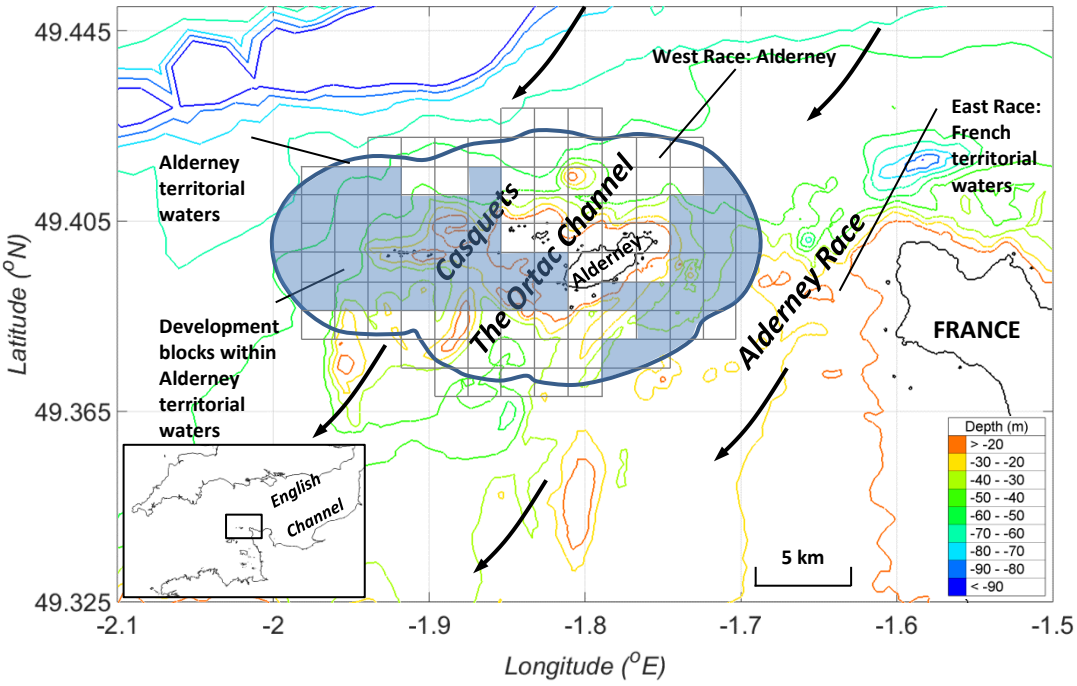

Figure 2. Location of development blocks (shaded) set out by Alderney Commission for Renewable Energy (ACRE) over Alderney Race and Casquets within Alderney territorial waters, which reach out 3 nm into Alderney Race. The East side of Alderney Race is located in French territorial waters. Arrows show the direction of the dominant ebb tide. The location of the Channel Islands is shown inset.

2. Previous estimates for electrical power generation in Alderney Race

Table 1 summarises results from previous studies that provide estimates of the electrical power generation from tidal flows through Alderney Race. These estimates vary significantly depending on the approach taken. In (Energy Technology Support Unit 1993), low spatial and temporal resolution data (typically hourly intervals at below twenty locations around Alderney Race) were used with the kinetic energy flux method, which fails to account directly for the changes in flow dynamics caused by adding tidal turbines to the flow. Later studies concluded that there is no simple relationship between the maximum average power and the average kinetic energy flux in the undisturbed case (Garrett & Cummins 2005). However, as turbines are added to a channel, the flow upstream of the turbines slows, increasing the tidal head and hence the forcing driving the flow, which the kinetic energy flux method does not account for. Estimates for electrical power generation using this approach vary significantly, between 1.35 - 7.4 TWh/year which corresponds to an average generated power ranging between 154 – 844 MW. This wide range is mainly due to the different array capacities considered and the different data sources used.

In other work flow data from tidal stream atlases and admiralty charts was used to estimate the kinetic flux through cross sections of Alderney Race (Black and Veatch 2005). A Significant Impact Factor (SIF) was introduced to quantify the percentage of the kinetic energy flux that could be extracted without significant detrimental environmental impact. The SIF was chosen initially at 20% then later reduced to 12%, giving an estimated annual power output ranging between 0.37 - 1.37 TWh/year, corresponding to an average generated power ranging between 42 – 156 MW. Such considerations also depended on the width of the channel cross section when estimating the kinetic flux, which ranged between 3.3 km – 5 km for different studies. Again these results assume no change in flow dynamics with the inclusion of energy extraction which has since been shown to be invalid (Garrett & Cummins 2005).

The analytical model developed in (Garrett & Cummins 2005) was used to quantify the maximum average power potential of Alderney Race (Black and Veatch 2011b). This is defined as the maximum total energy that can be extracted when averaged over a tidal cycle. The model gives the upper bound to energy extraction as between 20-24% of the peak tidal pressure head multiplied by the peak undisturbed mass flux through a channel with no side channels for flow diversion [15]. Using this approach it was concluded that 6% of the total tidal energy resource around the UK lies in Alderney Race (Black and Veatch 2005) . According to this study. This corresponded to a third of that estimated from the Pentland Skerries and approximately three quarters of the total resource in the Channel Islands [5]. However the 1 dimensional model developed in (Garrett & Cummins 2005) assumes a uniform flow across the channel in question so cannot account for the highly varied flow across Alderney Race caused by bathymetric features and asymmetric coastlines, bringing into question the accuracy of this approach presented in [5].

In (Coles et al. 2015) a new 2D hydrodynamic model was developed and used to simulate flow through Alderney Race at higher spatial and temporal resolution than previous work. Energy extraction was modelled by considering a single row of turbines spanning the width of Alderney Race using the distributed drag approach. The work showed that for a blockage ratio $\varepsilon=0.13$ (corresponding to a 1 diameter tip-to-tip lateral spacing between turbines), 0.78 TWh/year of electrical power could be generated, equivalent to 88 MW mean annual output. Further work modelled the energy extraction from multi-row turbine arrays spanning the width of Alderney Race (Coles et al. 2016). Here it was shown that when using an array density $\lambda=0.037$ (equivalent to a 2 diameter tip-to-tip lateral spacing between turbines and 7 diameters longitudinal spacing between rows) over a 3 km strip spanning the width of Alderney Race, an average annual power output of

3.86 GW is possible. This is comparable with results from studies commissioned by Alderney Renewable Energy Ltd (ARE) (ABPmer 2013) which conclude that the extractable energy contained within Alderneys territorial waters (shown in Figure 2) exceeds 4 GW, however it is unclear how this result was obtained.

Table 1. Summary of previous estimates for power generation using large tidal turbine arrays in Alderney Race.

Study	Data source(s)	Method	Estimated electrical energy output (TWh/year)	Mean annual power output (MW)
Energy Technology Support Unit, 1993 (Energy Technology Support Unit 1993)	Navigational charts	Farm, array covers 68 km^2 in waters deeper than 20 m. Array capacity=2.4 GW.	5.2	590
European Commission, 1996 (European Commission 1996)	Navigational charts	Kinetic energy flux method with low array density. Array capacity of 1.9 GW.	6.5	740
Bahaj & Myers, 2004 (Bahaj & Myers 2004)	Admiralty tidal stream atlas NP 264	Kinetic energy flux method, assuming a 5% wake deficit within sub arrays. Array capacity of 0.84 GW.	7.4	840
Black & Veatch, 2004 (Black and Veatch 2005)	Tidal stream atlases, admiralty charts	20 % of kinetic energy flux through a 3.3 km section of Alderney Race.	1.37	155
Black & Veatch, 2004 (Black and Veatch 2005)	Tidal stream atlases, admiralty charts	20% of kinetic energy flux through a 5km section of Alderney Race.	0.61	70
Black & Veatch, 2005 (Black and Veatch 2005)	Tidal stream atlases, admiralty charts and the Marine Energy Atlas	12% of kinetic energy flux through a 5km section of Alderney Race.	0.37	40
Myers & Bahaj, 2005 (Myers & Bahaj 2005)	Admiralty tidal stream atlas NP 264	Kinetic energy flux method combined with BEM simulation to optimise turbine performance, asymptotic wake deficit assumed within subarrays based on momentum theory. Total array capacity of 1.5 GW.	1.35	155
Black & Veatch, 2011 (Black and Veatch 2011b; Black and Veatch 2011a)	Marine Energy Atlas	2D hydrodynamic model of generic tidal stream used to obtain inputs to analytical model developed in (Garrett & Cummins 2005) to estimate maximum power potential. Arbitrary SIF used.	2.25	255
Coles, Blunden, Bahaj, 2015 (Coles et al. 2015)	European Shelf 2008 OTIS regional tidal solution (Egbert & Erofeeva 2014)	2D hydrodynamic model of English Channel, distributed drag method used to simulate energy extraction from single row array spanning the whole width of Alderney Race with blockage ε=0.13, corresponding to a lateral spacing between turbines of 1 diameter.	0.78	88
Coles, Blunden, Bahaj, 2016 (Coles et al. 2016).	European Shelf 2008 OTIS regional tidal solution (Egbert & Erofeeva 2014)	2D hydrodynamic model of English Channel, distributed drag method used to simulate energy extraction using a large multi-row array spanning the width of Alderney Race using a realistic array density λ=0.037 to parameterise uniformly distributed turbine array drag.	33.8	3860

Given the significant range of power output estimates presented in Table 1, it is clear that there is still a high degree of uncertainty as to the level of power that can realistically be generated from tidal flows within Alderney Race. Here we aim to quantify the likely level of power generation that is feasible within Alderney Race using the 2D hydrodynamic English Channel Model.

3. 2D hydrodynamic model of the English Channel

This section gives a brief overview of the setup and validation of the English Channel hydrodynamic model used to simulate flow at Alderney Race. The model was first used to quantify an upper bound for energy extraction (termed the maximum average power potential (Draper et al. 2014)) of Alderney Race, Casquets and Big Roussel (located between the Islands of Herm and Sark – see Figure 1). A more in depth description of the model is given in (Coles et al. 2016).

a. Model setup

Telemac 2D was used to build a new 2D hydrodynamic model of the English Channel which solves the shallow water equations using the finite element method. The model is driven by tidal elevation data extracted from the European Shelf 2008 model (Egbert & Erofeeva 2014) at three open boundaries located in the Irish Sea, Atlantic Ocean and English Channel (Figure 3). Bathymetry data was obtained and used predominantly from TCarta (TCarta 2014) at 90 m resolution for the whole of the English Channel. High resolution (1 m) multi swath bathymetry data was used for a small region off the South coast of Alderney, known as the Southbank. In regions at the far extremities of the domain which are not cover by this dataset such as the North Sea and Celtic Sea, GEBCO (Kapoor 1981) data at 900 m resolution was used. Bathymetry was mapped onto an unstructured mesh with 5km resolution in deep water (>50m), 1km around the Channel Islands and 100 m in Alderney Race to achieve mesh independence when simulating ambient flow and energy extraction (Coles et al. 2016).

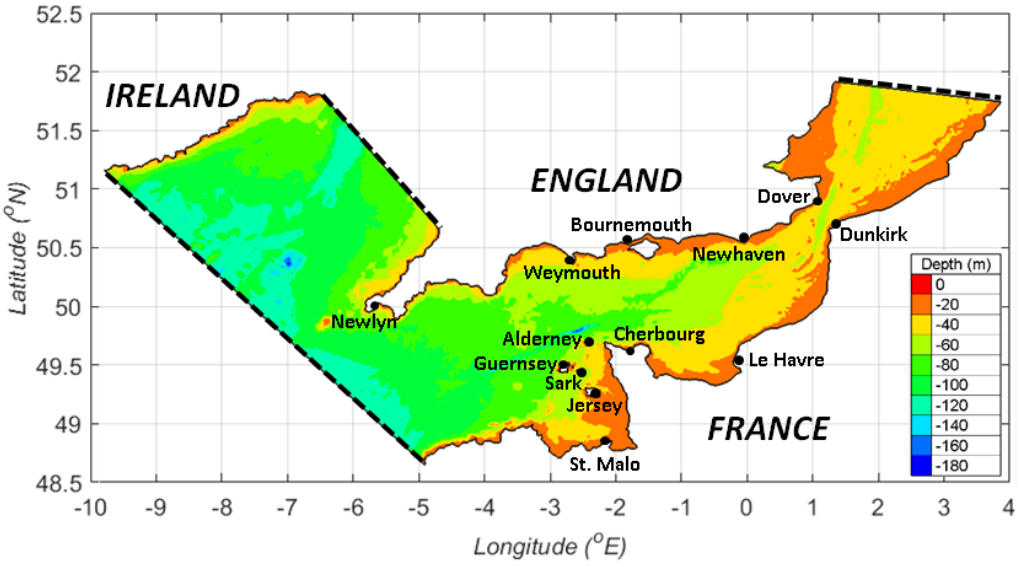

Figure 3. English Channel Model domain in Universal Transverse Mercator (UTM) projection, showing the location of three open boundaries (dashed lines) and depth in metres. Also shown are the location of thirteen ports used for validation.

a. Validation

The model was validated using elevation time series at thirteen ports around the domain, including six in the Channel Islands, as shown in Figure 3. M_2 and S_2 amplitudes and phases agreed within 10%

and 10° respectively of real values at nine of the thirteen ports, including all six around the Channel Islands where Alderney Race is located.

Good agreement was also achieved for the model results with flow time series data obtained from Acoustic Wave and Current Profiler (AWAC) deployments in Alderney Race, where all M_2 major axis results lie within 10% of the measured values. Phases and inclinations also show good agreement, with all results excluding one lying within 15 degrees of the true values (Coles et al. 2016).

b. Array layouts

In this study we use time averaged generated power per swept area $\bar{P}_\eta$ to assess the performance of tidal arrays of varying size and density in Alderney Race. This approach was first adopted for assessing the viability of adding rows of turbines spanning the width of the Pentland Firth (Adcock et al. 2013), where it was assumed that the performance of the added turbines must exceed 1 kW/m^2 to be feasible. This was based on the performance of offshore windfarms, which typically operate in the range 0.25-1 kW/m^2 (2013). Since large offshore windfarms based on 3 bladed horizontal axis turbines are the closest technology to tidal turbines used in arrays (farms), time averaged generated power per swept area ($\bar{P}_\eta$) was seen as the most suitable metric to assess arrays in Alderney Race at this stage of development. This will also allow direct comparison with results obtained in (2013) for the Pentland Firth.

Initially, ambient flow simulation results from the English Channel Model were used to estimate the time averaged kinetic power per swept area (Equation 1) of isolated turbines (referred to as $\bar{P}_{\eta,KF}$ from now on) positioned around Alderney Race and Casquets using the kinetic flux method.

$$\bar{P}_{\eta,KF} = \frac{1}{T}\int_0^T \frac{1}{2}\rho U^3 C_P \; dt \tag{1}$$

Where ρ is the density of seawater equal to 1025kg/m^3, C_p is the power coefficient of the turbine, assumed constant at C_p=0.3 and A_s is the swept area of the turbine, which assumes turbine diameter $d=1/3h$, where h is depth at each location. Power is time averaged over a period T=1 month to obtain estimates of the mean annual power from an isolated turbine at each location in the flow using flow velocities output from the model at 1 minute resolution. This preliminary approach for finding the most energetic flows assumes turbines have no effect on the ambient flow dynamics, so that the generated power can be estimated using the ambient flow velocities, which is analogous with the farm method discussed in §2. Since the farm method has been shown to be inappropriate for estimating power generation from large arrays, it was only used to identify the most energetic regions of the Race for tidal turbines to be placed. To overcome the limitations of the farm method, the distributed drag method was implemented to account for the increase in hydraulic resistance caused by adding turbines to the flow and its effect on the power output of arrays.

d. Energy extraction

As indicated earlier energy extraction was modelled using the distributed drag method, where the force exerted on the flow by turbines is added to the existing bed drag coefficient C_b using an equivalent added drag coefficient C_e applied over the array plot area, A_p. This added drag coefficient C_e is parameterised using the approach taken in (Plew & Stevens 2013; Walters et al. 2013), where the force exerted on the flow by n turbines each with swept area A_s is given by:

$$\bar{F} = \frac{1}{2}\rho u^2 C_T A_s n \tag{2}$$

Where *u* is the depth averaged flow speed at the turbine and C_T is the thrust coefficient of the turbine, which was assumed to remain constant at C_T=0.8 based on scaled down experimental results for the force exerted on a single rotor (A. S. Bahaj et al. 2007). This neglects the additional drag caused by the turbine support structure, which is likely to contribute significantly to the total added drag. This was deemed a sensible approach for this early stage investigation as not to favour any specific turbine and support structure, for which there is limited available data available to parameterise support structure drag. Further work is underway to investigate the effect of this added support structure drag on the generated power of large arrays. The added turbine drag is applied as a stress term τ_a in the momentum equations (Equation 3).

$$\tau_a = \frac{\bar{F_a}}{A_p} = \frac{1}{2}\rho u^2 C_T \lambda \tag{3}$$

Where λ is array density given by $\lambda = \frac{nA_S}{A_P}$. Stress is added to the momentum equations in the form $\frac{\tau_a}{\rho h}$ where *h* is the flow depth, giving an extra depth averaged source term:

$$\frac{\tau_a}{\rho h} = \frac{\lambda C_t}{2h}|u|u = \frac{C_e}{h}|u|u \tag{4}$$

The array drag coefficient C_e is parameterised using the array density λ and thrust coefficient of a single turbine C_T (Walters et al. 2013):

$$C_e = \frac{1}{2}\lambda C_T \tag{5}$$

The validity of this method was investigated experimentally using arrays of porous fences in a recirculating flume to simulate the wakes downstream of densely packed tidal stream turbines rows (Coles et al. 2016).. These results validated the distributed drag approach for arrays within the realistic density range of tidal turbine arrays (λ<0.07) for two different vertical inflow distributions of flow velocity and turbulence intensity in the vertical plane (Coles et al. 2016).

The time averaged power generated by each array was estimated using the new flow velocities within the array after implementing the distributed drag approach (Equation 6), integrated over time *T* and over the array plot area A_p:

$$P = \frac{\lambda}{T}\int_0^T \left(\iint_{A_p} \frac{1}{2}\rho u^3 C_P \, dA_p \right) dt \tag{6}$$

Where λ is the array density. The time averaged total power per swept area (now referred to as $\bar{P}_\eta$) is calculated here by simply dividing P from Equation 6 by the total swept area, nA_s. A potential error associated with this method is that flow velocity within the array is spatially averaged, making it unrepresentative of the flow velocity incident on each row of turbines. This was investigated experimentally in (Coles et al. 2016), and the results confirmed that the distributed drag method is robust for high row spacing and/or high ambient turbulence intensity cases, two features that improve wake recovery between rows of turbines (Coles et al. 2016).

4. Results

a. Ambient flow characterisation

Figure 4 shows the time averaged ambient velocity distribution in Alderney Race . The significant spatial variation in time averaged velocities across Alderney Race is caused by bathymetric features. For example, in the West Race (within Alderney Territorial Waters) off the North East tip of Alderney, a region of high mean velocity stretches out into Alderney Race. In this region, highest time averaged velocities exceeding 2 m/s are located around Race Rocks, two tower like rock formations in close proximity to one another that accelerate flow through and around them, creating strong jet flows during ebb tide. In this region, time averaged flow velocities exceed 2 m/s over an area of 2 km^2, and reach magnitudes of up to 5.4 m/s.

In the East Race (French Territorial Waters) a large region of high mean flow velocities exceeding 2 m/s is located 2 km off the French coast in a shallow region where depth decreases with distance from the French coast to around 15 m. In this region, time averaged flow velocities exceed 2 m/s over an area of 21 km^2 and reach flow speeds of up to 6 m/s.

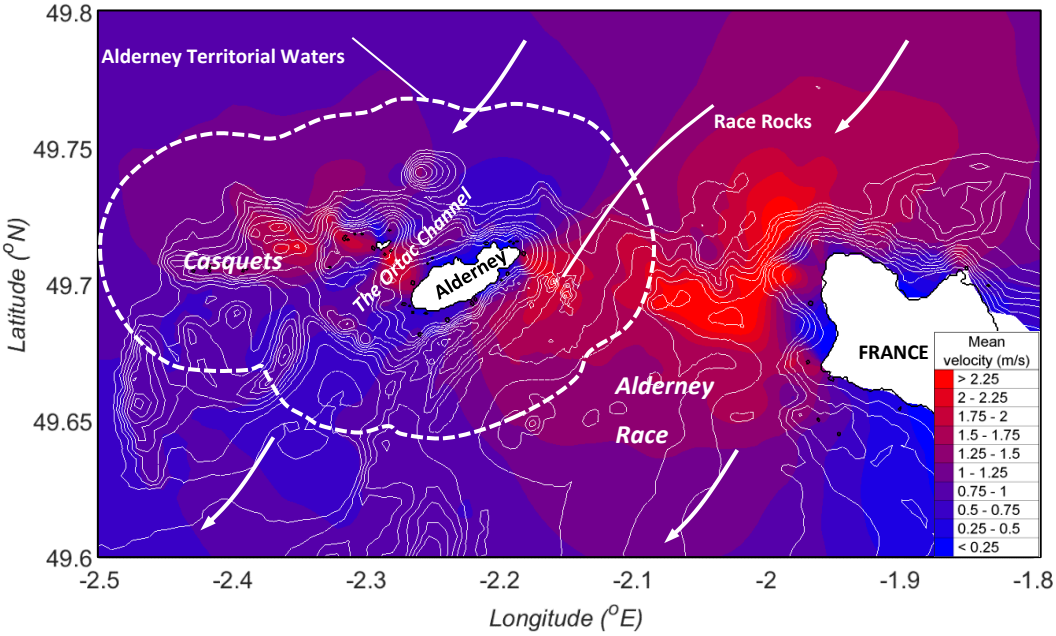

Figure 4. Time averaged distribution of flow velocity within Alderney Race and Casquets. The perimeter of Alderney Territorial Waters is shown by the white dotted line. The location of Race Rocks is also shown. Depth contours at 5 m intervals show the variation in depth across Alderney Race and Casquets, including the location of Race Rocks within Alderney Territorial Waters. Arrows show the direction of the dominant ebb tide.

In Casquets the total area for which time averaged velocities exceed 2 m/s is 0.5 km^2. Typically, the flows in Casquets are much shallower than the majority of Alderney Race, which is also true of the Ortac Channel, where depths rarely exceed 15 m. This would require turbines with a diameter not exceeding 5 m, so for this reason energy extraction in the Ortac Channel is not considered further in this work. In Casquets maximum velocities reach up to 4.2 m/s in depths greater than 15 m.

As described in §3c, to establish the most suitable areas for tidal energy development, a kinetic flux approach was taken to estimate the time averaged power available to isolated turbines placed in the flow (described by Equation 1). This approach assumes turbines have a diameter equal to one third of depth and that deploying turbines gives no disturbance to the ambient flow dynamics so that power is proportional to the kinetic power and turbines act as isolated devices. In reality this has been shown not to be the case (Garrett & Cummins 2005). However, such an approach provides a

reasonable starting point for locating the most energetic regions within Alderney Race and Casquets for array development.
Based on this approach four energy extraction scenarios were set out; three in Alderney Race and one in Casquets as outlined in Table 2 and shown diagrammatically in Figure 5. The perimeter of Arrays 1,2 and 3 (all located within Alderney Race) were set out to cover regions where the time averaged power per swept area exceeds 3 kW/m^2, 2 kW/m^2 and 1 kW/m^2 respectively. Array 4 in Casquets covers a region where the time averaged power per swept area exceeds 1 kW/m^2. Energy extraction scenario 2 contains turbines in two separate regions where the mean flow reached 2kW/m^2, one in the East Race covering an area of 16km^2 and one in the West Race, covering 1 km^2. In general, the array perimeters follow the contour lines for which power per swept area exceeds 3 kW/m^2, 2 kW/m^2 and 1 kW/m^2 respectively, however simplifications were made to make the array edges linear.

For each energy extraction scenario listed in Table 2, five simulations were run to model energy extraction using a range of array densities, where array density is defined as the ratio of the total swept area to the plot area. The distributed drag applied uniformly over each array area was increased incrementally to investigate the effect of adding more turbines to each array on the power output and the surrounding flow field.

Table 2. Characteristics of four energy extraction scenarios; Array 1: Alderney (small), Array 2: Alderney (medium), Array 3: Alderney (large) and Array 4: Casquets used to simulate energy extraction in Alderney Race and Casquets based on mean annual power per swept area $\bar{P}_{\eta,KF}$ using the kinetic flux method. Plot area A_p also shown.

Energy extraction scenario	$\bar{P}_{\eta,KF}(\min)(kW/m^2)$	$A_P\ (km^2)$	Array density
Array 1: Alderney (small)	3	9	0.01, 0.02, 0.04, 0.06, 0.08
Array 2: Alderney (medium)	2	16+1	0.01, 0.02, 0.04, 0.06, 0.08
Array 3: Alderney (large)	1	52	0.01, 0.02, 0.04, 0.06, 0.08
Array 4: Casquets	1	3	0.01, 0.02, 0.04, 0.06, 0.08

Whilst adding turbines will inevitably reduce the available power per swept area due to large scale blockage effects, this approach was taken to investigate the most energetic ambient flows within Alderney Race and Casquets based on available power per swept area, a metric used to assess the viability of tidal turbine arrays in the Pentland Firth (Adcock et al. 2013) through comparison with the performance of offshore windfarms (London Array 2016). For comparison, the time averaged available power per swept area of the London Array, the world's largest offshore windfarm, achieved 0.25 kW/m^2 during a maximum performance period in December 2015 (London Array 2016).

Figure 5 shows that within Alderney Territorial Waters, the distribution of time averaged available power per swept area exceeds 1 kW/m^2 in thirteen of the nineteen tidal energy development blocks set out by Alderney Renewable Energy (ARE (Race Tidal 2014)) that were originally described in Figure 2.

The greatest resource (in terms of kinetic power per swept area) is located in the East Race within French Territorial Waters (covered by Array 1 in Figure 5), where the time averaged available power per swept area exceeds 3 kW/m^2 over an area of 9 km^2 and exceeds 9 kW/m^2 within the centre of Array 1 where depths are shallowest.

In Casquets and the Ortac Channel, the distribution of time averaged available power per swept area exceeds 1 kW/m^2 in just seven of the twenty nine tidal energy development blocks set out by ARE. Of these seven, in three of the development blocks depths do not exceed 15 m.

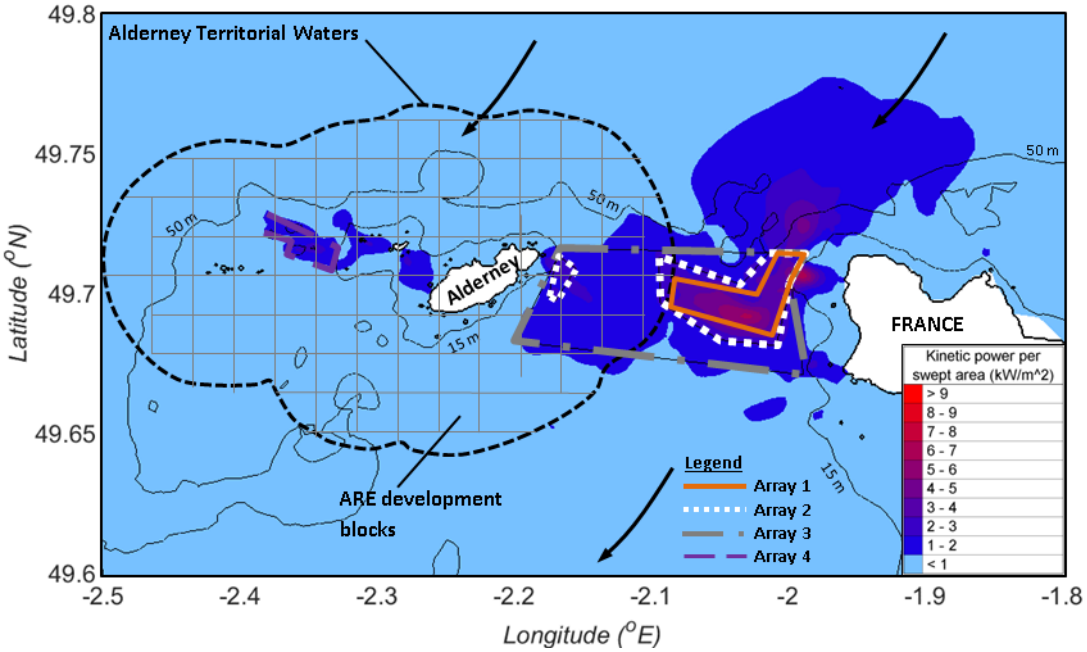

Figure 5. Arrays 1,2,3 and 4 located in Alderney Race and Casquets over regions of highest time averaged kinetic power per swept area within depths ranging between 15 m and 50 m. The perimeter of Alderney Territorial Waters is shown by the white dotted line, which contains development blocks set out by Alderney Renewable Energy (ARE). Arrows show the direction of the dominant ebb tide.

b. Power generation estimates in Alderney Race

Figure 6a depicts the average annual generated power of Arrays 1, 2 and 3 in Alderney Race when array density is incrementally increased. The mean annual power generated by Array 3 is far superior to that of Arrays 1 and 2, so much so that its minimum average annual generated power of 0.7 GW using λ=0.01 exceeds that of the maximum average power generated by Array 1 (0.65 GW using λ=0.078) by 8%. However, this is somewhat unsurprising given that the plot area of Array 3 is 475% greater than Array 1. For all three arrays, as array density increases, the rate of increase in average annual generated power reduces. For example, Figure 6a shows that when the density of Array 1 increases from λ=0.01 to 0.02, there is an increase in power of 0.15 GW (60%). However when the density of Array 1 increases from λ=0.06 to 0.07, there is only a 0.05 GW (8%) increase in average power. This is because the increase in array drag reduces the flow velocities upstream and within the array plot area, and also causes flow to divert around the array, taking a path of less resistance and reducing the available power within the array itself. Flow diversion around the arrays is extremely important when considering such sites and is quantified and discussed in more detail in §4e.

The difference in array plot area A_p is accounted for in Figure 6b by considering the average annual generated power per plot area, which is an indicator of the spatial efficiency of each array. Since Array 1 covers regions where for the ambient flow, $\overline{P}_{\eta,KF}$ exceeds 3 kW/m^2 only, it has the greatest spatial efficiency as it is positioned only in the most energetic flows.

The spatial efficiency of Array 2 is less than Array 1 for two reasons; the first is that to create Array 2, turbines are added in less energetic regions around the perimeter of Array 1 where $\overline{P}_{\eta,KF}$ exceeds 2 kW/m^2 (instead of 3 kW/m^2 for Array 1 as shown in Figure 5), so there is less energy to extract from the flow within this added area. Additionally the turbines added around the perimeter of Array 1 (to make Array 2) inhibit flow through the centre of the array (i.e. the flow incident on turbines within Array 3's plot area), therefore reducing the average annual generated power and spatial efficiency of these turbines.

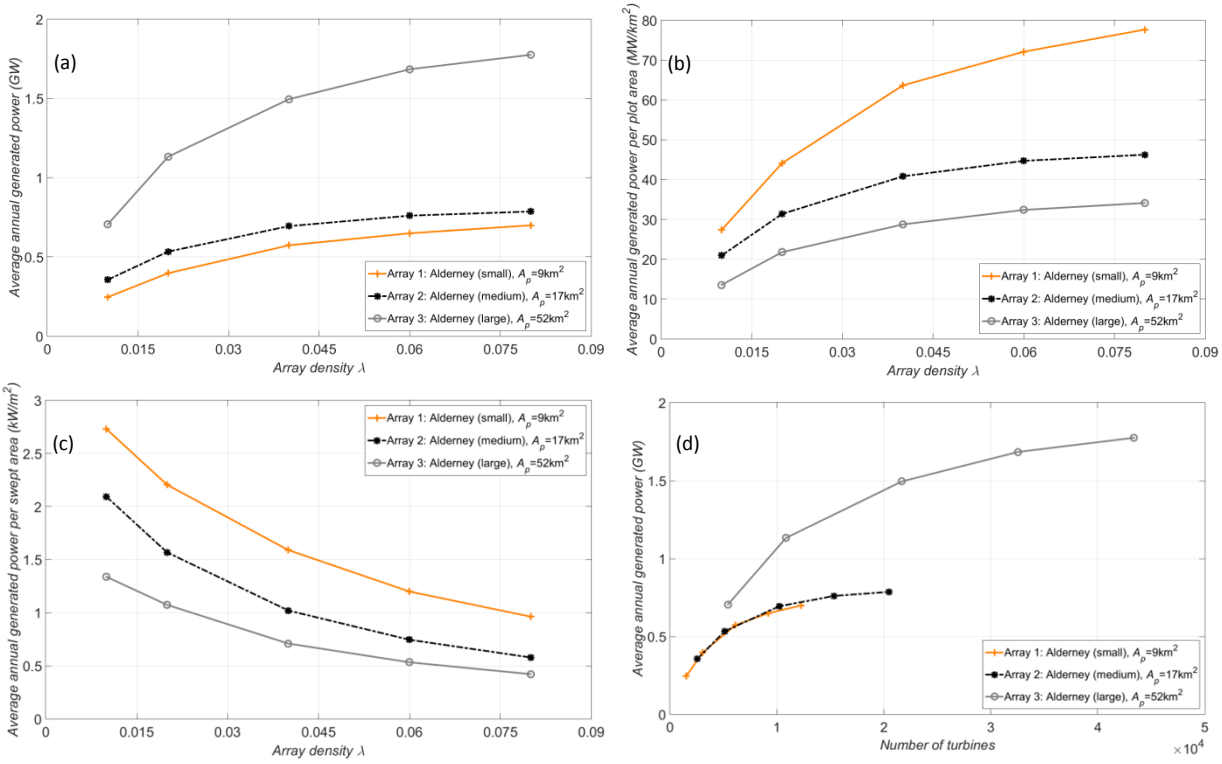

Figure 6 (a). Average annual generated power for Array plots 1 (small), 2 (medium and 3 (large) in Alderney Race with increasing array density, (b) Average annual generated power per plot area with increasing array density for Array plots 1 (small), 2 (medium and 3 (large) in Alderney Race, (c) Mean annual generated power per swept area for array plots 1, 2 and 3 with increasing array density, (d) Mean annual generated power for array plots 1, 2 and 3 for increasing array density in terms of the number of turbines assuming turbine diameter takes up 1/3 of mean sea depth.

Another efficiency indicator is the average annual generated power per swept area A_s, which as discussed, has been used in the literature to compare the performance of tidal farms with that of offshore windfarms (Adcock et al. 2013). For comparison, the London Array, currently the world's largest offshore windfarm, generated 0.25kW/m^2 during a maximum efficiency period in December 2015 (London Array 2016). Figure 6c shows the power per swept area of Arrays 1, 2 and 3. Since Array 1 is positioned in ambient flows that exceed $\bar{P}_{\eta,KF}$=3 kW/m^2, the power per swept area of Array 1 remains above 1 kW/m^2 (i.e. far exceeding that of the London Array) over the majority of the array density range, only dropping below 1 kW/m^2 for array density λ>0.075 (Figure 6c). At this limit using array density λ=0.075, the average annual generated power is estimated to be 0.67 GW. Encouragingly, at lower array density this 1 kW/m^2 limit is far exceeded, where for array density λ=0.01, the mean annual power per swept area is 2.75 kW/m^2, over ten times that of the maximum achieved by the London Array . Under this array configuration (λ=0.01) the tidal array generates an average annual power of 0.25 GW, 4% higher than the average generated power of London Array during its maximum efficiency period. Further performance comparisons with the London Array are discussed in §4c.

For Array 2 the average generated power per swept area exceeds 1 kW/m^2 for array density λ<0.04, where the average generated power reaches 0.69 GW for λ=0.04. The maximum acceptable array density to achieve an average power per swept area greater than 1 kW/m^2 for Array 2 is lower than for Array 1 because Array 2 has some turbines positioned in lower ambient energy flow, where $\bar{P}_{\eta,KF}$ exceeds 2 kW/m^2 instead of the 3 kW/m^2 for Array 1. Similarly, the maximum acceptable array density to achieve an average power per swept area of 1 kW/m^2 drops further for Array 3 to λ<0.02, where for λ=0.02 Array 3 generates an average power of 1.1 GW.

An assessment of energy extraction in the Pentland Firth (Adcock et al. 2013) based the viability of adding turbines to an array on the mean annual power per swept area of the *added* turbines only. This assumed the added turbines must exceed the upper bound limit of available power of offshore windfarms of 1kW/m^2 to be commercially viable. This approach was adopted here, with results presented in Table 3. For Array 1, this condition is met for array density not exceeding λ=0.04, but fails if array density is increased further. Using Array 1 with density λ=0.04 gives an average annual generated power of 0.55 GW. For Array 2 this condition is met for array density not exceeding λ=0.02, which gives an average annual generated power of 0.53 GW. For Array 3 this condition is only met for array density λ=0.01, giving an average annual generated power of 0.71 GW.

Table 3. Incremental increase in mean annual generated power and mean added power per added swept area for energy extraction using Arrays 1, 2 and 3 in Alderney Race.

Array	Array density increment	Increase in mean power (GW)	Mean added power/added swept area (kW/m^2)
1	0.01 to 0.02	0.15	1.67
1	0.02 to 0.04	0.17	0.98
1	0.04 to 0.06	0.07	0.42
1	0.06 to 0.08	0.05	0.28
2	0.01 to 0.02	0.18	1.05
2	0.02 to 0.04	0.16	0.47
2	0.04 to 0.06	0.07	0.21
2	0.06 to 0.08	0.03	0.09
3	0.01 to 0.02	0.42	0.81
3	0.02 to 0.04	0.36	0.34
3	0.04 to 0.06	0.19	0.18
3	0.06 to 0.08	0.09	0.08

The total number of turbines within each array is another important consideration since each individual device will require manufacturing, installation, cabling, commissioning, maintenance, and decommissioning operations to be completed during the project lifetime. A higher number of turbines could increase the number of operations necessary to keep the array generating power, hence increasing the cost of energy. This is especially prevalent given that the diameter of tidal turbines is restricted by depth, meaning that in comparison with a windfarm, a higher number of smaller turbines will be needed to achieve the same total swept area.

The total number of turbines within Arrays 1, 2 and 3 were estimated, where given the considerable spatial variation in depth within each array, it was assumed that each array contains turbines of different diameters. It was further assumed that the centroid height of each turbine (i.e. the hub height) is positioned at mid depth based on mean sea level and that each turbine diameter is equal to 1/3 of the flow depth (also based on mean sea level). Physically this means that to achieve a predefined uniform array density, in the shallower waters such as within Array 1 a high number of smaller diameter turbines are used whilst in deeper waters such as through the central channel of Alderney Race, a lower number of larger diameter turbines are used. The results of these considerations are shown in Figure 6d.

Parts of Array 1 are positioned in relatively shallow depths, where ambient mean sea level goes as low as 15 m (shown in Figure 2). For this reason Array 1 uses a relatively large number of smaller diameter turbines to generate power. For example, Array 1 with density λ=0.01 uses 1530 turbines to generate a time averaged power of 246 MW, equivalent to 0.16 MW/turbine. For comparison, the London Array uses 175 turbines to generate approximately the same time averaged power of 240 MW, equivalent to 1.37 MW/turbine. Array 3 also covers these shallow regions also covered by Array 1, however Array 3 also covers regions of higher flow depths in the central channel of the Race, up to 74 m. In these deeper regions larger turbine diameters can be adopted so that Array 3 is able

to use fewer, larger turbines to achieve the same uniform array density in comparison with the shallow regions covered by Array 1. This means that Array 3 with density λ=0.01 generates a time averaged power of 0.71 GW, approximately the same level as Array 1 using the highest array density (λ=0.08), but with 5425 turbines, 6800 less turbines than Array 1. Whilst velocities in the deeper West Race tend to be lower than the shallower East Race, these deeper waters in the West Race may be a more attractive proposition for developers who wish to minimise the number of turbines within an array, hence minimising the likely number of installation, maintenance and decommissioning operations without compromising on generated power output.

As the array density of Array 3 is increased, the number of turbines increases drastically, where for the maximum array density case (λ=0.08) Array 3 contains over 40,000 turbines to achieve an average annual power generation of 1.8 GW! This seems like an unrealistic number of turbines to be able to install, operate and maintain, adding complication that would inevitably push up the cost of energy.

c. Performance comparisons with a large offshore windfarm

To give a sense of the scale of the estimates of generated power presented above, Table 4 summarises the characteristics and performance of Array 1, 2 and 3 in comparison with the London windfarm array (London Array), the world's largest offshore windfarm currently in operation. For this analysis the maximum array densities that achieve a time averaged power per *added* swept area greater than 1 kW/m^2 are considered, as summarised in Table 3. (I.e. Array 1 with λ=0.01 and λ=0.04, Array 2 with λ=0.02 and Array 3 with λ=0.01).
Array 1 with array density λ=0.01 (Table 4, column 2) gives a mean generated power of 246 MW, approximately the same as that of the London Array (240 MW). However, Array 1 achieves this over an array plot area one tenth the size of the London Array and with half the array density. The mean generated power per swept area is 2.73 kW/m^2, which is over ten times that of the London Array. This is achieved with approximately 1534 turbines, nearly nine times the number of devices used by the London Array.

Increasing Array 1's array density to λ=0.04 (Table 4, column 3) gave an increase in mean generated power of 133% to 573 MW, reducing mean generated power per swept area by 27% to 1.59 kW/m^2. As discussed in §4b, any further increase in array density reduces the power per swept area of the added turbines below the 1 kW/m^2 threshold set in the literature (Adcock et al. 2013; London Array 2016). Array density λ=0.04 corresponds to a lateral spacing between devices of 2 diameters (tip-to-tip) and longitudinal spacing between rows of just 6.5 diameters. This makes it unlikely that array density will exceed this value in reality as sufficient space is needed between rows to allow for wake recovery (Coles et al. 2016). to ensure array efficiency in terms of generated power per swept area is maintained.

Table 4 also shows the performance of Array 2 using array density λ=0.02 (column 4), which was the upper limit for added turbines exceeding an average annual power per swept area of 1kW/m^2 discussed in §4b. In this case the average annual power generated by the tidal array is 533 MW, approximately double that of the London Array and only 7% lower than Array 1 with λ=0.04. The advantage of Array 2 (λ=0.02) over Array 1 (λ=0.04) is that it uses 1016 less turbines to generate approximately the same power, giving a time averaged generated power per turbine of 104 kW, 12% higher than Array 1 with λ=0.02.

In Table 4, Array 3 with λ=0.01 generates a time averaged power of 0.71 GW, the largest output of all the arrays considered here. This is achieved with a power/swept area of 1.34 kW/m^2 using 5425 turbines. This is the largest array featured, covering a plot area of 52 km^2, so is the least spatially

efficient tidal array with an average power per plot area of 14 MW/m^2. However its power output is still nearly six times that of the London Array.

Table 4. Comparison between the characteristics and performance of Array 1: Alderney (small) using array density λ=0.01, and λ=0.04, Array 2 with λ=0.02 and Array 3 with λ=0.01 and the London Array, the world's largest offshore windfarm.

	Array 1 (λ=0.01)	Array 1 (λ=0.04)	Array 2 (λ=0.02)	Array 3 (λ=0.01)	London array
Array characteristics					
Array plot area, A_p (km^2)	9	9	17	52	100
Turbine swept area, A_s (m^2)	176-1256	176-1256	176-1256	176-1256	11309
No. turbines, n	1534	6136	5120	5424	175
Array density, λ	0.01	0.04	0.02	0.01	0.02
Total swept area, nA_s (m^2)	$9x10^4$	$3.6x10^5$	$3.4x10^5$	$5.2x10^5$	$1.9x10^6$
Array performance					
Average power output (MW)	246	573	533	705	240*
Average power per swept area (kW/m^2)	2.73	1.59	1.57	1.34	0.25*
Average power per plot area (MW/km^2)	27	64	31	14	2.4*
Average power output per turbine (kW)	160	93	104	129	1371*

*Achieved during maximum efficiency period over December 2015, giving a power output of 369 GW h (London Array 2016).

Comparison with the performance of the London Array highlights the ability for tidal turbine arrays in Alderney Race to generate significant electrical power over a relatively small array plot area in comparison with large offshore windfarms. This high spatial efficiency can be advantageous from a spatial planning point of view, where at sites such as Alderney Race the activities of other sea users and industries are an important determining factor in array design. Utilising the highly energetic flows concentrated at specific areas such as within Array 1 can allow other regions of Alderney Race to be left in their current state. However, whilst the total swept area of the tidal arrays considered here is significantly less than the London Array, unlike wind energy extraction, tidal turbines are depth (bathymetry) constrained, hence tidal arrays require significantly more turbines at much lower rated capacities.

In order to ascertain the appropriateness of such large scale tidal turbine deployment, the relevant installation, operation and maintenance costs of a typical tidal turbine array will need to be established and modelled. As such information is unfortunately not currently available, as well as the uncertainty over the future financial support mechanisms for tidal energy, it is difficult to predict how many turbines could feasibly be installed at an economically acceptable cost.

d. Temporal variation in generated power and its transmission

As indicated earlier, most of the generated power from Alderney Race will have to be exported to high demand areas in the UK and France through the FABlink interconnector. Hence an understanding of the variability of power generation will be needed to ascertain the temporal variation in exported power and how this can be combined with the export of electrical power from other sources. Figure 7 shows the temporal variation in generated power over a one day period that includes the time of maximum power generation during spring tide using two of the arrays considered previously in §4c, Table 4 (Array 1: Alderney (small) with array density λ=0.04 and Array 3: Alderney Race (large) using array density λ=0.01).

Power generation using Array 1 reached a maximum value of 2.5 GW during the dominant spring ebb tide. This is 0.3 GW less than the 2.8 GW capacity of the proposed FABlink interconnector (Nauclér 2016) joining France, Alderney and Britain (where 1.4 GW of electrical power can be exported from Alderney to France and another 1.4 GW from Alderney to Britain as shown in Figure 1). This assumes that at spring tide the interconnector will not be used for exporting any other electrical power, which would use up some of its capacity. Similarly, power generation using Array 3 with array density λ=0.01 achieved a maximum power generation of 2.7 GW, just 0.1 GW below the 2.8 GW capacity of the proposed FABlink interconnector.

Since at spring tide the arrays considered here generate power close to the maximum capacity of FABlink, it may be necessary in the future to supplement tidal energy development with energy storage, assuming that some capacity will be taken up by the import/export of electrical power from other sources. Given that currently to the best of the authors knowledge there is no converter station planned for Alderney, this may be an important consideration if it is assumed an optimistic level of tidal energy development will be realised in the future. This is also important given that tidal energy development of neighbouring sites such as Casquets could increase power generation over the maximum capacity of the interconnector. Power generation using Array 4 in Casquets is quantified in §4f.

Figure 7 shows that for Array 1, there is a strong asymmetry between the power generated during the flood tide (P_f) and the following ebb tide (P_e) using Array 1. During spring tide, the power generated on the ebb tide is P_e=2.5 GW, 55% greater than that generated during the previous flood tide (P_f=1.6 GW). This is because there is a significant difference in velocities between the ebb and flood tide within Alderney Race, where spring ebb flows typically reach 5 m/s whilst flood velocities typically reach 3.5 m/s. Since power is a function of the velocity cubed, small differences between the ebb and flood tide velocities will lead to significant asymmetry in power generation between the ebb and flood tide.

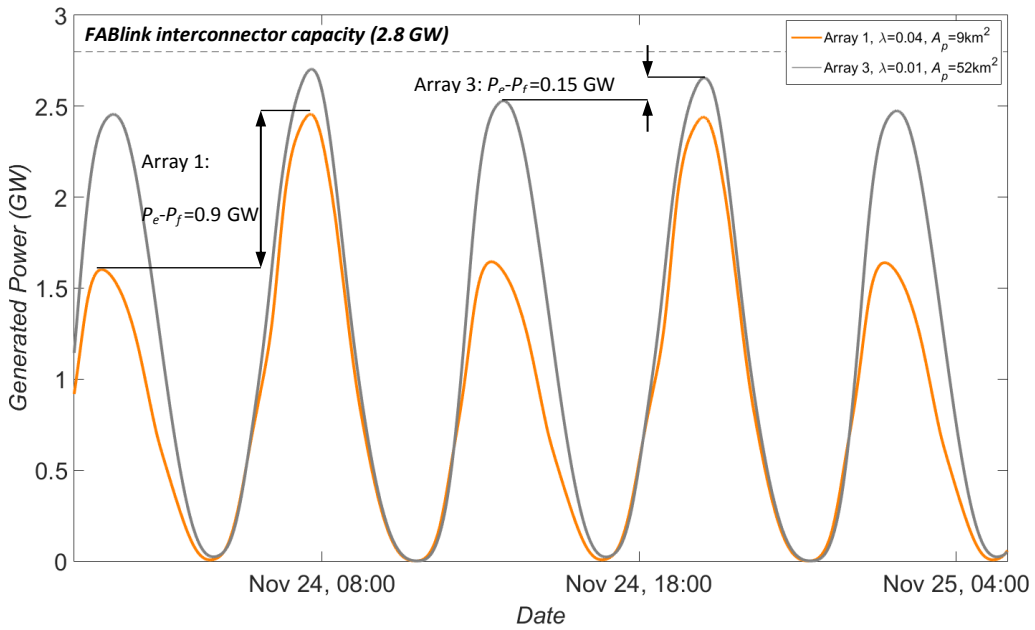

Figure 7. Temporal variation in generated electrical power using Array 1 and Array 3 over two flood ebb tidal cycles, which includes the time of maximum power generation during spring tide. Array 1 has an array density λ=0.04 whilst Array 3 has an array density λ=0.01.

For Array 3, there is a greater symmetry between the power generated over an ebb flood cycle in comparison with Array 1, where the power generated by Array 3 during the dominant spring ebb tide, P_e=2.70 GW, was up to 7% greater than the power generated during the previous flood tide

(P_f=2.55 GW) (Figure 7). This is because Array 3 covers a greater area, over which the average velocities show less asymmetry over an ebb-flood cycle. To demonstrate this, the ambient velocities within each of the array plot areas where extracted from the model results and averaged at each time step. Table 5 summarises the results, showing the maximum average velocity within Array plots 1, 2 and 3 during a spring flood and spring ebb tide. Results show that the difference between the ambient average velocities within Arrays 1, 2 and 3 is 0.35 m/s, 0.23 m/s and 0.05 m/s respectively.

Table 5. Comparison between the average ambient spring flood and following ebb flow velocity within Array plots 1,2 and 3.

Array	Max. average spring flood flow velocity (m/s)	Max. average spring ebb velocity (m/s)	Difference (m/s), (%)
1	4.72	4.37	0.35, 7.4
2	4.45	4.22	0.23, 5.2
3	3.55	3.50	0.05, 1.5

During neap tide flow velocities within Alderney Race are significantly lower in comparison with spring tides, reducing the available power. Table 6 summarises the maximum generated power from the arrays considered previously in §4c at times of spring and neap tide. The greatest difference between maximum spring/neap power generation was using Array 3 (λ=0.01), where the maximum power generated during spring tide was 2.7 GW, 2.29 GW higher than during neap tide.

Table 6. Comparison between the maximum generated power during spring and neap tide using Array 1 (λ=0.01 and λ=0.04), Array 2 (λ=0.02) and Array 3 (λ=0.01).

Array	Array density, λ	Maximum generated power during spring tide (GW)	Maximum generated power during neap tide (GW)	Difference (GW), (%)
1	0.01	0.88	0.15	0.73, 83
1	0.04	2.48	0.39	2.09, 84
2	0.02	1.75	0.22	1.53, 87
3	0.01	2.70	0.41	2.29, 85

e. Changes to the ambient flow field

Blockage by large arrays positioned in the flow in Alderney Race will cause an increase in hydraulic resistance in the region covered by the array, causing flow to divert around the array, following a path of less resistance. This is an important consideration when developing sites because such flow diversion will (a) alter the surrounding tidal resource, affecting the performance of other closely located arrays and (b) may cause detrimental environmental impacts such as sediment transport effects within Alderney Territorial Waters (Haynes 2015). This former point is important given that the Alderney Race is split into French and Alderney territorial waters, meaning that tidal development within French waters could have an impact on the tidal resource within Alderney territorial waters and vice versa. Here we quantify such impacts for the arrays discussed in §4c (Array 1 with λ=0.01, Array 1 with λ=0.04, Array 2 with λ=0.02 and Array 3 with λ=0.01).

Figure 8a shows that energy extraction using Array 1 (array density λ=0.01) causes a large wake region downstream, where the mean flow velocity distribution shows a region of reduced average flow velocity stretching 11 km downstream of the array (in both the ebb and flood direction). There are only very small regions where the mean flow shows increased average velocities (in the red regions) compared with the ambient case, located to the East of the array. Therefore the array, which is located in French territorial waters, does not have a significant impact on the flow within Alderney territorial waters to the West, where the volume flux through the cross section within Alderney territorial waters compared with the ambient case (i.e. Q_0) is Q/Q_0=1. In this case, the maximum increase in flow velocity reached 1 m/s at times of spring ebb tide in comparison with the ambient case in the region to the East of Array 1.

When the density of Array 1 was increased to λ=0.04, there was a significant increase in the flow velocities within Alderney territorial waters (Figure 8b), caused by the increase in hydraulic resistance from added turbines within Array 1's plot area. This gave an increase in the average volume flux through the cross section within Alderney territorial waters in comparison to the ambient case, giving Q/Q_0=1.05. The region of enhanced flow velocity between Array 1 and the French coast (i.e. East of Array 1) has also increased in comparison to the previous case (Array 1 with λ=0.01) so that it now covers an area of 1.7 km^2. Within this region there were times when flow velocities increased to greater than 2 m/s above the ambient case during spring ebb tide.

The wake length downstream of Array 1 (λ=0.04) also increased, so that the region of decreased flow velocity distribution compared with the ambient case now extends to 15 km (both in the ebb and flood direction). There are also regions of increased average velocity distribution within Casquets on the opposite side of Alderney, increasing the average volume flux through this region to Q/Q_0=1.02, improving the resource for energy extraction. This effect is investigated in more detail below in §4f using simulations of simultaneous energy extraction at Alderney Race and Casquets to compare with energy extraction in Casquets only. There are also regions of increased velocity in the region between Alderney Race and Sark, which is approaching Big Roussel, the channel located between the islands of Herm and Sark, which has also been identified as a site suitable for tidal energy development based on suitable depths and flow velocities.

In general, for energy extraction using Array 1, flow is diverted into the open section of Alderney Race through the central channel, keeping the overall mean volume flux through the entire cross section of Alderney Race within 10% of the natural regime over all array densities (i.e. up to λ=0.08). However, further work is needed to understand the environmental impact of these flow accelerations within Alderney Race.

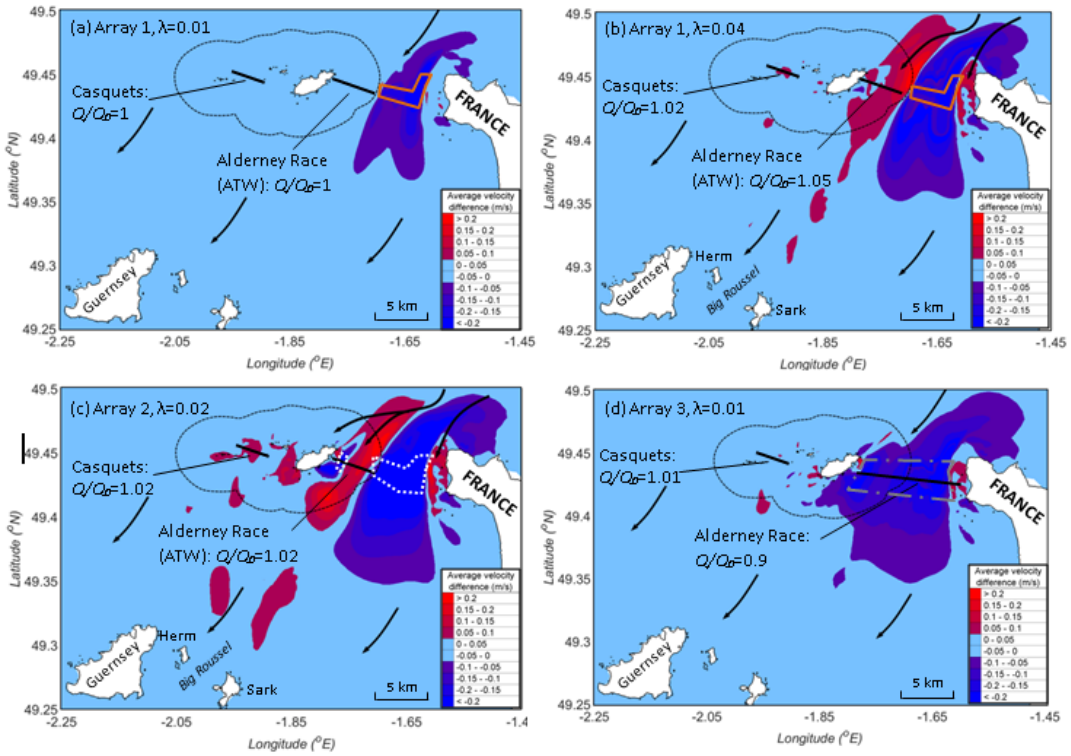

Figure 8. Mean velocity difference plot between the ambient case and energy extraction using (a) Array 1 with array density λ=0.01 (b) Array 1 with array density λ=0.04 (c) Array 2 with array density λ=0.02 and (d) Array 3 with array density λ=0.01. The change on average volume flux through Alderney Territorial Waters (ATW) within Alderney Race, the entire width of Alderney Race and Casquets are also shown, along with the outline of Alderney Territorial Waters. Arrows show the direction of the dominant ebb tide and the general nature of flow diversion caused by energy extraction.

Energy extraction using Array 2 with array density λ=0.02 (Figure 8c) also creates a region of increased average flow velocity within Alderney Race, between the large East Race array and the smaller West Race array. This increases the average volume flux through the cross section within Alderney territorial waters relative to the ambient case to Q/Q_0=1.02. In comparison with the ambient case, at times of spring ebb tide, flow velocities either side of Array 2 exceeded the ambient flows by over 2 m/s. Energy extraction using Array 2 also increased the region of enhanced flow velocity distribution at Casquets, increasing the volume flux through the cross section through Casquets in comparison with the ambient case to Q/Q_0=1.02. The region of reduced average flow velocity extends 15 km downstream of the East Race array in both the ebb and flood directions, exceeding that of Array 1.

As mentioned in §1, there are plans for a 300 MW array to be installed within Alderney Territorial Waters (ATW). In (ABPmer 2013) it is assumed that by using a turbine spacing of 40 m x 200 m, which is equivalent to an array density of λ=0.025, there will be no interaction between turbines. However, Figure 8c show this assumption to be invalid, since energy extraction using Array 2 with array density λ=0.02 causes a significant change in velocities across Alderney Race. Whilst the total plot area of Array 2 is significantly larger than that of the proposed 300 MW array, the small array in the West Race for energy extraction scenario 2 (listed in Table 2) is not, and still shows a reduction in velocities in and downstream of the array. This result highlights the need for further detailed investigation into the interaction between the flow and the proposed 300 MW array so that accurate power estimations can be made.
Energy extraction using Array 3 with density λ=0.01 reduced the average volume flux through the entire cross section of Alderney Race to Q/Q_0=0.9 (Figure 8d). Regions of increased average flow velocities are limited to small patches neighbouring the French coast directly to the East of Array 3, close to the North East tip of Alderney within Alderney Race and within Casquets. Within these regions at times of spring ebb tide, flow velocities exceeded ambient flow velocities by up to 1.8 m/s. The average volume flux through Casquets compared with the ambient case was Q/Q_0=1.01.

f. Interactions between the Casquets and Alderney Race sites

Array 4 covers an area of 3 km^2 in Casquets over the region of highest ambient flow, where $\bar{P}_{\eta,KF}$>1 kW/m^2 (shown in Figure 5). Results in Figure 9 show that for array density λ=0.01, the time averaged generated power by Array 4 is 38 MW with $\bar{P}_{\eta}$=1.3kW/m^2. When array density was increased to λ=0.02, the efficiency of the added turbines $\bar{P}_{\eta}$=0.62 kW/m^2, below the limit of 1 kW/m^2 set out in this work.

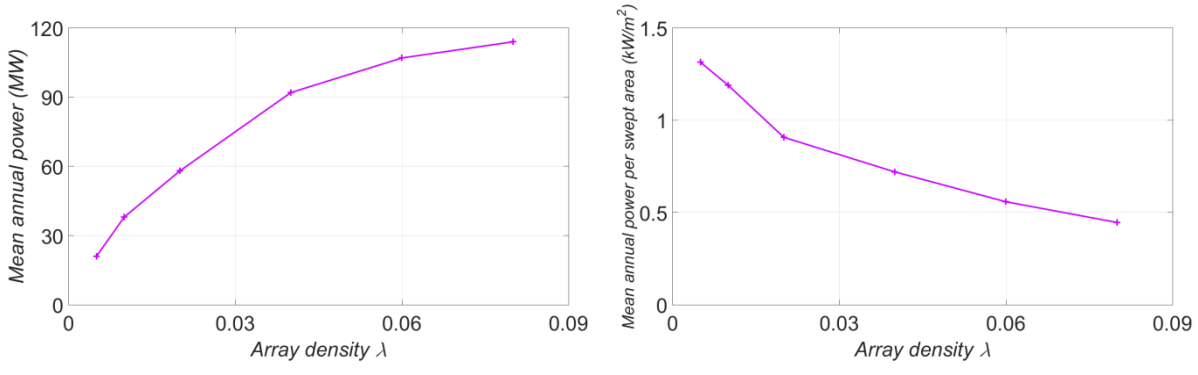

(a) (b)

Figure 9. (a) Mean annual generated power for Array plot 4 located in Casquets in the absence of energy extraction in Alderney Race. (b) Mean annual generated power per swept area for array plot 4 with increasing array density in the absence of energy extraction in Alderney Race.

In §4e it was shown that energy extraction in Alderney Race using Arrays 1 and 2 caused flow diversion into Casquets, increasing flow velocities within Casquets. To quantify the effect of energy extraction in Alderney Race on energy extraction using Array 4 in Casquets, a comparison was made between the power generated by Array 4 in Casquets without energy extraction in Alderney Race (i.e. the results presented in Figure 9) and simultaneous energy extraction using Array 1 (in Alderney Race) and Array 4 in Casquets. When energy extraction was simulated using Array 1 (with array density λ=0.04) and Array 4: Casquets simultaneously, the mean power output of Array 4 increased by 6 MW compared with Array 4 on its own, an increase of 15%. The distributed drag associated with Array 1: Alderney diverts flow around Alderney Race and into Casquets, resulting in a 2% increase in volume flux through the cross section of Array 4: Casquets aligned perpendicular to the flow (Figure 8). This increases the energy available in the flow ($\bar{P}_{\eta,KF}$) at Casquets for extraction when Array 4: Casquets is added. The mean power output of Array 1 remained unchanged with energy extraction at Casquets because the drag associated with Array 4: Casquets is not large enough to cause a significant change in flow through Alderney Race.

This result shows that for the energy extraction scenarios (Table 2) considered here, energy extraction at Alderney Race is independent of energy extraction at Casquets, however the reverse is not true. Table 7 shows that for Array 1: Alderney (small) and Array 4: Casquets, if Casquets was considered on its own it would lead to a 15% underestimation of generated power at Casquets. However this is still less than 1% of the power generated by Array 1: Alderney (small).

Table 7. Mean generated power using combinations of Array 1: Alderney (small) with array density λ=0.04 and Array 4: Casquets with λ=0.01.

	Alderney	Casquets	Total (MW)
Array 1: Alderney (small)	573	-	573
Array 4: Casquets	-	38	38
(Array 1: Alderney (small))+ Array 4: Casquets	572	44	614

During spring ebb tide the maximum combined power of Arrays 1 and 4 reached 2.68 GW, where Array 1 generated 2.5 GW and Array 4 generated 0.18 GW. Therefore the upper capacity limit of the FABlink interconnector of 2.8 GW is not exceeded, as was the case for energy extraction in Alderney Race only (shown in Figure 7). However this still assumes the interconnector will not be used for exporting electrical power from other sources at these times.

5. Conclusions

A 2D hydrodynamic model of the English Channel was used to simulate energy extraction using large tidal turbine arrays located in Alderney Race and Casquets. Arrays were positioned and sized based on the distribution of time averaged ambient available power, with the most energetic flows located in the shallower East Race in French Territorial Waters (FTW). Our results indicate that the time-averaged available power exceeded 1 kW/m^2 (the power available at offshore wind sites around the UK) over a much larger area of 52 km^2, both in French and Alderney Territorial Waters (ATW). Of the 48 tidal energy development blocks set out by Alderney Renewable Energy (ARE) within ATW's, only 22 had a time averaged available power greater than 1 kW/m^2, including 13 of 19 within Alderney Race.

In comparison with the power performance of the London Array, the world's largest offshore windfarm, in general the tidal arrays were more spatially efficient, generating a greater power per plot area and power per swept area. For example, a 9 km^2 tidal array (Array 1) located in the most energetic flows in the East of Alderney Race (in FTW) yielded a mean generated power of 0.25 GW, 25% greater than that of the London Array. The tidal array did this using only 9% of the plot area and

20% of the total swept area of the London Array. However, given that tidal turbine sizing is restricted by depth, this was achieved using approximately nine times the number of turbines. At times of spring ebb tide, the tidal array increased the flow velocities within ATW's by up to 1 m/s, however the overall volume flux though ATW remained relatively unchanged in comparison with the ambient case.

Increases in array density had a significant impact on the surrounding flow dynamics within Alderney Race and Casquets. For example increasing Array 1's density to λ=0.04 gave an increase in flow velocities within ATW's of up to 2 m/s, increasing the average volume flux through both a cross section of ATW and Casquets to Q/Q_0=1.02. This is an important finding given that in Alderney Race, tidal plots within ATW and FTW are currently being developed separately, with no clear consideration of the potential site-site interaction that could occur. Encouragingly results in this work indicate that from a power generation point of view, it is beneficial to develop Alderney Race (both ATW and FTW) and Casquets together, as the total power generated using all three sites is greater than the sum of its parts.

If large scale tidal energy development is to take place in Alderney Race and Casquets, developers and regulators from France and Alderney must collaborate to accurately quantify these effects. Only then can the positive impacts of tidal energy development within Alderney Race and Casquets be assessed, leading to the most suitable development of tidal power in the region.

Acknowledgments

This work is part of the activities of the Energy and Climate Change Division and the Sustainable Energy Research Group at the University of Southampton (www.energy.soton.ac.uk). It is also supported by EPSRC under the Supergen Marine research programme. We also wish to extend our thanks to Alderney Commission for Renewable Energy (ACRE) and Alderney Renewable Energy Ltd (ARE) for the supply of bathymetry data in Alderney Race and AWAC flow data, which were used for validating the English Channel Model.

References

[1] ABPmer, "Alderney Regional Environmental Assessment of Renewable Energy: Scoping Report," 2013.
[2] Race Tidal, "Race Tidal Alderney," http://www.openhydro.com/download/OPENHYDRO-RACE-TIDAL-PROJECT-FACT-SHEET.pdf, 2014.
[3] S. W. Funke, S. C. Kramer, and M. D. Piggott, "Design optimisation and resource assessment for tidal-stream renewable energy farms using a new continuous turbine approach," Renew. Energy, vol. 99, pp. 1046–1061, 2015.
[4] D. S. Coles, L. S. Blunden, and A. S. Bahaj, "Estimates for the power potential from tidal flows at Alderney Race (Raz Blanchard), Casquets and Big Roussel in the Channel Islands," Energy, Elsevier, no. In review, 2016.
[5] A. S. Balsells, "Management of the Electricity Supply in Alderney," MSc Thesis, Cranfield University, 2015.
[6] C. S. Nauclér, "FAB France Alderney Britain Interconnector, Project Summary," FAB Link Ltd, 2016.
[7] Energy Technology Support Unit, "Tidal Stream Energy Review," Technical report ETSU-T/05/00155/REP, Harwell Laboratory, 1993.
[8] A. S. Bahaj and L. Myers, "Analytical estimates of the energy yield potential from the Alderney Race (Channel Islands) using marine current energy converters," Renew. Energy, Elsevier, vol. 29, no. 12, pp. 1931–1945, Oct. 2004.

[9] L. Myers and A. S. Bahaj, “Simulated electrical power potential harnessed by marine current turbine arrays in the Alderney Race,” Renew. Energy, Elsevier, vol. 30, no. 11, pp. 1713–1731, Sep. 2005.
[10] Black and Veatch, “Phase II UK Tidal Stream Energy Resourse Assessment,” pp. 10-31, Report comissioned by the Carbon Trust, 2005.
[11] Black and Veatch, “UK Tidal Current Resource and Economics,” pp. 15-45, Report commissioned by the Carbon Trust and npower, Project number 121393, 2011.
[12] R. Vennell, S. W. Funke, S. Draper, C. Stevens, and T. Divett, “Designing large arrays of tidal turbines: A synthesis and review,” Renew. Sustain. Energy Rev. Elsevier, vol. 41, pp. 454–472, 2015.
[13] D. M. Culley, S. W. Funke, S. C. Kramer, and M. D. Piggott, “Integration of cost modelling within the micro-siting design optimisation of tidal turbine arrays,” Renew. Energy, Elsevier, vol. 85, pp. 215–227, 2016.
[14] European Commission, “The exploitation of tidal marine currents,” pp. 20-25, ISBN 92-827-5658-0, Report EUR 16683 EN, 1996.
[15] C. Garrett and P. Cummins, “The power potential of tidal currents in channels,” Proc. R. Soc. A, R. Soc., vol. 461, pp. 2563–2572, 2005.
[16] D. Coles, L. Blunden, and A. Bahaj, “Energy extraction potential from the Alderney Race,” in 11th European Wave and Tidal Energy Conference, 2015, pp. 1–9.
[17] V. T. Nguyen, S. S. Guillou, and Cruz, “Numerical Simulation of a Pilot Tidal Farm Using Actuator Disks, Influence of a time-varying current direction,” in Grand Renewable Energy 2014 Proceedings, 2010, p. O-Oc-6-1.
[18] O. A. Lo Brutto, J. Thiebot, S. S. Guillou, and H. Gualous, “A semi-analytic method to optimize tidal farm layouts - Application to the Alderney Race (Raz Blanchard), France,” Appl. Energy, vol. 183, pp. 1168–1180, 2016.
[19] J. Thiebot, P. Bailly du Bois, and S. Guillou, “Numerical modeling of the effect of tidal stream turbines on the hydrodynamics and the sediment transport - Application to the Alderney Race (Raz Blanchard), France,” Renew. Energy, Elsevier, vol. 75, pp. 356–365, 2015.
[20] Black and Veatch, “UK Tidal Current Resource & Economics : Appendix C,” pp. 24-52, Report commissioned by the Carbon Trust and npower, Project number 121393, 2011.
[21] G. Egbert and L. Erofeeva, “http://volkov.oce.orst.edu/tides/atlas.html,” OSU Tidal Data Inversion, [Date Accessed: 07/06/2014], 2014. .
[22] S. Draper, T. A. Adcock, A. G. L. Borthwick, and G. T. Houlsby, “Estimate of the tidal stream power resource of the Pentland Firth,” Renew. Energy, Elsevier, vol. 63, pp. 650–657, Mar. 2014.
[23] TCarta, “http://www.tcarta.com/home/,” [Date Accessed: 16/06/2014], 2014. .
[24] D. C. Kapoor, “General bathymetric chart of the oceans (GEBCO),” Mar. Geod. Taylor Fr., vol. 5, no. 1, pp. 73–80, 1981.
[25] T. A. A. Adcock, S. Draper, G. T. Houlsby, A. G. L. Borthwick, and S. Serhadlıoğlu, “The available power from tidal stream turbines in the Pentland Firth,” Proc. R. Soc. A, R. Soc., vol. 469, no. 2157, pp. 72–93, 2013.
[26] D. R. Plew and C. L. Stevens, “Numerical modelling of the effect of turbines on currents in a tidal channel – Tory Channel, New Zealand,” Renew. Energy, Elsevier, vol. 57, pp. 269–282, Sep. 2013.
[27] R. A. Walters, M. R. Tarbotton, and C. E. Hiles, “Estimation of tidal power potential,” Renew. Energy, Elsevier, vol. 51, pp. 255–262, Mar. 2013.
[28] A. S. Bahaj, A. F. Molland, J. R. Chaplin, and W. M. J. Batten, “Power and thrust measurements of marine current turbines under various hydrodynamic flow conditions in a cavitation tunnel and a towing tank,” Renew. Energy, Elsevier, vol. 32, no. 3, pp. 407–426, Mar. 2007.
[29] D. S. Coles, L. S. Blunden, and A. S. Bahaj, “Experimental validation of the distributed drag method for simulating large marine current turbine arrays using porous fences,” Int. J. Mar. Energy, Elsevier, vol. 16, no. 16, pp. 298–316, 2016.

[30] London Array, “Renewable Energy Record Achieved at London Array,” 2016. [Online]. Available: http://www.londonarray.com/project/renewable-energy-record-achieved-at-london-array/. [Accessed: 04-May-2016].
[31] A. S. Bahaj and L. E. Myers, “Shaping array design of marine current energy converters through scaled experimental analysis,” Energy, Elsevier, vol. 59, pp. 83–94, 2013.
[32] S. G. Haynes, “The Effects of Array Installation upon the Morphology of a Headland Associated Linear Sandbank,” pp 49-55, PhD: Transfer report, University of Southampton, UK, 2015.